The Study of Diffuse Warm - Hot Gas using Quasar Absorption Line Spectroscopy

A thesis submitted
in partial fulfillment for the degree of

Doctor of Philosophy

by

SACHIN PACHAT

Department of Earth & Space Sciences
INDIAN INSTITUTE OF SPACE SCIENCE AND TECHNOLOGY
Thiruvananthapuram - 695547

June 2018

CERTIFICATE

This is to certify that the thesis titled **The Study of Diffuse Warm - Hot Gas using Quasar Absorption Line Spectroscopy**, submitted by **Sachin Pachat**, to the Indian Institute of Space Science and Technology, Thiruvananthapuram, for the award of the degree of **Doctor of Philosophy**, is a bona-fide record of the research work done by him under our supervision. The contents of this thesis, in full or in parts, have not been submitted to any other Institute or University for the award of any degree or diploma.

Dr. Anand Narayanan
Supervisor
Address

Place: Thiruvananthapuram
June 2018

Counter signature of HOD with seal

DECLARATION

I declare that this thesis titled **The Study of Diffuse Warm - Hot Gas using Quasar Absorption Line Spectroscopy** submitted in fulfilment of the Degree of Doctor of Philosophy is a record of original work carried out by me under the supervision of **Dr. Anand Narayanan**, and has not formed the basis for the award of any degree, diploma, associateship, fellowship or other titles in this or any other Institution or University of higher learning. In keeping with the ethical practice in reporting scientific information, due acknowledgements have been made wherever the findings of others have been cited.

Sachin Pachat
SC13D013

Place: Thiruvananthapuram
June 2018

ACKNOWLEDGEMENTS

When I joined IIST for Ph.D., I had absolutely no idea what I was supposed to do here. After four years, when I look back, I can see a long way behind me. Many thanks to my research supervisor Dr. Anand Narayanan for leading me generously through the unknown. His insights, patience, and passion helped me to complete this endeavor successfully. This would have never happened without his generous support and motivation. His intimate nature made the working place less stressful and welcoming.

During the course, I got an opportunity to work with Dr. Raghunathan Srianand and his team at IUCAA. It was a great experience where I could learn plenty of new things related to quasar absorption spectroscopy and related stuff. My sincere thanks to Dr. Srianand Reghunadhan and IUCAA for this wonderful opportunity.

I express my thanks to all the Doctoral committee members Dr. K. G.Indulekha (MG University, Kottayam), Dr. Reghunathan Srianand (IUCAA, Pune), Dr. Samir Mandal (IIST, Thiruvananthapuram), Dr. Anandmayee Tej (IIST, Thiruvananthapuram), Dr. Pramod Gopinath (CUSAT, Kochi), Dr. A. Chandrasekar (IIST, Thiruvananthapuram) and Dr. Jinesh K B (IIST, Thiruvananthapuram) for their suggestions, evaluations and support at various stages of this work. This prompted me to think about the problems in a more general perspective.

I extend my thanks to all the faculty and staff in the Department of Earth & Space Sciences for their friendly talks, discussions, and motivations. I thank Dr. Vinay Kumar Dadhwal, Director of IIST, Dr. K. S. Dasgupta, Former Director, IIST for the facilities provided at IIST and for the financial support to attend workshops and conferences. The staff in administration, library were always generous and helpful. Many thanks to each one of you.

The Department of Earth & Space Sciences was always been like a family. No matter MS, Ph.D. or project you do, behind the doors of the lab, all come under the label of "mad people" and ratify the same. Though I'm not a regular person sitting in astronomy lab, I could share numerous funny experience behind the doors of this lab. Thank you all for a memorable time at IIST.

Having a tea is the major concern to visit D2 at daytime. Randeep, Shiju, Kiran, Roy and a bit of politics were the routine elements during this pursuit. The companionship of other fellow students and staffs, especially Manjunath, Swagat, Veena, Joel, Aneesha, Namitha, Praveen, Sai and nameless others were all interesting and cherishable. Thank you for your awesome company. I also thank my collaborates Vikram Khaire, Sowgat Muzahid, Bart P. Wakker, Blair D. Savage for their valuable suggestions during this period. Special thanks to Tanvir for introducing me to the VPFIT profile fitting routine.

Finally, I thank my parents and sister for their love and support throughout my life, especially during the bad times. I also thank my uncle for his support and being a source of inspiration for me.

ABSTRACT

The hydrodynamic simulations of structure formation suggest that nearly 40 % of the baryons at low redshift is outside of galaxies in a warm-hot intergalactic medium with temperature of $T \sim 10^5 - 10^7$ K. Though this is a large reservoir of baryons at low redshift, detecting it observationally has been challenging because of the diffuse nature of this gas ($n_H \sim 10^{-5}$ cm^{-3}). Most of our understanding of this medium has come from studying high ionization intervening absorption lines observed in the spectra of distant quasars. The doublet lines of O VI, Ne VIII and Mg X in the far & extreme UV regions are ions of this kind.

In this thesis, we present the detection and analysis of four instances of warm - hot baryon reservoirs towards three different quasar sightlines using O VI, Ne VIII and broad Lyα absorption features as diagnostics of physical conditions. Using photometric and spectroscopic data from the Sloan Digital Sky Survey (SDSS) database, we also present information on galaxies in the vicinity of each absorber. SDSS shows several galaxies in the vicinity of each of these absorbers. In one instance, the absorber is found to be within the virial radius of a very luminous galaxy and could be tracing gas in the galaxy's extended halo. In the remaining cases, the absorber can have an intergalactic origin or could be associated with the extended circumgalactic region around a sub-L* galaxy below the detection threshold of SDSS.

The thesis also reports the detection of Ne V absorbers for the first time in the high redshift intergalactic medium. The ionization modeling of this absorbers found the origin of Ne V to be ambiguous similar to O VI absorbers. The ion can be produced through photoionisation by the extragalactic UV background radiation, through collisional ionisaion in high temperature plasma, or through photoionization under the influence of local radiation field from quasars.

Broadly, this thesis work demonstrates how Ne VIII and O VI coupled with thermally broadened H I absorption, and Ne V can be useful diagnostics of the conditions in diffuse gas at T $> 10^5$ K in the intergalactic and circumgalactic space, which harbors more baryons than galaxies at low redshifts.

TABLE OF CONTENTS

LIST OF TABLES

LIST OF FIGURES

ABBREVIATIONS

IGM	Intergalactic medium
PIE	Photoionisation Equilibrium
CIE	Collisional Ionisation Equilibrium
WHIM	Warm - Hot Intergalactic Medium
UV	Ultra-Violet
AGN	Active Galactic Nuclei
SDSS	Sloan Digital Sky Surveys
CCD	Charge Coupled Devices
QSO	Quasi-Stellar Object
CMB	Cosmic Microwave Background
GRB	Gamma Ray Burst
DLA	Damped Lyman Alpha
LLS	Lyman Limit System
ICM	Intracluster Medium
EBL	Extragalactic Background Light
CGM	Circumgalactic Medium
BLA	Broad Lyman Llpha
STIS	Space Telescope Imaging Spectrograph
FUSE	Far Ultraviolet Spectroscopic Explorer
COS	Cosmic Origins Spectrograph
VLT	Very Large Telescope
UVES	Ultraviolet and Visual Echelle Spectrograph
FUV	Far Ultraviolet
NUV	Near Ultraviolet
BAL	Broad Absorption Line
NAL	Narrow Absorption Line
AOD	Apparent Optical Depth
HST	Hubble Space Telescope

S/N	Signal to Noise ratio
MAST	Mikulski Archive for Space Telescopes
SED	Spectral Energy Distribution
UVB	Ultraviolet Background
KS15	Khaire and Srianand 2015a
HM12	Haardt and Madau 2012

NOTATION

cm	Centimeter
Å	Angstrom
pc	Parsec, 1 pc = 3.086×10^{18} cm
kpc	Killo parsec
Mpc	Mega parsec
km	Killo meter
s	Seconds
$M_\star$	Schechter Magnitude
$L_\star$	Schechter Luminosity
$\frac{M}{L}$	Mass to light ratio
N	Column density
N (x)	Column density of x, x can be atoms/ions/molecules
n	Density
Δ	Overdensity
ρ	Mass density
Ω	$\frac{\rho}{\rho_c}$, ρ_c is the critical density of universe
Γ	Photoionisation rate
h	Planck's constant, $h = 6.62607004 \times 10^{-34}$ $\mathrm{m}^2 kg/s$
e^-	Electron
ν	Frequency
T	Temperature
λ	Wavelength
v	Velocity
U	Ionisation parameter
b	Broadening parameter
W_r	Equivalent width
Ryd	Rydberg

eV	Electron volt
Ly-α, $Ly - \beta$	Lyman series lines
Ne VIII	7 times ionised Neon
O VI	5 times ionised Oxygen and so on

CHAPTER 1

Introduction

1.1 Introduction

According to the standard cosmological model, the universe began 13.6 billion years ago with the 'Big Bang'. The universe was extremely hot and dense in the initial period after the Big Bang. The energy density of the universe in the early era was dominated by radiation (photons, neutrinos etc) and the baryonic matter was materialized in the form of hot ionized gas. The expansion of universe brought down the energy density of radiation much faster than matter leading to a radiation-matter energy density equality nearly 60,000 years after the big bang (z $\sim$ 3000). The expansion continued in the matter dominated era where matter slowly separated from radiation and collapsed under gravity. The adiabatic expansion of the universe decreased the temperature which led to the combination of ions and electrons to form neutral atoms. A fraction of this gas (mostly hydrogen and helium) collapsed under gravity to form the first generation of stars and galaxies. The gas in the universe underwent a second major phase transition from a neutral to ionized phase from their interactions with photons formed in those early galaxies and AGN's. In the present universe, only 10% of the baryons have gravitationally collapsed to form stars and galaxies. Remaining 90 % of the baryons are outside of galaxies mostly in a diffuse phase called the intergalactic medium (IGM).

The IGM being a very diffuse phase ($n_H \sim 10^{-4}$ cm^{-3}) is difficult to detect in emission. However, the medium can be studied from their absorption lines in the spectra of distant objects. The first attempt for such a study carried out by Field (1959) tried to detect the hyperfine 21 cm absorption towards an extragalactic radio source Cygnus A. The result was negative which only managed to establish an upper limit on the IGM opacity. The detection of first Quasi-stellar object (QSO) by Schmidt (1963) opened a new opportunity to study IGM absorption in the optical-UV region (Bahcall and Spitzer, 1969; Gunn and Peterson, 1965). Most of our understanding of the IGM for the last five decades has been from the intervening absorption line detections in the optical-UV spectra of such quasars. The low frequency radio observations of 21cm hyperfine line from H I, with telescope such as Murchison Widefield Array (MWA), LOw Frequency ARray (LOFAR), Precision Array to Probe the Epoch of Reionization(PAPER), Primeval Structure Telescope(PaST/21CMA), Square Kilometre Array(SKA) are viable alternative to quasar absorption line studies.

As of now, the nature of IGM is explored primarily through the absorption lines in the optical-UV regions in the background spectrum of quasars. One of the major limitation of this method is that it cannot give any information on the three-dimensional physical structure of the absorber. Early models regarded the absorption systems as discrete clouds gravitationally confined in a dark matter halo (Ikeuchi, 1986) or pressure confined by a hot medium (Sargent et al., 1980) which consist only a small fraction of baryonic matter in the universe. But later, the studies of Bechtold et al. (1994); Dinshaw et al. (1997); Smette et al. (1992) from the analysis of neighbouring QSO lines of sight showed that these absorbers have sizes of few hundreds of kiloparsecs. Such absorbers could account for a large fraction of the cosmic baryons which is not expected either from gravitationally confined or pressure confined models. This led to an alternative view in the understanding of IGM where we treat structures in the IGM as a nonlinear extension of the gravitational instability growth in the primordial dark matter density.

In this chapter, we will briefly discuss our present understanding of the cosmic budget of baryons and their evolution from observations and simulations. As baryons are the only form of matter which we can detect directly, the consistency of these measurements with the model prediction is an important test for the cosmological models as well.

1.2 Baryonic matter in the Universe

According to ΛCDM cosmology, ~ 95 % of the cosmic energy is in the form of dark matter and dark energy. Most of the remaining energy is associated with baryonic matter, the ordinary matter made up of atoms that we are familiar with in our day to day life and also through the astronomical observations using EM waves. The mass density fraction of baryonic matter is represented by $\Omega_b = \frac{\rho_b}{\rho_c} = 0.0486 \pm 0.00051$ (Planck Collaboration et al., 2015), where $\rho_c = 9.2 \times 10^{-30} h_{70}^2$ g cm^{-3} is the critical density of the universe, ρ_b is the mass density of baryons and h_{70} is the Hubble constant in units of 70 km s^{-1} Mpc^{-1} respectively.

How do we calculate Ω_b? This can be done in two different ways. One is by the comparison of the observed elemental ratios of lighter elements such as lithium, deuterium etc with big-bang nucleosynthesis model (Cyburt et al., 2016; Kawasaki et al., 2008). However, the atoms of deuterium can be easily destroyed in stars. Thus, for determining the primordial abundance of lighter elements, we have to look into the regions with low metal abundance (For eg, O'Meara et al. 2006). From such measurements, we have a tight constraint on the baryonic mass fraction, $\Omega_b = 0.043 \pm 0.003 h_{70}^{-2}$. Another estimate of Ω_b comes directly from the observed cosmic microwave background spectra(CMB). The CMB spectrum is isotropic up to an order of 10^{-5} and show weak fluctuations in scales below this. A careful analysis of these fluctuations using spherical harmonic functions reveal the fraction of baryons as $\Omega_b = \frac{\rho_b}{\rho_c} = 0.0486 \pm 0.00051$ from the latest estimates of Planck Collaboration et al. 2015.

The consistent values obtained from these two independent methods improve our confidence in the measurements. However, it is important to estimate the mass fraction of baryons directly by observation. The major sources of baryonic matter in the universe are the stellar components, molecular, neutral and ionized phases of ISM inside the galaxies, as well as ionized gas outside of galaxies, in the extended envelops and the intergalactic medium. In the following sections, we will discuss the detection of baryons in these phases at two different epochs, z $\sim$ 0 (local universe) and z $\sim$3 (high redshift universe).

1.2.1 Baryons at High Redshift

Let us begin the discussion with the stellar contribution to the baryon budget. At high redshifts (z $\geq$ 3), galaxies are mostly detected from their signatures of ongoing star formation. Lyα emitters, Lyman break galaxies, host galaxies associated with GRBs and sub-mm galaxies (Gawiser et al., 2007; Le Floc'h et al., 2003; Chapman et al., 2005) are some of this kind. Compared to this young population of galaxies, the galaxies with little star formation are less and are rarely detected at this epoch (Kriek et al., 2006; Belli et al., 2017). ie, most of the stellar mass density during this period is accounted by star-forming galaxies. Stellar mass associated with these galaxies are calculated from their observed luminosity by using $\frac{M_\star}{L}$ ratio. The stellar mass density thus calculated at this epoch is $0.005 \pm 0.002_b$ (Prochaska and Tumlinson, 2009).

The redshift of $z = 2 - 3$ is the period where star formation peaks. Therefore, it is natural to expect a significant hike in the molecular gas fraction at this epoch. As the H_2 molecule, with its zero dipole moment does not produce any emission lines, the week Lyman-Werner absorption lines detected in the optical-UV band of some systems is one way to look into molecular gas in galaxies. Another method is to use the molecular emission from CO molecule as a proxy to detect the medium (Decarli et al., 2016). However, the conversion factor of CO to H_2 is not well constrained at high redshift. Current studies of H_2 regions are mostly based on the targeted search for H_2 molecular Lyman absorption band towards line of sight where H I column density of N(HI) $> 10^{19}$ cm^{-2} are reported (Srianand et al., 2005; Petitjean et al., 2000; Ge and Bechtold, 1997). In short, the molecular survey at redshift $z \sim 3$ is not very well constrained. The calculated value of baryonic mass fraction of $\Omega_{H_2} = 0.001 - 0.1\Omega_b$ (Prochaska and Tumlinson, 2009) in molecular gas, therefore, has an order of magnitude uncertainty.

Survey of neutral hydrogen at low redshift is mostly done with 21 cm hyperfine transition of the hydrogen atom. Extending this method to higher redshifts require much more collecting area. Though such studies have been performed at high redshifts, firm detections are comparatively less (Briggs and Wolfe, 1983;

Kanekar and Chengalur, 2003). The effective method to study this neutral hydrogen gas is via Ly-α absorptions (Wolfe et al., 2005, 1986). However, H I column density of at least $N(\text{H I}) \sim 10^{20}$ cm^{-2} is required to shield the gas against ionisation by the extragalactic background UV radiation. The absorbers with column densities of this order generally show a damping wings in their absorption lines known as Damped Lyman Alpha Absorbers (DLA). The survey of DLAs using SDSS DR5 given $\Omega_{neutral} = 0.016 \pm 0.002\Omega_b$. ie, the gas in the neutral gas phase consists only 1- 2 % of the total baryonic budget.

So far, our discussions were based on baryonic matter associated with dense and compact objects. There is also a significant fraction of baryons outside the star forming regions of galaxies in a highly diffuse and ionised phase($f_{\text{HI}} = n_{\text{HI}}/n_{\text{H}} \sim 10^{-4}$). Most of the hydrogen atoms in this medium are in H^+ state which does not show any line transitions. The medium can be detected from the Lyα absorption of the tiny fraction of neutral hydrogen remaining in this phase. These Lyα forest absorptions corresponds to gas with densities of $n_{\text{H}} \sim 10^{-5}$ cm^{-3} (overdensities of, $\Delta = \rho/\bar{\rho} \sim 1 - 10$) and temperatures of $T \sim 10^4$ K (Rauch, 1998; Cen et al., 1994; Miralda-Escudé et al., 1996; Rauch et al., 1997; Hernquist et al., 1996; Bolton and Becker, 2009). With the current generation telescopes, absorption with $N_{\text{H I}} = 10^{12} - 10^{22}$ cm^{-2} can be detected. Gas with column density $> 10^{22}$ cm^{-2} are extremely rare and the absorbers with column density $N_{\text{H I}} < 10^{12}$cm^{-2} is limited by the S/N of the detector. For determining baryonic mass density from H I column density also need information of the ionization state of this gas. Here, we assume ionization conditions of gas in IGM is contributed by the UV background radiation. The details of UVB radiation is separately discussed in the later section. The approximate baryonic mass density calculated for the three column density interval is shown below.

$$N(\text{H I}) = 10^{19} - 10^{20}\text{cm}^{-2} \Rightarrow \Omega_{SLLS} = 0.02\Omega_b \tag{1.1}$$

$$N(\text{H I}) = 10^{16} - 10^{19}\text{cm}^{-2} \Rightarrow \Omega_{LLS} = 0.05\Omega_b \tag{1.2}$$

$$N(\text{H I}) = 10^{12} - 10^{14.2}\text{cm}^{-2} \Rightarrow \Omega_{Ly\alpha} = 0.65 - 0.95\Omega_b \tag{1.3}$$

where LLS corresponds to Lyman limit systems and SLLS corresponds to super Lyman limit systems.

This shows that a vast majority of baryons at high redshift is of the form of ionized gas detected from the Ly α absorption lines. The total baryonic fraction estimated at high redshift is in agreement with the big-bang photosynthesis model of deuterium abundance and also with the direct mass estimation from CMB power spectrum.

1.2.2 Baryons in the Present Universe

The luminosity function of galaxies in the local universe is precisely studied with different photometric and spectroscopic surveys (Skrutskie et al., 2006; Huchra et al., 2012; Colless et al., 2001; York et al., 2000). To determine the fraction of baryons associated with these galaxies, the observed galaxy luminosity must be translated to the corresponding baryonic mass of the galaxy. This can be done if we know the stellar mass to light ratio ($\frac{M}{L}$ ratio). This ratio can be calculated using the stellar population modelling for an observed color of the galaxies. Such an analysis performed by Kauffmann et al. 2003 for a sample of the SDSS galaxies determined the luminosity function weighted $< \frac{M}{L} >$ ratio of 1.5 with 20% uncertainty. Using this estimate and SDSS galaxy luminosity function, stellar mass density is calculated as $\Omega_\star = 0.06 \pm 0.03\Omega_b$ (Fukugita and Peebles, 2004; Blanton et al., 2003).

Molecular gas phase at low redshift is probed using CO molecule as a tracer. Though a detailed survey of these molecules at low redshift has not been performed yet, CO molecular mass density is calculated from other galaxy observables such as H I mass, infrared flux density etc (Young and Scoville, 1991; Zwaan and Prochaska, 2006; Keres et al., 2003). The calculated molecular gas mass density is $\Omega_{H_2} = 0.0029 \pm 0.009\Omega_b$.

Several 21 cm blind surveys have performed to detect matter in neutral H I phase (Meyer et al., 2004; Zwaan et al., 2005, 1997; Rosenberg and Schneider, 2002). HIPASS (Meyer et al., 2004) is an all Southern Sky Survey which identified 4315

Figure 1.1: The observed distribution of baryonic matter $z = 3$ & $z = 0$

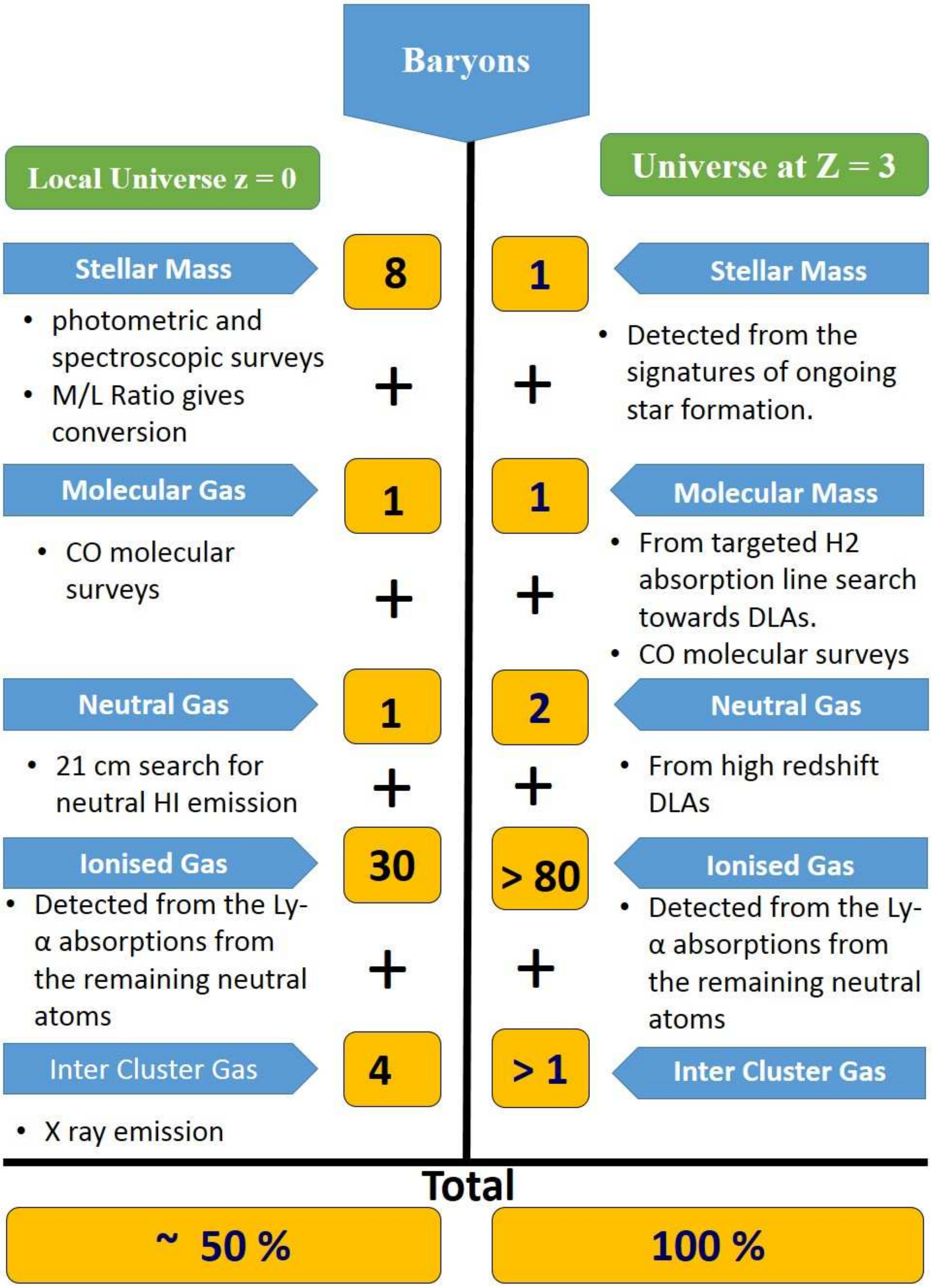

Figure 1.1 The schematic figure shows the distribution of baryonic matter at redshift $z = 3$ and $z = 0$ in different phases in the universe. Compared to redshift $z = 3$, nearly $\sim 40\%$ of the baryons are not detected in the low redshift universe. The hydrodynamic simulations of structure formation suggested that these baryons are shock-heated to a higher temperature $10^4 - 10^6$ K.

H I sources purely based on their H I content. The fraction of H I mass associated with neutral gas phase in this survey is estimated by Zwaan et al. (2005) given $\Omega_{neutral} = 0.011 \pm 0.001\Omega_b$.

During the formative stages of the universe, a large fraction of the baryonic matter has collapsed into the galaxy-cluster environment called intercluster medium (ICM) which then shock-heated to a high temperature with T $> 10^7$ K. The x-ray observations (eg, Reiprich and Böhringer, 2002; Boehringer et al., 2017; Allen et al., 2008) within the local universe revealed the presence of such a medium extending up to the virial radii of these galaxy clusters. Such observations at X-ray wavelength show that the ratio of the gas mass to the dynamic mass of all the clusters are more or less constant (f_{gas}, is $\sim 0.11 \pm 0.01$, Allen et al. 2008). Thus, for a known cosmological mass density of galaxy clusters, ICM contribution can be calculated by simply multiplying the mass density of galaxy clusters by their gas fraction (f_{gas}). Using the galaxy cluster mass function of Rines et al. 2008, Prochaska and Tumlinson 2009 calculated the contribution of ICM to the total baryonic density as $\Omega_{ICM} = 0.027\Omega_b$. This show that there is a significant fraction of baryons existing in the ICM of massive galaxy clusters.

Similar to the high redshift studies, gas in the ionized phase of IGM at low redshift is explored with the neutral fraction of H I in this gas phase. To calculate the baryonic mass density, we need to know the column density distribution, photoionization rate (Γ) and gas temperature (For a detailed description of this formalism, see Schaye 2001). By adopting $\Gamma = 10^{-13} s^{-1}$ (Scott et al., 2000; Shull et al., 1999; Weymann et al., 2001), $T_{IGM} = 38,000$ K (Paschos et al., 2009; Penton et al., 2002; Davé et al., 2001), and $f(N_{\mathrm{H\ I}}, X)$ (Schaye, 2001), Prochaska et al. 2008 calculated the baryonic density of neutral gas phase as $\Omega_{Ly_\alpha} = 0.17\Omega_b$. Similar calculations performed by Danforth and Shull 2008 for a sample of 650 Ly-α absorbers over a redshift path of $\Delta z = 5.27$ and found $\Omega_{Ly_\alpha} = 0.29\Omega_b$ associated with the photoionized gas phase. Compared to the baryonic density at high redshifts, both these measurements are significantly less.

The estimated photoionization rate (Γ) and IGM temperature are uncertain by several factors. Even if we count the uncertainties in Γ, temperature of IGM, H I frequency distributions etc, the maximum amount of baryons recovered from this phase can be $\Omega_{\mathrm{Ly}\,\alpha} = 0.6\Omega_b$. Thus, the total energy density of baryons in all the forms at the low redshift universe including the $\Omega_{\mathrm{Ly}\,\alpha}$ upper limit, $\Omega_{stars} + \Omega_{H_2} + \Omega_{neut} + \Omega_{ICM} + \Omega_{\mathrm{Ly}\,\alpha} \sim 0.75\Omega_b$. Compared to the similar estimates of baryons at redshift $z = 3$, the estimates lacks $\sim 30\%$ of baryons at low redshift (See, Figure 1.1). To understand this, we have to look carefully into the structure formation scenario of the universe.

1.3 Structure formation and Evolution of Universe

In the previous section, we have seen the discrepancy in the observed energy density of baryons at redshift $z \sim 3$ and $z \sim 0$. Here, we will try to understand the reason behind it with the help of hydrodynamic simulations of structure formation.

According to ΛCDM cosmology, the super-horizon growth of the primordial fluctuations is responsible for the formation of large-scale structures in the universe. Simulating the growth of perturbations is the most efficient way to understand the physical conditions and phase changes at various formative stages of the universe (Bechtold et al., 1994; Dinshaw et al., 1997; Smette et al., 1992). A recent simulation showing the evolution of a galaxy supercluster is shown in the right panel of Figure 1.2 (Vogelsberger et al., 2014). At $z = 4$, most of the IGM is in the form of the photoionized gas with temperature $T \sim 10^4$ K. The growth of perturbations and the formation of structures led to a change in the density of dark matter, baryonic matter and also the temperature and metallicity in the universe. Baryonic matter fell into the dark matter potentials of these structures later collapsed under gravity and formed more and more stars and galaxies. The radiation and shock waves from these sources can influence the thermal conditions of the gas in this region. The process increases the temperature, metallicity and the gas density of the gas in the circumgalactic regions.

The left panel of Figure 1.2 shows the observed galaxy distribution from the SDSS survey in the scales of few hundreds megaparsec. The size of a single dot in this plot could be of the size of a typical galaxy in the universe. On a large scale, the distribution of galaxies forms structures called the cosmic web which is more or less consistent with the predictions from the simulations.

Figure 1.2: Large Scale Structure of the Universe

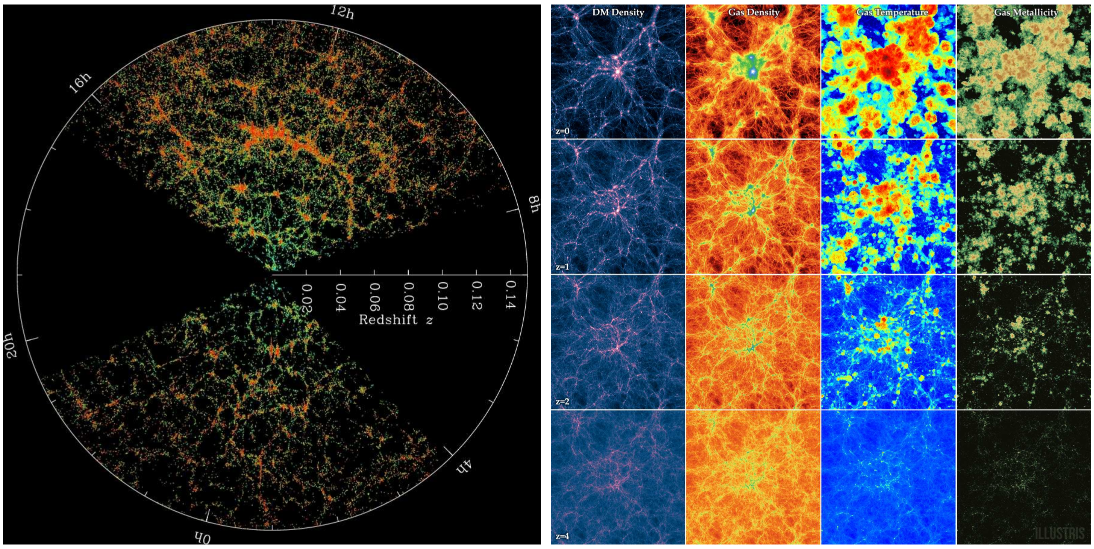

Figure 1.2 *Left Panel:* The observed galaxy distribution in the universe from SDSS survey is shown in this Figure. The centre of the plot corresponds to redshift $z = 0$ is the location of the observer from earth. As we move radially outwards from the centre, the distribution of galaxies at higher and higher redshift can be seen. *Right:* This panel shows the evolution of a galaxy super-cluster from an early epoch $z = 4$ to the present ($z = 0$) in the Illustris simulation. The individual panels from left to right are the dark matter, gas density, gas temperature and metallicity respectively.[Image credit : SDSS and (Vogelsberger et al., 2014)]

A mathematical representation of the growth of dark matter perturbations is as follows.

$$\frac{\partial^2 \delta}{\partial t^2} + 2\frac{\dot{a}}{a}\frac{\partial \delta}{\partial t} = 4\pi G \rho_b \delta_k + \frac{c_s^2}{a^2}\Delta_{\vec{x}}^2 \delta \tag{1.4}$$

$$\frac{\partial^2 \delta_k}{\partial t^2} + 2\frac{\dot{a}}{a}\frac{\partial \delta_k}{\partial t} = 4\pi G \rho_b \delta_k - \frac{c_s^2}{a^2}k^2 \tag{1.5}$$

where the equation 1.4 represent the growth of perturbations in the real space and equation 1.5 represent the same in the Fourier space. Here, $\delta(\vec{x}, t) = \frac{\rho(\vec{x},t)-\rho_b(t)}{\rho_b(t)}$ is the over-density of baryons, c_s is the velocity of sound in the medium, 'a' is the scale factor and ρ_b is the critical density of the universe respectively.

Without the expansion term in the equation 1.5 (this term acting as a drag force in this expression),

$$\ddot{\delta}_k = \omega^2 \delta_k \tag{1.6}$$

$$\omega^2 = 4\pi G \rho_b \delta_k - \frac{c_s^2}{a^2} k^2 \tag{1.7}$$

where $\omega^2 > 0 \Rightarrow$ yeilds growing solutions, $\omega^2 < 0 \Rightarrow$ yeilds oscillating solutions, $\omega^2 = 0 \Rightarrow$ is the Jean's length respectively. The equation should have $\omega^2 > 0$ for a realistic model of the universe.

The formation of structures is an exothermic process. During this process, a large amount of energy will be transmitted to the distant regions of IGM in the form of shocks. This can shock heat the IGM into a very high temperature of the order $T \sim 10^5 - 10^7$ K. The gas in these regions are difficult to detect via observations due to their low surface brightness (in emission) and low neutral hydrogen fraction (in absorption). Heating of gas through collisional ionization can also happen from shock waves produced by supernova explosions that occur in overdense regions. For example, in very large structures like galaxy clusters, these shock waves can increase the temperature of the medium to $T > 10^7$ K. The gas in such conditions are detected from their X-ray emission at the low-redshift universe. Similar events can raise the temperature of the medium to $10^5 - 10^6$ K in slightly smaller structures, like galaxy groups or even in the halo gas in isolated galaxies. The X-ray emission from galaxy groups and individual galaxies are too faint to be detected. The only way to detect this gas is from their absorption lines observed in distant QSOs which is challenging due to the low neutral hydrogen fraction. The undetected gas in these hot plasma at temperature $10^5 - 10^7$ K, predicted by simulations, is presumably the reason behind the $\sim 30\%$ of missing baryons in the low-redshift universe .

A detailed description of the phase transformations that happen to baryons as a result of the structure formation of the universe is given by the hydrodynamic simulations of Cen and Ostriker (2006, 1999). The simulation is normalized to the temperature measured from the CMB fluctuations (Bunn and White, 1997) and the observed abundance of galaxies and clusters (Cen and Ostriker, 1999; Ostriker et al., 1995; Riess et al., 1998) in the local universe. In the simulation,

Figure 1.3: Evolution of the Universe from Simulations

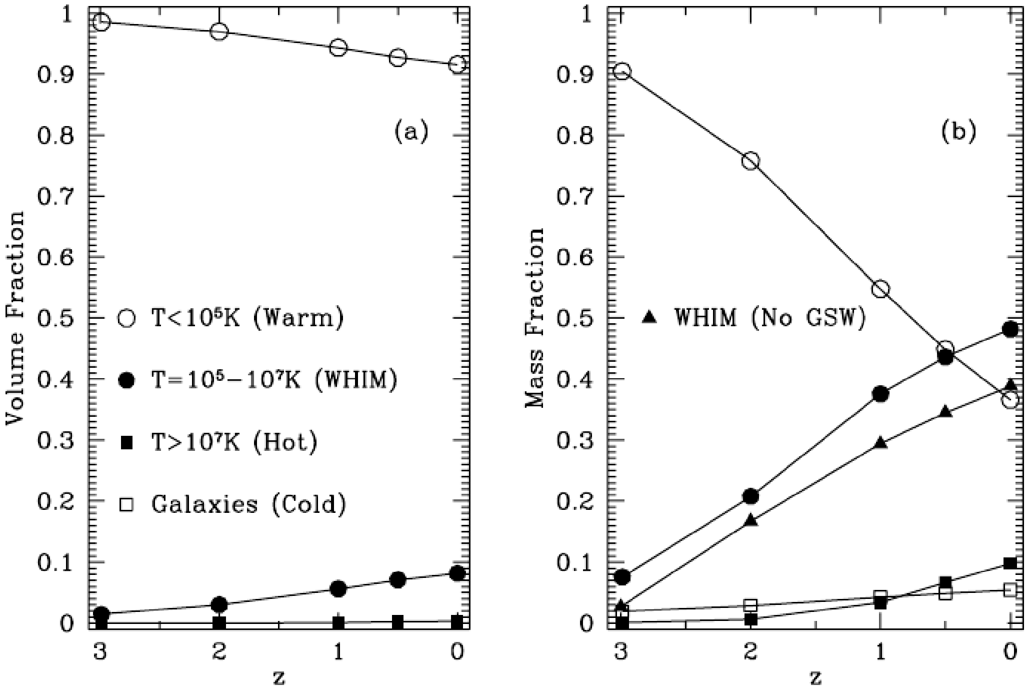

Figure 1.3 *Top Left:* The observed galaxy distribution from SDSS survey. The center of the plot is the observer's location. As you go out from the central region, you are probing higher and higher redshift. *Top Right:* Right panel shows the distribution warm hot baryons in the local universe from Cen and Ostriker (2006) simulation. The color code in the plot indicates the overdensity of the regions. The Green regions in the plot corresponds to an overdensity of 20-40, yellow corresponds to overdensity of 100 and red an overdensity of 1000 respectively.*Bottom Panels:* The left panel shows the dark matter structures of a large supercluster from Illustris simulation. The right panel shows the evolution of this structure from an early epoch of $z = 4$ to present $z = 0$ universe. The individual panels from left to right are dark matter, gas density, gas temperature and metallicity respectively. The Figures are taken from Cen and Ostriker 2006.

three of the major components affects the structure formation are dark matter, ordinary gas/baryons and galaxies and the changes in each of these components are closely followed. The star formation process in the young galaxies causes feedback flow into the CGM/IGM. This is given to the simulations in the form of supernova thermal energy output, UV photon output and also the mass injection from supernova explosions to reproduce the observed UV background, metallicity distribution, and star formation history. The Cen and Ostriker (2006) model improved with additional feedback in the form of galactic superwind.

The simulation classifies baryonic matter into four phases on the basis of their over-density and temperature (Davé et al., 2001; Cen and Ostriker, 1999, 2006). The gas corresponding to Lyα absorptions from the low-density intergalactic regions (diffuse gas phase $T \sim 10^5$ K, $\delta < 1000$), the matter associated in condensed objects like stars and galaxies condensed gas phase (condensed gas phase, $T \sim 10^5$ K, $\delta > 1000$), the X-ray emitting gas with temperature $T > 10^7$ K (hot phase, $T > 10^7$ K) and the warm - hot phase of IGM with temperature $10^5 < T < 10^7$ K. The evolution of these four phases in the simulation is shown in Figure 1.3.

The radiations in the early universe ($z \sim 3$) kept the IGM ionized and maintained the temperature around $T \sim 10^4$ K. The formation of structures led to an increase in density at some regions (over density) where the matter slowly condensed and formed galaxies. The formation of structures increased the temperature of the gas phase monotonically with time. The peak temperature of the medium calculated from shock waves formed during the formation of large-scale structures can be estimated using the following equation.

$$T_{nl} \propto c_{nl}^2 = K(HL_{nl})^2 \tag{1.8}$$

where T_{nl} is the peak temperature, L_{nl} is the length scale, t is the perturbation collapse timescale and K is a constant respectively. As the universe evolves, the shock-heating of IGM can increase the temperature of a significant fraction of the baryons to a high-temperature gas phase called Warm-Hot Intergalactic Medium.

1.4 Warm- Hot Intergalactic Medium [WHIM]

All the popular cosmological simulations predict approximately $\sim 30\%$ of the baryons in a Warm-Hot Intergalactic Medium (or WHIM) with temperature within $10^5 - 10^7$ K and an overdensity of $\delta \sim 20$ irrespective of the algorithm, resolu-

Figure 1.4: Physical Conditions of Warm - Hot baryons

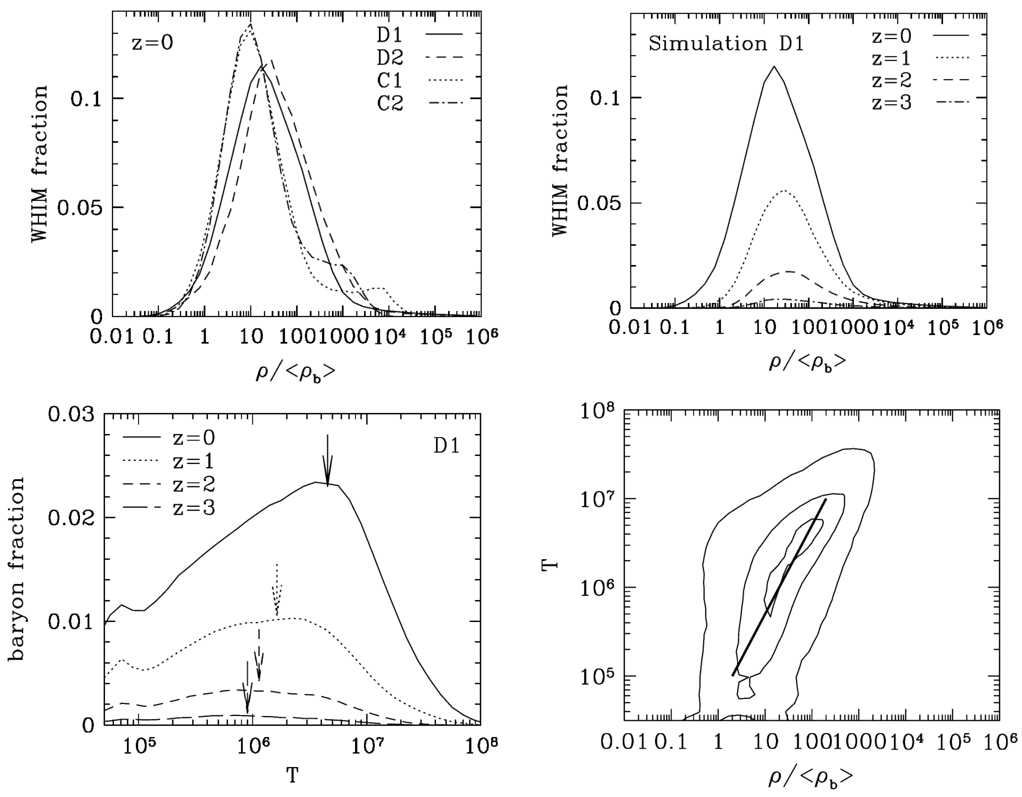

Figure 1.4 Physical conditions of WHIMs from simulations (Figures are from Davé et al. 2001). *Top Left:* The distribution of WHIM gas at redshift $z = 0$ from four different simulations are shown. Here, D1 & D2 are the simulations running with parallel tree smoothed particle hydrodynamics (PTreeSPH) and C1 & C2 are running with total variation diminishing particle-mesh (TVD-PM) algorithm. Irrespective of the code used, all these simulations predict maximum WHIMs in spacial locations with overdensiy of between 30 -100. *Top Right:* The plot show the spacial distribution of WHIMs at different epoch of the universe from simulation D1. *Bottom Left:* The panel shows the temperature evolution of WHIMs at different epoch. *Bottom Right:* The temperature density correlation of WHIM gas.

tion and input parameters (Davé et al., 2001; Cen and Ostriker, 2006, 1999). The natural occurrence of WHIM in simulations is a direct solution for the "missing baryon problem" at low redshift.

The Top left panel of Figure 1.4 show a spacial distribution of WHIM in four different cosmological simulations (Davé et al., 2001). The simulations D1 and D2 run with Parallel Tree SPH (Davé et al., 1997) algorithm and the C1, C2 simulations run with TVD-PM (Ryu et al., 1993) (For details, see Davé et al. 2001). The Figure shows the fraction of baryons associated with WHIM in all the four simulations dominates at an over-density of $\delta \sim 10-30$. An overdensity > 60 corresponds to a typical galaxy group/ cluster environment which consists of $\sim 10-25\%$ of WHIMs. This means a vast majority of WHIM gas resides outside of virialized structures probably in large-scale filaments of the cosmic web.

The evolution of WHIM with redshift in one of the simulation is shown in the Top right and Bottom left panels of the Figure 1.4. An increase in the baryonic fraction associated with WHIMs as the universe evolves from $z=3$ to $z=0$ is shown here. During the evolution, there is no significant change in the spatial distribution of WHIMs which is dominated in the regions with over-density δ between $10-100$. However, temperature distribution shows a shift in their peeks temperature from 10^6 K to 4×10^6 K with the evolution of the universe from $z=3$ to $z=0$.

How does the gas heat up to such a high temperature? One possibility is the heating of IGM via non-thermal processes such as supernova explosions. However, the effect of supernovae heating is dominated in the high-density regions which are less effective in the low-dense regions where most of the WHIM gas resides. Though supernova effects can have a non-zero contribution in the origin of WHIM, it is unlikely to be the process responsible for WHIM. The shock waves formed during the formation of large-scale structures can shock-heat IGM gas to very high temperature is one another possible scenario. The increase in peak temperature during the formation of mild nonlinear structures in the simulation can be calculated using the equation 1.8. For $K=0.3$, the peak temperature obtained from this formula is marked with a downward arrow in the bottom left panel of Figure 1.4. For all the redshift from $z=3$ to $z=0$, the temperature derived from this formula is consistent with simulations. Also, WHIM gas show a temperature - density correlation $\rho \propto T$ with significant scatter (Bottom right Figure 1.4). This is different from the typically observed relationship between ρ and T ($\rho \propto T^{1.7}$) in the diffuse gas phase. The consistency of WHIM with the temperature derived from gravitational shock waves, and also their inconsistency with a normal diffuse gas phase suggested a shock-heated origin of WHIM gas (Davé et al., 2001).

Though the existence of WHIMs is a natural outcome from simulations, their detection remains a challenging task for observational astronomers. At $10^5 - 10^7$ K temperature. A Bremsstrahlung continuum emission is expected from the medium, but the low surface brightness prevents their detection from the current generation X-ray telescope. However, in large virialized structures like galaxy clusters, free-free emission from this region is detectable. It is found that the matter in inter-cluster medium contributes to more baryons in clusters like this (Allen et al., 2002). There were several similar attempts to study X-ray emission/ absorption lines from WHIM. From the X-ray absorption of O vii K_α, a hot halo at temperature $\sim 10^6$ K is detected around the Milkyway using XMM-Newton and Chandra observations (Nicastro et al., 2002; Rasmussen et al., 2003; Williams et al., 2006, 2005; Wang et al., 2005; Fang et al., 2006; Bregman and Lloyd-Davies, 2007). As of now, there is no detection of WHIMs outside of the local group. A detection of WHIM towards Mrk 421 is claimed by Nicastro et al. 2005 from the X-ray absorption of O vii 21.60 line. However, an independent study of the source by Kaastra et al. 2006; Rasmussen et al. 2006 unable to find any evidence for it. Similarly, there are claims for the detection of WHIM towards H1821+643 which is not convincing either. In short, the gas in WHIM is not yet detected beyond local group in X-ray emission/ absorption.

UV absorption line studies of metal lines are one way to detect warm - hot baryons in the universe. At the lower end of WHIM temperature, most of the hydrogen will be in ionized state ($f_{\mathrm{H\ I}} = 10^{-6}$). At such low neutral H i fraction, detection of hydrogen transitions requires high S/N UV spectrum. However, the absorption lines from the highly ionized metal lines can be used to detect warm -hot baryons in the lower end temperatures ($10^5 - 10^6$ K).

1.5 Physical Conditions of gas in IGM/ CGM

Before proceeding further ahead, it is useful to discuss some of the processes that have kept the IGM ionised throughout the observable history of the universe. In this section, we discuss the two common ionization processes, photoionization and collision ionization in detail.

1.5.1 Photoionisation Process

Photoionization is the process in which the interaction of photons with atoms/ molecules/ ions changes their ionization state from a lower energy state to higher energy state. If X is the atom/ molecule/ ion in a lower ionization state, 'hν' is the energy of the incident radiation, then the process can be represented as shown below.

$$X + h\nu \rightarrow X^{+} + e^{-} \tag{1.9}$$

where X^{+} is the same atom/ molecule/ ion in their higher ionisation state and e^{-} is the electron ejected during this event. The inverse of this process is also possible, known as radiative recombination. In this process, an ion in a higher energy state combines with electron and forms atom/ molecule/ ion of lower energy state with the release of a photon of energy 'hν'.

$$X^{+} + e^{-} \rightarrow X + h\nu \tag{1.10}$$

The photoioniation rate (γ) per unit volume of an optically thin, pure hydrogen medium of neutral density n_{HI} is given by:

$$\gamma = n_{HI} \int_{\nu_L}^{\infty} \frac{4\pi J_{\nu} \sigma_H(\nu)}{h\nu} d\nu \tag{1.11}$$

where J_{ν} is the mean intensity of the radiation (ergs cm^{-2} $S^{-1} Hz^{-1}$), h is the Planck's constant, $\sigma_H(\nu)$ is the absorption cross-section of hydrogen atom at frequency 'ν'.The rate of recombinations per unit volume is given by $n_e n_p \sigma_A(T)$ where n_e, n_p are the density of radiation, $\sigma_A(T)$ is the ionization cross-section of the hydrogen atom at the particular energy state.

In general, the timescale for any dynamical change in the astrophysical conditions of a system is much higher than the ionization and recombination time scales. Hence, photoionization is a valid approximation in most astrophysical conditions. At photoionization equilibrium, both the rate of ionization and rate of recombination will be balanced. ie,

$$n_{HI} \int_{\nu_L}^{\infty} \frac{4\pi J_{\nu} \sigma_H(\nu)}{h\nu} d\nu = n_e n_p \sigma_A(T) \tag{1.12}$$

Figure 1.5: Evolution of UV background

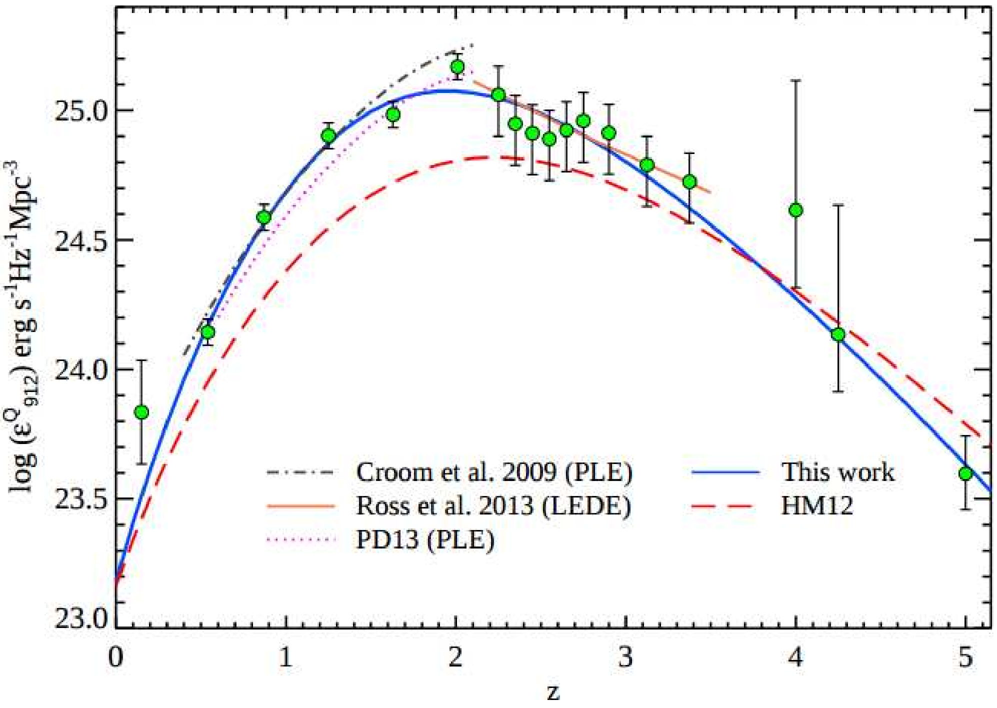

Figure 1.5 The emissivity of H I ionizing photons contributions from quasars calculated by (Haardt and Madau, 2012, hereafter HM12) and (Khaire and Srianand, 2015a, hereafter KS15) is shown for comparison. For redshift $z < 3.5$, the quasar emissivity of KS15 is higher than HM12 by a maximum difference of factor 2.1. The figure is taken from KS15.

The ionization ratio at photoionization equilibrium is given by : $\dfrac{n_{HI}}{n_p} = \dfrac{t_{\text{ionization}}}{t_{\text{recombination}}}$.

Here, n_{HI} is the neutral hydrogen density of the medium, n_{e^-} is the electron density, n_p is the proton density, $t_{\text{ionization}}$ is the ionization time scale and $t_{\text{recombination}}$ is the recombination time scale respectively.

UV Background Radiation

The study of quasar absorption lines showed that gas in IGM at $z < 6$ is mostly ionized with an average neutral H I fraction of $f_{\text{H I}} \sim 10^{-4}$. The ionization of this gas is by the radiation from luminous sources such as young star forming galaxies and quasars. As the gas in the IGM is located in the desolate regions of space where there is no influence from any local radiating sources, the average radiation from the global population of star forming galaxies and quasars will decide the nature of the ionization gas at an epoch. The Far UV region of this spectra with $\lambda < 1000$ Å responsible to keep the IGM gas ionized is known as UV background radiation. Radiation with wavelength $\lambda > 1000$ Å is known as Extragalactic Background Light (EBL).

UV background radiation is an essential ingredient required for the understanding of physical and chemical properties of IGM gas. This includes the study of re-ionization of H I and He II, ionization properties of various metal lines systems etc. It is also an important parameter required for cosmological simulations.

Generally, the intensity of UVB radiation at a frequency ν_0 can be calculated from the following expression.

$$J_{\nu_0}(z_0) = \frac{c}{4\pi}\int_{z_0}^{\infty} dz \frac{dt}{dz}\frac{(1+z_0)^3}{(1+z)^3}\epsilon_\nu(z)e^{-\tau_{eff}(\nu_0,z_0,z)} \tag{1.13}$$

where J_{ν_0} in unit of ergs cm^{-2} $S^{-1}Hz^{-1}$, τ_{eff} is the effective optical depth, ν is the photon frequency and z is the redshift respectively. Standard ΛCDM cosmology defines the term $\frac{dt}{dz}$ as follows:

$$\frac{dt}{dz} = (H_0(1+z)\sqrt{\Omega_m(1+z)^3+\Omega_\Delta})^{-1} \tag{1.14}$$

where the terms have their usual meaning in cosmology. For solving eqn 1.13, two observational inputs are required, τ_{eff} and ϵ_ν. If we assume the contribution of effective optical depth is only from hydrogen and helium,

$$\tau_{nu} = N_{\text{H I}}\sigma_{\text{H I}}(\nu) + N_{\text{He I}}\sigma_{\text{He I}}(\nu) + N_{\text{He II}}\sigma_{\text{He II}}(\nu) \tag{1.15}$$

With the lack of observations of helium column density, their measurement is derived from H I column density measurement. The contribution of ultraviolet background emissions are mainly be from QSOs, stars in galaxies and the diffuse emission from IGM clouds. The total emissivity of IGM from these sources can be calculated using

$$\epsilon_\nu(z) = (1+z)^3[\epsilon_\nu^Q(z) + \epsilon_\nu^G(z) + \epsilon_\nu^{diff}(z)] \tag{1.16}$$

It has been pointed out that Haardt and Madau (2012, hereafter HM12) ultraviolet background's estimate of the hydrogen ionizing rate at low-z is lower by a factor of $\sim 2-5$ (Kollmeier et al., 2014; Shull et al., 2015; Wakker et al., 2015). Khaire and Srianand (2015a, hereafter KS15) show that this discrepancy is resolved by incorporating in the synthesis of the background spectra, the recent measurements of quasar luminosity function (Croom et al., 2009; Palanque-Delabrouille et al., 2013) and star formation rate densities (Khaire and Srianand, 2015a). Figure 1.5 compares the emissivity from quasars calculated by KS15 with other popular models. At low redshift, the equilibrium fractions of high ionization species like O VI will be primarily affected by the factor of two increase in the QSO emissivity, whereas the low and intermediate ions will be affected by the enhancement in both galaxy and QSO emissivities. In the work presented in subsequent chapters of this thesis, we have investigated the physical & chemical properties of the intervening absorbers with the KS15 ultraviolet background.

1.5.2 Collisional Ionisation

Ionizations via collisions is one another plausible heating mechanism possible in the intergalactic medium. Here, the ions are produced by the collisions with other atoms/ molecules/ ions. The reverse process is known as recombination where an ion combines with electron and form a neutral atom or an ion with lower ionization state. In astrophysical conditions, it is not necessary that all processes have to satisfy the collisional equilibrium conditions. In fact, most of the processes that we are familiar are following the non-equilibrium cooling process. However, for simplicity, the analysis in this thesis considers only the collisional ionization equilibrium models with the changes expected from non-equilibrium conditions commented on.

A collisional ionization equilibrium is a balance between ionization and recombination processes via collisions. Let us consider I_z is the ionization rate of an atom to change from an ionization state z to $(z+1)$, R_z recombination rate from ionization state z to $(z-1)$. At Ionization equilibrium,

$$n_z I_z + n_{z+1} I_{z+1} = n_z R_z + n_{z+1} R_{z+1} \tag{1.17}$$

It the atoms are in their neutral energy state,

$$n_1 R_1 = n_0 I_0 \tag{1.18}$$

The equation 1.18 can be extended further using induction method. In general, the number of ions in any state in Collisional Ionisation Equilibrium(CIE) is given by

$$n_{n+1} R_1 = \frac{n_n I_n}{R_{n+1}} \tag{1.19}$$

This means, at collisional ionization equilibrium, the number of ions at an energy level is independent of density. It depends only on the rate of ionization and recombination which is a function of temperature.

1.5.3 Higher Ionization Absorption lines as a tracer of Warm - Hot baryons

From the simulations, it is clear that most of the WHIM gas is not a part of any virialized structure, but around 20% of these baryonic matter exists in the regions with over-density $(\delta) > 60$. Compared to the low density, low metallicity regions with $\delta < 30$, WHIMs in the regions with $\delta > 60$ are easy to detect from metal absorption lines.

Some of the common lines that serves as the diagnostics of WHIMs are O VI, O VII, Ne VIII and Mg X with ionization energy of 113.9, 138.1, 207.3 and 328 eV respectively. The energy produced by the stars in galaxies are not sufficient to produce these ions. However, the non-thermal radiation from quasars and other active nuclei can produce higher ions in their neighbourhood. The ionization conditions of the intergalactic medium will be decided by the average radiation from all the sources including quasars and galaxies. This radiation field (UV background) in some cases is found not hard enough to produce ions such as O VI and Ne VIII. In such cases, the detection of these ions in the intergalactic medium can be evidence for collisional ionization the existence of warm-hot plasma with temperature $10^5 - 10^7$ K. At present, the absorption studies in X-ray wavelength is not as efficient as in ultraviolet regime. Thus, most of our studies were based on the transitions of Ne VIII and O VI in the ultraviolet region.

The origin of Ne VIII in the intervening absorbers is ambiguous. An ionization process that simultaneously include collisional and photoionization processes associate Ne VIII with moderately dense gas with $n_{\mathrm{H}} \sim 10^{-5}$ cm^{-3} at warm temperatures of T $\sim 5 \times 10^5$ K with collisions dominating the ionizations (Narayanan et al., 2011a; Tepper-García et al., 2013). However, at this temperature and moderate density, the gas can radiatively cool rapidly within timescales of $t_{cool} < 10^8$ yrs to a gas phase of $T \sim 10^4$ K where photoionization dominates. By using the updated extragalactic background radiation of KS15, Hussain et al. 2017 showed that the Ne VIII absorbers are most likely to be tracers of collisionally ionized gas if the gas metallicity is low ($Z < 0.1\ Z_{\odot}$) such that the cooling is slow. If the metallicity is super-solar as Hussain et al. 2017 predict, then to keep the temperature to values of T $> 10^5$ K would require a constant injection of energy which can compensate for the rapid metal-line cooling. In the absence of such an energy input, gas at temperature T $> 10^5$ K with solar or higher metallicity will cooldown to T $\sim 10^4$ K within timescales of $t_cool < 10^8$ years. Thus, Ne VIII can have an origin in cool gas phase provided the abundances are super-solar. Production of Ne VIII through photoionization alone is possible in the presence of a hard radiation field such as the absorbers close to the central engines of quasars (Petitjean and Srianand, 1999; Ganguly et al., 2006; Muzahid et al., 2012).

The choice between photoionization and collisional ionization origin is much more divided for the O VI class of absorbers (Tripp et al., 2008; Oppenheimer and Davé, 2009; Tepper-García et al., 2011). One of the earlier work in the field by Tripp et al. 2000 quoted that theoretical considerations favour the origin of O VI via collisional ionization, but can not rule out the possibility of photoionization. Also, they predict the effect of cooling can vary the collisional ionization equilibrium conditions. The favourable scenario predicted by this model is a non-equilibrium cooling process. Examining the ionization processes in this absorbers are important in determining the total baryonic contents in these absorbers. O VI arising in collisionally ionized warm gas can hold 10 times more baryons than a photoionized cooler O VI gas phase. Quasar absorption line surveys have discovered more than 100 O VI absorbers at low-z (Tripp et al., 2000, 2008; Savage et al., 2002; Danforth and Shull, 2005; Thom and Chen, 2008a,c; Savage et al., 2014; Tumlinson et al., 2011a; Danforth et al., 2016). In a significant number of these cases, the O VI $1031, 1037$ lines are found to be consistent with gas at temperature ranging from 10^5 to 10^6 K (Tripp et al. 2000; Savage et al. 2002; Howk et al. 2002; Savage and Lehner 2006; Danforth and Shull 2008; Lehner et al. 2009; Narayanan et al. 2010a,b; Savage et al. 2011a; Narayanan et al. 2012; Savage et al. 2014; Pachat et al. 2016). Among these are also instances where the warm gas is directly evident (independent of ionization modelling) through the presence of thermally broad Lyα absorption (BLA, b(H I) > 40 km s^{-1}) associated with the O VI.

The first detection of O VI in the intervening absorber is Sargent et al. (1988). However, the detection is less certain because of the influence of Lyα forest. From a composite spectrum consist of C IV absorbers, Lu and Savage (1993) reported a firm detection of O VI doublet lines in the intervening absorber. From the GHRS and FOS spectra of Hubble Space Telescope, Savage et al. 1998 detected another O VI transitions towards H1 $821+643$ from an absorber at $z_{abs} = 0.225$. Later on with the much-advanced facilities like STIS/ FUSE, the detection of intervening O VI lines became a common practice (Tripp et al., 2000; Sembach et al., 2000; Savage et al., 2002).

The first major survey of a search of O VI absorbers was done by Danforth and Shull 2005. In this survey, they searched 30 AGN sightlines where 40 O VI absorbers were detected in a total of 129 Lyα absorbers. This study concludes that a maximum of $\sim 10\%$ baryons are present in the WHIM over a redshift path length of $\Delta z < 2.2$. A similar study of Tripp et al. (2008) detected 51 O VI absorbers with 77 individual components at redshift $z < 0.5$ towards 16 low redshift quasars. This followed by a series of O VI survey (Danforth and Shull, 2005; Danforth et al., 2006; Danforth and Shull, 2008; Tripp et al., 2008).

Figure 1.6: O vi Correlation

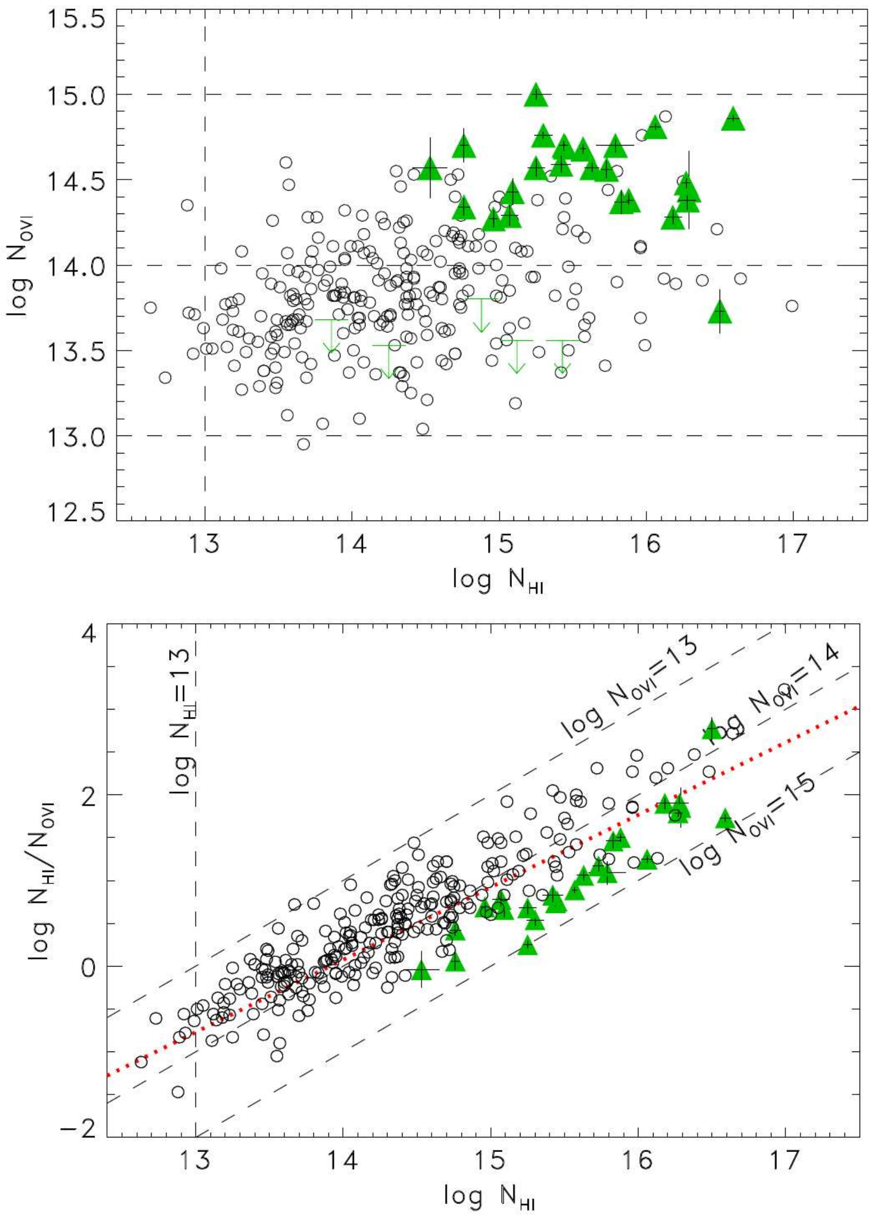

Figure 1.6 *Top Panel:* The plot show the column density of O vi and the corresponding H i from Danforth et al. 2016. The black circles are the samples from this study and the green triangles are the samples from COS-Halos survey of Tumlinson et al. (2011a). No correlation between O vi and H i column densities observed. *Bottom Panel:* The change in multiphase ratio $[N(\text{H I})/N(\text{O VI})]$ with H i column density is shown. A weak correlation correlation between these quantities with a power low index 0.86 ± 0.01 is observed which is marked with the dotted red line. The Figures are taken from Danforth et al. 2016.

The recent results of Danforth et al. 2016 reported 280 O VI absorbers is the largest O VI survey sofar. The comparison between H I and O VI column density is shown in Figure 1.6 which is not showing any correlation between these two ions. The plot shows the column density of O VI varies within $10^{13} - 10^{15}$ cm^{-2} whereas associated H I varies in a larger$10^{12} - 10^{18}$ cm^{-2} range. Danforth et al. 2006 defined a quantity called multiphase ratio [N(H I)/N(O VI)] is plotted in the bottom panel of this figure show a weak correlation between these quantities N(H I)/N(O VI) $\propto$ N(H I)/(10^{14}) cm^{-2}.

The evolution of O VI absorbers with redshift can be followed by $d\mathcal{N}/dz$, the cumulative distribution of O VI with redshift can be fitted with a broken power low with a break around log N(O VI) $\sim$ 13.9. For weaker absorbers, a power law index, $\beta \sim 0.55$ is used whereas for stronger absorbers $\beta \sim 2.5$ for strong absorbers. From the $d\mathcal{N}/dz$, it is found that $\sim$ 11% of the IGM gas can be detected from O VI absorptions. The value calculated here is less than previous estimates (Danforth and Shull, 2008; Danforth et al., 2006) due to the improved ionization corrections used.

Compared to the detection of O VI, the detection of Ne VIII is rare. So far, there are only 10 instances of Ne VIII detection in the intervening absorbers (Savage et al., 2005, 2011a; Narayanan et al., 2009, 2011a; Meiring et al., 2013; Hussain et al., 2015; Qu and Bregman, 2016; Tripp et al., 2011; Bordoloi et al., 2016). Among them, only one absorber at $z = 0.5996$ towards PG $1407 + 265$ is favouring an origin via photoionization (Hussain et al., 2015). The remaining absorbers were tracing a gas phase with $T \sim 5 \times 10^5$ with subsolar metallicity. Hence, the detection of Ne VIII line is a better tracer of WHIMs compared O VI. A better understanding of these absorbers required to have a large sample Ne VIII absorbers.

Along with a search of higher ions by seeking the evidence for warm-hot baryons at low redshift, it is also important to establish the evolution of these ions over time. For example, the high redshift O VI survey of Muzahid et al. 2012 detected 72 O VI absorbers from 105 C IV sample towards 18 QSO sightlines where they find the column density distribution and gas temperatures are similar to the low redshift absorbers, but the absorptions are systematically narrower with a lowered non-thermal contribution. The limits in FUV observations make a similar study of most of the ions impossible. Hence, it is useful to find new candidates which can probe similar ionization conditions at high redshift. We find, Ne v 357 which have an ionization energy comparable with O vi ions is accessible from COS wavelength range at redshift $z > 2.2$. In a search towards the quasar sightline HE 2347-4342, we detected five intervening Ne v absorbers. The thesis also discusses the detection of these Ne v absorbers where their origin has a similar ambiguity observed for O vi ions in the low redshift IGM.

1.6 Organisation of the thesis

This thesis is an observational study of warm - hot baryonic matter in the intergalactic & circumgalactic medium. The detection of this gas phase is an important task in low redshift universe as it contributes a significant fraction of baryons at the present epoch. The detection of warm -hot baryons is expected even at high redshift even though the frequency of their detection can be very small. Though there is evidence from simulations that a significant fraction of baryons is there in warm-hot intergalactic phase, it is also important to detect them observationally. In this thesis, we discuss some of the intervening absorbers which show the evidence for such a warm-hot medium. We investigated three different metal line absorbers, O vi, Ne viii and Ne v in this thesis.

1.6.1 Chapter 2 - Quasar Absorption Line Spectroscopy

This chapter will provide an overview of the quasar absorption line spectroscopy. In this chapter, I will discuss the technique of quasar absorption spectroscopy, methods of line identification, the classes of absorbers, estimation of line parameter such as equivalent width, apparent optical depth, column density etc.

1.6.2 Chapter 3 - Detection of a Ne VIII absorber at $z = 0.61907$ probing warm-hot gas

This chapter discuss the detection of a Ne VIII absorber at $z = 0.61907$ in the *HST*/COS spectrum of background quasars SDSS $J080908.13 + 461925.6$. The Ne VIII 770 line is at $\sim 3\sigma$ significance. The Ne VIII is found to be tracing gas with $T \gtrsim 10^5$ K, predominantly collisionally ionized, with moderate densities of $n_{\rm H} \lesssim 10^{-4}$ cm^{-3}, sub-solar metallicities and total hydrogen column densities of $N({\rm H}) \gtrsim 10^{19}$ cm^{-2}. The low, intermediate ions and O VI are consistent with an origin in photoionized gas, with the O VI potentially having some contribution from the warm collisional phase traced by Ne VIII. The absorbers are residing in regions where there are several luminous ($\gtrsim L^*$) galaxies.

1.6.3 Chapter 4 - Detection of a Ne VIII absorber at $z = 0.57052$ probing warm-hot gas

Another detection of a Ne VIII absorber at redshift $z = 0.57052$ in the *HST*/COS spectrum of background quasar SBS $1122 + 594$ is discussed in this chapter. The absorber has H I absorption in at least three kinematically distinct components, with one of them having $b({\rm H\ I}) = 49 \pm 11$ km s^{-1}. The intermediate ionization lines, O VI and Ne VIII are coincident in velocity with this component. Their different line widths suggests warm temperature of $T = (0.5 - 1.5) \times 10^5$ K for the absorber which is predominantly collisionally ionized, with moderate densities of $n_{\rm H} \lesssim 10^{-4}$ cm^{-3}, sub-solar metallicities and total hydrogen column densities of $N({\rm H}) \gtrsim 10^{19}$ cm^{-2}. The absorber is within the virial radius of a $2.6L^*$ galaxy, possibly associated with shock heated circumgalactic material.

1.6.4 Chapter 5 - Detection of a pair of O VI absorbers at $z \sim 0.4$ probing warm-hot gas

This chapter discuss the detection of two O VI absorbers at $z = 0.41614$ and 0.41950 separated by $|\Delta v| = 710$ km s^{-1}, towards the background quasar SBS 0957+599. The low and intermediate metal species in the $z = 0.41614$ absorber are consistent with an origin in a medium dominated by photoionization. The O VI line in the absorber has a velocity structure different from other metal species. Corresponding to the centroid velocity of O VI, the Lyα shows a shallow and broad feature. The different line widths of these lines solve for a temperature of $T = 7.1 \times 10^5$ K where the absorber is dominated by collisional ionization. The total column density of this phase is $N(\mathrm{H}) = 2.8 \times 10^{20}$ cm^{-2}, which is an order of magnitude higher than the total hydrogen in the cooler photoionized gas. The second absorber is detected only in H I and O VI where the origin of O VI is from a low-density photoionized gas. A broad component observed in the Lyα provided an evidence for a separate gas phase with temperature $T \lesssim 2.1 \times 10^5$ K. The distribution of galaxies relative to the absorbers suggests that the line of sight could be intercepting a large-scale filament connecting galaxy groups.

1.6.5 Chapter 6 - Ne V absorbers at at high redshift IGM

This chapter will discuss the detection of five intervening Ne V absorbers at redshift $z = 2.7356, 2.4382, 2.3475, 6910$ and 2.3132 respectively. The metal lines of C IV, O VI, and Ne V is consistent with a photoionized origin in the $z = 2.3132$ absorber. None of the remaining absorbers can explain the observed ion ratios with simple photoionization. The ionization ratio of the $z = 2.6910$ absorber can be reproduced neither via photoionization nor collisional ionization. A neighbouring foreground quasar within 100 km s^{-1} from this absorber is observed which can influence the ionization conditions of this absorber. Similarly, a foreground quasar is observed within $\sim$ 3400 km s^{-1} of the $z = 2.7356$ absorber. Another two absorbers at $z = 2.4382$ and $z = 2.4887$ also can not produce via photoionization of UVB alone, does not show any evidence for proximity effect from any detected quasar suggest the possibility of warm - hot baryons at this redshift.

1.6.6 Chapter 7 - Summary & Conclusions

This chapter will provide a summary of the thesis, conclusions and future directions to address the detection of warm-hot baryons in the universe.

CHAPTER 2

Quasar Absorption Line Spectroscopy

2.1 Introduction

Quasars are distant bright objects with a relatively flat continuum in the entire electromagnetic region. The study of absorption lines in the spectra of these objects is the most successful method to understand the diffuse gas in the intergalactic and circumgalactic regions. This chapter is an overview of the technique of quasar absorption spectroscopy, classification of absorbers and some of the terms and definitions used in QSO spectroscopy.

2.2 Quasar Absorption Line Spectroscopy

From the discussions of chapter 1, we have seen that majority of the baryonic matter in the universe resides outside of virialized structures in a diffuse gas phase known as the intergalactic medium. When the light from distant quasars passes through the medium, various chemical elements in this medium selectively absorb a certain wavelength of the quasar continuum produces absorption lines on top of it. From the study of these absorption lines, the physical conditions and chemical abundances of the medium can be determined. This method of analyzing the quasar spectra and deriving the properties of the medium is known as Quasar Absorption Line Spectroscopy is illustrated in the cartoon 2.1. The method is not biased towards the brighter objects is one of the major advantages of this.

Most of the prominent atomic transitions from atoms/ ions are in the far ultraviolet region. The most common line in a quasar spectra is the Lyα line with a restframe wavelength of $\lambda_{rest} = 1215.67$. Absorption lines from higher order Lyman series lines and metals lines such as O, N, C, S etc are typically seen. Some of the common lines observed in quasar spectra are tabulated in Table 2.1.

Figure 2.1: Quasar Absorption Spectroscopy

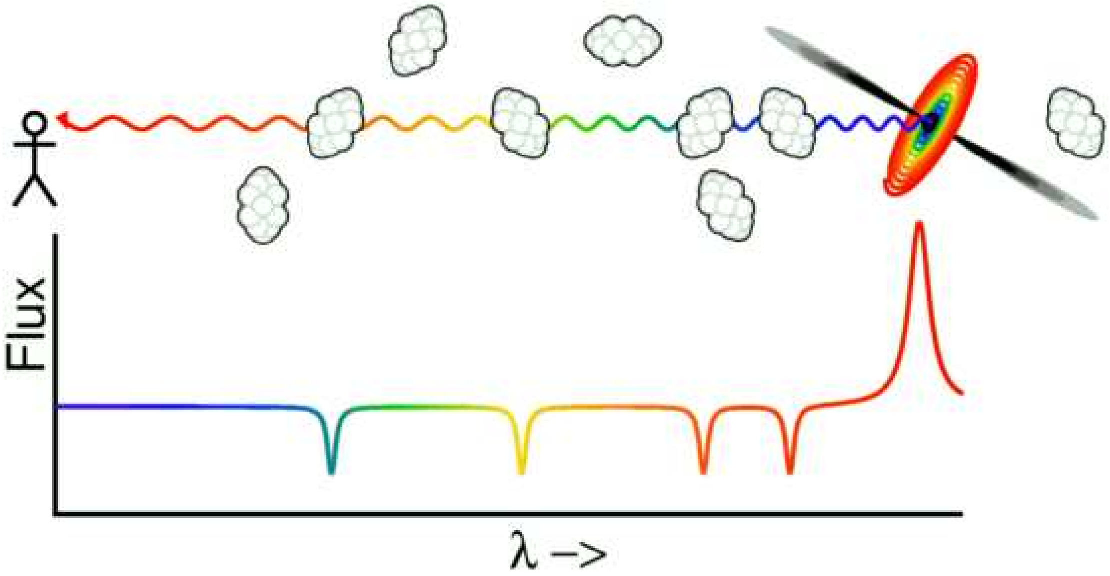

Figure 2.1 The cartoon illustrates QSO absorption spectroscopy. The red bi-lobular structure shows the background QSO. The radiation from this quasar passing through intergalactic medium interact with the diffuse gas in this medium. This produce absorption signature on the top of the quasar spectrum which can be detected from earth/ space with different telescopes. An illustration of the spectra is shown in the bottom panel. The change in colour observed on the spectra corresponds to the of cosmological redshift due to the expansion of the universe. This figure was adapted from Edward L. Wright web site.

If the absorber is at high redshift, these transitions will be shifted to optical- IR region due to Hubble expansion which then becomes detectable with ground-based telescopes. However, the study of low redshift IGM requires observations in the ultraviolet regions which is possible only with space-based observations.

The observed spectra of a quasar HE $2347 - 4342$ in the visible and far ultraviolet regions are shown in Figure 2.2. The broad emission line observed at $\lambda = 4750$ Å is the Lyman-α line associated with HE $2347 - 4342$. Bluewards of this emission line, plenty of narrow absorption lines are observed. Most of these lines are Lyman-α absorptions produced from the intergalactic gas with redshift $z_{abs} < z_{em}$. These narrow lines are called Lyman-α forest lines. The narrow lines

Table 2.1: Some Common lines observed in QSO Spectra

Transition	λ (Å)	f	γ
H I 1216	1215.6701	0.416400	6.265E8
H I 1026	1025.7223	0.079120	1.897E8
H I 972	972.5368	0.029000	8.126E7
...	...	...	...
C II 1335	1334.5323	0.127800	2.870e8
C II 1036	1036.3367	0.1231	2.270e9
Si II 1260	1260.4221	1.180000	2.950E9
Si II 1193	1193.2897	0.582000	4.070e9
Si II 1190	1190.4158	0.292000	4.080E9
C IV 1548	1548.195	0.190800	2.654E8
C IV 1551	1550.770	0.095220	2.641E8
Si IV 1394	1393.7602	0.513000	8.800e8
Si IV 1403	1402.7729	0.254000	8.620e8
N V 1239	1238.821	0.157000	3.411e8
N V 1243	1242.804	0.078230	3.378e8
O VI 1032	1031.9261	0.132500	4.149e8
O VI 1038	1037.6167	0.065800	4.076e8
...	...	...	...

Table 2.1 Some of the commonly observed lines in the QSO spectra are tabulated. The columns from left to right are the atomic transitions, the wavelength of the transitions, oscillator strength of each transition and gamma values of these transitions. The atomic data is taken from Morton 2003.

redwards of the emission lines include FUV absorption from metal species and higher-order Lyman series lines. The HST/COS spectra of the quasar show a strong Lyman-α emission from Milkyway at $\lambda \sim 1216$ Å. The stong lines observed at $\lambda < 1190$ Å is from He II absorption.

In general, depending on the separation from background quasar, absorbers are broadly classified into Intrinsic and Intervening absorbers. The classification of absorbers are separately discussed in Section 2.3.

2.2.1 Analysis of the Spectra

Line Identification & Selection of Absorbers

The focus of this thesis is to study the properties of highly ionized metal lines of O VI, Ne VIII and Ne V absorbers. Among this, O VI and Ne VIII ions have doublet transitions in the far ultraviolet region which is accessible at $z > 0.4$ for HST/COS. The wavelength separation between doublet lines scale with redshift as $(1 + z)$, and their absorption strength is proportional to $(f \times \lambda)$, both of which help in the identification of doublet lines. Once a line is identified, from the observed redshift of this absorber, remaining lines can be detected. All the absorbers discussed in this thesis are identified from a search for the comparatively strong doublet transitions of O VI ions.

From the detected O VI absorbers, we find two of the system shows a marginal detection of Ne VIII and one with a presence of a Broad Lyman Alpha (BLA) component. In a search towards the high redshift quasar sightline, we also detected intervening Ne V 357 absorbers. These are the samples discussed in this thesis.

Absorber Redshift

The observed spectrum of an extragalactic source will be shifted towards higher wavelength due to the expansion of the universe. The shift in the spectral line is

Figure 2.2: Spectra of the quasar HE 2347 − 4342

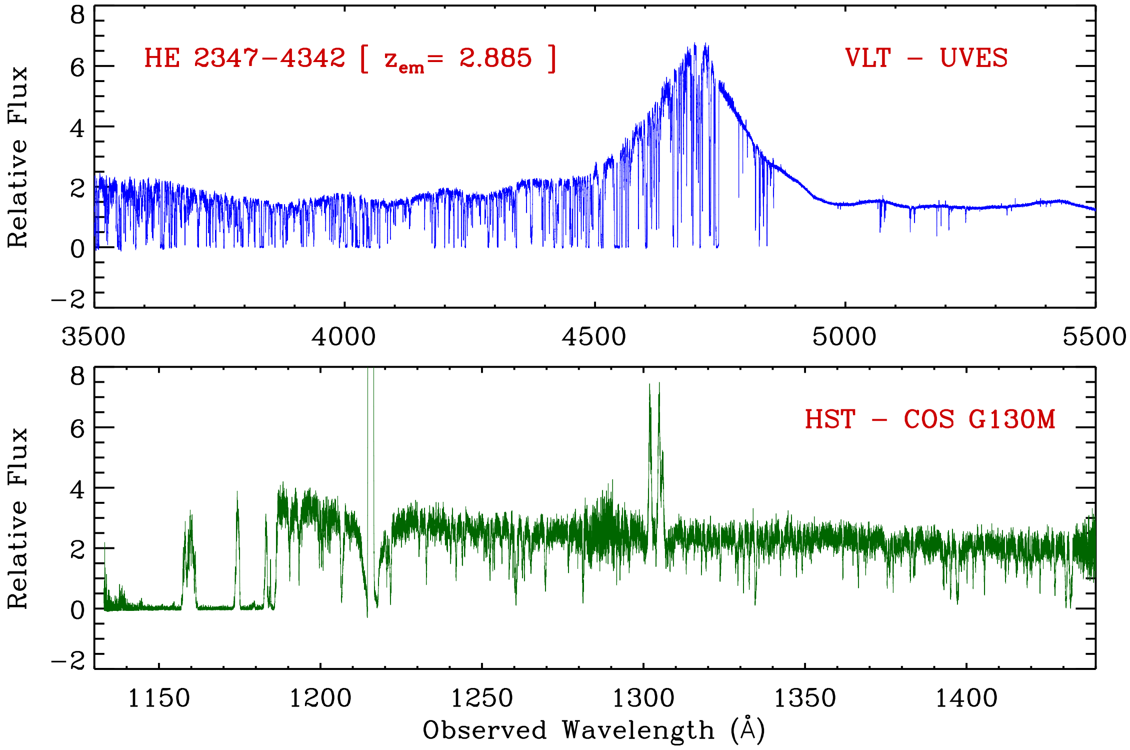

Figure 2.2 The observed spectra of HE 2347 − 4342 using Very Large Telescope (VLT/UVES) and HST/COS is shown in the above panels. The broad emission line observed at $\lambda \sim 4700$ Å is the intrinsic Lyman α line. The dence forrest lines in the spectra with $\lambda > 4700$ Å is the intervening Lyman-α forest lines. The lines observed at $\lambda < 4700$ Å are mostly metal lines. At $\lambda \sim 1150$ Å, there is a stong absorption He II absorption. This spectra also contain FUV absortpions from intervening and associated metal lines.(The VLT/UVES spectrum shown here is observed as a part of the programme 'The Cosmic Evolution of the IGM' (Bergeron et al., 2004). COS data is obtained from the MAST public archive.)

represented by the quantity called redshift (z).

$$(1 + z_{\rm abs}) = \frac{\lambda_{\rm obs}}{\lambda_{\rm rest}} \tag{2.1}$$

The redshifts of the absorbers quoted are based on any of the unsaturated metal lines in the absorber. For the absorbers with multiple components, the median

Figure 2.3: Spectral Lines

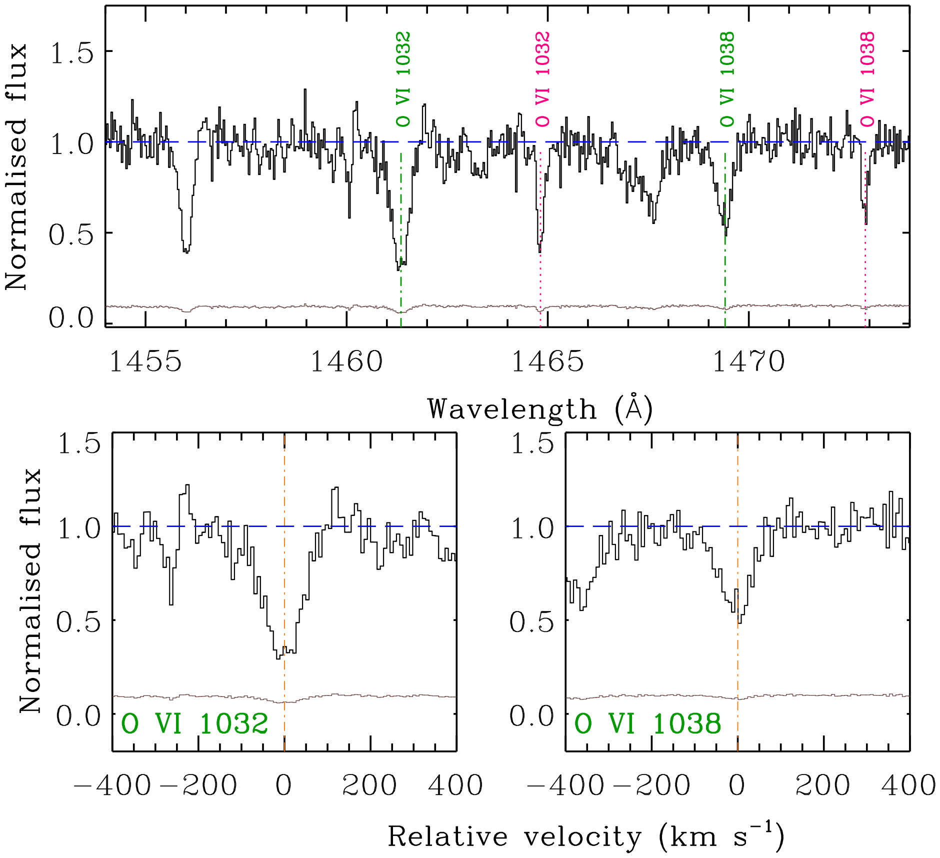

Figure 2.3 *Top Panel* A small region of the normalized spectra of SBS 0957 + 599 from HST/COS observation is shown. The O VI doublet transitions from two neighboring absorbers at redshift $z = 0.41614$ and $z = 0.41905$ are marked with green dashed and pink dotted lines. *Bottom Panel* The O VI transitions in the $z = 0.41614$ absorber is represented in the restframe of the absorber.

of their optical depth is taken as the absorber redshift. For example, in Figure 2.3, the O VI 1032 transition of an absorber is observed at $\lambda = 1461.35$ Å. From the shift in the wavelength from 1031.9261 Å to 1461.35 Å, the redshift of the absorber is calculated as $z_{abs} = 0.41614$.

Restframe velocity of the absorber

TThe absorbers are usually represented in their restframe velocity. A transformation from the observed wavelength to the rest frame velocity of the absorber can be obtained using the following formula.

$$v = c[\frac{((1+z_1)^2 - (1+z_{abs})^2}{((1+z_1)^2 + (1+z_{abs})^2}] \quad (2.2)$$

where c is the velocity of light, z_{abs} is the absorbers redshift and z_1 is the redshift of the pixel for which we have to calculate the velocity separation.

The representation of O VI doublet lines in the absorber $z_{abs} = 0.41614$ in their velocity space using the above equation is shown in the bottom panel of Figure 2.3.

Apparent Optical depth

The optical depth of an absorber is the logarithm of the ratio of incident to the transmitted power of the radiation. When a beam of light with specific intensity I_ν passes through a gas medium, some fraction of their energy is absorbed by the medium. For a pure absorbing medium, the intensity of outcoming radiation can be written as:

$$I_\nu(\text{out}) = I_\nu(\text{in}) e^{-\tau_\nu} \quad (2.3)$$

where τ_ν is the optical depth of the cloud. Observationally, optical depth (τ_ν) of an absorption can be calculated from the spectra as follows:

$$\tau_\nu = \log \frac{I_{\text{in}}(\nu)}{I_{\text{out}}(\nu)} \quad (2.4)$$

I_{in} and I_{out} are the incident and transmitted flux at frequency ν.

Column density

For absorption line studies along a given line of sight, the information on the three dimensional size of the absorber, and therefore the number density, is not readily available. What one measures from line of sight spectroscopy is the column density of any given species. The number of particles per unit area in the sky is defined as column density. The relationship between density and column density is as follows:

$$N(\mathrm{cm}^{-2}) = \int n(\mathrm{cm}^{-3})dl \tag{2.5}$$

The optical depth and column density per unit velocity related as,

$$\tau(v) = \frac{\pi e^2}{m_e c} f\lambda N(v) = 2.654 \times 10^{-15} f\lambda N(v) \tag{2.6}$$

where N(v) is the column density is in the units of atoms cm^{-2} (km s^{-1})$^{-1}$. Thus, total column density of an unsaturated line of any ion can be calculated from apparent optical depth using the following equation.

$$N(\mathrm{cm}^{-2}) = \int N(v)dv = \frac{m_e c}{\pi e^2 f\lambda} \int \tau(v)dv \tag{2.7}$$

$$= \frac{m_e c}{\pi e^2 f\lambda} \int \log \frac{I_{\mathrm{in}}(v)}{I_{\mathrm{out}}(v)} dv \tag{2.8}$$

A detailed desscription of this method can be found in Savage and Sembach 1991.

Equivalent Width

The equivalent width (W) measurement is useful to compare the strength of absorption lines within the same absorber or between different absorbers. Here, we compare the area of an absorption line with the area of a perfect dark absorption line with a rectangular profile (as shown in Figure 2.4). The height of this imaginary dark line is the continuum normalised flux (F_C), area equal to the area of the absorption line, and the width is called equivalent width usually expressed in the units of Å. Equivalent width depends on the width of absorption profile and the total number of atoms/ions in the source of absorption. ie, it depends on temperature, electron pressure and atomic constants, but is independent of the spectral resolution. Note that for an absorption line $W > 1$ and for an emission line $W < 1$.

Equivalent width can be calculated from an absorption line using the following expression:

$$\mathrm{W} = \Sigma \frac{F_C - F_\lambda}{F_C} \delta\lambda \tag{2.9}$$

where F_C = flux at the continuum level, F_λ = flux at wavelength λ respectively.

In the study of extragalactic absorbers, the width of absorption lines will be modified due to the expansion of the universe. ie, the strength of the absorption will be enhanced by a factor of (1+z). The restframe equivalent width of a line can be calculated as follows:

$$\mathrm{W_{rest}} = \frac{1}{(1+z)} \Sigma \frac{F_C - F_\lambda}{F_C} \delta\lambda \tag{2.10}$$

A detailed technical discussion on the calculation of equivalent width and the associated errors can be seen in Sembach and Savage 1992.

Voigt Profile Function

None of the absorption lines is infinitely sharp with cutting-edge borders. These lines usually have a spread in their spectra can be represented by a suitable line spread functions. The common mechanisms which cause a spread in an atomic transition are natural, collisional and Doppler broadening. A combination of these three is called Voigt Profile Function which represents an absorption line in general.

- **Natural Broadening** The origin of this broadening is quantum mechanical in nature. For an atom, the spread of an energy state and the duration of an electron at that state related by Heisenberg uncertainty principle as $\Delta E.\Delta t \sim h/2\pi$. This suggests that an atomic transition from one state of the atom have a "rate" than an instantaneous energy drop. Such a transition rate in time can be observed as a spread in the frequency. This is called natural broadening and the line can be represented by the following equation.

$$\phi_\nu = \frac{\pi e^2}{m_e c} f \frac{\Gamma/4\pi^2}{(\nu - \nu_0)^2 + \Gamma/(4\pi)^2} \mathrm{cm}^{-2} \tag{2.11}$$

  For the lines in optical - UV wavelength range, the contribution of natural broadening is very small.

- **Collisional Broadening** Collisional broadening is similar to natural broadening, can be represented by the Lorentz profile. In this case, the collisional process can modify the emitted radiation randomly.

Figure 2.4: Equivalent width & Comparison of line profiles

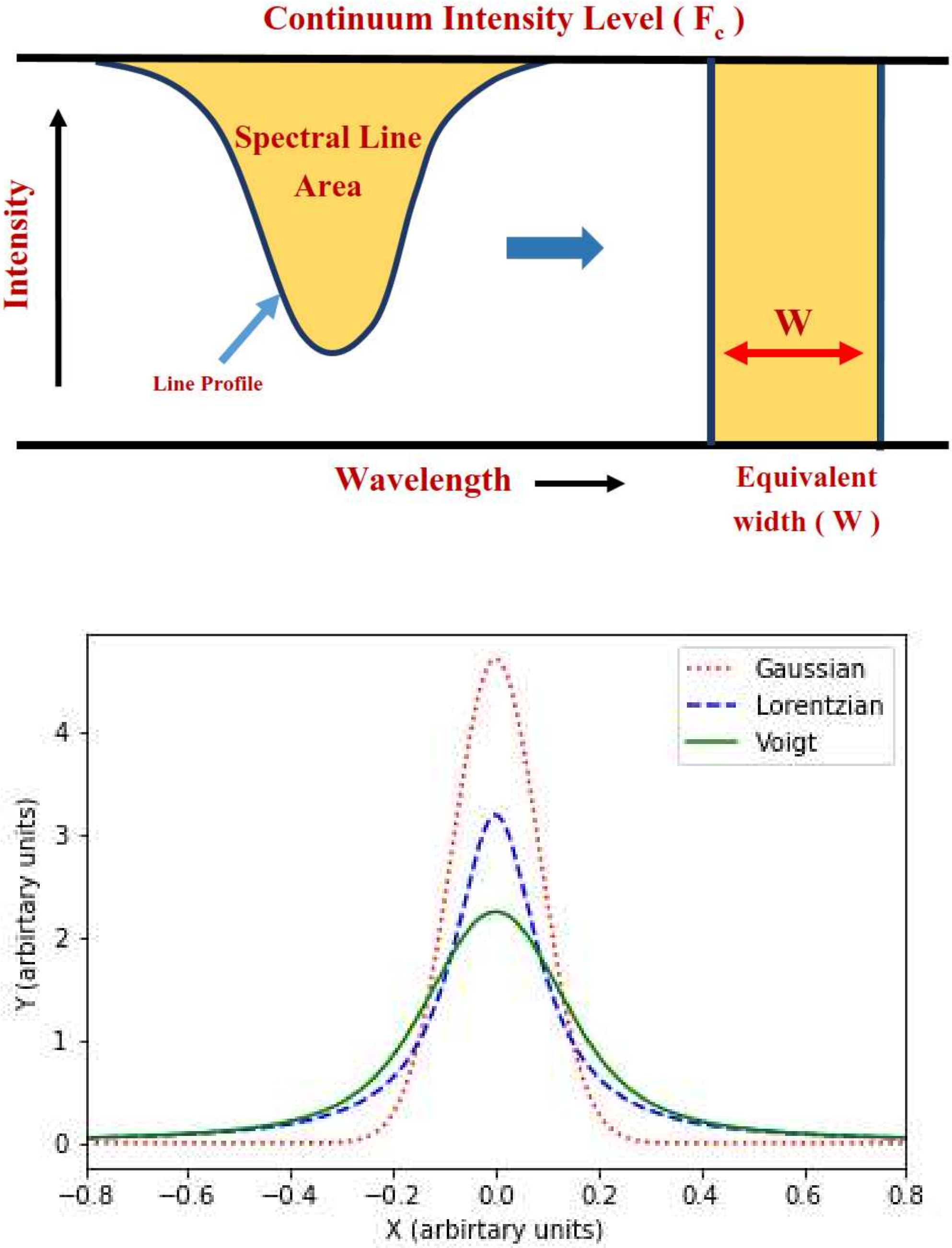

Figure 2.4 *Top Panel* The cartoon illustrate equivalent width of an absorption line. Here, the area of the absorption line is translated to the area of a rectangle (equivalent to a perfect dark absorption line) where one of its side is equal to the continuum flux and the width is called equivalent width of the line. *Bottom Panel* The figure shows a comparison of Gaussian, Lorentzian and Voigt profiles. Voigt profile is a convolution of a Gaussian and Lorentzian profiles.

- **Doppler Broadening** In local thermodynamic equilibrium, the velocity of atoms is represented by Maxwellian distribution. The internal velocity of each atom causes a Doppler shift in the frequency of emission/absorption. This leads to a Doppler broadening in the absorption line. The Doppler line spread can be represented by:

$$\phi_\nu = \frac{1}{\Delta\nu_0\sqrt{\pi}} exp^{-}[\frac{(\nu-\nu_0)^2}{\Delta\nu_0}]\mathrm{cm}^{-2} \tag{2.12}$$

In general, an absorption line is a combination of these broadening mechanisms.

$$\phi(\nu) = \frac{\Gamma}{4\pi}\int_{-\infty}^{\infty}(\frac{m}{2\pi kT})^{\frac{1}{2}} exp(\frac{-mv_z^2}{2kT})(\nu-\nu_0-\nu_0\nu_z/c^2) + \frac{\Gamma}{4\pi}^{\frac{1}{2}} \tag{2.13}$$

The convolution of Gaussian and & Lorentzian profile represent the function called Voigt profile.

$$H(a,u) = \frac{a}{\pi}\int_{-\infty}^{\infty} exp{-}y^2)a^2+(u-y)^2 \tag{2.14}$$

ie, the line spread can be written using Voigt profile as :

$$\phi(\nu) = (\Delta\nu_D)^{-1}\pi^{-\frac{1}{2}}H(a,u) \tag{2.15}$$

where $a = \frac{\Gamma}{4\pi\Delta v_D}$, $u = \nu - \nu_0\Delta v_D$ respectively.

Curve of Growth

The change in the strength of an absorption line with the number of atoms/ ions producing these absorptions is known as Curve of Growth (COG). The strength of the line (or equivalent width) depends on column density (N) and broadening parameter (b). Depending on the relationship between N, b, and W, COG plot has divided into three major regions, 1. The linear regime, 2. The logarithmic regime and 3. The square root regime. The changes in N, b, and W at these three regions are discussed below.

- **The linear regime**

  The equivalent width of an absorption line with $\tau << 1$ grow linearly with the increase in column density in the linear regime of COG. This relationship

Figure 2.5: Curve of Growth

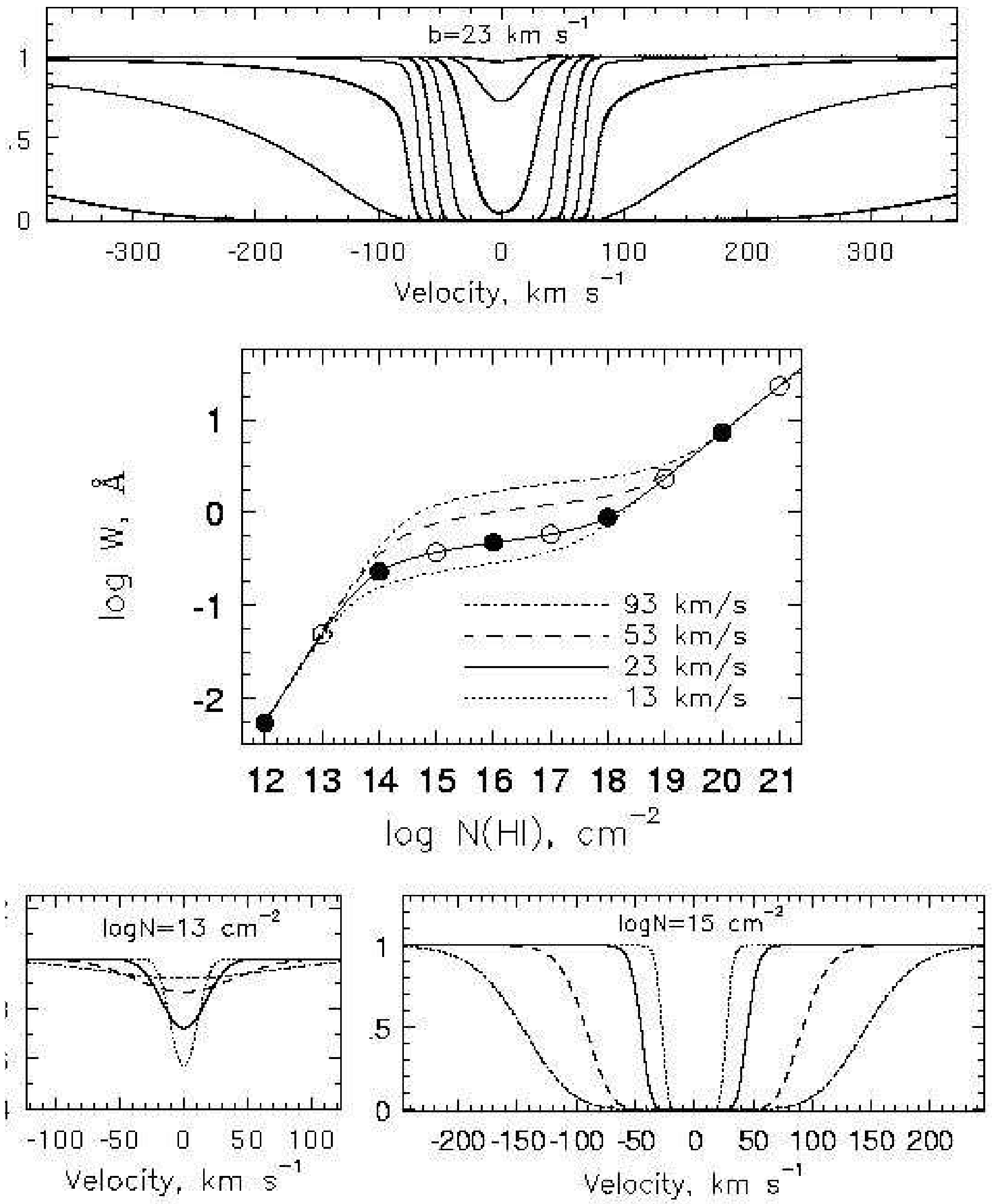

Figure 2.5 The change in line profile of the Ly-α absorption with b = 13, 23, 53, and 93 km s^{-1} is shown along with the corresponding curve of growth. *Top* This plot show the change in line profile of a line with a fixed b of 23 km s^{-1} for a range of column density from 10^{12} to 10^{20} cm^{-2}. *Bottom Panels* The absorption profiles are shown for a fixed column density in the linear and logarithmic regimes of COG. In the linear regime, the absorber with smaller b show larger depth and larger b show a smaller depth respectively. *Middle Panel* The curve of growth of Ly-α absorption.(Image credit: Charlton and Churchill 2000)

can be used to calculate the column density of an absorption line from the 'total missing power' (equivalent width) of the line. This method is useful for unresolved absorbers where the line width of their individual components is difficult to determine.

An approximate relationship between W and N is shown below where the notations have their usual meaning.

$$W = \frac{f\pi e^2\lambda^2}{mc^2}N \tag{2.16}$$

Note that in this regime, equivalent width is not related to the broadening parameter. For example, see the *Bottom Left Panel* of Figure 2.5. This figure shows the Ly-α absorption line with a fixed column density of hydrogen log N(H I) = 13 cm^{-2} for four different b , 13, 23, 53, and 93 km s^{-1} respectively. As the equivalent width is independent of b, all of these lines should have the same area. Hence, an increase in b value makes the absorption line shallower.

- **The logarithmic regime**

  As the column density of atoms/ions increases, the absorption lines become stronger and stronger and reaches a saturation stage. Once, the line is saturated ($10 \leq \tau \leq 10^3$), the core Gaussian components of absorption cannot increase the strength of the lines further. The contribution from Lorentzian damping wings are insignificant at this stage and hence, the strength of the absorption (equivalent width) increases only slowly or almost nil with the further increase in the number of particles. This is the flat part of the curve of growth (See Figure 2.5).

  An approximate relationship between W, b, and N in this regions is as follows.

$$W = b\frac{\lambda}{c}(\ln[\frac{\pi^{\frac{1}{2}}e^2}{mc}\frac{\lambda}{b}Nf])^{\frac{1}{2}} \tag{2.17}$$

$$\text{ie,} W \propto b\sqrt{\ln\ (\mathrm{N/b})} \tag{2.18}$$

The *Bottom Right Panel* of Figure 2.5 illustrate this situation. The Ly-α line with column density log N(H I) = 15 cm^{-2} for four different b values, 13, 23, 53, and 93 km s^{-1} are shown here. From the figure, it is clear that the area

Figure 2.6: HST/COS optical path

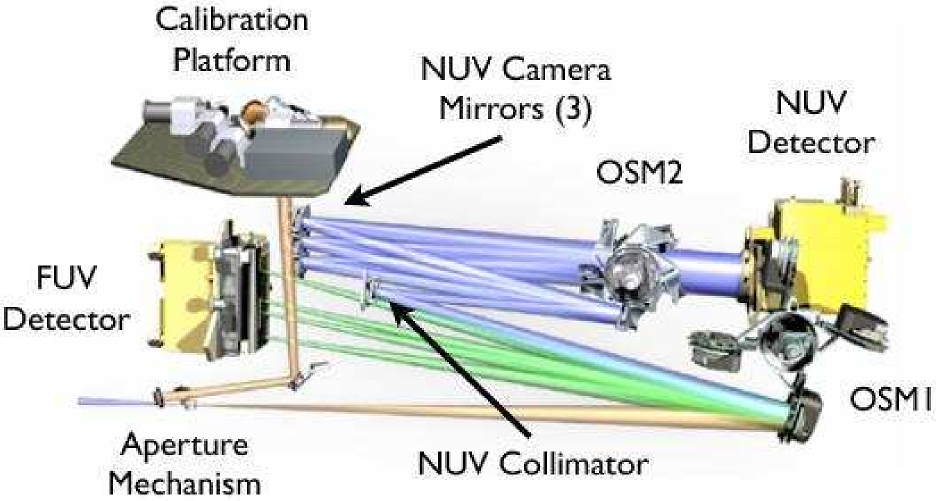

Figure 2.6 The optical path and instrumental locations of HST/COS are shown in this figure. The light from HST Optical Telescope Assembly (OTA) enters through the entrance apertures (In most COS science observations Primary Science Aperture(PSA) is used) reach Optics Select Mechanism (OSM1) where the gratings and mirrors present. There are 3 gratings and one mirror in this unit. The flat collimating mirror (NCM1) passes the beam to NUV channel and the three gratings G130M, G160M and G140L direct the beam into the FUV channel. (Image credit: Cosmic Origins Spectrograph Instrument Handbook)

of absorption increase as the b value increases. This shows that equivalent width is sensitive to the b values in the logarithmic region of COG.

- **The square root regime**

  When the absorption line is very strong such that $\tau > 10^4$, the contribution from Lorentzian increases drastically due to the broad wings of the absorption. In practical situations, this part of COG can observe only for Ly-α transitions. The change in the line profile of a Ly-α absorption with an increase in column density can be seen in Figure 2.5 *Top Panel*.

$$\text{In this region,} W \propto \sqrt{N} \tag{2.19}$$

2.2.2 Detectors

The study of warm -hot gas in the low-redshift universe requires observations in the far ultraviolet region (FUV). Hubble Space Telescope (HST) is the most successful telescopes which yield such an opportunity to open an observational window in both NUV and FUV wavelength. With the Installation of Cosmic Origin Spectroscope on HST in May 2009, the spectroscopic capabilities of HST got enhanced significantly. For this thesis work, we mostly used the data from HST/COS observation.

2.2.3 Cosmic Origin Spectrograph/ Hubble Space Telescope

The Cosmic Origins Spectrograph (COS) is essentially is a slitless spectrograph with a field of view of 2.5 arcsec. It consists of two independent channels of observations. In the Far Ultra Violet region, it covers wavelength of 900 -2150 Å and in near UV from 1650 – 3200 Å where each of this channels is equipped with low (3000) and medium (R $\sim$ 20,000) resolution gratings. The wavelength dependent resolution of each of the FUV gratings is compared in Figure 2.7.

Though the spherical aberration of HST primary mirror is corrected by COS optics, midfrequency wavefront errors (MFWFEs) and zonal irregularities cause extended wings and a broad and shallow core components in the lines in COS spectra. Hence, for an accurate modelling of the spectral lines, a model LSF has to be incorporated (Kriss et al., 2011). The comparison of the model for G130M grating at $\lambda = 1309$ Å with a Gaussian profile is shown in Figure 2.7.

Figure 2.7: Resolving Power and Line Spread Function of COS Gratings

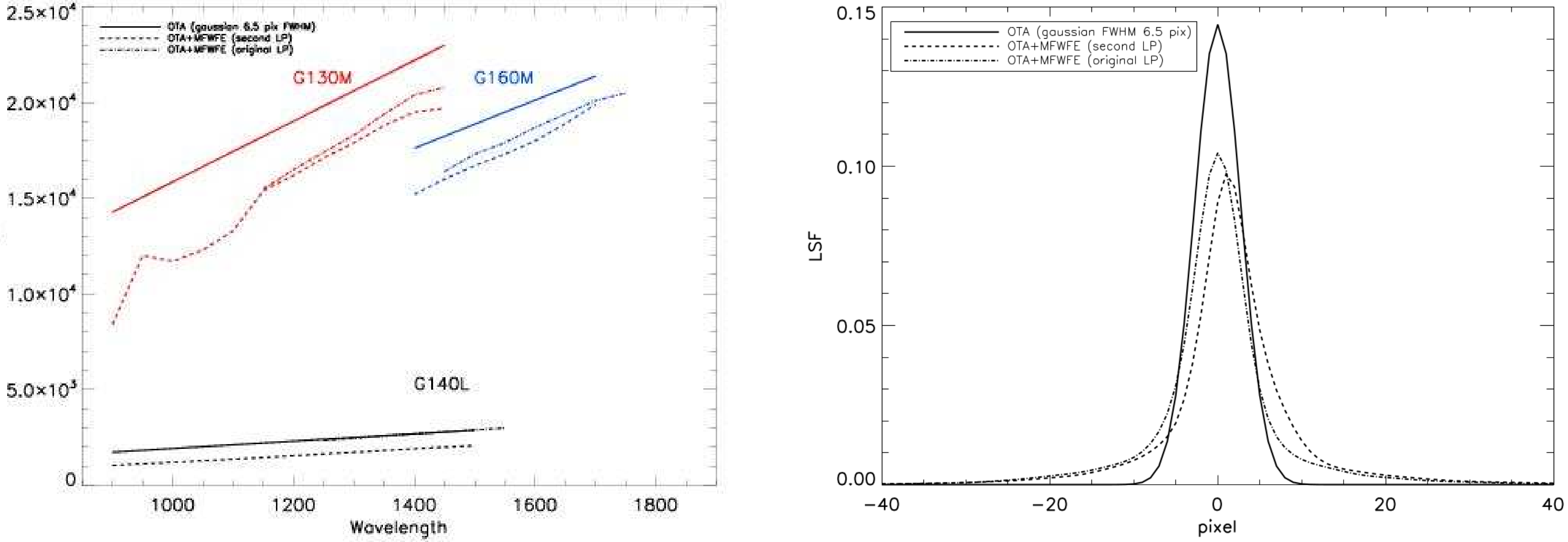

Figure 2.7 *Left Panel* shows the wavelength-dependent variation of resolving power of G130M, G160M and G140L gratings respectively. The solid line represents a Gaussian with FWHM=6.5 pixels, dot-dash lines represent the measured resolution using the Line Spread Functions(LSF) with one orbit MFWFE (mid- frequency wavefront errors) included at the original lifetime and dashed lines represents resolution using LSF with one orbit MFWFE included at the second-lifetime position.In the *Right Panel*, a comparison of COS line spread functions of G130M grating at 1309 Å with a Gaussian profile of width FWHM 6.5 pixels is shown. The dotted line included HST mid frequency wavefront errors at the original lifetime position and the dashed line represents the same at second life position. (Image credit: Cosmic Origins Spectrograph Instrument Handbook)

2.2.4 Ultraviolet and Visual Echelle Spectrograph (UVES) / Very Large Telescope

The high-resolution UVES spectrograph is one of the units in the ground-based telescope VLT, which can operate with high efficiency from the atmospheric cut-off at 3000 Å onwards. The limit of detection at a longer wavelength is decided by the CCD around 11000 Å. The spectrograph have a maximum resolution of 80,000 (blue) or 110,000 (red) respectively.

2.3 Classification of Absorbers

2.3.1 Intrinsic and Intervening Absorbers

Some of the absorption lines in the quasar spectra are produced by the gas in the quasar/ host galaxy called intrinsic absorption. These lines can be broad with thousand or more km s^{-1} in width (Broad Absorption Line - BAL) or narrow (with tens to hundreds of km s^{-1}) depending on the region where it originates.The BAL is produced by the gas emitted from the associated quasar and the redshift of these absorbers will always close to the quasar redshift. With similar redshift, absorption lines with a narrow width are also observed. These are generally called associated absorber or NAL. However, most of the absorption in the spectra are unrelated to the quasar probing gas in the intergalactic medium at different redshifts. These are known as intervening absorbers(Sargent et al., 1980).

Distinguishing intervening absorption from NAL is easy for absorbers with velocity $\geq 10,000$ km s^{-1} away from the background quasar. As there is no known physical mechanism which can produce such high-velocity jets, the observed velocity is most likely the consequence of Hubble flow. For the absorbers with velocity $< 10,000$ km s^{-1}, determine the real nature of the absorption is difficult. In such cases following methods can be used to get some insights about the nature of the absorption, though all the associated systems need not show these features.

- Partial coverage: When the absorber is close to the background source, there is a possibility that the absorber cannot completely shield the light from the background source. This will modify the spectra as the light received by the detector is a combination of light which passed through the absorber and also the light coming directly. The effect of partial coverage can be understood from the column density profile of absorption lines.

- Outflows: Another possibility is that whether the absorber corresponds to some quasar driven outflows. Generally, such outflows have significantly saturated higher ionization lines such as O VI, Ne VIII etc.

- The high velocity of the AGN outflows caused by the winds from the disk of the associated quasar. Hence, it is expected to have variability in the absorption lines. (Muzahid et al., 2016; Teng et al., 2013)

- For the absorbers close to the quasars, the observed ion ratios are produced by the hard UV radiation field of a quasar. In intervening systems, ionization conditions are maintained by UV background radiation. Hence, the observed ion ratios can give some clue regarding the origin of the absorber.

Another classification of absorbers is in terms of the H I content in the component. Typically H I column density in the rang $10^{12} - 10^{22}$ cm^{-2} can be detected by absorption. This is classified as:

- Lyman-α systems: Most of the H I absorptions seen in IGM are with log N(H I) $\leq 10^{17}$ cm^{-2}. These systems are highly ionised gas with lower metalicity and density.

- Lyman Limit System : These are systems observed with H I column density $> 2 \times 10^{17}$ cm^{-2}. These are believed to be originating in galaxy halos. Generally strong associated metal absorptions are detected along with these systems.

- Damped Ly-α systems : Absorption lines with H I column density $> 10^{20}$ cm^{-2} show a damping wing in the Ly-α absorption profile is called Damped Ly-α which harbours $\sim 80\%$ of the neutral mass density at redshift z $<$ 1.65 (Rao and Turnshek, 2000; Noterdaeme et al., 2012). From SDSS DR9 survey, Noterdaeme2012 compiled a sample of 12081 DLAs within redshift $z = 2.15 - 5.2$ which accounts for most of the neutral baryons at high redshift. Identification of optical counterparts of DLA at low redshift suggests that it could be associated with galaxies of all sort of morphology, luminosity etc (Rao et al., 2003; Turnshek et al., 2001).

CHAPTER 3

Detection of a Ne VIII Absorber at $z = 0.61$ Probing Warm Gas

3.1 Introduction

As discussed in chapter 1, the common diagnostics for detecting the WHIM are the absorption lines of highly ionized metals such as O VI, Ne VIII, and Mg X (Qu and Bregman, 2016; Tripp et al., 2001, 2008; Savage et al., 2002, 2005; Danforth and Shull, 2008; Narayanan et al., 2009, 2012). Compared to O VI lines, Ne VIII is a less ambiguous tracer of collisionally ionized warm - hot baryons. However, the recent study of Hussain et al. (2017) using a revised extragalactic background (KS15) find that photoionization is a plausible scenario for the production of Ne VIII, provided the gas phase metallicities are super solar. This necessitates a much careful analysis of Ne VIII absorbers which are a vital part to understand the otherwise, observationally less evident warm -hot baryons at low redshift. A statistical study of these absorbers is difficult with the limited sample of Ne VIII absorbers. There are only 10 instances of intervening Ne VIII detections so far and hence, each detection of a Ne VIII absorber has a great role in the understanding of WHIM. This chapter will discuss the discovery of a new Ne VIII absorber at $z = 0.61907$ towards a background quasar SDSS J080908.13+461925.6. Using the revised extragalactic background of KS15, we analyzed the absorber in detail and rule out the possibility of a photoionized origin for the Ne VIII. Also, we discuss the possible origin of the absorber from the limited galaxy sample available in the SDSS database, where we detect several luminous ($\gtrsim L^*$) galaxies in the extended neighborhood of the absorber.

This chapter is organised as follows. Section 3.2 presents information on the COS archival observations of both sightlines and the data analysis techniques used. Section 3.3 describe our measurements on the properties of the absorption system,

Table 3.1: Individual COS integrations for the quasar SDSS J080908.13+461925.6

MAST ID	DATE	GRATING	λ_c (Å)	t (S)
LBHO77010	06 -10-2010	G130M	1291	1556
LBHO77010	06 -10-2010	G130M	1309	1590
LBHO77010	06 -10-2010	G160M	1577	2561
LBHO77010	06 -10-2010	G160M	1623	2434

Table 3.1 Table show the details of individual exposures used to generate the final spectra. The column from left to right corresponds to the name of the exposure in MAST database, date of the observation, grating used for the observation, central wavelength of the grating and the exposure time respectively.

with emphasis on the Ne VIII lines. The ionisation mechanisms, physical properties and chemical abundances of the absorber towards SDSS J080908.13+461925.6 are discussed first in section 3.4, followed by Section 3.5 consists of information on the galaxies identified by the SDSS that are coincident in redshift with the absorber. The main results are summarised in section 3.7.

3.2 The HST/COS Data

The SDSS J 080908.13 + 461925.6 ($z_{em} = 0.6587$) quasar data presented here are far-UV medium resolution (instrumental FWHM $\sim$ 17 km s^{-1}) spectra retrieved from the *Hubble Space Telescope* / Cosmic Origins Spectrograph (COS) MAST archive[1]. The instrument capabilities and in-flight performance are described in detail by Froning and Green 2009, Dixon 2010, Osterman et al. 2011, and Green et al. 2012. The observations were carried out in 2010 as part of a COS dwarf galaxy halos project (PI. Jason Tumlinson, Prop ID: 12248, Bordoloi et al. 2014). The separate science exposures were processed using the STScI CalCOS (v2.17.3) pipeline. The data consists of G130M and G160M grating spectra of 4.9 ks and 3.0 ks integration times respectively. For each grating setting, there

---

[1] https://archive.stsci.edu/

were multiple FP-position exposures. These individual science exposures were combined in flux units weighted by their exposure times using the coaddition routine developed by Charles Danforth[2] and as described in Danforth et al. (2010). The pipeline reduced COS spectra are over-sampled at 6 pixels per 17 km s^{-1} resolution element. The spectra were therefore binned to the optimal Nyquist sampling of 2 pixels per resolution element. The resultant fully combined spectrum has a $S/N \sim 10-20$ per pixel over much of the wavelength range between 1135 Å and 1790 Å. The spectral resolution of COS is wavelength dependent with a maximum of $R = \lambda/\Delta\lambda \sim 20,000$ at near-UV wavelengths and decreasing monotonically to values of $R \sim 17,000$ at the edge of the far-UV covered by the G130M grating. The spectra were continuum normalized by fitting lower order polynomials across wavelength intervals of approximately 20 Å, avoiding regions containing absorption or strong emission features.

3.3 The $z = 0.61907$ Absorber towards SDSS J $080908.13 + 461925.6$

The continuum normalised regions of the COS spectrum covering important transitions of the absorber at $z = 0.61907$ are shown in Figure 3.1, 3.2. The absorption system has H I Lyman series (Lyα – H I 915), C II 903.9, 903.6, C III 977, N III 990, N IV 765, O III $702, 833$, O IV 788, O VI 1038, S IV 748, S V 786, S VI $933, 945$ and Ne VIII 770 lines detected at $\geq 3\sigma$ significance. In addition, the spectrum also covers O II 834, N II 916, and Ne VIII 780 which are non-detections. For the lines which are not detected, we quote the 3σ upper limit by integrating the spectrum through the same velocity range over which O VI is detected.

The absorber is displaced from the systemic redshift of the quasar ($z_{em} = 0.6587$, Hewett and Wild 2010) by $\Delta v = -7252$ km s^{-1} which is beyond the typical velocity offset cutoff of $\Delta v \lesssim 5000$ km s^{-1} used to differentiate associated absorbers from intervening systems e.gs., (Foltz et al., 1986; Shen and Ménard, 2012). To rule out the possibility of the absorber being associated with the AGN, we compared the apparent column density profiles of higher order Lyman series

---

[2] http://casa.colorado.edu/∼danforth/science/cos/costools.html

Figure 3.1: The absorber at $z = 0.61907$ in restframe

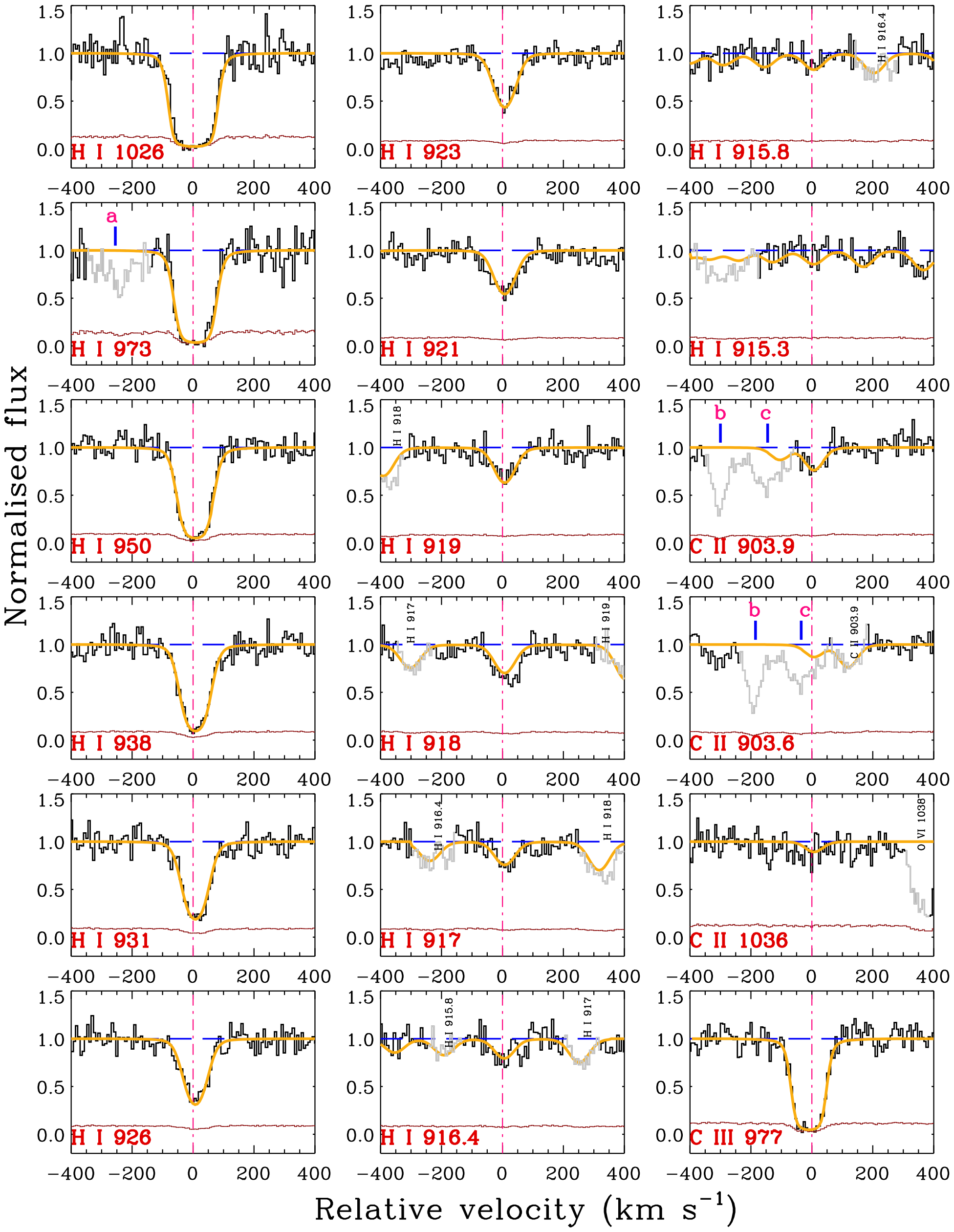

Figure 3.1 System plot showing the important transitions against the rest-frame velocity of the $z = 0.61907$ absorber. The centroid of the absorbing component is marked with a red vertical tick mark. The absorption system covers a host of Lyman series lines, metal lines such as C II, C III, N III, N IV, O III, O IV, O VI, S IV and S V. The lines N II 916, N II 1084 and Ne VIII 780 are 3σ non detections. C III 977 is significantly saturated. Voigt profile fits are superimposed on the respective features as *yellow* curves. The *gray* regions indicate contaminations, i.e., absorption unrelated to this particular absorber. Contaminations are identified as (a) H I 950 associated with the quasar, (b) possible Lyα from $z = 0.2027$ and (c) O VI 1032 at $z = 0.4176$ confirmed by the detection of the corresponding O VI 1038.

Figure 3.2: The absorber at $z = 0.61907$ -continuation

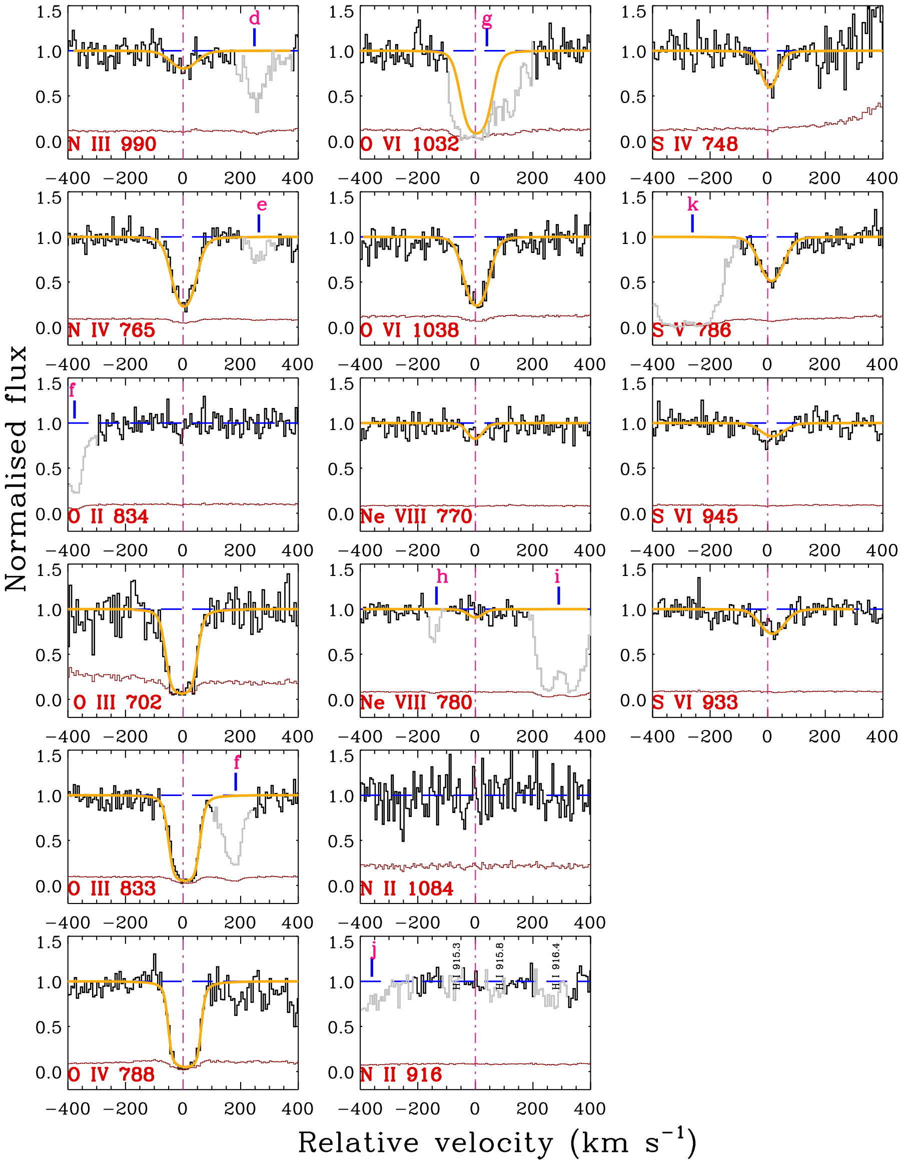

Figure 3.2 Continuation of the system plot for the $z = 0.61907$ absorber shows single component Voigt profile fits to fairly well detected lines. The transitions of O III and O IV are significantly saturated. The O VI 1032 line is heavily blended with Galactic Al II 1671. The expected O VI 1032 profile is superimposed on it's in *yellow*, based on the evidences from O VI 1038. The contaminations in the various panels are (d) H I 1026 at $z = 0.5637$, for which the corresponding H I 972 is detected, (e) possibly H I 1216 at $z = 0.020$ (f) O VI 1032 at $z = 0.3076$ confirmed by the presence of the weaker O VI 1038 line, (g) Galactic Al II 1671, (h) Si II 1206 at $z = 0.0466$ for which other metal lines are also detected (i) H I 1216 at $z = 0.0403$, (j) - and (k) possibly H I 1216 at $z = 0.0465$ respectively.

lines (see Figure 3.3). The lines show similar apparent column density across the full range of the velocity of absorption, implying little partial coverage of the background AGN continuum. More generally, the high ionization lines associated with outflows are expected to be significantly stronger and saturated than the absorption in Ne VIII, O VI, or the unsaturated absorption in S V or S VI seen for this system (Muzahid et al., 2013; Fox et al., 2008). Based on the absence of any observational signatures, we conclude that the absorption is not tracing quasar-driven outflows or gas close to the AGN central engine.

The Voigt-profile fitting software VPFIT (ver 10.0)[3] was used to estimate the column density, Doppler b-parameter and the rest-frame velocity centroids of the lines. The atomic line list and oscillator strength values used for fitting are from Morton (2003) for $\lambda > 912$ Å and from Verner et al. (1996) for $\lambda \leq 912$ Å. The atomic data for Ne VIII $770, 780$ are $\lambda = 770.4089$ Å, 780.3240 Å, and $f_{770} = 0.1030$, $f_{780} = 0.0505$ respectively (Verner et al., 1996). The spectral resolution of COS is known to be wavelength dependent. Therefore, while fitting, we used the empirical line spread functions developed by Kriss et al. (2011) for the respective COS gratings. The synthetic Voigt profiles were convolved with the COS line spread function nearest in wavelength to the redshifted location of the absorption line. Profile fit results are shown in Table 3.1. The line profile models are shown in Figure 3.1, 3.2. The errors listed from the profile fit are a combination of statistical errors and continuum placement errors. The latter quantity was estimated by exploring a few different continuum fits and the resultant range of values obtained for column densities and b-values by fitting the region. Overall, we found the statistical noise in the data to be more significant than the systematic errors.

We have relied on single component profiles to model the absorption seen in H I and the various metal lines. A few of the Lyman series lines (particularly H I 923 and H I 926) suggest a multi-component structure to the core absorption in H I, albeit at low significance. The N IV 765 line also suggests possible kinematic substructure. The apparent column density profiles of these lines are compared in Figure 3.3. A free-fit to the N IV line recovers three components at $v \sim -30, +6, +43$ km s^{-1}. A similar three component structure is not visibly evident in the unsaturated higher order Lyman lines, except H I 923 and H I 926, although there appears to be complexity to the H I velocity structure.

---

[3] http://www.ast.cam.ac.uk/∼rfc/vpfit.html

Table 3.2: Voigt Profile Measurements of the absorber at $z = 0.61907$

Transition	v (km s^{-1})	b (km s^{-1})	log (N) (cm^{-2})	Total log [N(cm^{-2})]
N IV 765	-30 ± 4	14 ± 4	13.47 ± 0.11	
(3 comp)	6 ± 2	15 ± 5	13.85 ± 0.06	
	43 ± 3	11 ± 3	13.37 ± 0.07	14.09 ± 0.06
N IV 765(single)	3 ± 2	41 ± 2	14.05 ± 0.02	
H I 919-1026	-31	30 ± 9	15.50 ± 0.08	
(3 comp)	5	18 ± 9	15.82 ± 0.05	
	44	15 ± 4	15.52 ± 0.06	16.10 ± 0.05
H I 919-1026(single)	-4	41	16.13 ± 0.02	
O VI 1038	4 ± 2	44 ± 3	14.88 ± 0.20	14.88 ± 0.20
O IV 788	6 ± 1	24 ± 4	16.53 ± 0.70[1]	16.53 ± 0.70[1]
O III	4 ± 2	32 ± 3	15.52 ± 0.15[1]	15.52 ± 0.15[1]
C III 977	-10 ± 1	33 ± 3	14.71 ± 0.20[1]	14.71 ± 0.20[1]
C II 903.9	8 ± 6	37 ± 9	13.42 ± 0.10	13.42 ± 0.10
S IV 748	7 ± 3	32 ± 5	13.59 ± 0.05	13.59 ± 0.05
S V 786	13 ± 3	47 ± 4	13.35 ± 0.03	13.35 ± 0.03
Ne VIII 770	11 ± 12	69 ± 20	13.96 ± 0.09	13.96 ± 0.09
C II 903.6 -1036	7 ± 6	36 ± 9	13.42 ± 0.07	13.42 ± 0.07
S VI 934	17 ± 5	52 ± 7	13.49 ± 0.05	13.49 ± 0.05
N III 990	-4 ± 9	51 ± 16	13.83 ± 0.10	13.83 ± 0.10

Table 3.2 Comments: . Voigt profile measurments on the various lines associated with the $z = 0.61907$ towards SDSS J080908.13 + 461925.6. The doublet / multiplet lines were separately and simultaneously fitted. Among the metal lines, C III, O III and O IV are strongly saturated. The formal errors given by the profile fitting routine, listed in the table, are too small and do not account for the uncertainty due to the saturation of the line feature. In the ionization models, we use the AOD column density measurements on these lines as lower limits(3.3).

Table 3.3: AOD column density measurements for $z = 0.61907$ absorber

Transition	$W_r(m)$	log $[N$ (cm^{-2})$]$	[-v,v](km s^{-1})
O VI 1038	248 ± 18	14.79 ± 0.06	[-85, +77]
N IV 765	182 ± 10	13.95 ± 0.05	[-85, +77]
O IV 788	276 ± 11	> 15.0	[-85, +77]
N III 990	58 ± 17	13.78 ± 0.15	[-85, +77]
C III 977	393 ± 12	> 14.1	[-75,50]
O III 833	281 ± 10	> 15.0	[-85, +77]
O III 702	267 ± 16	> 15.0	[-85, +77]
C II 1036	< 63	< 13.8	[-85, 77]
C II 904.9	67 ± 12	13.50 ± 0.08	[-85, 77]
C II 904.6	< 140	< 14.2	[-85, 77]
S IV 748	80 ± 14	13.59 ± 0.09	[-85, +77]
S IV 809	46 ± 13	13.93 ± 0.12	[-85, +77]
S V 786	110 ± 10	13.25 ± 0.06	[-85, +77]
S VI 945	< 66	< 13.63	[-85, +77]
S VI 934	60 ± 10	13.30 ± 0.08	[-85, +77]
Ne VIII 770	28 ± 8	13.76 ± 0.14	[-85, +77]
H I 1026	> 515	> 15.2	[-105,110]
H I 972	> 423	> 15.6	[-105,110]
H I 950	> 365	> 15.9	[-105,110]
H I 938	317 ± 12	16.00 ± 0.05	[-105,110]
H I 931	266 ± 13	16.08 ± 0.06	[-105,110]
H I 926	213 ± 13	16.08 ± 0.05	[-105,110]
H I 923	126 ± 13	16.14 ± 0.06	[-100,100]
H I 921	134 ± 14	16.13 ± 0.06	[-100,100]
H I 919	73 ± 11	15.97 ± 0.09	[-60,75]
H I 918	100 ± 13	16.25 ± 0.09	[-60,75]
H I 917	50 ± 12	16.03 ± 0.11	[-60,75]
H I 916.4	55 ± 12	16.15 ± 0.11	[-60,75]

Table 3.3 Comments: . Apparent optical depth (AOD) measurments of all the detected lines in the absorber $z = 0.61907$ are tabulated. In the ionization models, we use the AOD column density measurements as lower limits for the saturated lines C III, O III and O IV. For non-detections, AOD measurement is taken as upper limit.

Figure 3.3: AOD column density profiles comparison

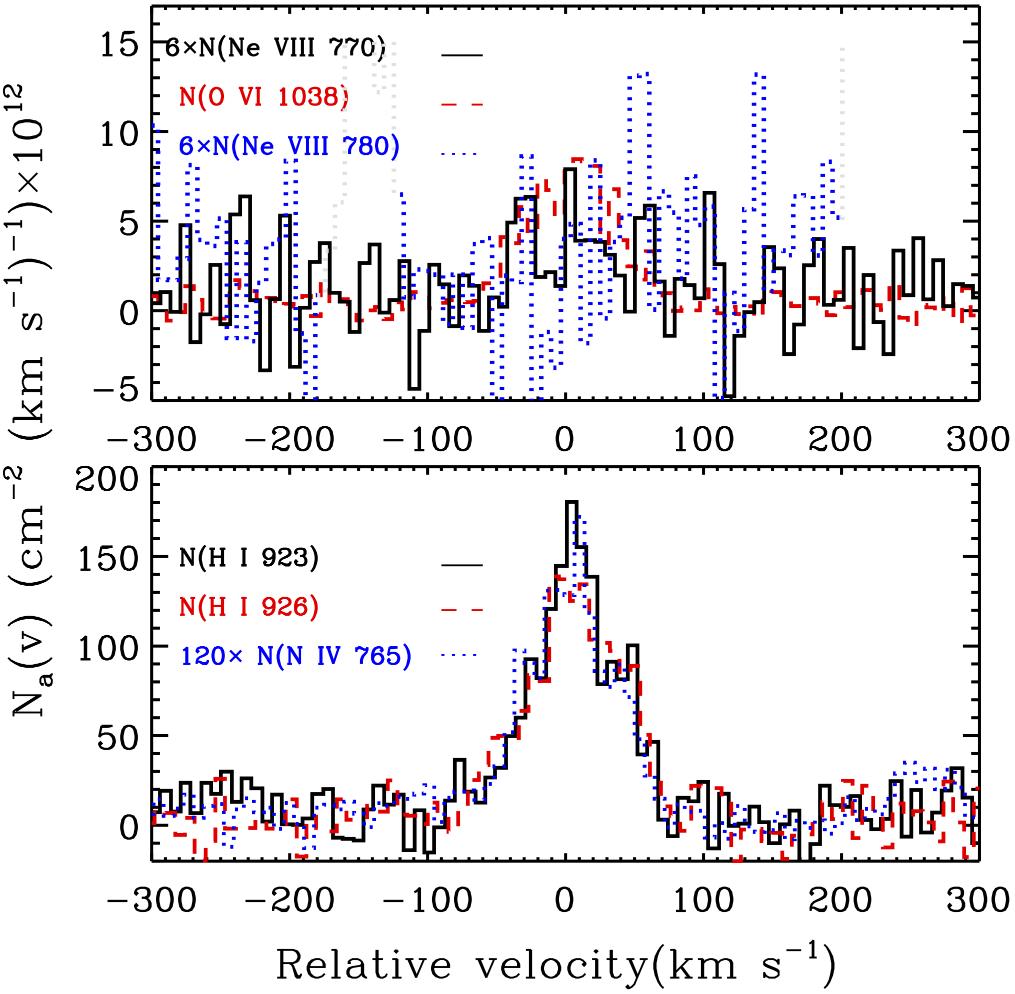

Figure 3.3 Top panel is a comparison of the apparent column density profiles of Ne VIII 770, 780 and O VI 1038 lines in the $z = 0.61907$ absorber. The apparent column density profile of Ne VIII 780 is truncated between [-180 -120] km s^{-1} and $v > 200$ km s^{-1} where they suffer from contamination. The coincidence in velocity between Ne VIII 770 and O VI lends support to the detection of Ne VIII 770. In the bottom panel the apparent column densities of two of the unsaturated Lyman series lines and N IV 765 are shown.

Taking a cue from the component structure seen in N IV, we attempted a simultaneous three component fit to the Lyman series lines to determine the H I corresponding to the components of N IV. The fit results are given in Table 3.1. The column density profiles of the various Lyman series lines slightly differ from each other due to statistical fluctuations in the noise spectrum. Because of this, the multi-component profile models do not fit all the Lyman series lines equally well. The errors on column densities and b-parameters derived from the simultaneous fit reflect this. In Sec 3.4.2, we discuss how the ambiguity in the component structure for H I affects the elemental abundance estimate for a warm plasma traced by the Ne VIII in this absorber.

No unique sub-component structure is evident in the unsaturated S IV 748, S V 786, S VI 933, 945 lines, and hence these lines are fitted with a single component. The comparatively strong O III, C III and O IV lines are saturated. We fit these lines also with single components. The true errors in the profile fit results for such saturated lines are likely to be larger than what the fitting routine suggests.

Using the apparent optical depth (AOD) method of Savage and Sembach (1991), we estimated the total column density of the various ions by integrating over the full velocity range over which each line feature is seen. Using this method we also derived upper limits on column densities for lines which are nondetections and lower limits for the lines which are heavily saturated. These values are also tabulated in 3.3.

The COS spectrum provides information on O II, O III, O IV and O VI. The O II is a nondetection, whereas the O III and O IV lines are strong and quite probably saturated. The similarities in the profile structure of O III and O IV suggest a possible origin in the same gas phase. Single component Voigt profile models explain fairly well the absorption in O IV and also the doublet lines of O III, with χ^2 goodness of fit values close to one. However, the profile fit results for these intermediate ionization lines are not unique. We find line saturation effects dominating the uncertainty in the profile fits. As a result, models with different combinations of N and b can explain the observed absorption in O III and O IV without compromising on the quality of the fit. We therefore adopt the integrated apparent column density lower limits of log N_a(O III) > 15.0 and log N_a(O IV) > 15.0 for subsequent analysis. In the case of C III also we use the log N_a(C III) > 14.1, for similar reasons. The C II 903.6 line suffers from blending with O VI 1032 from an absorber at $z = 0.4176$. We use the C II 903.9 line to constrain the C II column density.

The O VI 1032 line is heavily blended with Al II 1671 absorption from local

ISM. The O VI 1038 is, however, a clean feature, which we use for constraining the column density and b-parameter. A single component fit to the O VI 1038 yields $\log N(\text{O VI}) = 14.88 \pm 0.20$ and $b(\text{O VI}) = 44 \pm 3$ which is comparable to the integrated apparent optical depth column density of $\log N(\text{O VI}) = 14.79 \pm 0.06$ to within their 1σ uncertainty range. This implies that the O VI 1038 is adequately resolved by COS. From the N and b-values measured from O VI 1038, we synthesized the O VI 1032 line profile. The synthetic profile, when superimposed on the data reveals the extent of contamination from Galactic Al II (see the model profile in the O VI 1032 panel of Figure 3.1), which is significant and difficult to correct for.

3.3.1 The Ne VIII $770, 780$ Detection

The Ne VIII $770, 780$ is a very weak feature in the $z = 0.61907$ absorber. The ion is detected with $\gtrsim 3\sigma$ significance only in the stronger member of the doublet. The transitions fall at the blue end of the G130M grating exposures. The three G130M integrations add to 3.1 ks of exposure time at the redshifted wavelength location of Ne VIII $770, 780$ lines. The exposures were obtained with two different G130M central wavelength settings (one exposure centred at 1291 Å and two exposures at 1309 Å) which result in the dispersed light getting shifted in the detector space. This helps to reduce the detector fixed pattern noise features during coaddition.

The Ne VIII 770 line has a rest-frame equivalent width of $W_r = 28 \pm 8$ mÅ when integrated over [-85, 77] km s^{-1}. This is the same velocity range over which absorption from C III, O III, O IV, and O VI 1038 are detected. The Ne VIII 770 feature is thus detected with a significance of 3.5σ. The uncertainty quoted for the equivalent width is inclusive of statistical and continuum placement errors. A more stringent estimate on the detection significance can be arrived at by including a systematic uncertainty of $\sim$ 10 mÅ from residual fixed pattern noise features that could be present in COS data (Savage et al., 2014). This would bring the Ne VIII 770 significance down to 2.2σ. The non-detection of Ne VIII 780 at $\geq 3\sigma$ is consistent with the expected $2:1$ equivalent width ratio between the two lines of the doublet.

The non-detection of Ne VIII 780 prompted us to investigate the validity of

Figure 3.4: Ne VIII profile comparison with model

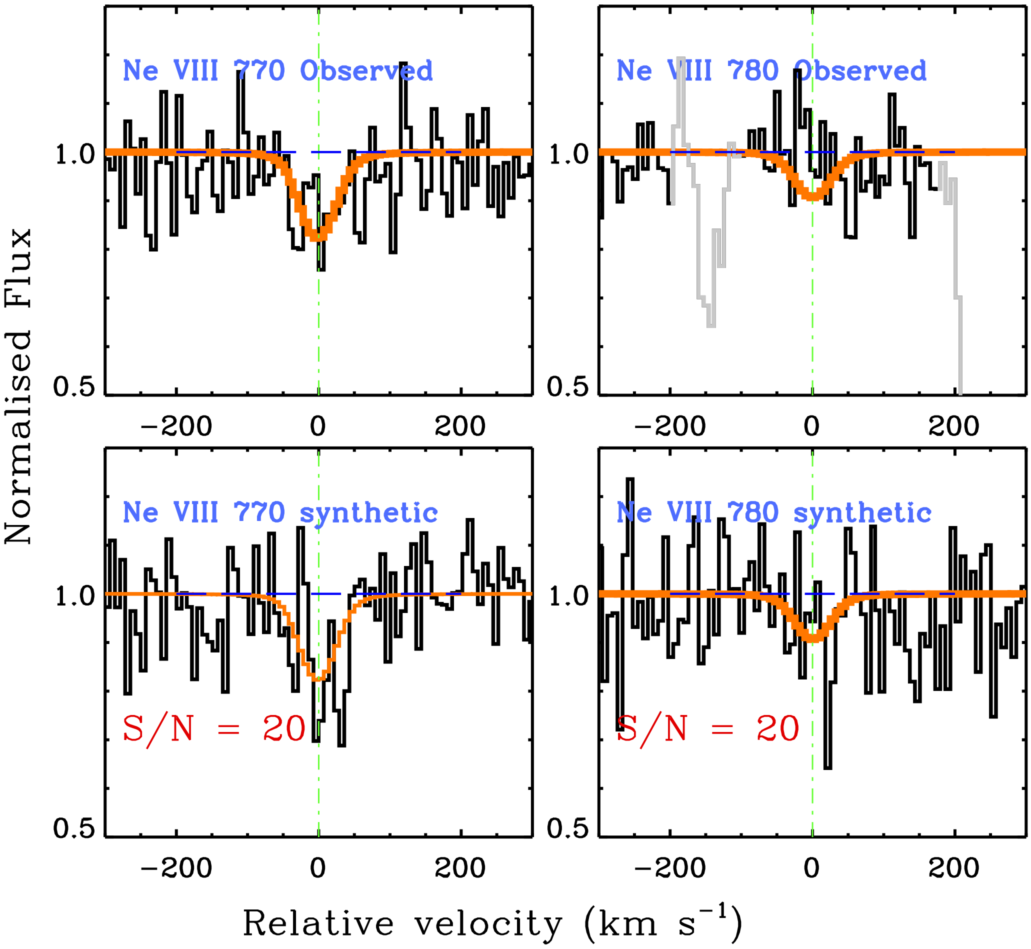

Figure 3.4 The top panel of the first column shows the observed Ne VIII 770 in the $z = 0.61907$ absorber, with the Voigt profile model superimposed. The bottom panel is a synthetic Ne VIII 770 feature with identical N and b as the observed line at $S/N = 20$. The top and bottom panels of the second column show the corresponding observed and synthetic Ne VIII 780 spectra respectively. The synthetic spectra suggests that the weak Ne VIII can be a non-detection in the 780 Å line at the S/N of the data, in agreement with observations.

the Ne VIII detection in greater detail. We synthesized Ne VIII 770, 780 lines by convolving a model absorption feature (of N, and b-value obtained from fitting the Ne VIII 770) with a Gaussian kernel of FWHM = 17 km s^{-1} (resolution of COS). Poisson noise was added to this synthetic profile to simulate $S/N = 20$ per wavelength bin (1/2 a resolution element). This approximately matches the S/N of the data in the region where the Ne VIII occurs. The result of this exercise, shown in Figure 3.4, is consistent with the low significance of Ne VIII 770 and the non-detection of the Ne VIII 780 lines.

In the independent line identifications for this sightline done by Danforth et al. (2016) and one of the co-authors (Bart Wakker), the Ne VIII 770 absorption at $\lambda = 1247.35$ Å is not identified with any line associated with other absorbers along this sightline. Nonetheless, we cannot fully eliminate the possibility of the Ne VIII 770 absorption being a weak low redshift Lyα interloper.

We measured the strength of the Ne VIII 770 in the separate G130M integrations as well. The absorption feature is detected with an equivalent width of $W_r = 28 \pm 11$ mÅ in the exposure with grating central wavelength of $\lambda_c = 1291$ Å, and $W_r = 51 \pm 20$ mÅ and $W_r = 36 \pm 20$ mÅ in the two exposures with central wavelengths of $\lambda_c = 1309$ Å. The feature thus has a mean detection significance of 2.3σ in the individual science exposures.

We made a closer investigation to find out whether fixed pattern noise or similar instrumental artefacts are affecting our measurement in any way. Since two out of the three integrations of the G130M grating were carried out with the same central wavelength and FP-SPLIT position set-up of the grating, we cannot compare the individual exposures to know whether a fixed pattern feature is occurring at the Ne VIII 770 Å redshifted wavelength of 1247.35 Å. Instead, we looked at this detector space in five other quasar observations done approximately in the same period with identical grating settings and found no evidence for any instrumental contamination.

In Figure 3.2, we compare the apparent column density profiles of Ne VIII and O VI. Though the Ne VIII line is much weaker than O VI, in the approximate velocity range of $[-100, 100]$ km s^{-1} the absorption seen in O VI is well matched by the absorption in Ne VIII. The similarity in the kinematics lends further support to the identification of the Ne VIII 770 line.

The detection significance of Ne VIII 770 line is lower than the significance of most of the COS Ne VIII detections reported thus far (Narayanan et al., 2009, 2011a; Tripp et al., 2011; Narayanan et al., 2012; Meiring et al., 2013; Hussain et al., 2015) but is similar to the first Ne VIII detection in the IGM reported by Savage et al.

(2005), where the 770 line was detected with a significance of 3.1σ. However, in the Ne VIII detection reported by Savage et al. (2005), the weaker 780 line was also a formal detection with 2.3σ significance, resulting in a higher detection significance of 3.9σ jointly for the lines of the doublet.

3.4 Ionization & Abundances in the $z = 0.61907$ Absorber

To assess the density and temperature phases traced by this absorber, and the relative chemical abundances within them, we turn to time independent photoionization-recombination equilibrium models and collisional ionization models. We first describe the results from photoionization modelling. The models were computed using the standard photoionization package Cloudy (ver 13.03) last described by Ferland et al. (2013a). Cloudy models the absorbing gas as constant density plane parallel slabs irradiated by ionizing photons. The intensity and shape of the ionizing spectrum are assumed to be the extragalactic background radiation coming from AGNs and star-forming galaxies in the universe. The ionizing radiation field (hereafter EBR) we adopt is the upgraded model of KS15, which incorporates the most recent measurements of quasar luminosity function (Croom et al. (2009), Palanque-Delabrouille et al. (2013)) and star formation rate densities (Khaire and Srianand, 2015b). A source of uncertainty in the models for extragalactic background radiation is the escape fraction of Lyman continuum photons from star-forming galaxies. KS15 find that an escape fraction of 4% is required to match the observed IGM H I photoionization rate as measured by Kollmeier et al. (2014); Wakker et al. (2015) and 0% to match the measurements by Shull et al. (2015), Gaikwad et al. (2016a), Gaikwad et al. (2016b). Bearing in mind this uncertainty, we computed photoionization models for both $f_{esc} = 4\%$ and $f_{esc} = 0\%$, and discuss the results for both cases. For brevity, we only display the modeling predictions for the $f_{esc} = 4\%$ case. In the models, we assume the solar relative elemental abundances given by Asplund et al. (2009) and finetuned the abundance to illustrate the most likelier single-phase solution of the absorber.

Figure 3.5: PIE model of the absorber at $z = 0.61907$

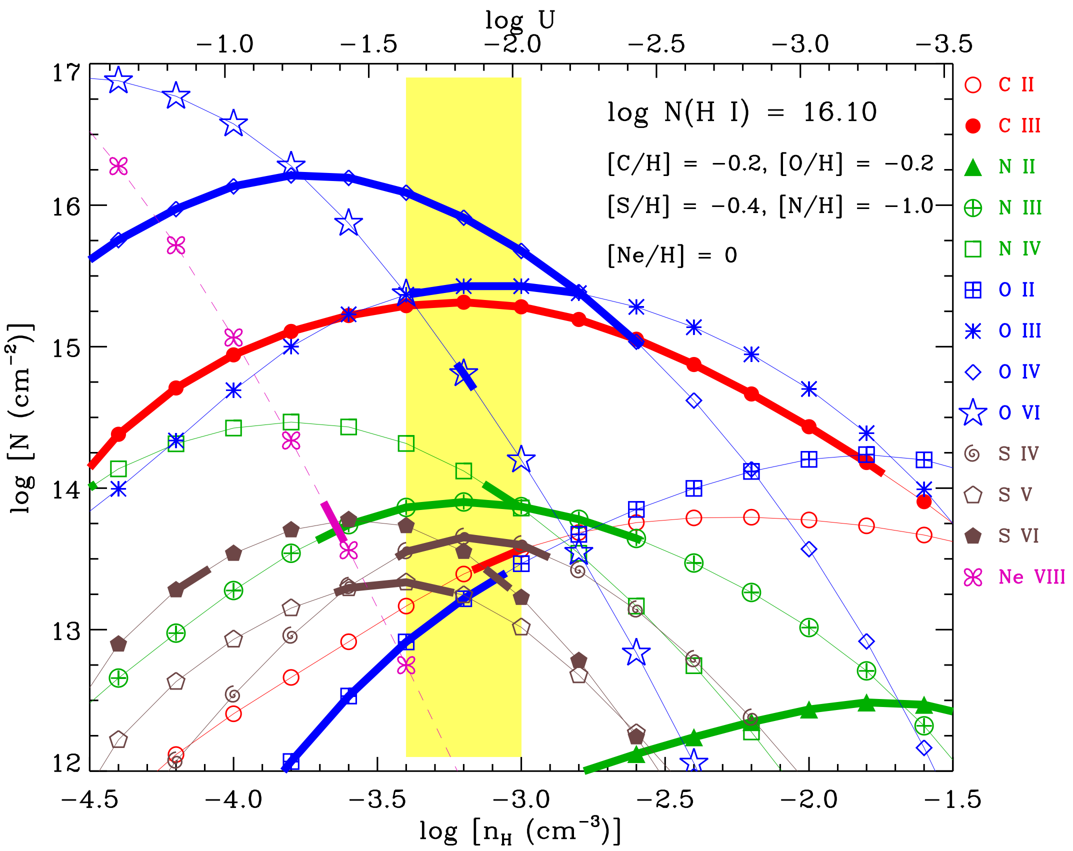

Figure 3.5 Photoionization equilibrium models for the absorber at $z = 0.61907$. The ionizing source is the KS15 extragalactic background radiation with $f_{esc} = 4\%$ escape fraction of hydrogen ionising photons. The thin curves show the model predicted column densities for the various ions at different densities. The thick portion in each curve is the region where the model is consistent with the observed column density to within 1σ. The predicted column density ratios of N III/N II, N IV/N III, C III/C II, S IV/S V and S V/S VI are simultaneously consistent with observations for the narrow density range of $n_H \sim (0.3 - 1 \times 10^3)$ cm^{-3}. This region (marked in *yellow*) is the single phase solution for all the ions except Ne VIII.

3.4.1 Photoionization Equilibrium Models

Figure 3.5 shows the column density predictions from photoionization for the various ions at different gas densities. The models were generated for a H I column density of 16.1 dex, the value obtained from simultaneously fitting the Lyman series lines with a single component. The coverage of successive ionization stages of carbon, nitrogen, oxygen, and sulfur offer useful constraints for the ionization calculations. The density is best constrained by the measured column density ratios of log[N(N IV)/N(N III)] = 0.27 ± 0.16, log[N(S V)/N(S IV) = −0.24 ± 0.06, log[N(S VI)/N(S V) = 0.01 ± 0.05, and the lower limits log[N(C III)/N(C II) $\gtrsim$ 0.7, log[N(N III)/N(N II) $\gtrsim$ 0.2 and log[N(O III)/N(O II) $\gtrsim$ 1.9. These ionic column density ratios are simultaneously valid for a gas density of $n_{\rm H} = (0.4 - 1) \times 10^{-3}$ cm^{-3}. At the mean value of $n_{\rm H} = 0.7 \times 10^{-3}$ cm^{-3}, the model predicts a total hydrogen column density of N(H) = 19.5, a gas temperature and pressure of $T = 1.5 \times 10^4$ K and $p/K = 10.5$ cm^{-3} K, and line of sight thickness of L = 14.6 kpc. The photoionization predicted temperature implies that the broadening of H I and the intermediate and low ion lines are due to non-thermal motion.

The single phase photoionization model with f_{esc} = 4% suggests a near-solar abundance for C, and O. [C/H] is given by the unsaturated C II column density. [C/H] is $\gtrsim -0.4$ for the model prediction to be consistent with the observed N(C II). Similarly, from the column density measurements of N III, and S IV and the lower limit on O III, we obtain abundances of [N/H] $\gtrsim -1.0$, [O/H] $\gtrsim -0.2$ and [S/H] $\gtrsim -0.4$. For these ions to be coming from the same gas phase, the abundances have to be [C/H] = [O/H] = −0.2, [N/H] = −1.0, and [S/H] = −0.4. The single phase solution with these abundances is shown in Figure 3.5.

The predictions from the models with an EBR of f_{esc} = 0% are not widely different. They yield similar density for the low ionization gas phase, with a 0.2 dex increase in the relative elemental abundances. Also at energies > 4 Ryd, changing the spectral shape of the EBR within the measurement uncertainty of the AGN composite continuum given by stevans et al. (2014), would result in a ∼ 0.2 dex change in the hydrogen density. The abundance estimations thus carry an approximate uncertainty of ± 0.3 dex because of the ambiguity in the escape fraction of ionizing photons, the spectral shape of the EBR, and from the uncertainty in the H I column density.

This single phase with $n_{\rm H} \sim 0.7 \times 10^{-3}$ cm^{-3} is also consistent with the observed N(O VI). For [O/H] = −0.2 dex, the photoionized gas phase simultaneously explains the observed O VI along with its lower ionization stages. However, the predicted Ne VIII at this ionization parameter is ∼ 2 dex smaller than the observed value for both versions of EBR with different f_{esc}. Producing the required amount of Ne VIII from the same gas phase would require increasing [Ne/H] by a factor of 100 from its solar value. The presence of Ne VIII thus points to a separate higher ionization phase in the absorber. This separate gas phase is unlikely to be dominantly photoionized for the following reasons.

For solar [Ne/H], the observed N(Ne VIII) is produced at ionization parameters of $\log U \geq -1.4$, corresponding to a densities of $n_{\rm H} \leq 2 \times 10^{-4}$ cm^{-3} and for log N(H I) ≤ 16.1. There are two discrepancies that emerge from such a separate higher photoionized phase. Firstly, at $\log U \sim -3.7$, this higher ionization phase also produces significant amount of C III, N III, O III, N IV, O IV, and O VI even for low values of H I. The combined column densities for these ions from the two gas phases will contradict the observed values by several factors. Secondly, the H I column density associated with this high ionization gas is likely to be much smaller than the observed log N(H I) < 16.1. To produce Ne VIII at lower values of N(H I) would require the line of sight to pass through very low-density columns of plasma that extend over several Mpc. For example, if the H I associated with the Ne VIII gas phase has $\log N$(H I) $\lesssim 14$ dex, then the observed N(Ne VIII) will be recovered for solar [Ne/H] only for $\log U \gtrsim -0.5$ corresponding to $\log n_{\rm H} \lesssim -4.5$. The absorbing region, in this case, has to be spread over a large path length of $\gtrsim 0.5$ Mpc, which is nearly equal to the full virial cross-section of L^* galaxies ($R_{vir} \sim 200 - 300$ kpc). It is unlikely for gas spread over such a large length to maintain velocity dispersions of a few tens of km s^{-1}. The other possibility is that the absorber mass has not yet decoupled from the universal expansion. In such a case, the absorption lines will suffer a velocity broadening due to Hubble expansion, which will be $v(z) = H(z)\ L \sim 50$ km s^{-1}, where $L \geq 0.5$ Mpc. The observed b-value for the well measured H I lines are 40% narrower than the expected broadening due to Hubble flow.

We emphasize here that the photoionization models are not exact because of the simplistic assumptions built into them (the absorbing cloud in the models have a plane parallel geometry with uniform density and temperature) and also due to the lack of information on the exact column densities and any sub-component structure in the saturated metal lines and H I. However, the model prediction that the Ne VIII is not consistent with photoionization is important. In the next section, we discuss the results from collisional ionization models for the Ne viii bearing gas.

3.4.2 Evidence for a Warm Gas Phase

Collisional Ionization Equilibrium Models

In collisional ionization equilibrium (CIE) models, the ionization fractions of elements depend only on the equilibrium temperature. In Figure 3.7 we plot the Ne viii to O vi column density ratio predictions made by the CIE model of Gnat and Sternberg (2007) for a range of plasma temperatures. The CIE is a good approximation for calculating the ionization of H i, Ne viii and O vi at $T > 2 \times 10^5$ K since the gas cools relatively slowly at such higher temperatures. For lower temperatures, non-equilibrium ionization effects (recombination lagging behind the cooling of the gas) become important (Savage et al., 2014).

The column density ratio of Ne viii to O vi cannot be used directly to ascertain the temperature of the gas, as much of the O vi is possibly tracing the cooler photoionized medium. Nonetheless, the presence of O vi can be used to place a lower limit on the temperature of the collisionally ionized gas. As shown in the bottom panel of Figure 3.7, the ratio of log $[N(\text{Ne viii})/N(\text{O vi})] \gtrsim -1.25$ is valid for $T \gtrsim 4.3 \times 10^5$ K. If this warm gas phase has more Ne viii compared to O vi, then a lower limit of $T \gtrsim 5.0 \times 10^5$ K is obtained from the CIE models.

To determine the metallicity and the total hydrogen column density in this warm phase, we need an estimate on the associated H i. Even at the conservative lower limit of $T = 4.3 \times 10^5$ K, the neutral fraction of hydrogen at CIE is $f(\text{H i}) = 7.9 \times 10^{-7}$, suggesting that most of the mass in the Ne viii gas phase is in an ionized form. Consequently, nearly all of the strong absorption in H i is potentially tracing the cooler photoionized medium. Given the low H i optical depth and the warm temperature of the gas, we expect the absorption from the residual H i to be thermally broad and shallow. The absence of coverage of Lyα makes it implausible to know whether a BLA is associated with the Ne viii gas. At the low S/N of the data, it is difficult to search for the presence of a broad H i feature in the weaker Lyβ line. We, therefore, use the Lyβ to place a useful upper limit on the H i column density associated with this warm gas.

In Figure 3.6 are superimposed synthetic BLA profiles on top of the Lyβ absorption. The BLA profiles were synthesized for the CIE temperature lower limit of $T = 4.3 \times 10^5$ K with different H I column densities. The temperature corresponds to a pure thermal line width of b(H I) $= 85$ km s^{-1}. We explored both single component and three component (refer Table 3.1) models for the narrow and strong absorption that forms the core of the H I profile. The three component model is based on the weakly resolved kinematic sub-structure seen in the H I 923 and 926 lines, and also N IV 765. Statistically, the three components result in a better fit ($\chi^2_\nu = 1.2$) to the core absorption in Lyβ compared to a single component ($\chi^2_\nu = 1.7$), although in the latter case the fitting model is within 1σ of the flux values. Irrespective of whether the core absorption is modeled by a single component or multiple components, the thermally broad H I associated with the Ne VIII gas phase has to have log N(H I) $\lesssim 14.2$ to go undetected in the Lyβ profile. If the temperature in the Ne VIII gas phase is higher, this H I limiting column density will also be higher. The H I column density upper limit of log N(H I) $= 14.2$ constrains the [Ne/H] $\lesssim -0.5$ in the warm gas.

Adopting log $[N$(H I)$] \lesssim 14.0$, CIE models predict a total hydrogen column density of log $[N(\mathrm{H})] \gtrsim 20.1$ for $T \gtrsim 4.3 \times 10^5$ K. This lower bound on baryonic column density is an order of magnitude more than the amount of total hydrogen present in the photoionized gas phase.

Extending the collisional ionization scenario further, we also computed models that simultaneously consider ion-electron collisions and ion-photon interactions as sources of ionization. Insights from these *hybrid* models are discussed next.

Figure 3.6: Evidence for BLA from H i 1026

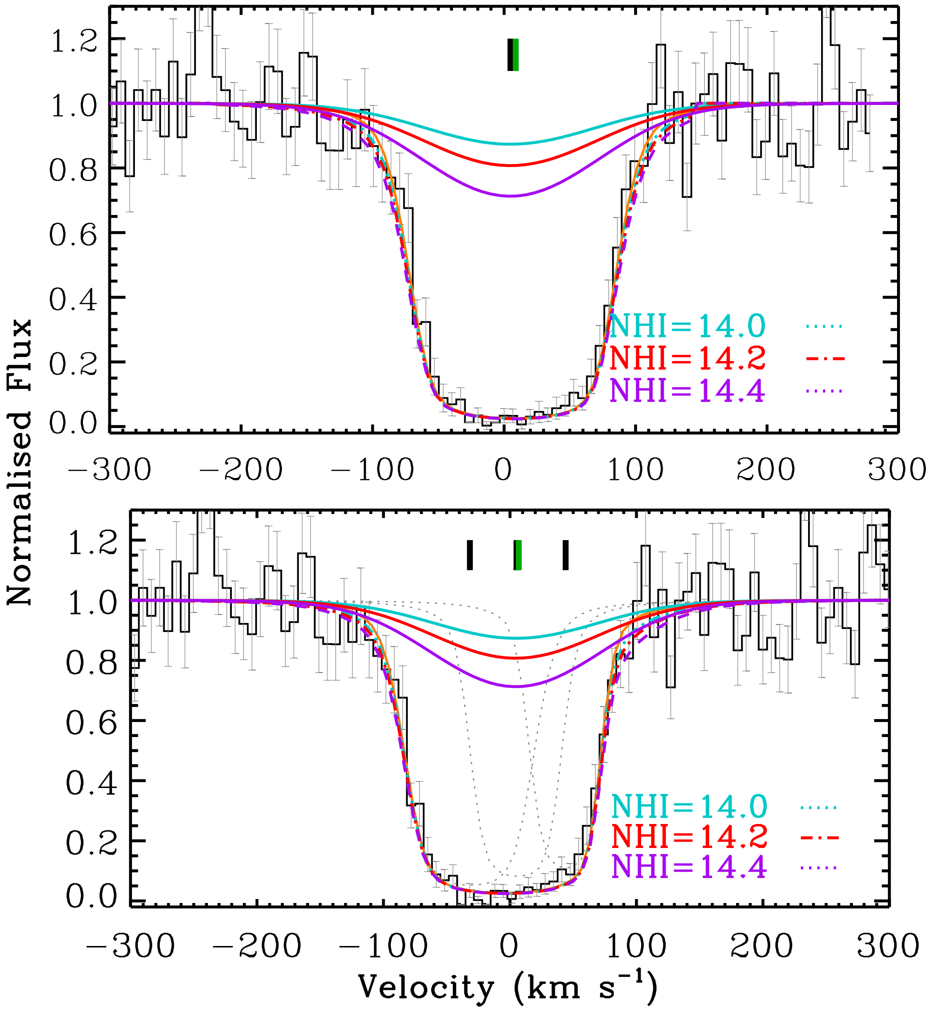

Figure 3.6 The figure shows the H i 1026 feature of the $z = 0.61907$ absorber towards SDSS J080908.13 + 461925.6. Superimposed on the data are different Voigt profile fits. The top and bottom panels assume a single component ($\chi^2_\nu = 1.7$) and a three component ($\chi^2_\nu = 1.2$) fit to the core absorption. The fit parameters are given in Table 1. To this are added broad H i profiles with a fixed $b = 85$ km s^{-1} and log N(H i) $= 14.0, 14.2, 14.4$ dex centered at the velocity where Ne viii absorption is seen (show as solid curves of different color). The composite of the broad and narrow H i absorptions are overlaid on the data as *dashed* lines. The $b = 85$ km s^{-1} is how broad the H i absorption from the Ne viii gas phase would be, based on a temperature lower limit estimate for this phase. Addition of such a thermally broad and shallow H i component affects only the wings of the profile and not the core absorption. From this, we estimate an upper bound to the H i column density in the Ne viii phase as log N(H i) $\lesssim 14.2$ dex.

Figure 3.7: CIE & hybrid models

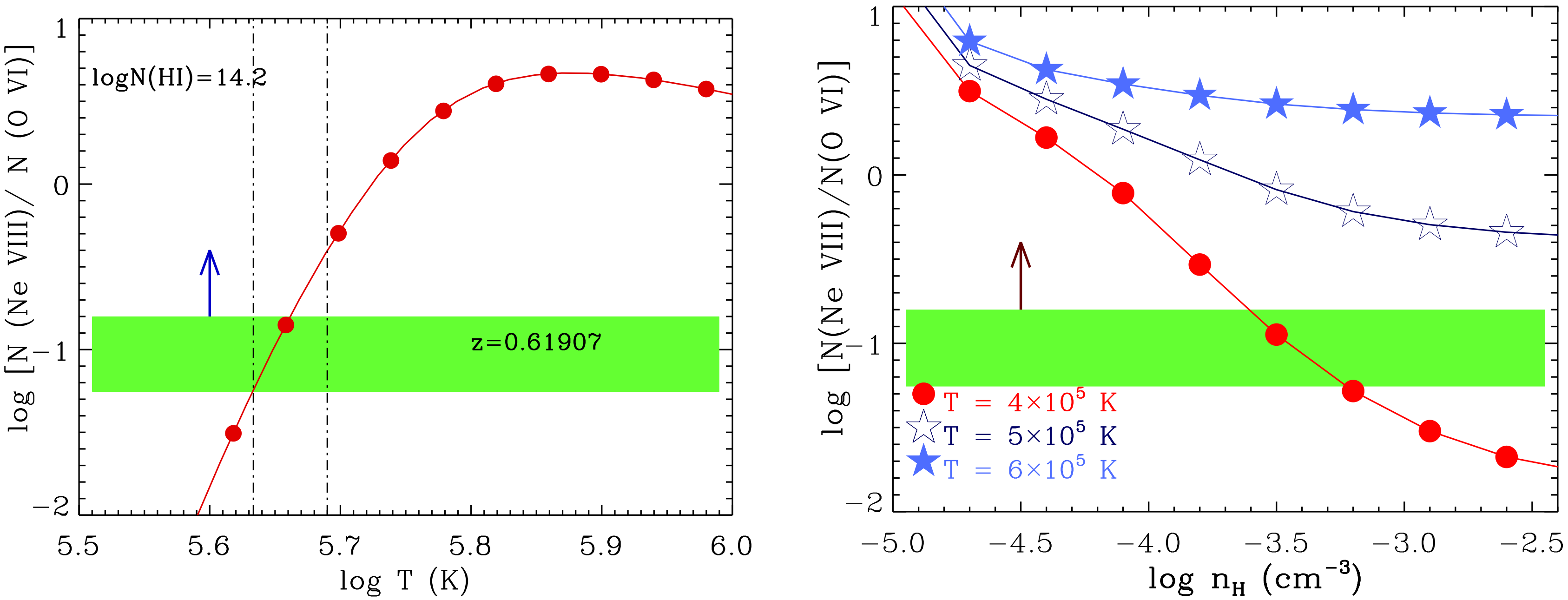

Figure 3.7 Figure on the *top* panel shows the column density ratio of Ne VIII–O VI predicted by CIE models of Gnat and Sternberg (2007) for different equilibrium temperatures and solar elemental abundance. The green shaded region is where the model predicted ratio matches with the observation for the absorber at $z = 0.61907$ towards SDSS J080908.13 + 461925.6. The upward arrow is to indicate that the observed Ne VIII - O VI column density ratio can be only considered as a lower limit on the true column density ratio between these two ions in the collisionaly ionized gas phase, since O VI can have a significant contribution from the $T \sim 10^4$ K photoionized phase of this same absorber. The *bottom* panel is the same ionic column density ratio predicted by photoionization - collisional ionization hybrid models for three different equilibrium temperatures of $T = 4 \times 10^5$ K, $T = 5 \times 10^5$K and $T = 6 \times 10^5$K respectively. The CIE models predict the Ne VIII to be from a warm gas phase with $T > 4.3 \times 10^5$ K. There is no clear constrain on the density from the hybrid models, since the Ne VIII–O VI column density ratio is only a lower limit.

Hybrid of Photoionization & Collisional Ionization

Using Cloudy we computed *hybrid* models for different warm gas temperatures, with the photoionizations caused by the extragalactic ionizing background radiation as given by KS15. The Ne VIII to O VI column density ratio predicts a temperature lower limit of $T \sim 4 \times 10^5$ K from CIE. At this temperature, the hybrid models require gas densities of $n_{\rm H} < 10^{-3}$ cm^{-3} to be consistent with the lower bound of the Ne VIII to O VI column density ratio. The number density corresponds to a baryonic overdensity of $\Delta = \rho/\bar{\rho} \gtrsim 1000$ (using $n_{\rm H}({\rm cm}^{-3}) = 1.9 \times 10^{-7}\ (1+z)^3\ \Delta$). Simulations associate such $T - \Delta$ combinations typically with hot halos (Figure 5 of Gaikwad et al. (2016a)). For the approximate H I upper limit of $N(\text{H I}) = 10^{14.2}$ cm^{-2} derived earlier, this gas phase model predicts, $N(\text{H}) \sim 4.3 \times 10^{20}$ cm^{-2} and an absorption path length of $L \sim 88$ kpc. Such a prediction is also consistent with the lower limit on Ne VIII to S VI. At that temperature and H I column density, the [Ne/H] $= -0.5$ dex to match the observed $N(\text{Ne VIII})$ at any density. Higher temperatures for the Ne VIII gas phase would predict higher density upper limits (as shown in Figure 3.7). We emphasize here that given the lack of observational constrain on the amount of O VI and H I associated with the Ne VIII, the hybrid models are only as useful as the CIE models in setting limits on the physical conditions of the warm gas. Furthermore, if the true temperature of the gas is $T \lesssim 2 \times 10^5$ K, the hybrid models should assume non-CIE calculations along with photoionization for a truly valid explanation of the physical conditions.

3.5 Galaxies Near the Absorber

In this section, we discuss the galaxies that lie in the neighbourhood of $z = 0.61907$ absorber. The SDSS DR12 spectroscopic database is 90% complete down to an r-band magnitude of $r < 17.8$ (Strauss et al., 2002). This translates into a luminosity of $\gtrsim 6\ L*$ at $z \sim 0.6$ (Ilbert et al., 2005), implying that the SDSS is sampling only the very brightest galaxies at the redshifts of these absorbers.

Within a projected separation of 30×30 arcmin from the line of sight towards SDSS $J080908.13 + 461925.6$, there are 7 galaxies with spectroscopic redshifts that place them within $|\Delta v| = 1000$ km s^{-1} rest-frame velocity of the $z = 0.61907$ absorber. Information on the galaxies are listed in Table 3.4, and their relative locations are shown in Figure 3.9. The impact parameters of these galaxies range from $0.7 - 11.4$ Mpc. The galaxy nearest to the absorber, though close-by in velocity ($|\Delta v| = 152.9$ km s^{-1}), is at a projected separation of 1.91 Mpc. The halo radius of this galaxy can be estimated from its scaling relationship with luminosity given by Stocke et al. (2014).

$$\log R_{vir} = 2.257 + 0.318\mathrm{C} + 0.018\mathrm{C}^2 - 0.005\mathrm{C}^3 \tag{3.1}$$

where $\mathrm{C} = \log(L/L^*)$. The estimated luminosity of $0.1L^*$ suggests a halo radius as $R_{vir} = 91$ kpc, which is 20 times smaller than the projected separation in the plane of the sky between the absorber and the galaxy. Given this large separation, the Ne VIII - O VI absorber is unlikely to be coming from gas embedded within the hot halo of the galaxy. We cannot rule out the possibility of the absorber being associated with a $\leq L^*$ galaxy (or even brighter) closer to the sightline, but undetected by SDSS. Indeed, galaxies close-by in velocity and physical separation to Ne VIII absorbers are known to span a wide range in luminosities from sub-L^* to $> L^*$ (Chen and Mulchaey, 2009; Mulchaey and Chen, 2009; Tripp et al., 2011; Meiring et al., 2013).

The 7 galaxies that are coincident in redshift with the absorber have a narrow velocity dispersion of $\sigma \sim 85$ km s^{-1} and an average systemic velocity that is $\sim 485 \pm 16$ km s^{-1} with reference to the absorber redshift. The abundance of $\gtrsim L^*$ galaxies within such a narrow range of projected physical separation and velocity offset indicates that the line of sight is possibly passing through a group medium. Given the limited number count of galaxies at the redshift of the absorber and the incompleteness of the sample for even $L*$ luminosities, it is not realistic to formally define a galaxy group through a friends of friends approach, or similar standard algorithms.

Figure 3.8: Galaxy distributions at $z \sim 0.6$

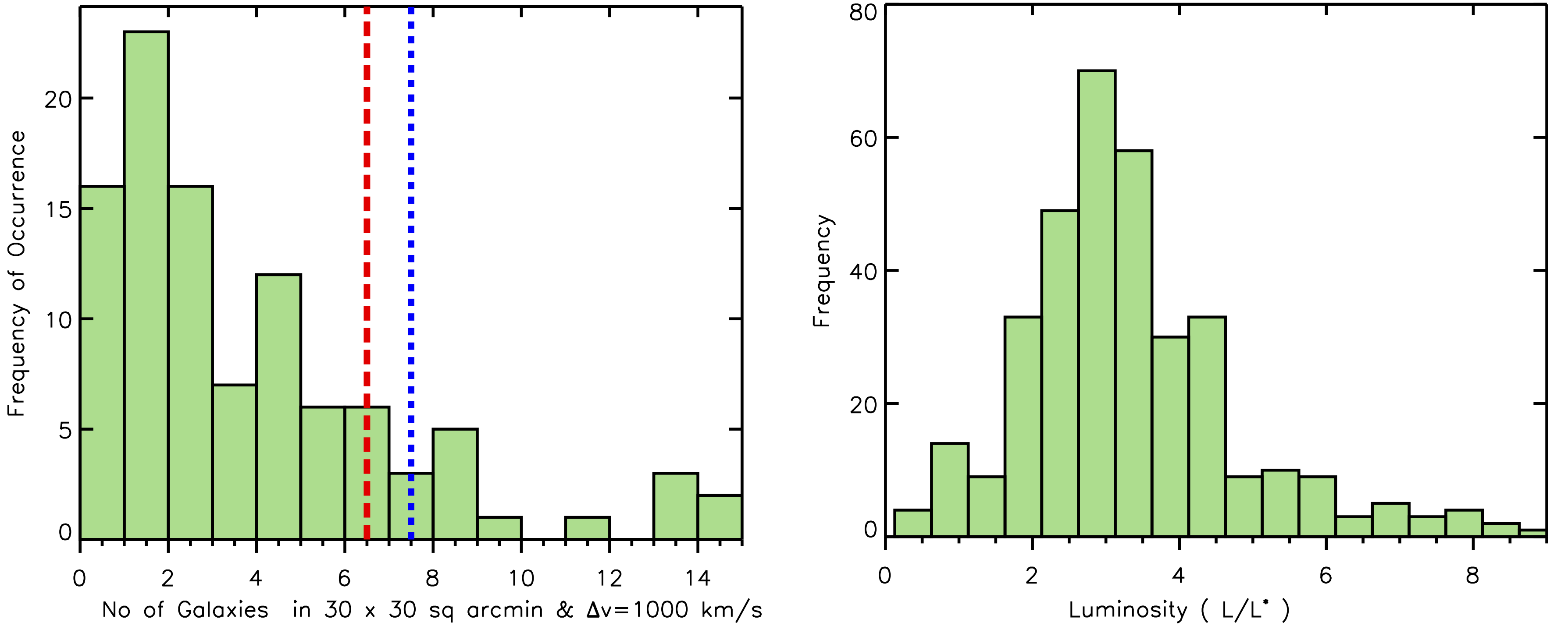

Figure 3.8 The *Left panel* shows the distribution of galaxies within 30 × 30 arcmin and $|\Delta v| = 1000$ km s^{-1} of $z = 0.6$ in 100 locations randomly sampled from the SDSS footprint. The distribution indicates that only a small (15%) probability of finding more than 6 galaxies in the sampled volume. Thus, 7 galaxies detected in the simialr seperation around $z = 0.61707$ absorber is less likely be a random coincidence. In the *Right panel* is the luminosity distribution of the galaxies from the random sampling, indicating that the completeness of SDSS is poor for $L \leq L^*$ at $z = 0.6$, which is inturn consistent with the large luminosities that we find for the galaxies in the extended environment around both Ne VIII absorbers.

Figure 3.9: Galaxy Distribution Near the $z = 0.61907$ Absorber

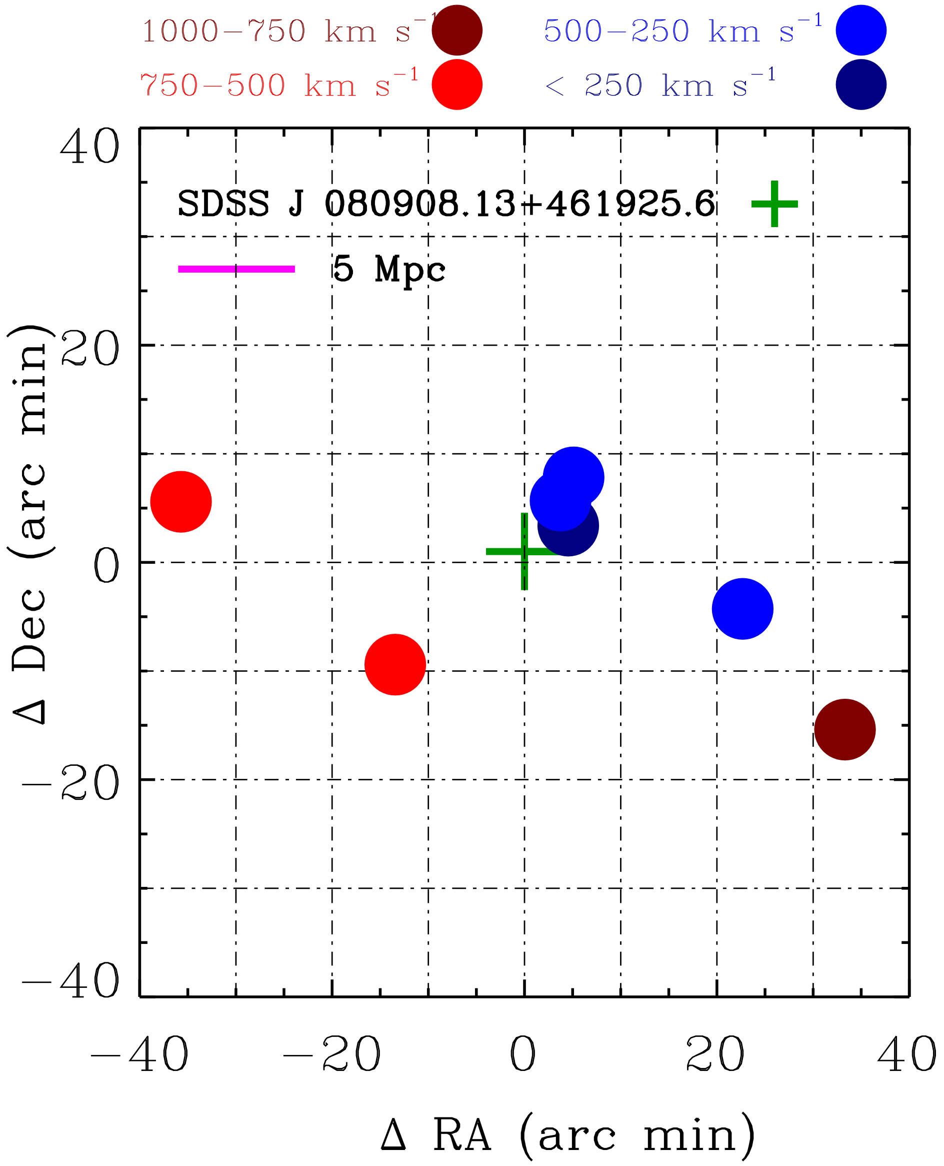

Figure 3.9 Figure shows the galaxies observed in SDSS survey within 30 × 30 arcmin and 1000 km s^{-1} from the absorber detected at $z = 0.61907$ towards the QSO sightline SDSS $J080908.13 + 461925.6$. Galaxies associated with this absorber is shown with filled circles where the colour coding corresponds to the velocity separation of the galaxy from the absorber. The line of sight is indicated by the "+" sign.

Table 3.4: Galaxies associated with the absorbers

R.A.	Dec.	z	Δv km s^{-1}	η (arcmin)	ρ (Mpc)	g(mag)	r(mag)	M$_g$	$(L/L^*)_g$
$z_{abs} = 0.61907$ ($v = 0$ km s^{-1}) Absorber towards SDSS $J080908.13 + 461925.6$									
122.360	46.3802	0.6199 ± 0.0002	153 ± 40	4.62868	1.9	24.4 ± 0.9	21.0 ± 0.1	-18.9	0.1
122.346	46.4186	0.6207 ± 0.0002	301 ± 40	6.25086	2.6	22.0 ± 0.1	21.2 ± 0.1	-22.0	2.3
122.662	46.2525	0.6212 ± 0.0002	385 ± 40	16.2716	6.7	23.7 ± 0.7	21.7 ± 0.2	-21.8	1.9
122.060	46.1669	0.6223 ± 0.0002	590 ± 40	13.2152	5.5	23.0 ± 0.4	20.7 ± 0.1	-21.4	3.6
122.369	46.4542	0.6215 ± 0.0003	449 ± 55	8.58469	3.5	22.7 ± 0.3	20.9 ± 0.2	-22.7	4.3
121.689	46.4168	0.6157 ± 0.0001	-620 ± 30	25.2369	10.4	20.7 ± 0.1	20.1 ± 0.1	-22.8	5.1
122.839	46.0672	0.6239 ± 0.0002	897 ± 40	27.7513	11.4	23.4 ± 0.4	21.7 ± 0.2	-21.9	2.1
122.746	46.4922	0.61 ± 0.04^p		21.6522	8.9	23.0 ± 0.2	21.2 ± 0.1	-22.3	3.3

Table 3.4 Comments: Information on the the galaxies identified by SDSS within 1000 km s^{-1} and $\sim$ 30 arcmin from the two absorbers are listed here. The equatorial coordinates of the galaxies are in the first two columns. The third column lists the spectroscopic redshifts of the galaxies as given by SDSS. The radial velocity separation between the absorber and the galaxy is in the fourth column. The angular separation between the absorber and the galaxy in the plane of the sky, and the corresponding projected physical separation are given in the next two columns. The projected separation was estimated assuming a ΛCDM universe with $H_0 = 69.6$ km s^{-1} Mpc^{-1} , $\Omega_m = 0.286$ and $\Omega_\Lambda = 0.714$. The apparent magnitude in the g-band is given in column 7. The absolute magnitude listed in column 8 was K-corrected using the emperical K-correction given by Westra et al. (2010). The last column provides the luminosity in terms of the Schechter luminosity of $M_\star = -21.06$ at $z = 0.6$ obtained from Ilbert et al. (2005). For estimating the projected separation and luminosity distance to these galaxies, we have used the cosmology calculator of Wright (2006).

We used random sampling to investigate whether the line of sight is indeed probing an overdensity region, or if the detection of galaxies is consistent with their random distribution in space. We selected 100 different locations within the SDSS footprint at random and searched for galaxies at $z = 0.6$ that lie within 30×30 arcmin and $|\Delta v| = 1000$ km s^{-1} of each location. The frequency distribution from this random sampling, shown in Figure 3.8, suggests that there is only a 15% chance of finding more than 6 galaxies within the sampled volume. During more than half the number of times ($\sim 56\%$), our sampling found only 2 galaxies or less in the search window, indicating that the region intercepted by SDSS $J080908.13+461925.6$ at the location of the absorber is most likely an overdensity region, such as a group or cluster environment.

In the case of the $z = 0.61907$ absorber, the SDSS data only suggests that the Ne VIII is in a high density region of luminous, massive galaxies. This general picture is consistent with more exhaustive absorber-galaxy surveys that have repeatedly found warm absorbers closely associated with galaxy overdensity regions (e.gs, Wakker and Savage 2009, Chen and Mulchaey 2009, Narayanan et al. 2010b, Stocke et al. 2014, Werk et al. 2016). Only by extending the galaxy completeness to fainter magnitudes will it be possible to say whether the Ne VIII is coincidental with the warm extended envelope of a sub-L^* galaxy or the shock-heated phase in intergalactic filaments.

3.6 Origin of the Ne VIII absorber

To discriminate the origin of an absorber only from the information of a single line of sight is a challenging task. Hence, we discuss some general possibilities of the origin of the absorber.

With the limited sample of Ne VIII absorbers, the absorber-galaxy association of Ne VIII ion is not well understood. However, it is found that most of the Ne VIII absorbers detected so far are from a galaxy overpopulated region. A similar trend is also observed in the absorber discussed in this chapter where a random sampling of galaxies at redshift $z = 0.6$ showed that Ne VIII absorption is coming from a galaxy overdensity regions.

The halo size estimates of these galaxies suggest that the absorber is not associated with the halo of any of these galaxies. However, at $z \sim 0.6$, SDSS can detect only very bright galaxies with $\gtrsim 6\ L*$ with 90% completeness. Thus, it is still possible that the absorber can be associated with galaxies which are not detected in the SDSS survey. The near solar metallicity and strong H I column density observed in the photoionized gas phase of the absorber are favorable for such a scenario.

Another possibility is the intergroup origin of the absorber. The hydrodynamic simulations of structure formation suggested that a large fraction of baryons in the low-redshift universe exist in the form of warm - hot baryons outside of galaxies. These baryons are dominated in the regions with overdensity of $30 - 100$, which is extended to the region of over-density of $\delta \sim 1000$ (See Figure 1.4). This is consistent with the theoretical predictions of Mulchaey et al. 1996 that the intragroup medium can have gas with temperature $T \sim 10^5 - 10^6$ K. Presently, such a medium can be probed only through high ionization absorption lines such as O VI, Ne VIII and thermally-broad Lyα against the light from background QSOs. The absorber detected here could be from such a gas phase. As the gas in the medium constantly interacting with the galaxies through the various feedback mechanism, the metallicity determined for the absorber is not far away from a reality.

3.7 Summary

The chapter discusses the detection of an intervening Ne VIII absorber at $z = 0.61907$ towards the background quasars SDSS $J080908.13 + 461925.6$. The key results are the following.

1. The $z = 0.61907$ absorber is seen in H I, C II, C III, N III, O III, N IV, O IV, O VI, and Ne VIII. The Ne VIII 770 line is detected with a significance of 3.0σ taking into account the statistical and systematic uncertainities. The total column density of the ion is estimated to be log $[N(\text{Ne VIII}), \text{cm}^{-2}] = 13.76 \pm 0.14$. The Ne VIII 780 line is a non-detection.

2. Ionization models suggest a two-phase solution for the $z = 0.61907$ absorber. The low and intermediate ions are most consistent with photoionized gas with $n_{\rm H} \sim 7 \times 10^{-4}$ cm^{-3}, $T \sim 1.5 \times 10^4$ K, $p/K \sim 10.5$ cm^{-3} K, and an absorption path length of $L \sim 14.6$ kpc. The ionic column densities yield abundances of [C/H] = [O/H] = −0.2, [N/H] = −1.0 and [S/H] = −0.4, with an uncertainty of ± 0.3 dex. The O VI is also consistent with an origin in this photoionized gas phase.

3. The Ne VIII in the $z = 0.61907$ absorber is found to be tracing a higher temperature gas phase that is dominantly collisionally ionized. The observed log $[N(\text{Ne VIII})/N(\text{O VI}) \gtrsim -1.25$ indicates collisional ionization equilibrium temperatures of $T \gtrsim 4.3 \times 10^5$ K for this phase. Using hybrid models of photoionization and collisional ionization, we find this warm phase of the gas to be at $n_{\rm H} \leq 10^{-3}$ cm^{-3}, corresponding to an overdensity of $\Delta \sim 1000$. The H I absorption associated with this gas phase is unknown. Hence the total hydrogen column density, absorber line-of-sight thickness and neon abundance are only approximately constrained to $N(\text{H}) \sim 2.7 \times 10^{20}$ cm^{-2}, $L \sim 87$ kpc and [Ne/H] ~ -0.5.

4. The absorber is tracing regions where there are a number of galaxies. Over a uniform projected physical separation of ~ 10 Mpc and a velocity separation of $\Delta v \sim 1000$ km s^{-1}, 7 galaxies are identified by SDSS near to this absorber.

CHAPTER 4

Detection of a Ne VIII Absorber at $z = 0.57$ Probing Warm Gas

4.1 Introduction

In this chapter, I discuss the detection and characterization of another Ne VIII absorber at redshift $z = 0.57052$ towards the background quasar SBS $1122 + 594$ probing warm - hot gas. This is the twelfth detection of intervening Ne VIII absorber, made possible by the high sensitivity of COS at far UV wavelength. The formal significance of Ne VIII detection is $\sim 2.8\sigma$. The uncontaminated broad lines of O VI and H I together constraint the thermal broadening of the absorption, which gave, a model-independent measure of temperature ($T \sim 1 \times 10^5$ K). The estimated temperature is too high for photoionization. We find a hybrid ionization model of gas with temperature $T = 1 \times 10^5$ K and sub-solar metallicity can reproducing the properties of the absorber. From the SDSS database, we find several luminous ($\gtrsim L^*$) galaxies in the vicinity of the absorber. The absorber is most likely the gas in the circumgalactic medium of a $2.6L^*$ galaxy.

The chapter is organized as follows. In Section 4.2, the information on the COS archival observations of SBS $1122 + 594$ and the data analysis techniques is briefly explained. The general description of the absorber and their properties are presented in Section 4.3. The ionization modelling, the derived physical and chemical abundances of the absorber are discussed first the next Section 4.4, followed by Section 4.5 consists of information on the galaxies identified by the SDSS that are coincident in redshift with the absorber. The results are summarized in section 4.8.

Table 4.1: Individual COS integrations for the quasar SBS $1122 + 594$

MAST ID	DATE	GRATING	λ_c (Å)	t (S)
LB4R11010	7 -11-2009	G130M	1291	2524
LB4R11020	7 -11-2009	G130M	1300	2450
LB4R11030	7 -11-2009	G130M	1309	2450
LB4R11040	7 -11-2009	G130M	1318	2450
LB4R11050	7 -11-2009	G160M	1589	2600
LB4R11060	7 -11-2009	G160M	1600	2600
LB4R11070	7 -11-2009	G160M	1611	2600
LB4R11080	7 -11-2009	G160M	1623	2601

Table 4.1 Table show the details of individual exposures used to generate the final spectra. The column from left to right corresponds to the name of the exposure in MAST database, date of the observation, grating used for the observation, central wavelength of the grating and the exposure time respectively.

4.2 The HST/COS Data

The SBS $1122 + 594$ ($z_{em} = 0.8514$) COS individual exposures were also retrieved and processed in a similar manner. The quasar was observed for 9.8 ks with the COS G130M grating and 10.5 ks with G160M grating settings. Under each grating setting, multiple exposures with different central wavelengths were used for covering the wavelength gap between the two detector segments of the instrument. The coadded spectrum has continuous wavelength coverage in the range $1135 - 1790$ Å. The Nyquist sampled spectrum has S/N varying in the range $5 - 15$ per pixel, with the peak S/N occurring at $\lambda \sim 1200$ Å, which is incidentally close to the redshifted location of Ne viii $770, 780$ lines in the absorber identified along this sight line. For both sightlines, our coadded version of the spectra agree with the independent extraction method of Bart Wakker, discussed in the appendix of Wakker et al. (2015).

Figure 4.1: $z = 0.57052$ absorber in restframe

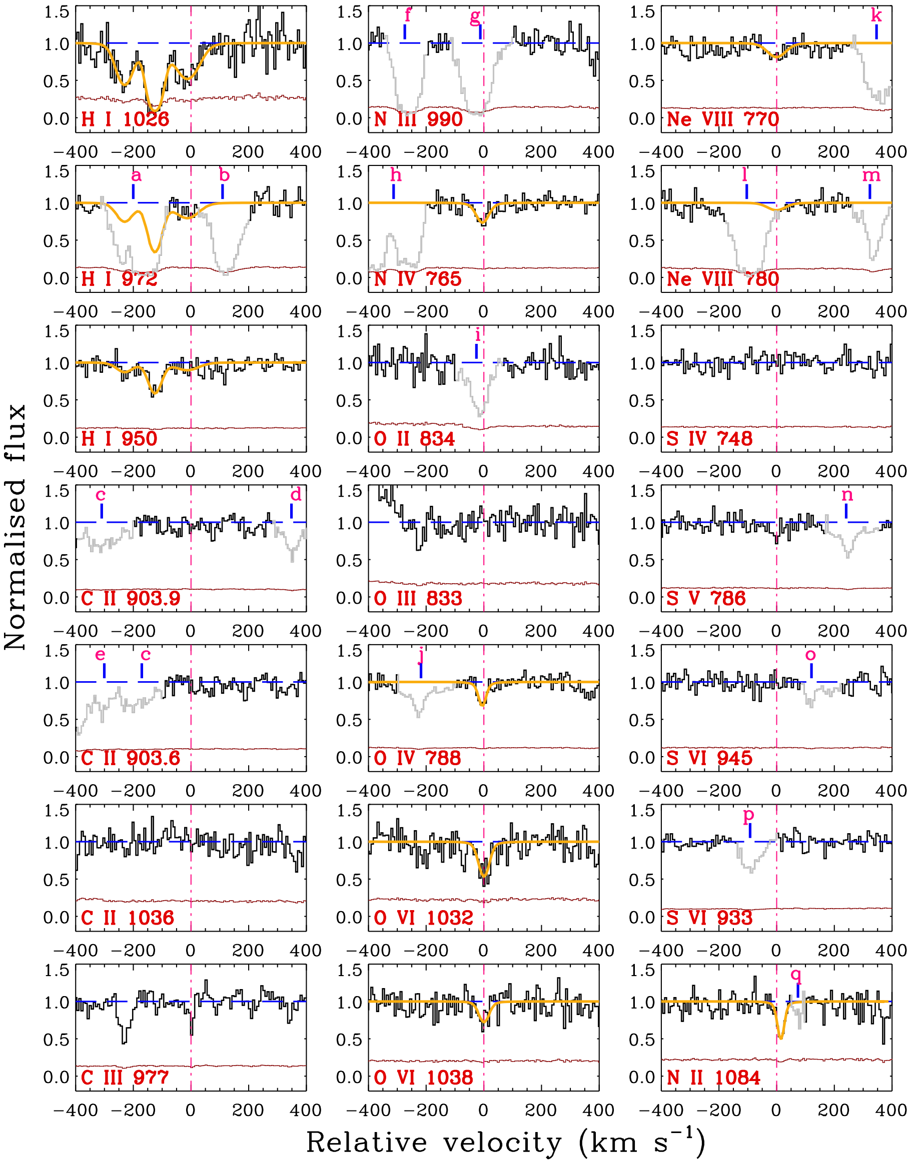

Figure 4.1 The continuum normalised spectra of the $z = 0.57052$ absorber towards SBS $1122 + 594$. The *gray* regions in the various panels indicate contamination, i.e., absorption not associated with this system. Some of the major contaminations are (a) and (b) Galactic Si II 1527, (c), (d), and (e) associated Ne VIII 770, (f) Lyα at $z = 0.2777$ for which corresponding Lyβ and Lyγ are identified, (g) C IV 1548 at $z = 0.0040$ for which corresponding Lyα, Si IV $\lambda\lambda 1394, 1403$, Si III lines are present (h) Galactic 1200, (i) Lyβ at $z = 0.2777$ for which corresponding Lyα and Lyγ are present, (j) possibly Lyα at $z = 0.0169$, (k) Si III 1206 at $z = 0.0040$ confirmed by the presence of corresponding Lyα, C IV $\lambda\lambda 1548, 1550$, Si IV $\lambda\lambda 1394, 1403$ lines (l) Lyβ at $z = 0.1944$ for which other Lyman series lines, O VI $1031, 1037$ etc are identified (m) possibly Lyα at $z = 0.0093$, (n) possibly Lyα at $z = 0.0163$, (o) possibly Lyα at $z = 0.2207$, and (p) O VI 1032 at $z = 0.4201$ for which higher order Lyman series lines are identified.

4.3 The $z = 0.57052$ Absorber towards SBS $1122 + 594$

The absorber is detected in H I, O IV, N IV, O VI and Ne VIII. Continuum normalized velocity plots of important transitions are shown in Figure 4.1. The H I clearly shows three distinct components at at -8, -122, -227 km s^{-1}. The metal lines are all aligned with the -8 km s^{-1} component, which interestingly is not the strongest component in H I. The COS spectrum also covers wavelength regions where lines from C II, C III, O III, S IV, and S VI are expected. The line measurements are given in Table 4.2. The O VI $1031, 1037$ lines were simultaneously fitted freely with Voigt profiles. The lines fall in a comparatively low S/N (~ 6 per 17 km s^{-1} resolution element) part of the spectrum, which is reflected in the large uncertainty associated with the fit parameters, and in the unusual equivalent width ratio between the two lines of the doublet. The doublet lines have a combined detection significance of 4.1σ. The column density from profile fitting is similar to the integrated apparent column density obtained for the 1032 Å and 1038 Å lines. This indicates little unresolved saturated structure in the O VI profiles. The same is also true for Lyβ, N IV 765 and O IV 788 transitions.

The Lyβ and Lyθ lines were also simultaneously fitted with three components. The Lyγ transition was excluded from the profile fitting as the region is severely contaminated by Galactic Si II 1527 and a Lyα absorber at $z = 0.2569$. From profile fitting, we find that the H I component associated with the metal lines is fairly broad ($b \sim 50$ km s^{-1}). This component is undetected in Lyθ, as we expect it to be too weak. Our assumption of a simple three-component model for the H I can be a source of systematic uncertainty in the line measurements. Given the low S/N of data, we cannot ascertain whether the true kinematic nature of the H I is more complex. Future observations involving the near-UV channel of COS will allow coverage for Lyα associated with this system, offering valuable constraints on the velocity profile of H I.

The O IV 788, and N IV 765 lines were also fitted with single component Voigt profiles. Figure 4.1 shows the profile models for these various transitions.

At the location of S V 786 there is a very weak feature detected at 2.2σ significance. We find this feature to be inconsistent with being S v as none of the ionization models (discussed later) are able to simultaneously explain the detection of S v with the non-detections of its adjacent ionization stages, namely S iv and S vi. It is quite likely that this is an unidentified interloping feature.

4.3.1 The Ne viii 770, 780 Detection

The Ne viii 770, 780 absorption falls at a region of the spectrum where the $S/N \sim 12$ per wavelength bin, which is a factor of 2 higher compared to the S/N at the Lyβ or the O vi lines. The Ne viii 770 feature has a rest-frame equivalent width of $W_r = 26 \pm 9$ mÅ when integrated over the velocity range from -60 km s^{-1} to 40 km s^{-1}. This corresponds to a formal detection significance of 2.9σ. The statistical and the continuum placement errors have been taken into consideration in the error estimation. Including an additional 5 mÅ to account for possible detector fixed pattern residual noise features would bring the detection significance down to 2.5σ. The redshifted wavelength of the accompanying Ne viii 780 feature is contaminated by a strong Lyβ feature from an absorber at $z = 0.1944$ for which corresponding Lyα, C iii, O vi and several other metal lines are seen. The contamination renders a measurement on Ne viii 780 impossible.

In the individual exposures, the Ne viii 770 has rest-frame equivalent widths of $W_r = 31 \pm 19$ mÅ, $W_r = 17 \pm 20$ mÅ, $W_r = 24 \pm 18$ mÅ and $W_r = 28 \pm 18$ mÅ for observations with G130M grating central wavelengths of 1291 Å, 1300 Å, 1309 Å and 1318 Å respectively. All of these observations have the same FP-SPLIT position. As with the previous case, we compared the spectra of a set of five quasars with the same COS grating settings and find no evidence for fixed pattern noise in this region of detector space. The absorption reported as Ne viii 770 occurs at $\lambda = 1209.85$ Å. This is not identified as an interloping line from other absorbers discovered along this sightline in the independent line identifications done by Danforth et al. (2016) and one of the co-authors (Bart Wakker).

Table 4.2: Line Measurements for the absorber at $z = 0.57052$

Voigt Profile Measurements

Transition	v (km s^{-1})	b(km s^{-1})	log [N (cm^{-2})]
H I 950-1026	-8 ± 7	49 ± 11	14.46 ± 0.07
	-122 ± 2	26 ± 3	14.97 ± 0.04
	-227 ± 5	34 ± 7	14.44 ± 0.06
O VI 1032-1038	4 ± 5	20 ± 6	13.95 ± 0.06
O IV 788	0 ± 4	12 ± 6	13.84 ± 0.09
N IV 765	0 ± 5	25 ± 7	13.15 ± 0.07
Ne VIII 770	-2 ± 10	38 ± 7	13.92 ± 0.14
N II 1084	10 ± 2	10 ± 4	13.93 ± 0.09

Integrated Apparent Optical Depth Measurements

Transition	$W_r(m)$	log [N (cm^{-2})]	[-v,v](km s^{-1})
Ne VIII 770	26 ± 9	13.72 ± 0.15	[-60, 40]
Ne VIII 780	< 22	< 13.9	[-15, 40]
C III 977	< 40	< 13.0	[-60, 50]
O III 833	< 45	< 13.8	[-60, 50]
S VI 933	< 33	< 13.0	[-60, 50]
S VI 945	< 36	< 13.3	[-60, 50]
S IV 748	< 30	< 13.1	[-60, 50]
C II 903.9	< 30	< 13.0	[-60, 50]
C II 903.6	< 30	< 13.3	[-60, 50]
C II 1036	< 60	< 13.7	[-60, 50]
N II 1084	52 ± 17	13.75 ± 0.18	[-40, 20]
H I 1026	142 ± 23	14.40 ± 0.14	[-60, 50]
H I 972	45 ± 13	14.31 ± 0.13	[-60, 50]
H I 950	32 ± 13	14.47 ± 0.14	[-60, 50]
O VI 1032	82 ± 21	13.92 ± 0.13	[-60, 50]
O VI 1038	25 ± 19	< 14.0	[-60, 50]
O IV 788	25 ± 9	13.66 ± 0.15	[-40, 10]
N IV 765	41 ± 10	13.16 ± 0.12	[-60, 50]

Table 4.2 Comments: The line measurments were done using apparent optical depth and Voigt profile fitting techniques. The various columns list the rest-frame equivalent width, centroid velocity of the absorbing components, their b parameters, column densities, and the velocity range of integration used to estimate these parameters.

Figure 4.2: Ne VIII profile comparisan with model

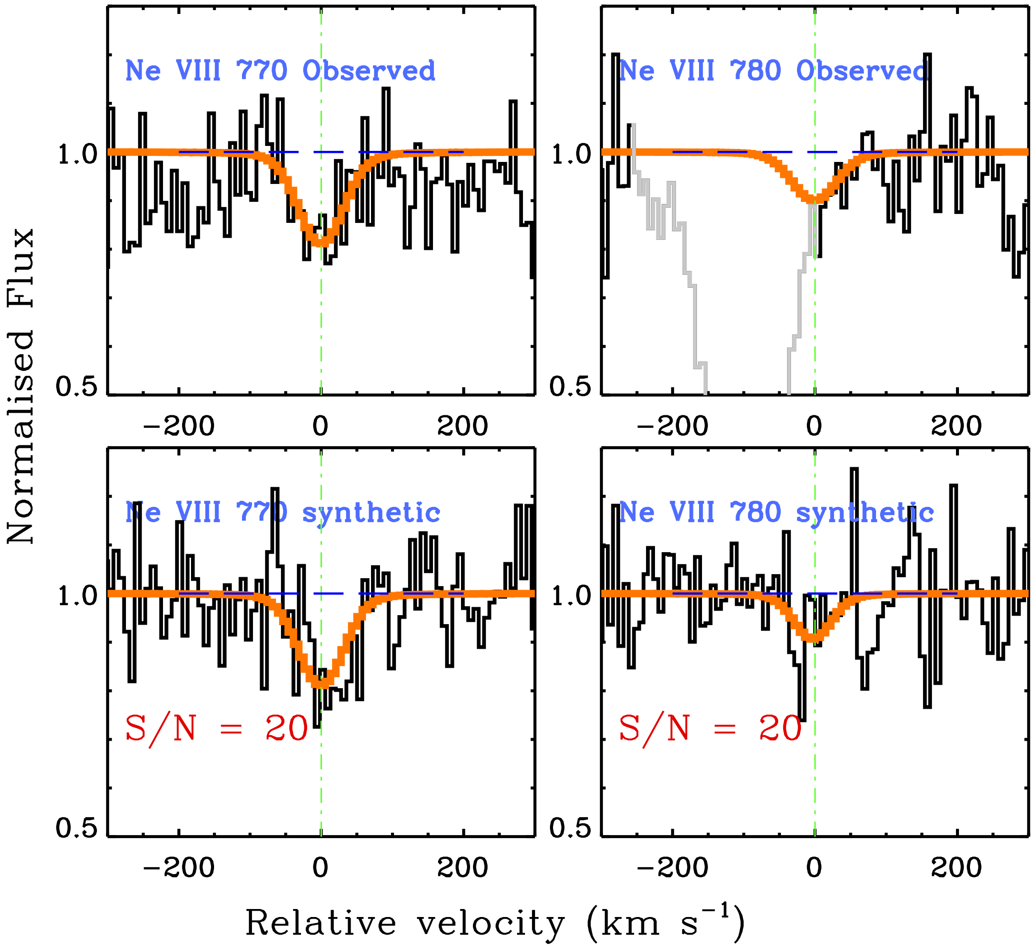

Figure 4.2 The top panel of the first column shows the observed Ne VIII 770 in the $z = 0.57052$ absorber, with the Voigt profile model superimposed. The bottom panel is a synthetic Ne VIII 770 feature with identical N and b as the observed line at $S/N = 20$. The top and bottom panels of the second column show the corresponding observed and synthetic Ne VIII 780 spectra respectively. The synthetic spectra suggests that the weak Ne VIII can be a non-detection in the 780 Å line at the S/N of the data, in agreement with observations.

4.4 Ionization & Abundances in the $z = 0.57052$ Absorber

The absence of low ionization species like C II, O II, C III and O III suggests moderate to high ionization conditions in this absorber. Photoionization predicted column densities using Cloudy for the various metal ions are shown in Figure 4.3. The models were computed for an H I column density of 14.46 dex which we measure for the $v \sim -8$ km s^{-1} component. The metal ions are all coincident in velocity with this H I component. The ratio between the observed O IV and O VI is valid for a density of $n_{\rm H} = 1.8 \times 10^{-4}$ cm^{-3}. At this density, the models are able to recover the observed column density of N IV, O IV, O VI for a metallicity of [X/H] $= -0.8$ dex. This single phase solution, shown in Figure 4.3, is also consistent with the non-detection of the low ionization species. The single phase model with $n_{\rm H} = 1.8 \times 10^{-4}$ cm^{-3} yields a total hydrogen column density of N(H) = 18.6, a temperature of $T = 2.7{\times}10^4$ K, a gas pressure of $p/k = 4.9$ cm^{-3} K and a line of thickness of $L = 47.2$ kpc for the absorbing medium.

The Ne VIII column density from this gas phase is ~ 1.8 dex lower than the observed value. To explain Ne VIII from the same phase would require the [Ne/H] to be ~ 10 greater than solar, whereas the C, N, O abundances are significantly sub-solar. The alternative of the Ne VIII arising in a separate photoionized phase at higher ionization parameter can also be ruled out, as such a phase will also produce significant O VI, and O IV in it, which will make the two-phase solution incompatible with the observed column densities of these ions.

There is also a contradiction in the temperature arrived at through photoionization modelling and the measured b-values of H I and O VI. The different b-values for the reasonably well aligned H I and O VI suggests the temperature of this gas phase to be $T = (0.5 - 1.5) \times 10^5$ K, where the range corresponds to the 1σ uncertainty in the b-values. Similar limits for temperature are obtained if we use the b-values of H I and O IV. The values are too high for UV photoionization heating. Such a conclusion rests on the assumption that the metal lines and Lyα are adequately resolved by COS. In the O IV 788, S V 786 and O VI 1032 lines there is no immediate evidence for kinematic substructure. The N IV 765 shows slight assymetry in the bluer side of its profile. At the given resolution and S/N, it is difficult to rule out whether the lines are narrower than what is seen by COS.

Figure 4.3: PIE model of the absorber at $z = 0.57052$

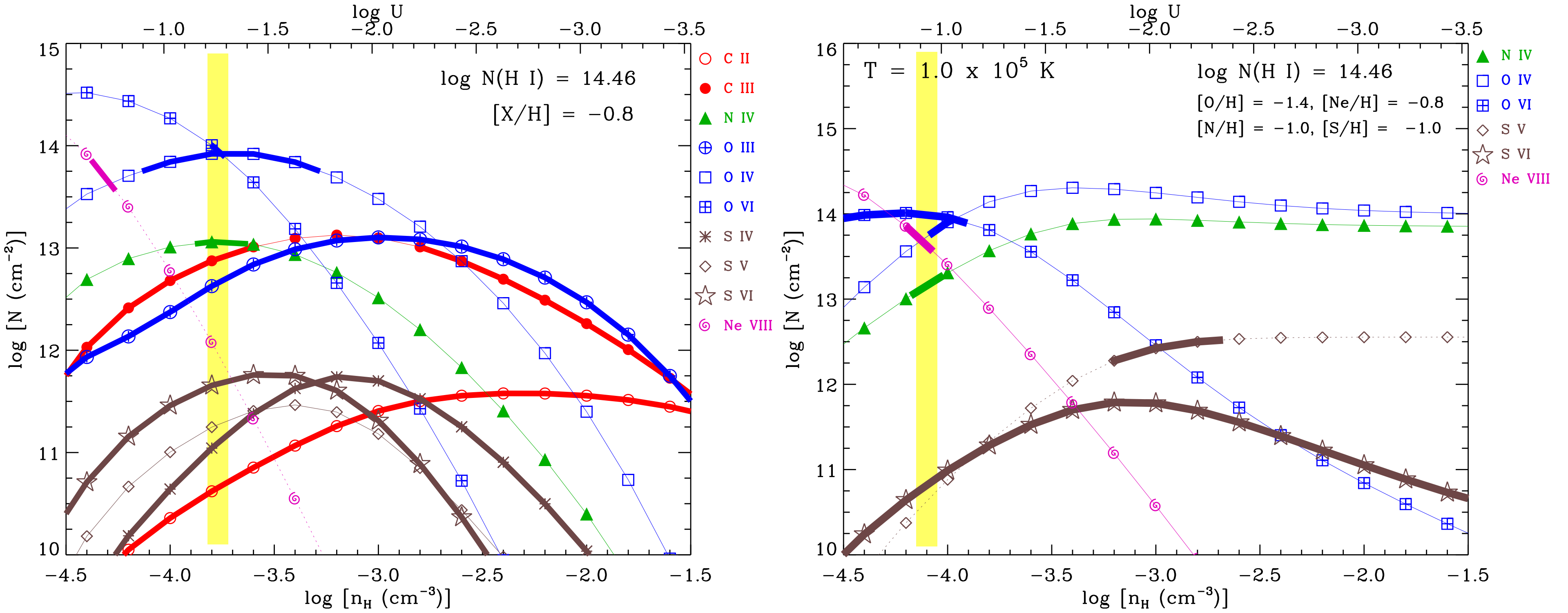

Figure 4.3 The figure on the left panel is the PIE model for the absorber at $z = 0.57052$ with a $f_{esc} = 4\%$ in the KS15 ionizing background. The curves correspond to column density predictions at different densities for each ion, and the thick regions on each curve is where the model is consistent with the observation to within 1σ. For a sub solar metallicity of -0.8 dex and at a density of $n_{\rm H} \sim 5 \times 10^{-3}$cm^{-3}the PIE model can explain the observed column density of all the ions except S V and Ne VIII. The right panel shows the hybrid ionization model predictions for a temperature T=1×10^5 K and the KS15 EBR with $f_{esc} = 4\%$. The temperature used is based on comparing b(O VI) with b(H I). In the hybrid models, the various ions are produced from a single phase with $n_{\rm H} \sim 10^{-4}$ cm^{-3} for elemental abundances of [O/H] $= -1.4$, [Ne/H] $= -0.8$, [N/H] $= -1.0$ and [S/H] $= -1.0$.

The low S/N of the data not withstanding, the higher temperatures suggested by the line widths could mean that the collisional processes may be playing a significant role in controlling the ionization in this gas. A more realistic model for this *warm* plasma could be one where electron collisions as well as photon interactions are simultaneously considered. Such *hybrid* models are discussed in the next section.

Hybrid ionization models

In Figure 4.3, we have also shown the predictions from hybrid models for an EBR with $f_{esc} = 4\%$. The temperature of the plasma was set to $T = 10^5$ K, which is the mean of the temperature range obtained from the thermal broadening of H I and metal absorption lines. This temperature is closer to where O VI reaches its peak ionization fraction, compared to the peak in Ne VIII. From the observed O IV to O VI ratio, the density is constrained to $n_{\rm H} \sim 10^{-4}$ cm^{-3}, with only a slight difference between the predictions from the two flavors of EBR.

The hybrid models suggest that it is possible for N IV, O IV, O VI and Ne VIII to be coming from the same gas phase with $n_{\rm H} \sim 10^{-4}$ cm^{-3}, for non-solar relative elemental abundances. This gas phase model yields a total hydrogen column density of $N(\rm H) = 4.8 \times 10^{19}$ cm^{-2}, a line of sight thickness of $L \sim 196$ kpc, and represents a baryonic overdensity of $\Delta \sim 100$. The observed column densities are recovered for [O/H] $= -1.4$, [Ne/H] $= -0.8$, and [N/H] $= -1.0$. The baryonic column density and absorber size reduces to half, and the elemental abundances increase by 0.2 dex for hybrid models with $f_{esc} = 0\%$.

The higher than solar (Ne/O) ratio may appear unusual. However, the solar abundance of Ne is a poorly determined quantity. The lack of strong photospheric Ne transitions in the optical or UV is the major source of uncertainty in solar Ne abundance measurements. From X-ray spectroscopic observations of a sample of stars in the 100 pc neighborhood of the Sun, Drake and Testa (2005) estimate a value for (Ne/O) that is 2.3 times higher than the solar value of (Ne/O) $= -0.76 \pm 0.11$ given by Asplund et al. (2009). Adopting this revised estimate for (Ne/O) with an increase of $+0.3$ dex will make the [Ne/H] $\sim$ [O/H] in the warm gas phase.

Figure 4.4: Galaxy Distribution Near the $z = 0.57052$ Absorber

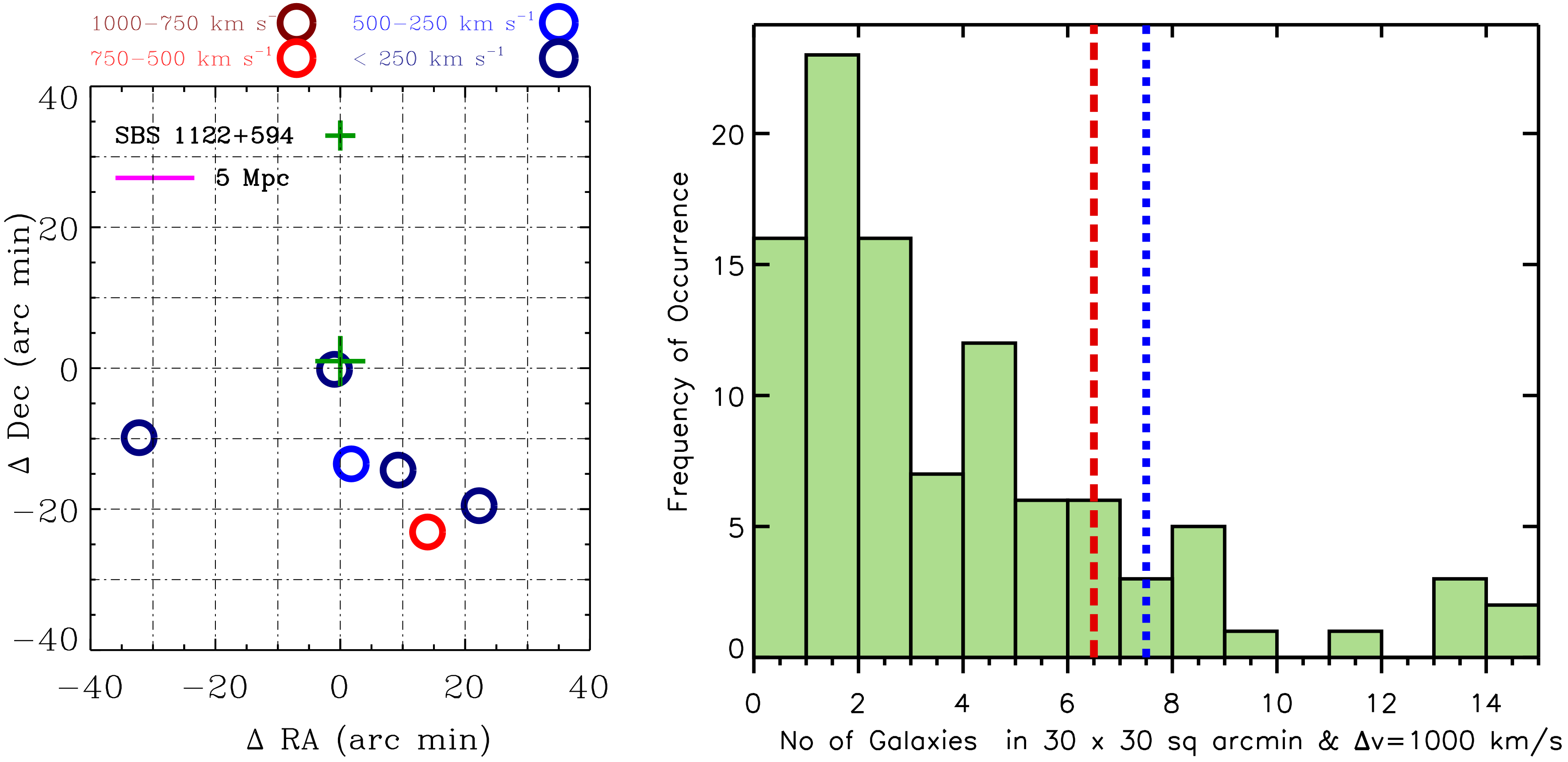

Figure 4.4 The left panel shows the galaxies observed in SDSS survey within 30 × 30 arcmin and 1000 km s^{-1} from the absorber detected at $z = 0.57052$ towards SBS 1122 + 594. Galaxies associated with this absorber is shown with open circles where the colour coding corresponds to the velocity separation of the galaxy from the absorber. The line of sight is indicated by the "+" sign. The right panel shows the distribution of galaxies within a similar seperation towards 100 locations randomly sampled from the SDSS footprint. The distribution indicates that only a small (15%) probability of finding more than 6 galaxies in the sampled volume. Thus, 6 galaxies(red dashed vertical line) detected in the simialr seperation around $z = 0.57052$ absorber is less likely be a random coincidence.

Table 4.3: Galaxies associated with the absorbers

R.A.	Dec.	z	Δv km s^{-1}	η (arcmin)	ρ (Mpc)	g(mag)	r(mag)	M$_g$	$(L/L^*)_g$
		$z_{abs} = 0.57052$ ($v = 0$ km s^{-1}) Absorber towards SBS $1122 + 594$							
171.45883	59.169975	0.570542 ± 0.00014	8 ± 30	0.497249	0.197	22.3 ± 0.2	20.9 ± 0.1	-22.2	2.6
171.50348	58.946364	0.568724 ± 0.00017	-339 ± 50	13.613460	5.395	22.8 ± 0.3	21.0 ± 0.1	-22.1	3.0
171.62853	58.931547	0.569372 ± 0.00050	-215 ± 100	15.236410	6.039	22.2 ± 0.2	20.6 ± 0.1	-22.6	4.0
170.93717	59.008323	0.570136 ± 0.00020	-69 ± 70	19.265253	7.635	22.1 ± 0.1	20.8 ± 0.1	-22.3	3.2
171.70715	58.785227	0.573197 ± 0.00019	514 ± 70	24.341730	9.648	21.2 ± 0.1	20.1 ± 0.1	-22.9	5.4
171.84478	58.847470	0.570971 ± 0.00018	90 ± 50	22.627742	8.968	22.3 ± 0.2	20.7 ± 0.1	-22.4	3.4

Table 4.3 Comments: Information on the the galaxies identified by SDSS within 1000 km s^{-1} and $\sim$ 30 arcmin from the two absorbers are listed here. The equatorial coordinates of the galaxies are in the first two columns. The third column lists the spectroscopic redshifts of the galaxies as given by SDSS. The radial velocity separation between the absorber and the galaxy is in the fourth column. The angular separation between the absorber and the galaxy in the plane of the sky, and the corresponding projected physical separation are given in the next two columns. The projected separation was estimated assuming a ΛCDM universe with $H_0 = 69.6$ km s^{-1} Mpc^{-1} , $\Omega_m = 0.286$ and $\Omega_\Lambda = 0.714$. The apparent magnitude in the g-band is given in column 7. The absolute magnitude listed in column 8 was K-corrected using the emperical K-correction given by Westra et al. (2010). The last column provides the luminosity in terms of the Schechter luminosity of $M_\star = -21.06$ at $z = 0.6$ obtained from Ilbert et al. (2005). For estimating the projected separation and luminosity distance to these galaxies, we have used the cosmology calculator of Wright (2006).

4.5 Galaxies Near the Absorber

The SDSS DR12 spectroscopic database is 90% complete only for galaxies with luminosities $\gtrsim 6\ L*$ at $z \sim 0.6$ (Ilbert et al., 2005). This means that at any intermediate redshift, SDSS would be revealing information only on those galaxies that occupy the bright end of the luminosity function for that epoch. In this section, we discuss the galaxies identified by SDSS DR12 in the neighbourhood of $z = 0.57052$ absorber and the general conclusions derived from it.

The $z = 0.57052$ absorber towards SBS 1122 + 594 resides in a galaxy overdensity region with 6 galaxies identified within $|\Delta v| = 1000$ km s^{-1} of the absorber. The distribution of galaxies is shown in Figure 4.4 with open circles, and their information is listed in Table 4.3. The nearest galaxy with a spectroscopically confirmed redshift is nearly at the systemic velocity of the absorber, at a close-by projected separation of $\rho = 197$ kpc. The halo radius of this galaxy can be estimated from its scaling relationship with luminosity as shown below.

$$\log R_{vir} = 2.257 + 0.318\mathrm{C} + 0.018\mathrm{C}^2 - 0.005\mathrm{C}^3 \tag{4.1}$$

where $\mathrm{C} = \log(L/L^*)$. The $L = 2.6\ L^*$ luminosity of the galaxy suggests that the absorber is residing well within the galaxy's virial radius of $R_{vir} = 245$ kpc. The impact parameter is also comparable to the size of O VI absorbing halos around luminous galaxies at low-z (Tumlinson et al., 2011a; Werk et al., 2013; Muzahid, 2014). The second closest galaxy to the absorber is at a projected distance of ~ 5 Mpc and displaced in velocity by $|\Delta v| \sim 339$ km s^{-1}. The average systemic velocity of the galaxies relative to the absorber is -27 ± 26 km s^{-1} and the velocity dispersion is 111 km s^{-1}. The abundance of $\gtrsim L^*$ galaxies within such a narrow range of projected physical separation and velocity offset indicates that the line of sight is possibly passing through a group medium. Given the limited number count of galaxies at the redshift of the absorber and the incompleteness of the sample for even $L*$ luminosities, it is not realistic to formally define a galaxy group through a friends of friends approach, or similar standard algorithms.

We used random sampling to investigate whether the line of sight is indeed probing an overdensity region, or if the detection of galaxies is consistent with their random distribution in space. We selected 100 different locations within the SDSS footprint at random and searched for galaxies at $z = 0.6$ that lie within 30×30 arcmin and $|\Delta v| = 1000$ km s^{-1} of each location. The frequency distribution from this random sampling, shown in Figure 4.4, suggests that there is only a 15% chance of finding more than 6 galaxies within the sampled volume. During more than half the number of times ($\sim 56\%$), our sampling found only 2 galaxies or less in the search window, indicating that the region intercepted by SBS 1122+594, at the location of the absorber is most likely an overdensity region, such as a group or cluster environment.

The densities predicted by the hybrid models correspond to overdensities ($\Delta = \rho/\bar{\rho} \gtrsim 10^2$) that are reminiscent of hot halos and the warm-hot intergalactic gas in simulations (Smith et al., 2011; Gaikwad et al., 2016a). The $z = 0.57052$ absorber is well within the virial radius of a 2.6 L^* galaxy. Using the r-band magnitude and halo mass (M_h) relationship given by Tinker and Conroy (2009), we estimate that this galaxy resides in a halo of minimum mass $M_h \sim 10^{14}$ M$_\odot$. The corresponding virial temperature of the dark matter halo comes out to be $T_{vir} \sim 10^7$ K. Since the halo mass is greater than the critical mass of $M_h \sim 10^{11}$ M$_\odot$ for virial shocks (Birnboim and Dekel, 2003), any gas accreted by the galaxy from the surrounding will be initially shock heated to the halo virial temperature. Subsequently, the gas can radiatively cool falling out of hydrostatic equilibrium with the halo. With our estimates of $T \sim 10^5$ K, $n_{\rm H} \sim 10^{-4}$ cm^{-3}, and [X/H] ~ -1.0, the instantaneous radiative cooling time scale comes out as $t_{cool} \sim 20$ Myrs (Sutherland and Dopita, 1993). These estimates hint at the possibility that the $z = 0.57052$ absorber, with its comparatively low metallicity, could be material infalling into the hot extended corona of the galaxy.

Table 4.4: Intervening Ne VIII detections so far

Line of sight	z_{abs}	Transition	$W_r(m)$	log[N]	log[$N(H)$]	$logT$ K	[X/H]	Origin of Ne VIII
HE 0226-4110	0.2070	Ne VIII 770	32.9 ± 10.5	$13.85^{+0.12}_{-0.17}$	20.06	5.68	—	Collisional
(Savage et al., 2005)		Ne VIII 780	24.9 ± 10.6	$14.03^{+0.15}_{-0.24}$	—	—	—	
(Savage et al., 2011a)		Ne VIII 780	24.9 ± 10.6	$14.03^{+0.15}_{-0.24}$	—	—	—	
		O VI	—	14.38 ± 0.01	—	—	-0.89	
3C 263	0.32566	Ne VIII 770	47 ± 11.9	$13.98^{+0.10}_{-0.13}$	—	5.80	—	Collisional
(Narayanan et al., 2009)								
PKS 0405-123	0.4951	Ne VIII 770	45 ± 6	13.96 ± 0.06	19.67	5.70	-0.6	Collisional
(Narayanan et al., 2011a)		Ne VIII 780	29 ± 5	14.08 ± 0.07	—	—	-0.6	
		O VI 1038	153 ± 5	14.48 ± 0.01	—	—	—	
PG1148+549	0.6838	Ne VIII 770	51 ± 12	13.98 ± 0.09	19.80	5.69	> -0.5	Collisional
(Meiring et al., 2013)		O VI 1032	234 ± 19	14.47 ± 0.03	—	—	> -0.5	
		O VI 1038	149 ± 23	14.50 ± 0.06	—	—	> -0.5	
	0.7015	Ne VIII 770	28 ± 5	13.75 ± 0.07	19.00	5.69	> -0.2	Collisional
		Ne VIII 780	18 ± 6	13.86 ± 0.11	—	—	>-0.2	
		O VI 1032	168 ± 19	14.29 ± 0.04	—	—	>-0.2	
		O VI 1038	113 ± 19	14.35 ± 0.06	—	—	>-0.2	
	0.7248	Ne VIII 770	26 ± 8	13.70 ± 0.12	18.90	5.72	> 0	Collisional
		Ne VIII 780	19 ± 5	13.87 ± 0.10	—	—	>0	
		O VI 1032	71 ± 20	13.84 ± 0.10	—	—	>0	
		O VI 1038	37 ± 12	13.87 ± 0.15	—	—	>0	

Table 4.4 Comments: The table is a compilation of all intervening Ne VIII detections so far. Column 4 is the equivalent width in the rest-frame of the absorber, column 5 is the apparent optical depth measured column densities, column 6 lists the total hydrogen column density, column 7 is the temperature reported by the authors for the Ne VIII gas phase, and column 8 is the dominant ionization mechanism for the production of Ne VIII as concluded by the respective authors.

Table 4.5: Intervening Ne VIII detections so far

Line of sight	z_{abs}	Transition	$W_r(m)$	log$[N]$	log$[N(H)]$	$logT$ K	$[X/H]$	Origin of Ne VIII
PG 1407+265	0.5996	Ne VIII 780	52.8 ± 6.6	14.15 ± 0.18	19.40	4.80	> 0	Photoionised
(Hussain et al., 2015)		O VI	—	14.57 ± 0.05	—	—	—	
LBQS 1435-0134	1.1912	Ne VIII	—	13.96 ± 0.17	19.92	—	0.3	Collisional
(Qu and Bregman, 2016)		O VI	—	14.49 ± 0.05	—	—	—	
PG 1206+459	0.927	Ne VIII -1	—	13.71 ± 0.29	19.4	5.4	3	Collisional
(Tripp et al., 2011)		Ne VIII -2	—	14.08 ± 0.08	20.3	5.6	1	
		Ne VIII -3	—	14.07 ± 0.04	—	—	0.5	
		Ne VIII -4	—	14.53 ± 0.04	20.4	5.6	1	
		Ne VIII -5	—	14.21 ± 0.05	—	—	—	
		Ne VIII -6	—	13.30 ± 0.27	—	—	—	
		Ne VIII -7	—	13.78 ± 0.09	—	—	—	
QSO J1154+4635		Ne VIII 770	—	14.65 ± 0.08	—	—	—	
(Bordoloi et al., 2016)		O VI	—	14.71 ± 0.01	—	—	—	
SDSS J080908+	0.61907	Ne VIII 770	28 ± 8	13.76 ± 0.14	20.45	> 5.6	< 0.5	Collisional
461925.6 (this work)		O VI 1038	248 ± 18	14.79 ± 0.06	—	—	—	
SBS $1122 + 594$	0.57052	Ne VIII 770	26 ± 9	13.72 ± 0.15	19.70	5.0	$<$ -0.8	Collisional
(this work)		O VI 1032	82 ± 21	13.92 ± 0.13	—	—	-1.4	

Table 4.5 A continution of Ne VIII detection sofar. See Hussain et al. 2017 for a remodeling of 7 of these absorbers using the updated KS15 ionizing background, and the likelihood of a photoionization origin for the Ne VIII at supersolar metallicities.

4.6 The Origin of $z = 0.57052$ Absorber

The galaxy information available in SDSS database shown that the absorber $z = 0.57052$ is only 0.197 Mpc (projected separation) separated in the sky and ~ 50 km s^{-1} in velocity from the $L = 2.6\ L^*$ galaxy is most likely associated with the halo of this galaxy. The total mass of the halo could be of the order of $M_h \sim 10^{14}\ M_\odot$ which can have a virial temperature of 10^7 K. Thus, a gas cloud infalling to the halo from desolate regions of IGM can be heated up to a temperature of $\sim 10^6$ K. The sub-solar metal abundance for this absorber is consistent with such a scenario.

4.7 On the Origin of Ne VIII Absorbers

Recently, Hussain et al. (2017) remodelled 7 out of the 10 previously known Ne VIII absorbers by replacing the earlier UV background models of Haardt and Madau (1996, 2012) with the KS15. The KS15 radiation field, with the recently updated QSO emissivities and SEDs, has a ~ 3 times higher intensity compared to Haardt and Madau (2012) at energies > 4 Ryd where the ionization potentials of O VI and Ne VIII lie. They found that in the absence of any direct evidence for warm-hot temperatures (i.e., the detection of a thermally broad Lyman-α line), the Ne VIII can also be explained through photoionization. The KS15 background yields an order of magnitude higher values for density and metallicity compared to the Haardt & Madau UV background. This results in the absorber line-of-sight thickness decreasing from an unrealistically large $\gtrsim$ Mpc scale to $10 - 200$ kpcs, thereby making the photoionization solution a viable alternative. But in the same models, the photoionized Ne VIII gas requires solar, and in most cases supersolar (nearly ten times solar) metallicities to match the observed metal line column densities Hussain et al. (2017). This is suggestive of the absorption tracing gas that is directly enriched by star formation, and not the canonical low metallicity WHIM distant from galaxies, that simulations predict. On the other hand, the sample of absorbers discussed in this chapter have sub-solar metallicities. Interestingly, in the $z = 0.57052$ system for which we have an ionization model independent measure on the warm temperature, the [Ne/H] ~ -1.0 dex, in agreement with the general predictions of Hussain et al. (2017) that at low metallcities, Ne VIII can stay longer at high temperature and is a good predictor of warm gas.

Through cosmological simulations, Tepper-García et al. (2013) had investigated the physical origin of Ne VIII systems. Their analysis demonstrates that the peak ionization fraction of f(Ne VIII) $\sim$ 10% is achieved through photoionization only at very low densities of $n_{\rm H} \sim 10^{-6}$ cm^{-3} (with the KS15 background this changes to 10^{-5} cm^{-3}) and $T \sim 10^4$ K in contrast to collisional ionization ($n_{\rm H} \sim 10^{-4}$ cm^{-3}, $T \gtrsim 10^5$ K). As a result, for the same metallicity, the N(Ne VIII) $\propto (n_{\rm H}\ T)^{1/2}$ comes out as $\sim 1 - 2$ orders of magnitude more when it is tracing a warm (collisionaly ionized) phase compared to a photoionized case. Observationally, collisionally ionized Ne VIII will be therefore easier to locate in spectra of adequately high sensitivity. Considering this, it is possible that most of the Ne VIII detections reported till now (Table 4.4, 4.5) are likely to be tracers of warm plasma and to a lesser extent photoionized gas. It needs to be mentioned here that the results of Tepper-García et al. (2013) differ from the simulations of Oppenheimer et al. (2012) who find Ne VIII to be predominantly from $T \sim 10^4$ K phase of the low-z IGM. The simulations are inconclusive because of the differences between them in the treatment of physics, the assumptions made and in the implementation of Galactic scale processes. Given such circumstances, the interpretation of observations based on simulations should be done with prudence.

In certain cases, the data cooperate in a way that allows one to infer the thermal conditions in the absorber without depending on ionization models. For example, in the Ne VIII absorbers reported by Savage et al. (2005, 2011a) and Narayanan et al. (2009, 2012), the presence of a BLA (albeit at low significance) offered a direct measure on the temperature ($T \sim 5 \times 10^5$ K) of the Ne VIII phase of the gas. Similarly, for the z = 0.57052 absorber in this chapter, the temperature of the warm plasma was ascertained from the different b-values of the metal lines and H I. Identifying BLAs in metal line systems traced by O VI and Ne VIII is possibly one of the best ways to infer the presence of warm-hot gas. Detection of thermally broad and shallow H I components in an unambiguous way, particularly in multiphase absorbers, will depend on the availability of high ($S/N \gtrsim 50$) spectroscopic observations with HST /COS.

4.8 Summary

1. The $z = 0.57052$ absorber has H I, N IV, O VI and Ne VIII lines detected. The Ne VIII 770 line has a significance of 2.9σ. The b-parameters for O VI and the corresponding H I component indicates temperature in the range of $T = (0.5 - 1.5) \times 10^5$ K, which is also consistent with the line widths of O IV and N IV, and supports collisional ionization.

2. At temperature $T \sim 10^5$ K, the hybrid models offer a single phase solution with $n_{\rm H} \sim 10^{-4}$ cm^{-3} for all the detected ions, corresponding to overdensities of $\Delta \sim 100$. This warm gas phase has a total hydrogen column density of N(H) $= 4.8 \times 10^{19}$ cm^{-3}, and a thickness of $L \sim 196$ kpc, with [Ne/H] $\sim$ [O/H] ~ -1 dex.

3. The absorber tracing regions where there are a number of galaxies. Over a uniform projected physical separation of $\sim$ 10 Mpc and a velocity separation of $\Delta v \sim 1000$ km s^{-1}, 6 galaxies are identified by SDSS near to the $z = 0.57052$ absorber. In the latter case, the absorber is within the halo virial radius of a $2.6L^*$ galaxy and could be tracing an infalling shock heated gas cloud in to the halo of the galaxy.

CHAPTER 5

Detection of a Pair of O VI Absorbers at $z \sim 0.4$ Probing Warm Gas

5.1 Introduction

In the previous two chapters, we discussed the detection of warm hot baryons in the low redshift universe using Ne VIII as a probe. Compared to Ne VIII, O VI is ubiquitous in the universe because of the higher cosmic abundance of oxygen. The lines of O VI can be easily detected even at low S/N through it's strong 1032, 1038 Å doublet transitions. Ultraviolet surveys have therefore relied a great deal on O VI as probes to locate undetected warm hot baryons at low-z (Tripp et al., 2008; Danforth et al., 2006; Danforth and Shull, 2008; Savage et al., 2014).

However, the origin of O VI in IGM is ambigous. It is found that cool ($T \lesssim 10^4$ K) photoionized gas at very low densities ($n_{\rm H} \sim 10^{-5}$ cm^{-3}) can produce strong O VI absorption of N(O VI) $\gtrsim 10^{14}$ cm^{-2} (Thom and Chen, 2008b,c; Tripp et al., 2008; Prochaska et al., 2011; Muzahid et al., 2015). On the other hand, there are instances where O VI seems to be clearly associated with shock-heated warm gas with $T \sim 10^5 - 10^6$ K (Narayanan et al., 2010a,b; Savage et al., 2011c,b; Muzahid et al., 2012; Savage et al., 2014). In complex multiphase absorbers, the distinction between these two scenarios are often blurred.

In this chapter, I will discuss on the detection of two O VI absorbers, kinematically proximate to each other, identified in the HST/COS far-UV spectrum of the quasar SBS 0957 + 599. In both absorbers, a BLA is detected, but only in one of them, the broad-H I is coincident in velocity with the O VI. The coincidence of the BLA with the O VI allows us to discriminate between a collisional ionisation and a photoionization scenario. In one of the absorbers, the O VI is tracing $T \sim 7 \times 10^5$ K gas. On the other hand, O VI is consistent with cooler $T \sim 4.6 \times 10^4$ K photoionized gas in the second detection. In Sec 5.2, a description

Table 5.1: Individual COS integrations for the quasar SBS $0957 + 599$

MAST ID	DATE	GRATING	λ_c (Å)	t (S)
LBHO65010	18 -03-2011	G130M	1291	1618
LBHO65020	19 -03-2011	G130M	1309	1682
LBHO65030	19 -03-2011	G160M	1600	2710
LBHO65040	19 -03-2011	G160M	1623	2491

Table 5.1 Table show the details of individual exposures used to generate the final spectra. The column from left to right corresponds to the name of the exposure in MAST database, date of the observation, grating used for the observation, central wavelength of the grating and the exposure time respectively.

of the spectroscopic data is given. Sec 5.3 offers details on both absorbers and the respective line measurements. The ionisation mechanisms, absorber physical properties and the chemical abundances are discussed in Secs 5.4 & 5.5. Sec 5.6 provides the information on the galaxies detected near the absorber. The possible origin of both multiphase absorbers are dealt within Sec 5.7 and Sec 5.8 provides a summary of the significant results.

5.2 The HST/COS Data

The ultraviolet *HST*/COS (Green et al., 2012) spectroscopic observations for SBS 0957+599 ($z_{em} = 0.746$) were extracted from the MAST public archive[1]. The quasar was observed as part of the COS program to map the gaseous halos of dwarf galaxies (PI. J Tumlinson, Prop ID 12248). The data were reduced using the STScI CalCOS (v3.0) pipeline. The observations consists of far-UV spectra obtained with the G130M and G160M gratings for total integration times of 3.3 ks and 5.2 ks respectively. The combined spectrum has a wavelength coverage of $1150 - 1800$ Å, and a wavelength dependent resolution of $R \sim 15,000 - 20,000$ which progressively increases towards longer wavelengths. The COS wavelength calibration has residual errors of ~ 20 km s^{-1}, which are at the level of a resolution

---

[1] https://archive.stsci.edu/

Figure 5.1: The absorbers at $z \sim 0.4$

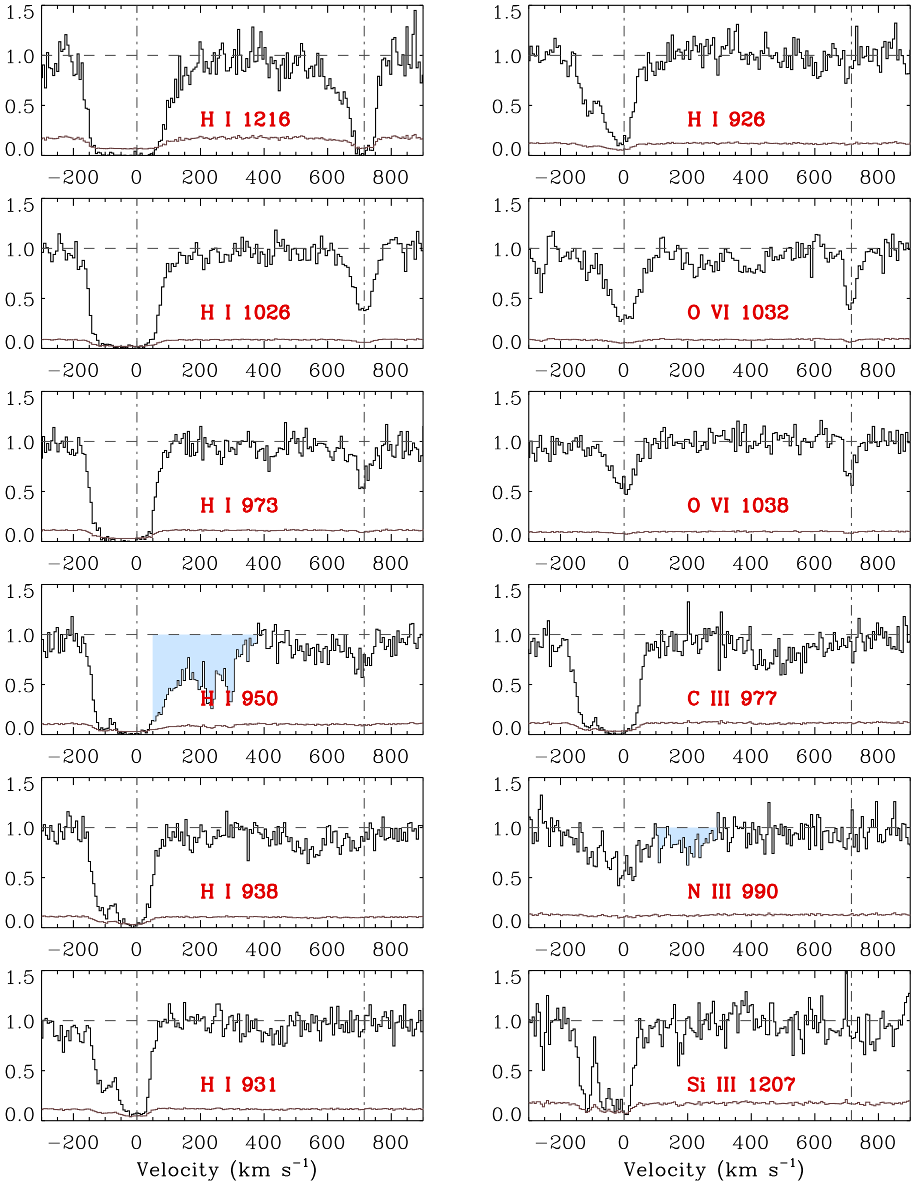

Figure 5.1 Continuum normalized spectral regions of prominent lines associated with the $z = 0.41614$ ($v \sim 0$ km s^{-1}) and $z = 0.41950$ ($v \sim 710$ km s^{-1}) absorbers. The vertical lines indicate the relative velocities of the absorbers. Only H I 1216 – 950, and O VI are $> 3\sigma$ detections for the $z = 0.41950$ system. The 1σ error spectrum can also be seen at the bottom of each plot window. The shaded portions indicate absorption unrelated to the line. The absorption contaminating H I 950 is identified as O VI 1032 at $z = 0.3036$ for which the corresponding O VI 1038, H I, C III, Si III are also detected. Similarly, the contamination to N III 990 could be from interstellar Si IV 1403 Å.

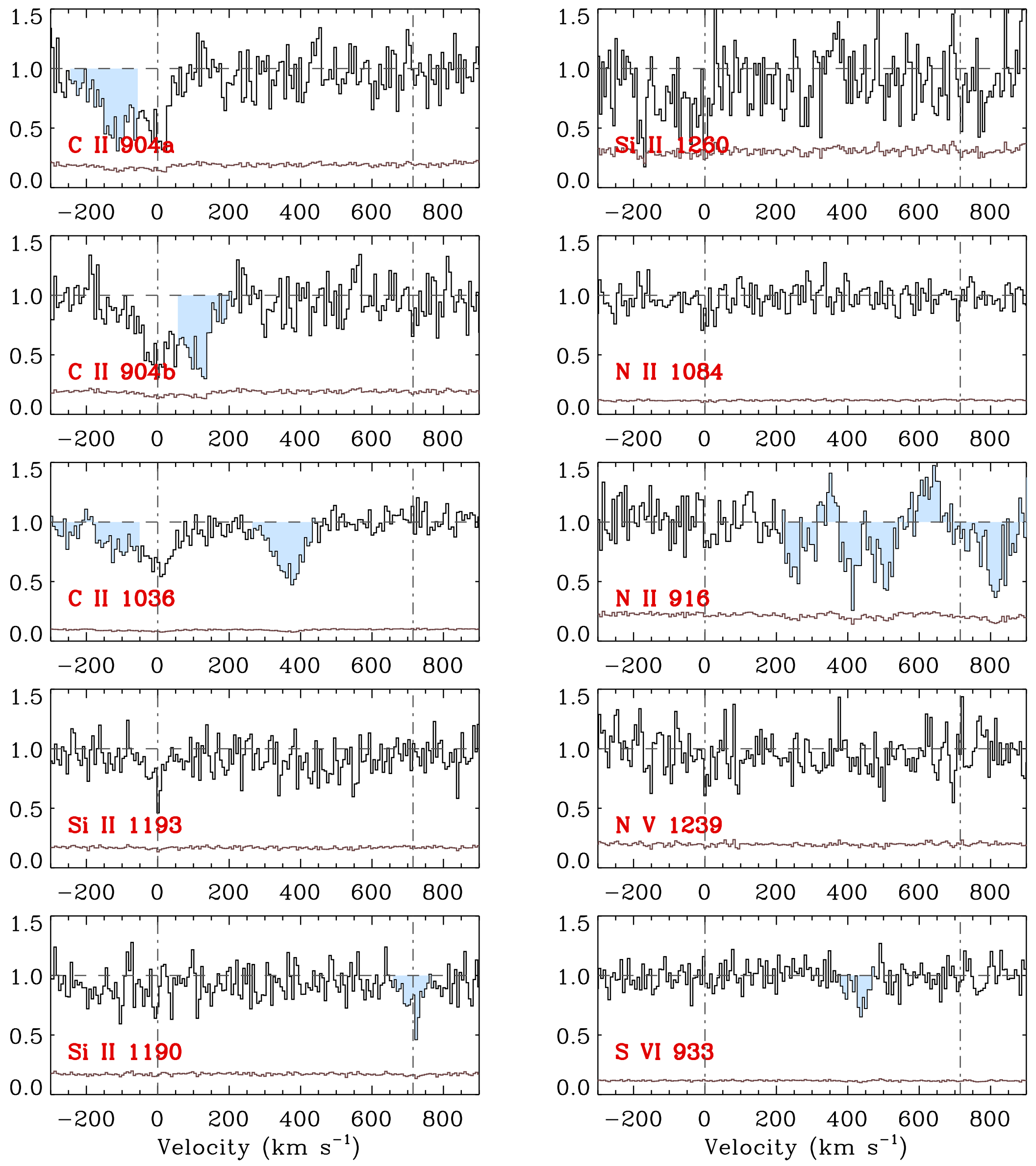

Figure 5.1 continue. For the $v \sim 0$ km s^{-1} absorber, Si II 1190, Si II 1260, N V and S VI are non-detections at $> 3\sigma$. The C II 904a ($\lambda = 903.9616$ Å) and C II 904b ($\lambda = 903.6235$ Å) are mutually blended at $v < -50$ km s^{-1} and $v > 50$ km s^{-1} respectively. Their wavelength separation is only 0.5 Å in the observed frame. The absorption at $v \sim 400$ km s^{-1} in the C II 1036 panel is O VI 1038 from the absorber discussed in this chapter. Similarly the feature at $v \sim 710$ km s^{-1} in the Si II 1190 panel is Si II 1193 at $v \sim 0$ km s^{-1}.

element of the instrument (Savage et al., 2011c; Meiring et al., 2013). Within an exposure, the residual errors are found to vary with wavelength. To reduce the impact of these wavelength dependent offsets between exposures, we adopted an algorithm of comparing the position of Galactic ISM and IGM lines between expo-

Figure 5.2: Voigt profile model for the absorber at $z = 0.41614$

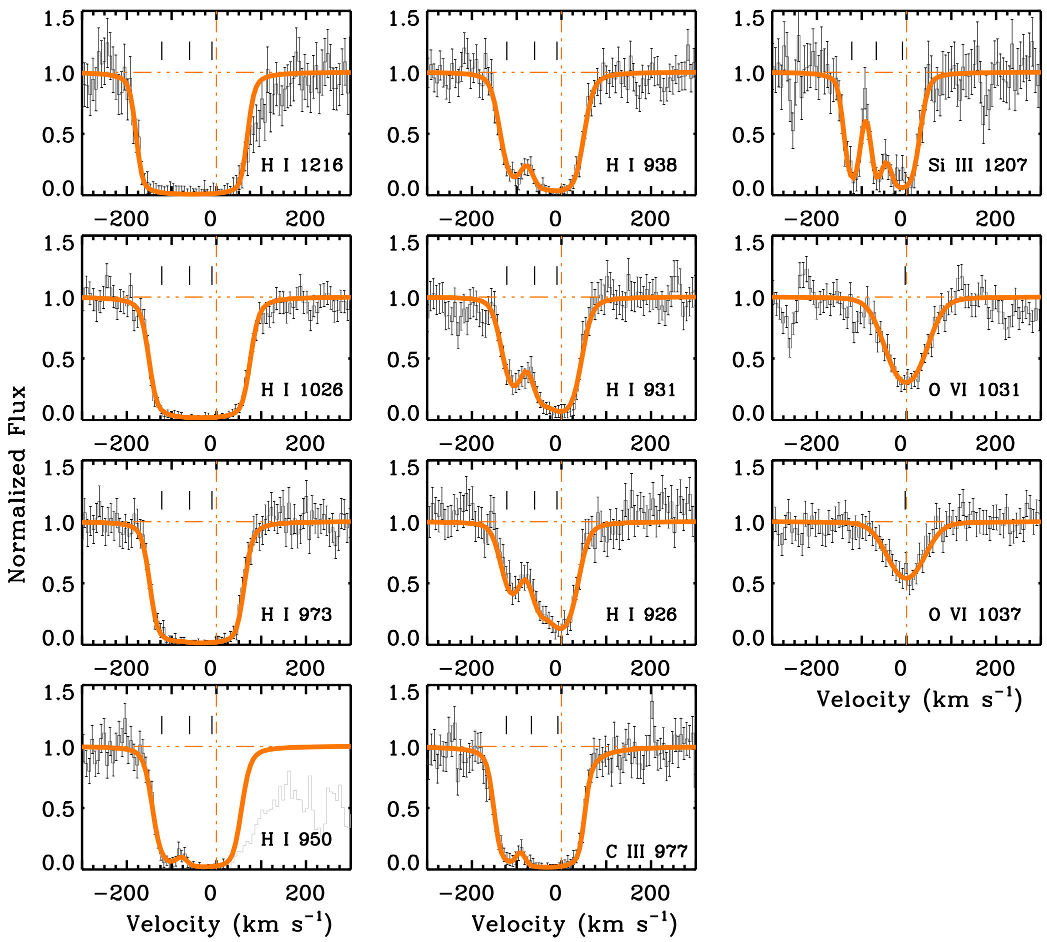

Figure 5.2 Voigt profile models are shown superimposed on the continuum normalized data with 1σ error bars. The H I absorption is modeled by simultaneously fitting the Lyman series lines. The H I is best fitted with three kinematically distinct components, the positions of which are indicated with the vertical tick marks. The H I 950 Å line is strongly contaminated at $v > 0$ km s^{-1} by O VI 1032 at $z = 0.3036$. While fitting, the contaminated pixels were deweighted by artifically enhacing the noise associated with those pixels. A three component model similar to H I is also obtained from independently fitting the C III and Si III lines. In contrast, the O VI 1031, 1037 are simultaneously fitted with a single component. The kinematic profile of O VI is distinct from H I or the intermediate and low ionization lines of other elements. The higher order Lyman lines, C III and Si III at $v \sim -10$ km s^{-1} are significantly saturated. The fit results are given in Table 5.1.

sures and applying a polynomial fit to their wavelength dependent offset variations. The fit was used to determine the necessary offset to each exposure and bring the different exposures to mutual alignment. The separate exposures thus aligned were coadded. The correct wavelength scale is finally determined by matching the ISM lines with the velocity of Galactic 21-cm H I emission. The full details of this apporach is described in Wakker et al. 2015. The COS spectra obtained from the pipeline is oversampled with 6 pixels across one resolution element. For our analysis, we rebinned the coadded spectra to the optimal sampling of 2 pixels per resolution element, thereby increasing the S/N. The spectrum was normalized to the level of the continuum determined by fitting lower-order polynomials.

5.3 The Multiphase Absorbers

5.3.1 The $z = 0.41614$ Absorber

The absorber is detected at $> 3\sigma$ significance in a number of hydrogen Lyman series lines, O VI, C III, N III, Si III, and C II. The continuum normalized line profiles are shown in Figure 5.1. The COS spectra also covers Si II, N II, S II, N V, and S VI which are non-detections. The $z = 0.41614$ redshift is the optical depth weighted center of the O VI 1032 Å line. For H I, O VI, C III, and Si III we have obtained line parameters by Voigt profile modeling using the Fitzpatrick and Spitzer (1997) routine. For decomposing the line profiles, the models were convolved with the empirically determined line-spread functions of Kriss (2011) at the redshifted wavelength of each line. The fit results are shown in Figure 5.2 and Table 5.1.

The H I clearly shows absorption at its core from three kinematically distinct components at $v \sim -122$ km s^{-1}, $v \sim -61$ km s^{-1}, and $v \sim -10$ km s^{-1}. The H I column densities for these components were obtained by simultaneously fitting the Lyman series lines H I 1216 − 926 Å. The unsaturated higher order Lyman lines provide a unique solution to the H I absorption profile. The total H I column density of $\sim 10^{16.5}$ cm^{-2} obtained from profile fitting indicates that the absorber is only partially optically thick at the Lyman limit. The derived value is comparable within its errors with the H I column density of $\sim 10^{16.3}$ cm^{-2} estimated from the optical-depth at the partial Lyman-limit of $\tau_{\rm LL} \sim 0.3$. An accurate measurement

Table 5.2: Voigt Profile Measurements

z_{abs}	Transition	v (km s^{-1})	log [N (cm^{-2})]	b(km s^{-1})
0.41614	H I $1216 - 926$	-122 ± 4	15.82 ± 0.05	25 ± 3
		-61 ± 6	15.87 ± 0.31	21 ± 8
		-10 ± 4	16.30 ± 0.37	30 ± 5
		-3	14.02 ± 0.23	115 ± 7
	O VI $1032, 1038$	-3 ± 4	14.54 ± 0.04	48 ± 4
	C III 977	-120 ± 4	14.45 ± 0.13	16 ± 5
		-67	15.14 ± 0.58	10 ± 7
		-8	16.63 ± 0.63	20 ± 6
	Si III 1207	-123 ± 3	13.49 ± 0.18	13 ± 5
		-67 ± 5	13.60 ± 0.25	9 ± 6
		-8 ± 5	15.17 ± 0.47	14 ± 8
0.41950	H I $1216 - 926$	-3 ± 3	14.57 ± 0.06	30 ± 4
		-72 ± 5	13.48 ± 0.42	58 ± 6
	O VI $1032, 1038$	0 ± 2	14.15 ± 0.06	14 ± 3

Table 5.2 Comments: In the $z = 0.41614$ absorber, the multi-component structure is clearly discernible for Si III and H I. The C III line is saturated and hence we obtain the N and b values by fixing the centroid of two of its components to match Si III. We found that for the $v = -8$ km s^{-1} component, changing the b-parameter by a small amount alters the estimated column density significantly indicating that the line is in the flat part of the curve of growth. We adopt a value of $\log N(\text{C III}) = 16.63^{+0.63}_{-1.10}$ accounting for the uncertainty in column density from the range of b-values possible for this component. Moreover, this component is possibly a blend of narrower components unresolved by COS. Similarly, for Si III, we adopt a column density measurement of $\log N(\text{Si III}) = 15.17^{+0.47}_{-1.43}$. Compared to the $v \sim -8$ km s^{-1}, the $v \sim -67$ km s^{-1} and $v \sim -123$ km s^{-1} components are not severly saturated. The fit parameters for the broad component in H I were obtained by fixing its velocity to that of O VI. The error in the BLA's b-parameter is the stastical error given by the fitting routine. The true error in b will be larger than this estimation as we discuss in Sec 5.3.1. The Voigt profiles of the separate components in H I are displayed in Figure 5.3. The $z = 0.41950$ absorber is detected only in H I and O VI.

Table 5.3: AOD Measurements for the $z = 0.41614$ Absorber

Line	$W_r(m)$	log $[N\ (\mathrm{cm}^{-2})]$	[-v, +v] (km s^{-1})
C II 1036	< 60	< 13.8	[-180, -100]
	38 ± 7	13.57 ± 0.09	[-100, -55]
	107 ± 9	14.06 ± 0.07	[-55, 50]
C III 977	208 ± 11	13.85 ± 0.06	[-200, -85]
	> 456	> 14.3	[-85, 100]
N III 990	43 ± 9	13.67 ± 0.11	[-180, -100]
	42 ± 8	13.70 ± 0.10	[-100, -55]
	106 ± 11	14.10 ± 0.31	[-55, 40]
O VI 1032	256 ± 12	14.49 ± 0.06	[-100, 100]
O VI 1038	150 ± 13	14.48 ± 0.05	[-100, 100]
Si II 1260	< 195	< 13.3	[-180, 50]
Si II 1193	< 93	< 13.2	[-180, 50]
Si II 1190	< 90	< 13.4	[-180, 50]
Si III 1207	157 ± 14	13.13 ± 0.06	[-180, -100]
	142 ± 11	13.12 ± 0.07	[-100, -55]
	> 272	> 13.4	[-55, 50]
N II 1084	< 57	< 13.7	[-180, 50]
N V 1239	< 105	< 13.7	[-180, 50]
S VI 933	< 55	< 13.3	[-180, 50]

Table 5.3 Comments - C II 904*a* ($\lambda = 903.9616$ Å) & C II 904*b* ($\lambda = 903.6235$ Å) are separated by only ~ 0.5 Å in the observed frame. The C II 904*b* at $v > 50$ km s^{-1} has significant overlap with C II 904*a*. We therefore adopt the measurements done on C II 1036. The blue end of C II 1036 is contaminated because there is no corresponding absorption seen in C II 904*b* which is expected to be 20% stronger than C II 1036. The C II and N III lines do not show a distinct component structure that can be modeled using Voigt profiles. Hence we have integrated the apparent column density along the velocity interval over which absorption from each component is likely to dominate the contribution from the others. For the lines which are not detected at $\geq 3\sigma$, an upper limit is obtained by integrating over the full velocity range where we expect to find the absorption.

Table 5.4: AOD Measurements for the $z = 0.41950$ Absorber

Line	$W_r(m)$	log $[N\ (\mathrm{cm}^{-2})]$	[-v, +v] (km s^{-1})
C II 1036	< 31	< 13.5	[-50, +50]
C II 904*b*	< 51	< 13.4	[-50, +50]
C III 977	< 33	< 12.8	[-50, +50]
N III 990	< 36	< 13.6	[-50, +50]
O VI 1032	88 ± 9	13.97 ± 0.05	[-50, +50]
O VI 1038	39 ± 10	13.88 ± 0.11	[-50, +50]
Si II 1193	< 60	< 12.9	[-50, +50]
Si III 1207	< 57	< 12.5	[-50, +50]
N II 1084	< 39	< 13.6	[-50, +50]
N V 1239	< 69	< 13.6	[-50, +50]
S VI 933	< 33	< 13.0	[-50, +50]

Table 5.4 Comments - All metal lines except O VI are non-detections at the $> 3\sigma$ significance level.

of τ_{LL} requires modeling the full QSO continuum including the higher order Lyman series lines. Here we have attempted a crude estimation of τ_{LL} by defining a flat continnum around the partial Lyman-limit at $\lambda \sim 1292$ Å. In addition to the strong absorption in the core, the Lyα line shows a broad and shallow absorption in its red wing over the velocity range $[-v, +v] = [70, 200]$ km s^{-1}. This shallow absorption is not recovered by the three component fit. The significance of this red wing is discussed in Sec 5.3.1.

The Si III 1207 Å line shows a three component profile coinciding in velocity with the H I. However, we note that the component at ~ -10 km s^{-1} can have sub structure to it, which is ambigious at the limited resolution of COS. In the case of C III, the absorption over the $-90 < v < 100$ km s^{-1} interval is saturated. We therefore adopt the velocities of the two central components of Si III to fit the corresponding C III feature.

In contrast, the O VI absorption does not show the kinematic complexity seen in H I, C III, Si III and N III. The absorption in either lines of the O VI doublet is consistent with a single component. This kinematic difference is suggestive of O VI having a different origin compared to other metal lines. The COS data shows a difference of 7 km s^{-1} in the velocity centroid of O VI with the nearest component seen in H I, C III and Si III. However, this offset is within the 1σ uncertainty of the velocity of the model profile, and the wavelength calibration residuals expected for COS spectra. More consequential for the presence of multiphase is the difference in the kinematics of the absorption of O VI compared with H I and the other metal lines.

The C II 904*a* ($\lambda = 903.9616$ Å) is blended with absorption from C II 904*b* ($\lambda = 903.6235$ Å). The weaker C II 1036 profile suggests evidence for multiple components but at low contrast. We note that the feature at $v < -70$ km s^{-1} in C II 1036 is most likely a blend as the corresponding absorption in the stronger C II 904*a* is not seen. Our fitting routine is unable to converge on a three component fit to the C II data. We therefore resort to the apparent optical depth (AOD) technique of Savage and Sembach (1991) to determine the integrated column densities of C II separately for the velocity intervals of the three components seen in Si III. The details of the apparent column density measurements and equivalent widths are given in Table 5.2. The N III 990 line also has component structure that cannot be uniquely identified from profile fitting. We use AOD method to determine the apparent column density for N III as well. There should be no contamination from Si II 990 line in the N III 990 line, since the stronger Si II 1260, 1193, and 1190 lines are non-detections.

Our profile fitting analysis shows that the central two components of C III and Si III are saturated. A free-fit to the Si III line gives a value of $\log N(\text{Si III}) = 15.17 \pm 0.47$ and $b(\text{Si III}) = 14 \pm 8$ km s^{-1} for the strongest component. Assuming a scenario of pure non-thermal line broadening, $b(\text{Si III}) \sim b(\text{H I}) = 30$ km s^{-1} for the $v \sim -10$ km s^{-1} component, we obtain a fit to the line profile with a column density that is ~ 1.4 dex smaller. The strong dependancy of column density on b-parameter implies that the line is in the flat part of the curve of growth. Voigt profile fitting does not yield a unique solution for such saturated lines. The errors returned by the profile fitting routine also do not reflect this uncertainty in column density due to saturation.

If the C III and Si III lines are predominantly non-thermally broadened, then from the better constrained $b(\text{H I})$, we can estimate a lower limit on the column density for C III and Si III that are 1.10 dex and 1.43 dex lower than the estimated value. Alternatively, if the lines are fully thermally broadened, then $b(\text{C III}) \sim 7$ km s^{-1} and $b(\text{Si III}) \sim 5$ km s^{-1} for the $v \sim -10$ km s^{-1} component. For these very narrow line widths, the Voigt profile models do not suitably fit the data. From this exercise, we conclude that whereas either component of C III and Si III could be as broad as the corresponding H I, they cannot be much narrower than what is seen at the resolution of COS. We therefore adopt a $\log N(\text{Si III}) = 15.17^{+0.43}_{-1.43}$ and $\log N(\text{C III}) = 16.63^{+0.63}_{-1.10}$ for the $v \sim -10$ km s^{-1} component.

The Broad Ly-α Absorption

The Lyα profile shows excess absorption in the velocity range $[-v, +v] = [70, 200]$ km s^{-1} over the red wing of the core components. A three component fit to the H I series lines produces an acceptable fit to the strong narrow core components, but does not explain the wing in Lyα. To fit this broad feature, we have to introduce a shallow component to the absorption model. By fixing this component

Figure 5.3: Broad Lyman Alpha Absorption for the absorber at $z = 0.41614$

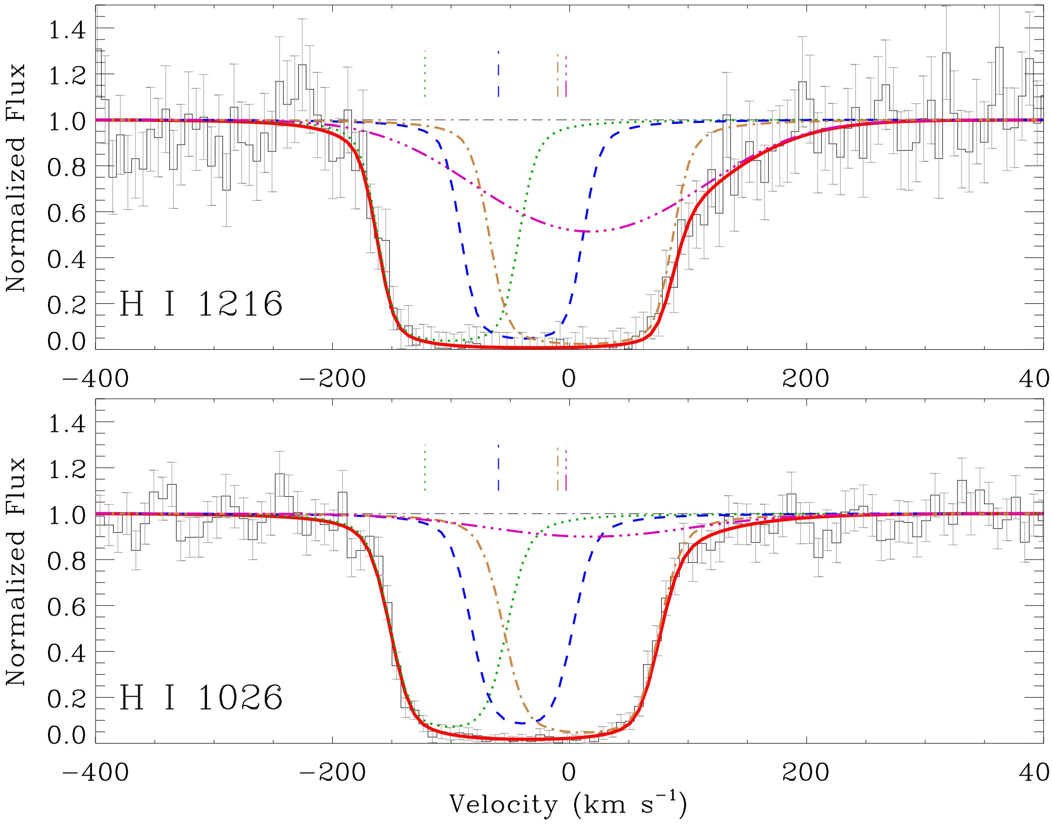

Figure 5.3 Top and bottom panels are Voigt profile fits to Lyα and Lyβ. The core absorption is simultaneously fitted with three narrow components at $v \sim -122$ km s^{-1}, -61 km s^{-1}, ~ -10 km s^{-1} shown here as dashed blue curve, dotted green curve and dash-dotted brown curve. The absorption in the red wing of the Lyα is fitted by a shallow and broad component with $b \sim 115$ km s^{-1}. The presence of the BLA is consistent with the Lyβ profile where it is not detected. The solid red curve is the combined contribution of all the four components of H I.

at the same velocity as O VI, a simultaneous fit to the Lyα and Lyβ estimates this fourth component of H I to be a BLA with log N(H I) = 14.02 ± 0.23 dex and b(H I) = 115 ± 7 km s^{-1}. The fit results are given in Table 5.1 and the contributions from the four separate components are shown in Figure 5.3. Being a shallow feature, the broad component is not discernible in Lyβ or any of the higher order Lyman series lines. Therefore, including these higher order lines to the simultaneous fit does not change the parameters we extract for the BLA.

The profile fitting routine underestimates the uncertainties in the fit parameters for the BLA. The 1σ uncertainty in column density of the core H I components, the uncertainties in their b-parameters and their line centroids as well as the uncertainty in the v of O VI will influence the fit values the BLA can have. To account for these additional sources of uncertainty in the BLA fit results, we fitted profiles to Lyα and Lyβ lines simultaneously with the 1σ uncertainty range of values for v, N, and b of the core components.

Combining these deviations from the measured value in quadrature with the statistical uncertainty, we estimate the breadth of the BLA component to be $b(\text{H I}) = 115^{+17}_{-19}$ km s^{-1}. This is the measurement that we adopt for the BLA for the rest of the analysis. In the case of column density, the statstical error from Voigt profile fit of 0.23 dex dominates the uncertainty. The placement of the continuum could also influence the line measurement. But we find that the continuum is well defined within $\Delta v \sim 4000$ km s^{-1} of the Lyα. The large b-value implies a temperature of log $T(\text{K}) = 5.91^{+0.12}_{-0.16}$, if the broadening is purely thermal. The BLA reveals the presence of a considerably warm temperature phase to the absorber.

5.3.2 The $z = 0.41950$ absorber

The second O VI absorber is offset from the previous system by $\Delta v = +710$ km s^{-1}. This is a kinematically simple system compared to the $z = 0.41614$ absorber. Only H I and O VI are detected at this redshift with $> 3\sigma$ confidence. Figure 5.4 shows the profile fit on these lines and Table 5.1 lists the column density measurements from profile fitting. The upper limits on column densities for the other metal ions are given in Table 5.3. The Lyα shows H I absorption in two components. A Voigt profile fit identifies the two components at $v = -3$ km s^{-1} and $v = -72$ km s^{-1} with the second component being broader having $b(\text{H I}) = 58$ km s^{-1} (BLA). The O VI is kinematically coincident with the $v = -3$ km s^{-1} H I component, as shown by a free fit to the O VI doublet lines. This indicates that the O VI resides in the same gas phase the narrower H I component. The difference in b-parameter between H I and O VI implies a kinetic temperature of $T = 4.6^{+0.3}_{-0.2} \times 10^4$ K for this gas phase.

The broader H I component (BLA) suggests the presence of gas at $T =$

Figure 5.4: Voigt profile models for the $z = 0.41950$ absorber.

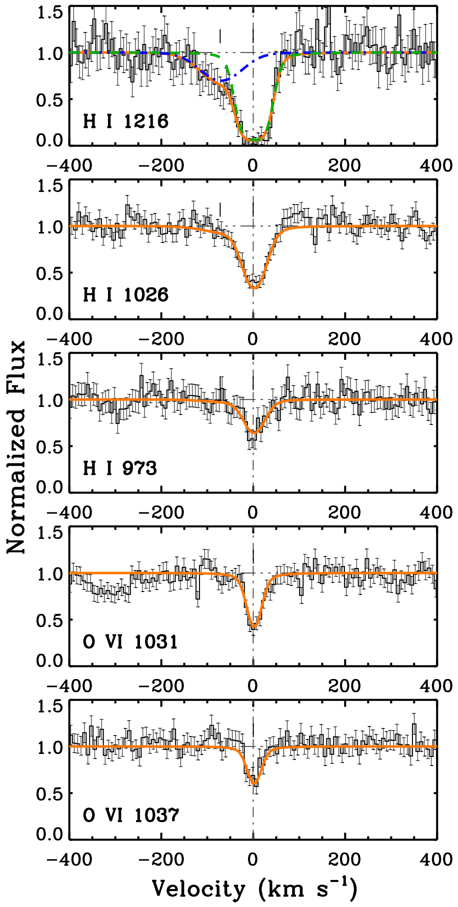

Figure 5.4 Voigt profile models are shown superimposed on the continuum normalized data with 1σ error bars for the $z = 0.41950$ absorber. The location of the components are indicated by the vertical tick marks. The separate components for H I are shown by the blue dash-dot curve and the green dashed curve. At $v = -72$ km s^{-1} is a broad component of H I with $b \sim 58$ km s^{-1} (blue dash-dot line). The orange solid curve superimposed on the Lyman series lines is the composite of the narrow and the broad H I components. As is evident, the broad component's non-detection in the higher order Lyman lines is consistent with its shallow profile seen in Lyα. The O VI coincides in velocity with the narrow strong component of H I. The fit results are given in Table 5.1.

2.1×10^5 K, if the temperature is purely thermal. At the velocity of this BLA, no metal line absorption is detected. The BLA feature is not detected in the higher order Lyman lines which is consistent with its shallow profile in Lyα. The possibility that this feature is a contamination from IGM absorption occuring at

Figure 5.5: KS15 UV background radiation at $z = 0.4$

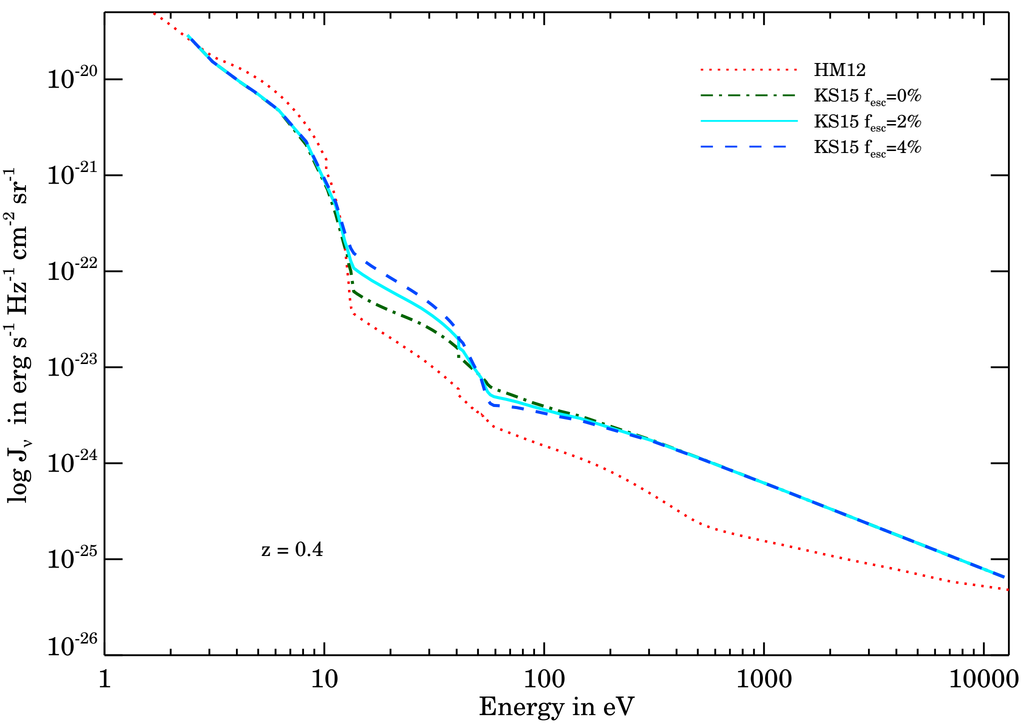

Figure 5.5 The specific intensity of the extragalactic ionizing background radiation for $z = 0.4$. The red dotted curve is the conventional HM12 ultraviolet background. The other curves are the KS15 modeling of the ionizing background which incorporates the more recent measurements on the quasar luminosity function and estimates on escape fraction of Lyman continuum photons from young star forming galaxies. The different curves are for different escape fractions. The trend seen around the He II ionizing edge (54.4 eV), where increasing the escape fraction of photons decreases the intensity of He II ionizing UVB is explained in Khaire and Srianand (2013). Throughout our photoionization modeling, we use the background with $f_{esc} = 4\%$, which will produce the H I photoionization rate required by Kollmeier et al. (2014) to solve the apparent photon underproduction crisis.

another redshift cannot be ruled out, although we have searched and elimited the possibility of absorption associated with the quasar at $z_{QSO} = 0.7475$ occuring at this wavelength.

5.4 Ionization & Abundances in the $z = 0.41614$ Absorber

5.4.1 Photoionized Gas Phase

With the intermediate ions like Si III and C III showing evidence for saturation, there are not enough constraints to develop complete ionization models. We draw only general conclusions about the physical state of the absorber from the photoionization models. The photoionized gas in this absorber is modeled using Cloudy (Ferland et al., 2013b, v13.03). The elemental abundances used are the most recent solar abundances from Grevesse et al. (2010). We model the ionization in the $v \sim -122, -61, -10$ km s^{-1} components of the absorber separately.

It has been pointed out that HM12 ultraviolet background's estimate of the hydrogen ionizing rate at low-z is lower by a factor of $\sim 2-5$ (Kollmeier et al., 2014; Shull et al., 2015; Wakker et al., 2015). KS15 show that this discrepancy is resolved by incorporating in the synthesis of the background spectra, the recent measurements of quasar luminosity function (Croom et al., 2009; Palanque-Delabrouille et al., 2013) and star formation rate densities (Khaire and Srianand, 2015b). Figure 5.5 compares the specific intensity of the HM12 background at $z = 0.4$ with the KS15 model for different escape fractions of Lyman continuum photons. The equilibrium fractions of high ionization species like O VI will be primarily affected by the factor of two increase in the QSO emissivity, whereas the low and intermediate ions will be affected by the enhacement in both galaxy and QSO emissivities. In our photoionization calculations, we use the KS15 ultraviolet background with 4% escape fraction of hydrogen ionizing photons to be consistent with the H I photoionization rate estimates of Kollmeier et al. (2014).

The photoionization model predictions for the $v \sim -122$ km s^{-1} component are shown in Figure 5.6 (left panel). This feature appears adequately resolved and has, among the three components, well determined H I, C III and Si III column densities least affected by saturation. For the observed column density of log N(H I) = 15.82, the photoionization curves of Figure 5.6 show the column density predictions for the different ions at various gas densities. The

Figure 5.6: PIE column density prediction of $z = 0.41614$ absorber

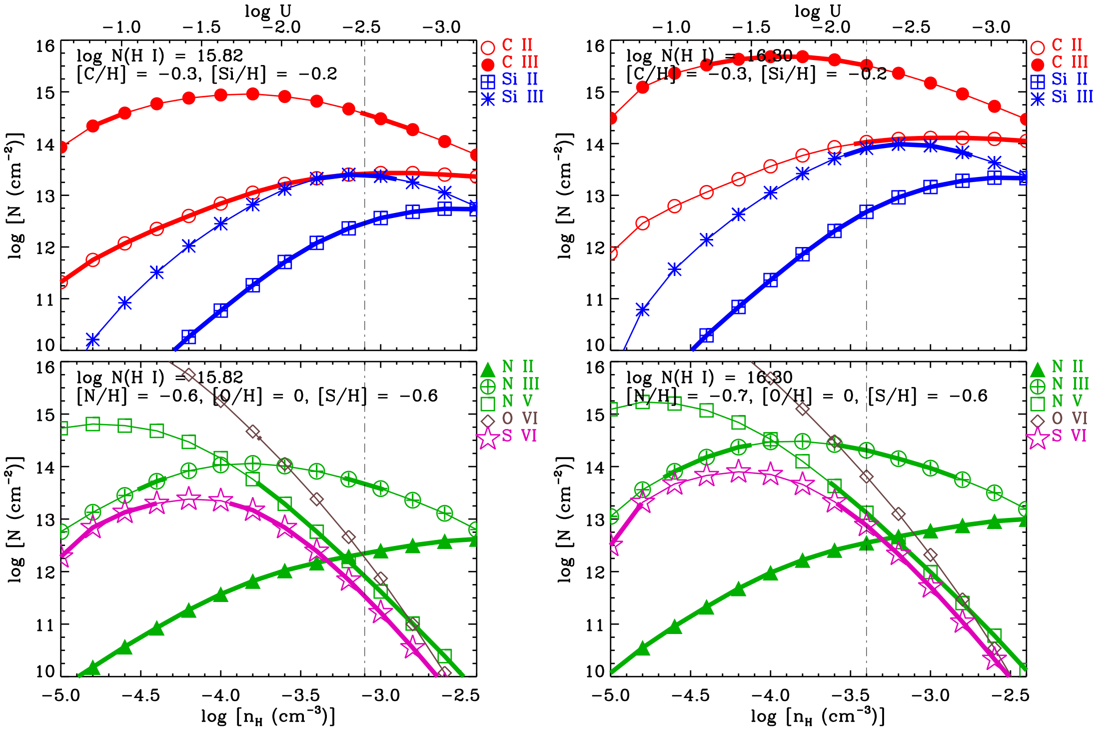

Figure 5.6 Ionic column density predictions from photoionization equilibrium models for the $v = -122$ km s^{-1} (left top and bottom panels), -10 km s^{-1} (right panels) components of the $z = 0.41614$ absorber. For clarity, ionic column density predictions are split into top and bottom panels for each of the three components. The Cloudy models for each component were generated for the respective H I column densities obtained from profile fitting the Lyman series lines. The bottom axis is hydrogen number density, the top axis is the ionization parameter defined as $\log U = \log n_\gamma - \log n_{\mathrm{H}}$, where n_γ is the photon number density at energies greater than 1 Ryd. The ionization is from the extragalactic UV background modeled by KS15. In the models, we assume the solar relative elemental abundances given by Grevesse et al. (2010) as an initial guess and finetuned the abundance to illustrate a most likelier single-phase solution of the absorber.The thick portion of the curves, for each ion, mark the 1σ boundary for the observed column density. For C III and Si III, the uncertainties in column density are comparitively larger due to significant line saturation. The O VI is plotted here for reference. The difference in the velocity sub-structure of O VI from the rest of the ions suggest a different origin for O VI, which is discussed in Sec 5.4.2

Si abundance in this component is constrained to $[\mathrm{Si/H}] \gtrsim -0.2$, below which Si III will be underproduced for all densities. For this lower limit on abundance, the observed Si III and the non-detection of Si II are explained by the models for $n_{\rm H} = (0.4 - 1.3) \times 10^{-3}$ cm^{-3}. A single phase model that is consistent with the observed C III, N III and the upper limits on C II, N II is possibe at $n_{\rm H} \sim 0.8 \times 10^{-3}$ cm^{-3} for [C/H] $= -0.3$ and [N/H] $= -0.6$. The statistical errors in the measured column densities of the metal lines and H I result in a $\pm$ 0.2 dex error to the estimated abundances. For this moderately ionized gas phase, the model predicts a total hydrogen column density of $\log N({\rm H}) = 18.5$, a line of sight thickness of $L = 1.3$ kpc, and $T = 1.1 \times 10^4$ K.

The photoionziation curves for the $v \sim -67$ km s^{-1} is shown in Figure 5.6 (middle panel). The observed Si III for this component is valid for [Si/H] $\gtrsim -0.2$, and $n_{\rm H} = (0.4 - 1.6) \times 10^{-3}$ cm^{-3}. The unsaturated C II provides an estimate for the carbon abundance in this component. For [C/H] $\lesssim -0.2$, C II becomes a non-detection. Thus [C/H] $\gtrsim -0.2$ for $n_{\rm H} \geq 0.4 \times 10^{-3}$ cm^{-3}, densities at which the C II ionization fraction has a maximum. The predicted column densities for the various low and intermediate ions are within the permissible range for $n_{\rm H} \sim 0.8 \times 10^{-3}$ cm^{-3} as shown in Figure 5.6 (middle panel). This model also predicts a $\log N({\rm H}) = 18.6$, $L = 1.6$ kpc, and $T = 1.1 \times 10^4$ K, similar to what we obtain for the $v \sim -122$ km s^{-1} component. The uncertainties in the measured column densities contirbute a 0.6 dex, 0.4 dex and 0.3 dex uncertainty to the derived abundances of C, N and Si respectively.

For the component at $v \sim -10$ km s^{-1}, the abundances for C and Si can be arrived using C II and Si III, but with significant uncertainities of $\sim$ 0.5 dex coming from the statsitical uncertainty in the corresponding H I column density. At [Si/H] $= -0.2$, Si III is explained for $n_{\rm H} = (0.3 - 2) \times 10^{-3}$ cm^{-3} and N III for [N/H] $= -0.7$ with nearly the same density range. The model predicted C II is consistent with the observed value for [C/H] $= -0.3$ and $n_{\rm H} \geq 0.3 \times 10^{-3}$ cm^{-3}. Based on these abundance constrains, a single phase solution for the low and intermediate ions is one where $n_{\rm H} = 0.4 \times 10^{-3}$ cm^{-3}, corresponding to $\log N({\rm H}) =$ 19.4, $L = 18.9$ kpc, and $T = 1.2 \times 10^4$ K (see Figure 5.6, right top and bottom panels).

The difference in velocity sub-structure of O VI with what is seen for C III, Si III and H I clearly precludes the possibility that the O VI ion is tracing this photoionized gas. The O VI prediction for $n_{\rm H} \sim 0.4 \times 10^{-3}$ cm^{-3} of the photoionized gas phase is $\sim$ 0.8 dex lower than the observed value even for solar [O/H]. Furthermore, the O VI from photoionization has a steeply declining dependency with log $n_{\rm H}$ (e.g., see Figure 5.6). This means that for sub-solar oxygen relative abundances, the O VI contribution from this photoionized phase will also come down significantly. The O VI clearly favors an origin in a separate gas phase, which we discuss next.

5.4.2 The Origin of O VI Absorption

The differences in the component structure of O VI from the low, intermediate metal species and the core H I absorption provide the strongest indication that the O VI could be from a phase other than the $T \sim 10^4$ K photoionized gas. The O VI is consistent with having the same origin as the BLA discussed in Sec 5.3.1. The temperature of this gas phase follows from the large line width of H I compared to O VI. The separate b-values of $b(\text{H I}) = 115^{+17}_{-19}$ km s^{-1} and $b(\text{O VI}) = 48 \pm 2$ km s^{-1} imply a temperature of $T = 7.1^{+2.7}_{-2.6} \times 10^5$ K, with thermal broadening of $b_t(\text{H I}) \sim 108$ km s^{-1} and $b_t(\text{O VI}) \sim 40$ km s^{-1}. Whereas for the O VI, the thermal and non-thermal contributions to line broadening are almost equal, for the BLA, 94% of the line broadening is due to the high temperature of the gas. At these high temperatures, the ionization will be dominated by collisions.

Figure 5.7 shows Gnat and Sternberg (2007) collisional ionization equilibrium (CIE) model predictions for O VI at various kinetic temperatures. The column density of H I in these models is the BLA column density of $\log N(\text{H I}) = 14.02$. For the CIE models to match the observed O VI at $T = 7.1 \times 10^5$ K, the oxygen abundance has to be $[\text{O/H}] = -0.3 \pm 0.2$ dex. For higher metallicity, O VI is overproduced for this equilibrium temperature, and for lower metallicity it is underproduced. However, as we describe in the next paragraph, models that simultaneously consider photoionization and collisional ionization scenarios favor lower oxygen abundance considering realistic values for the size of the warm gas.

At $T = 7.1 \times 10^5$ K, the CIE conditions predict a very low neutral hydrogen ionization fraction of $f(\text{H I}) = N(\text{H I})/N(\text{H}) = 3.7 \times 10^{-7}$. This suggests a total

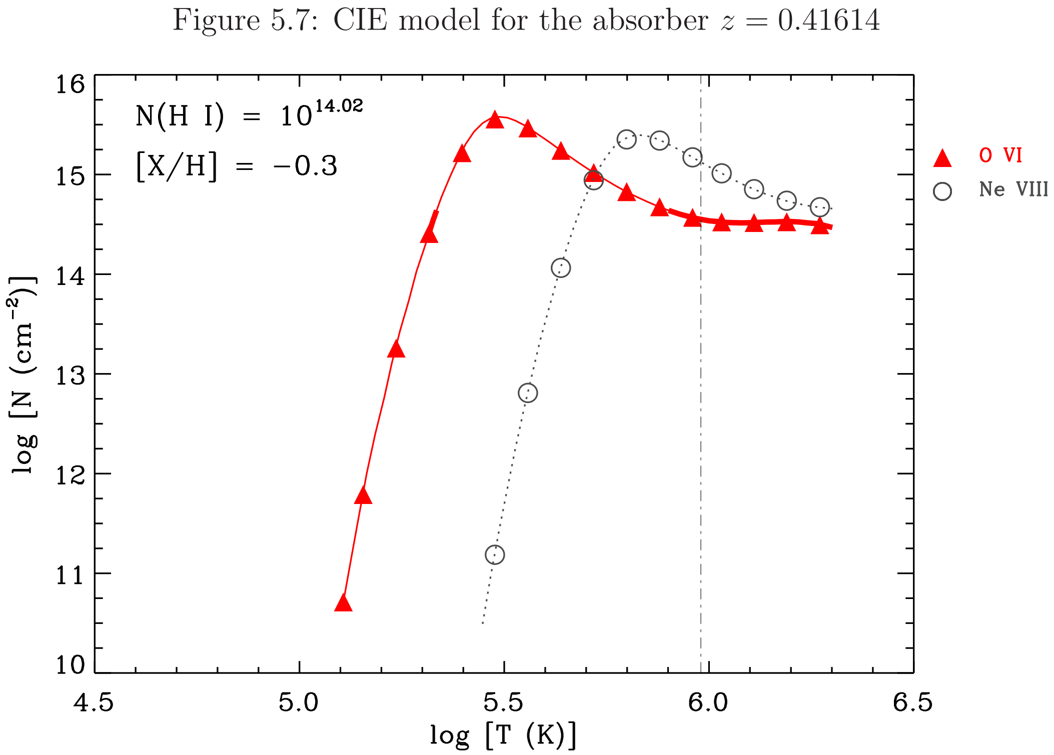
Figure 5.7: CIE model for the absorber $z = 0.41614$

Figure 5.7 Gnat and Sternberg (2007) CIE model for the H I column density measured for the BLA in the $z = 0.41614$ absorber. The veritcal dash-dotted line is at $T = 7.1 \times 10^5$ K, obtained from solving for the temperature using the b(H I) from the BLA and b(O VI). The [O/H] $= -0.3$ dex is set by the need to recover the observed N(O VI) at the given temperature of the gas. The Ne VIII is shown just for comparision, as it is a frequently sought after tracer of warm-hot gas. Both oxygen and neon are modeled for half solar abundance.

hydrogen column density of $N(\mathrm{H}) = 2.8 \times 10^{20}$ cm^{-2}, which is a factor of ~ 10 more than the total hydrogen column density in the cooler photoionized gas. At $T > 3 \times 10^5$ K, the recombination and cooling rates are comparable, with no differences between the equilibrium and non-equilibrium collisional ionization fraction predictions for metals (Sutherland and Dopita, 1993). The large baryon content in the O VI gas phase, compared to the strongly absorbing neutral gas, supports the view held by Fox et al. (2013); Lehner et al. (2013) that a proper accounting of the warm O VI phase can double the contribution of such partial/Lyman limit systems (log N(H I) $\sim 16.1 - 16.7$ dex) towards the cosmic baryon budget.

Even when the ionization in the gas is dominated by collisions, the presence of extragalactic background photons cannot be overlooked. By including the UV ionizing background while keeping the temperature of the gas fixed to $T = 7.1 \times 10^5$ K in Cloudy, we generated hybrid models that simultaneously allow for collisional and photoionization reactions. The hybrid models show that for $n_{\rm H} \gtrsim 10^{-5}$ cm^{-3}, the ionization fractions of the various elements are predominantly controlled by collisions. Above that limit, the O VI ionization fraction shows only a weak dependancy on density. For densities below this limit, photoionization begins to alter the ion fractions from the pure collisional predictions. At $n_{\rm H} \sim 10^{-5}$ cm^{-3}, the hybrid models require a thickness of $\sim$ 4 Mpc for the absorber, an exceedingly large value which is difficult to reconcile with the kinematically simple, single component absorption profile of O VI and the BLA. Thus, very low densities of $n_{\rm H} \lesssim 10^{-5}$ cm^{-3} for the BLA - O VI gas phase can be ruled out. The premise that the absorbing cloud should have a realistic size serves as a constrain on the [O/H] in the hybrid model. For [O/H] $\lesssim -0.6$ dex, the observed N(O VI) is produced for $n_{\rm H} \geq 3 \times 10^{-4}$ cm^{-3} corresponding to N(H) $\leq 2.5 \times 10^{20}$ cm^{-2} and $L \leq 260$ kpc. The 1σ range for the temperature of this warm gas and the associated BLA H I column density, result in an uncertainty in the oxygen abundance of $\sim$ 0.2 dex. But the conclusion from CIE, that the BLA - O VI phase possesses a factor of $\sim$ 10 more baryons than the moderately ionized gas, is valid for the hybrid ionization scenario as well.

We note that the Ne VIII from the collisionally ionized warm gas will be stronger than O VI at the predicted temperature of $T = 7.1 \times 10^5$ K, for [Ne/H] $\sim$ [O/H]. The absorber could have been a candidate for Ne VIII detection, but the incidence of a Lyman limit absorber at $z = 0.31$ leaves little flux at $\lambda < 1200$ Å. The properties of the warm gas, nevertheless, are consistent with the general physical state of Ne VIII absorbers given by both observations and simulations (Tepper-García et al., 2013).

5.5 Ionization & Abundances in the $z = 0.41950$ Absorber

The kinetic temperature $T = 4.6^{+0.3}_{-0.2} \times 10^4$ K, measured by the narrow H I and O VI line widths is consistent with temperature of the gas being driven by photoionization. At these temperatures, electron impacts will not contribute significantly to the ionization of H I or metals and hence collisional ionization can be

Figure 5.8: PIE model for $v = -3$ km s^{-1} component in $z = 0.41950$ absorber

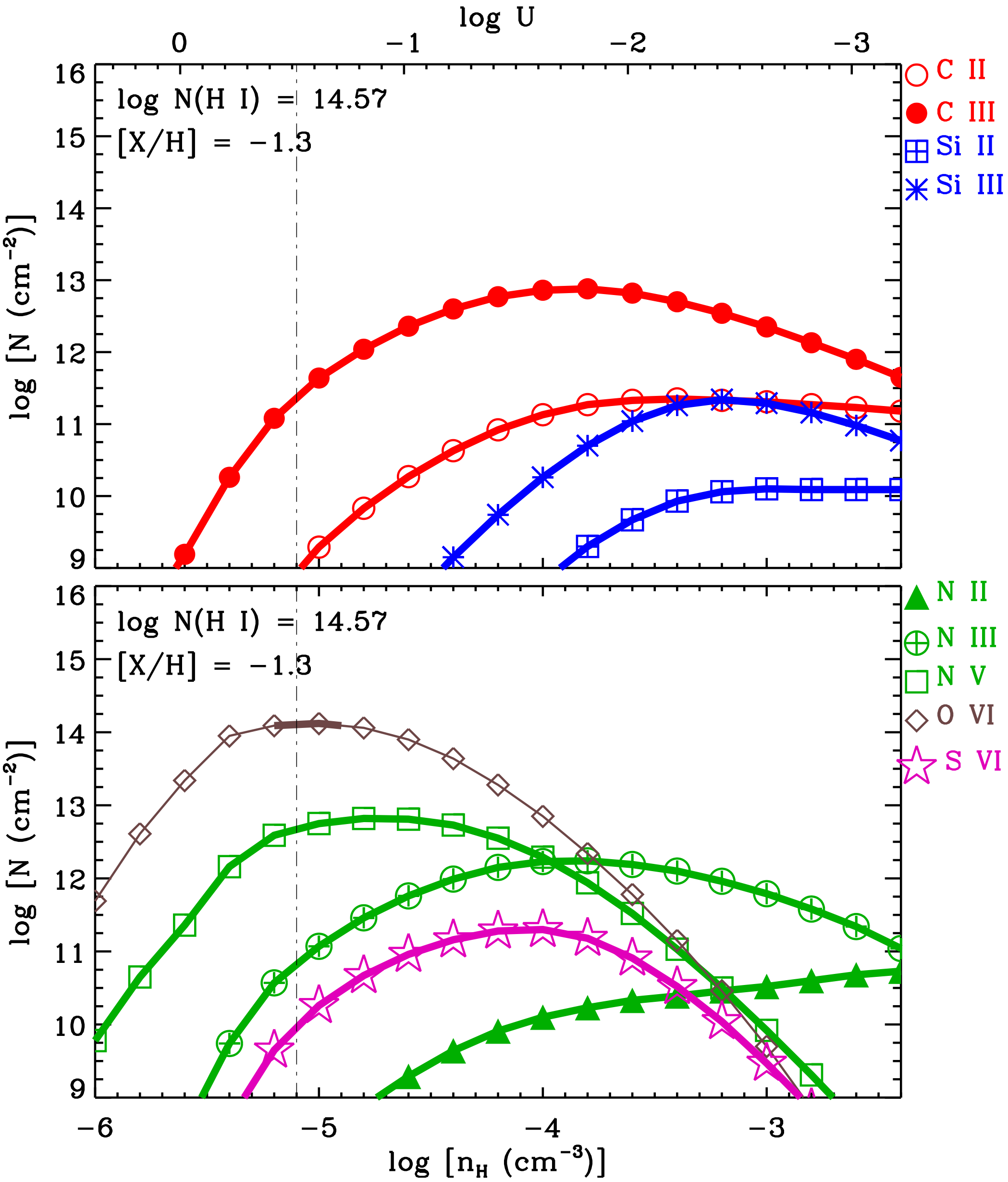

Figure 5.8 Column density predictions from photoionization equilibrium models for the $v = -3$ km s^{-1} H I - O VI absorber at $z = 0.41950$. For clarity, the model predictions for the different ions are split into top and bottom panels. The thick portion of the curves mark the 1σ boundary for the observed column density. Except O VI, all other metal lines are non-detections. The dash-dot line indicates the ionization parameter at which O VI is reproduced by the models simultaneously being consistent with the upper limits for the rest of metal ions.

neglected. Figure 5.8 shows the photoionization models for the narrow H I - O VI cloud when irradiated by the KS15 ionizing spectrum. The observed N(O VI) allows us to impose a lower limit on the oxygen abundance. For [O/H] ≤ -1.3 dex, O VI is underproduced for all densities. The photoionziation models of Figure 5.8 are for this metallicity lower limit for oxygen. At that limiting abundance, the required O VI is produced for $n_{\rm H} = 7.9 \times 10^{-6}$ cm^{-3}. Such low densities would result in large path lengths of $L = 2.5$ Mpc. Over a megaparsec scale it is common to expect discrete velocity and ionization substructures in the absorbing cloud. Given the simple Gaussian like optical depth profile of O VI and the narrow H I, it is unlikely that the absorption is happening across such vast length scales. The O VI can come from clouds of smaller size, provided the densities are higher. As the photoionization curves show, O VI has a steep dependency on density. Hence higher density photoionziation solutions would also require higher oxygen abundances. For example, at [O/H] ~ -1.0 dex, the observed N(O VI) is recovered from $n_{\rm H} = 2.5 \times 10^{-5}$ cm^{-3}, tracing a total baryonic column of N(H) $= 1.3 \times 10^{19}$ cm^{-2} over a significantly smaller cloud thickness of $L = 129$ kpc. The above gas phase is consistent with the upper limits from the non-detection of N II, N III, N V, Si II, Si III and S VI for the 1/10th solar metallicity. The photoionization predicted temperature of $T = 4.1 \times 10^4$ K also agrees with the line widths of H I and O VI. Such higher density solutions require departures from solar [C/O] if the models are to be consistent with the absence of C III from the same gas phase. For example at a metallicity of -0.5 dex, the [C/O] ~ -0.3 dex for the C III to be a non-detection. Significant variation in [C/O] abundance would require a different nucleosynthesis enrichment history, as both C and O are primary elements synthesized by massive stars. Such lower abundances of C to O are seen for higher column density H I systems like DLAs and LLSs (Lehner et al., 2013; Dutta et al., 2014). Assuming [C/O] of solar, the constraint on oxygen abundance will be $-0.7 \lesssim$ [O/H] $\lesssim -1.3$ dex.

The ionization and physical conditions in the $v \sim -72$ km s^{-1} cloud is less precisely determined given the absence of any metal lines to go with the broad H I. Photoionization models for the estimated column density of log[N(H I)] = 13.48 show that abundances [X/H] ≤ 0 and densities of $n_{\rm H} < 5 \times 10^{-5}$ cm^{-3} satisfy the upper limits on the metal ion column densities. The model predicted gas temperature of $T = 2 \times 10^4$ K would imply that $\sim 70\%$ of the H I line width is due to non-thermal broadening.

Alternatively, if $b(\text{H I}) = 58 \pm 6$ km s^{-1} is pure thermal broadening, the corresponding temperature will be in the range $T = (1.7 - 2.5) \times 10^5$ K. Contributions from turbulence in the gas, along with Hubble broadening ($b_{\text{Hubble}} < 30$ km s^{-1} typically for $\sim$ kpc structures, Valageas, Schaeffer, & Silk 2002) would result in lower temperatures. Given the lack of information to resolve the mechanisms contributing towards line broadening, the temperature estimated can be considered as an upper limit. At $T = 2 \times 10^5$ K, if collisional processes are dominating the ionization in the gas, then the total baryon column density in the broad component will be $N(\text{H}) = 3 \times 10^{19}$ cm^{-2}, assuming CIE fractions (Gnat and Sternberg, 2007). The total gas content in this shallow and broad H I component thus comes out as an order of magnitude more than the amount of baryons present in the kinematically adjacent photoionized gas phase of the absorber. AT $T = 2 \times 10^5$ K, the column density limit from non-detection of log $N(\text{O VI}) < 13.3$ dex, places an upper limit of $[\text{O/H}] < -0.8$ dex in the collisionally ionized gas.

Hybrid models suggest that for O VI to be a non-detection at $T = 2 \times 10^5$ K, the oxygen abundance in the BLA gas phase has to be $[\text{O/H}] < -0.7$, which is consistent with the corresponding upper limit in the kinematically adjacent H I - O VI cloud. For $[\text{O/H}] < -0.7$, density is $n_{\text{H}} \lesssim 3 \times 10^{-3}$ cm^{-3}, $N(\text{H}) > 10^{19}$ cm^{-2} and $L > 1$ kpc.

Table 5.5: Galaxies in the vicinity of the absorbers

R.A.	Dec.	z_{gal}	Δv (km s^{-1})	η (arcmin)	ρ (Mpc)	g (mag)	M_g	$(L/L^*)_g$
$z_{abs} = 0.41614$ ($v = 0$ km s^{-1}) Absorber								
150.14156	59.72934	0.41437	-376 ± 21	3.6	1.2	20.97 ± 0.09	-20.08	0.91
150.42517	59.73372	0.41303	-659 ± 16	5.0	1.7	20.49 ± 0.06	-20.56	1.42
150.43219	59.81284	0.42062	$+947 \pm 15$	6.9	2.3	21.04 ± 0.07	-20.02	0.87
150.15218	59.61503	0.41422	-406 ± 17	8.0	2.7	20.76 ± 0.10	-20.29	1.11
150.20506	59.43657	0.41189	-901 ± 18	18.1	6.0	20.85 ± 0.09	-20.20	1.02
150.88540	60.04693	0.41456	-334 ± 21	26.4	8.8	20.77 ± 0.06	-20.28	1.10
149.66518	60.11736	0.41496	-249 ± 17	28.9	9.6	20.97 ± 0.05	-20.08	0.91
$z_{abs} = 0.41950$ ($v = +710$ km s^{-1}) Absorber								
150.43219	59.81285	0.42062	$+236 \pm 14$	6.9	2.3	21.04 ± 0.07	-20.08	0.91
149.66516	60.11746	0.41497	-959 ± 16	29.0	9.7	20.97 ± 0.06	-20.08	0.91

Table 5.5 Comments. - Galaxies within 30 arcminute of projected separation and within $|\Delta v| = 1000$ km s^{-1} of the absorbers. The z values are SDSS spectroscopic redshifts. Δv correspond to the systemic velocities of the galaxies with respect to the absorber. The error in velocity separation comes from the uncertainty in the spectroscopic redshift. The projected separation ρ was calculated from the angular separation assuming a ΛCDM universe with parameters of $H_0 = 69.6$ km s^{-1} Mpc^{-1}, $\Omega_m = 0.286$, $\Omega_\Lambda = 0.714$ (Bennett et al., 2014). The absolute magnitude was calculated using the distance modulus expression M $-m = -41.05$ using a luminosity distance of $d = 1623.2$ Mpc for $z = 0.42$ (Wright, 2006). The Schechter absolute magnitude $M_g^* = -20.177$ for $z = 0.4$ was taken from Ilbert et al. (2005). The distribution of galaxies near the $z = 0.41614$ absorber is shown in Figure 5.9.

5.6 Galaxies Near the Absorber

The SBS0957+599 sightline is along the SDSS footprint. We searched the DR12 SDSS database for galaxies proximate to the absorbers. Within $|\Delta v| = 500$ km s^{-1} velocity separation and $30' \times 30'$ ($\sim$ 10 Mpc) projected separation of the $z = 0.41614$ absorber are four galaxies with SDSS spectroscopically determined redshifts. The galaxy distribution at the location of the absorber is shown in Figure 5.9 and their information summarized in Table 5.4. The nearest galaxy with a spectroscopic redshift is at a projected separation of 1.2 Mpc from the absorber. This 0.91 $L*$ galaxy has an extended morphology and an emission line spectrum. The flux at Hα is $f_{\mathrm{H}\alpha} = 14.3 \times 10^{-17}$ erg cm^{-2} s^{-1}. Using the conversion factor given by Kennicutt et al. (1994), we estimate a star formation rate of SFR(Hα) $=$ 0.7 M$_\odot$ yr^{-1}, typical of normal galaxies. The scaling relation $R_{\mathrm{vir}} = 250\ (L/L*)^{0.2}$ kpc given by Prochaska et al. (2011) yields a virial radius of $R_{\mathrm{vir}} \sim 245$ kpc for this galaxy. The separation of the galaxy from the line of sight is a factor of $\sim$ 5 larger than this. Given this wide separation and the low SFR, it is unlikely that the absorber has an origin in gas bound to the galaxy. The impact parameters of the other three galaxies range from $\sim 3 - 10$ Mpc. These four galaxies have a narrow velocity dispersion of $\sim$ 59 km s^{-1} and an average velocity of ~ -342 km s^{-1} with reference to the absorber. Three more galaxies are seen by SDSS with their spectroscopic redshifts within 1000 km s^{-1} and 10 Mpc projected separation. The SDSS database show four additional galaxies with photometrically confirmed redshifts that place them within $|\Delta v| = 500$ km s^{-1} and $\rho = 5$ Mpc distance of the absorber. The projected distance to the nearest galaxy is $\sim$ 1.9 Mpc. The errors associated with the photometric redshifts are $\delta z/z \sim 0.03 - 0.3$, which allow for uncertainties of $\sim 10^3 - 10^4$ km s^{-1} in the systemic velocities of these galaxies. In any case, the preponderance of galaxies suggests that the environment is one of galaxy groups, with the absorption tracing gas near to 1 Mpc of this group.

There is only one galaxy with spectroscopic redshift within $\Delta v = 500$ km s^{-1} of the $z = 0.41950$ absorber, but at a large impact parameter of 2.3 Mpc (see Table 5.4). The galaxy shows an emission line dominated spectrum with $f_{\mathrm{H}\alpha} = 131.1 \times 10^{-17}$ erg cm^{-2} s^{-1}. The corresponding SFR(Hα) $=$ 6.7 M$_\odot$ yr^{-1} (Ken-

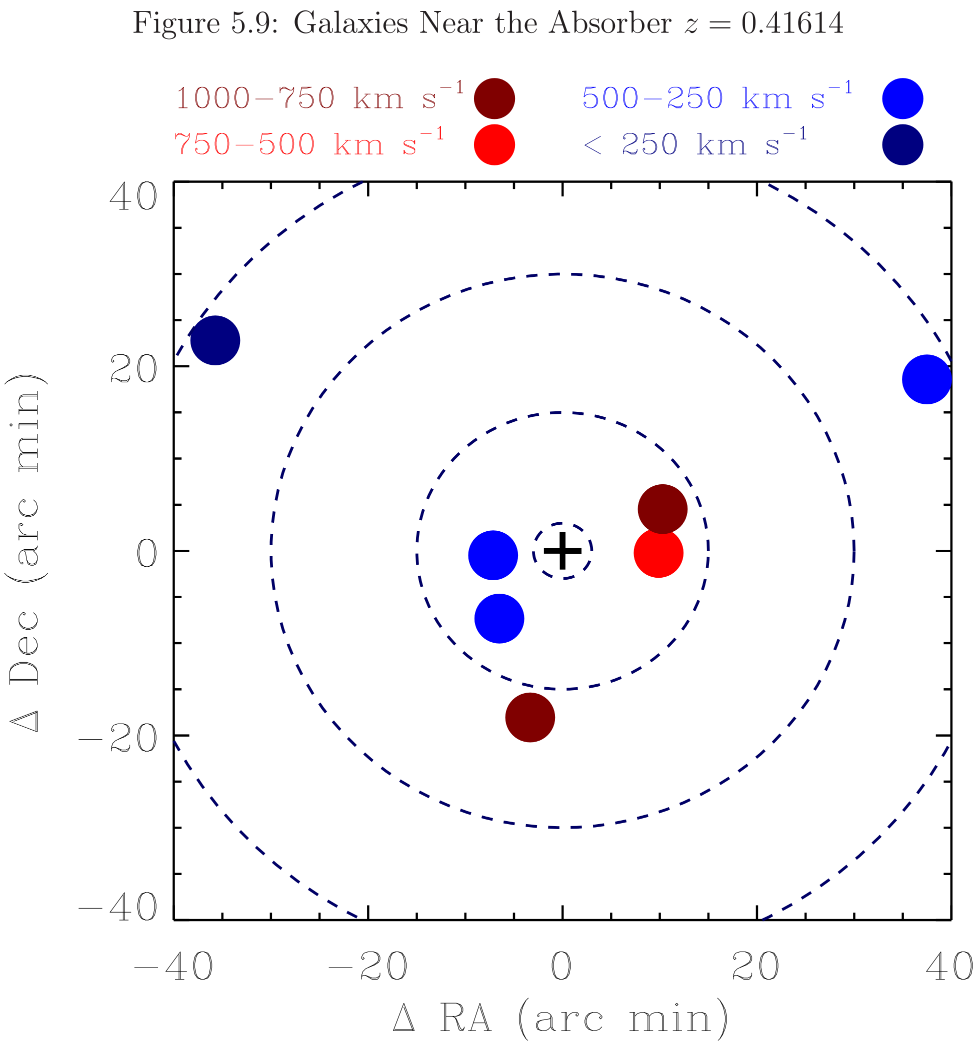

Figure 5.9 The distribution of galaxies with spectroscopically confirmed redshifts that place them within $|\Delta v| = 1000$ km s^{-1} and projected separation of ~ 10 Mpc from the $z = 0.41614$ absorber. The "+" sign corresponds to the line of sight towards the background quasar. Further information on these galaxies is given in Table 5.4. The multiphase absorber seems to be residing in a galaxy group environment.

nicutt et al. 1994) indicates that the galaxy is moderately star-forming. One additional galaxy with spectroscopic redshift is present at $\rho = 9.7$ Mpc and at 1000 km s^{-1} of the absorber. Given the velocity offsets between the absorber and the galaxies and the large impact parameters, the likelihood of the line of sight tracing the gaseous envelope of either galaxy is negligible. We note that there are three more galaxies with photometric redshifts within 500 km s^{-1} and $\rho < 5$ Mpc of the absorber. The nearest of these galaxies is at 2.2 Mpc impact parameter. However, the photometric redshift errors signficiantly extend the uncertainty in the velocity offset of these galaxies with the absorber.

5.7 On The Origin of the Absorbers

Surveys that explore the association between galaxies and absorbers find a wide spatial distribution for O VI around galaxies compared to low ionization metal lines (Wakker and Savage, 2009; Prochaska et al., 2011; Tumlinson et al., 2011b; Stocke et al., 2014). In regions where multiple galaxies co-habit, there is an ehnancement in the covering fraction of O VI, with detections extending out to impact parameters which are as much as ~ 3 times the halo virial radii of the nearest galaxies (Johnson et al., 2015; Mathes et al., 2014). Such an enhancement is not found for the cooler ($T \sim 10^4$ K), dense ($n_{\rm H} \sim 10^{-3}$ cm^{-3}) gas probed by C II, Si II, Mg II and similar low ionization lines. This environmental dependence is reflected in the absorbers discussed here. In the $z = 0.41950$ absorber, we find evidence only for high ionization gas, which is consistent with the relatively sparse density of $\sim L^*$ galaxies close to the line of sight. In comparison, the $z = 0.41614$ absorber, with its mix of low and high ionization gas, is residing within a few Mpc of an overdense region of space. The trend is predictable, as galaxy interactions, ram-pressure stripping and similar environmental effects are pathways by which multiphase ISM can be dragged to large separations from galaxies.

The galaxies identified by SDSS are at $\rho > 1$ Mpc of either absorbers. Furthermore, they are all luminous $\sim L*$ galaxies. As the $z = 0.41614$ absorber is a partial Lyman limit system with log N(H I) ~ 16.6 dex, one may wonder whether the magnitude limited observations of SDSS has missed fainter galaxies closer to this absorber, but below the survey's completeness limit (95% completeness for $g < 22.2$, corresponding to $L > 0.3\ L^*$). This remains a possibility, although uncertain in the light of some recent results. From studying a sample of 14 galaxies that lie within $\rho \sim 3\ R_{vir}$ of background quasars, Mathes et al. (2014) find a significantly lower incidence of O VI around low mass halos ($\sim 10^{11.5}$ M$_\odot$). The frequency of O VI detections near low mass galaxies suggest a fairly large escape fraction of $\sim 65\%$ for halo gas, compared to a modest $\sim 5\%$ from high mass halos (Mathes et al., 2014). Thus, low mass galaxies may not retain much of O VI bearing outflows. But the possibility still remains that the $z = 0.41614$ O VI - partial Lyman limit absorber, though no longer dynamically linked to any galaxy, could still be a result of the nearby IGM getting preferentially enriched with outflowing gas, or tidally stripped material from a closer-by fainter galaxy unidentified by SDSS.

Based on models of structure formation, it has been hypothesized that galaxy groups can have intragroup gas at $T \sim 10^5 - 10^6$ K, temperatures too low to discrimate their emission from the soft X-ray background (Mulchaey et al., 1996). Presently, such a medium can be probed only through high ionization absorption lines such as O VI, Ne VIII and thermally-broad Lyα against the light from background QSOs. It is important to explore this gas reservoir, as it potentially harbours as much as $\sim$ 4% of the total baryons in the low-z universe, on a par with the fraction of baryons trapped inside galaxies (Savage et al., 2014). A recent example is given by Stocke et al. (2014) where their sample of BLA - O VI warm absorbers are likely to be from intragroup gas than individual galaxy halos. The warm O VI is hypothesized to arise in conductive interface layers between cold $T \lesssim 3 \times 10^4$ K clouds and a hitherto undetected diffuse $T \sim 10^{6.5}$ K intragroup medium.

Hydrodynamic simulations also predict that a substantial fraction of baryons are to be found along large scale filaments networking galaxy overdensity regions. In Narayanan et al. (2011b), a BLA - O VI absorber is identified as tracing $T \sim 1.4 \times 10^5$ K intergalactic gas along a nearby ($v_{\mathrm{HELIO}} = 3081$ km s^{-1}) galaxy filament, with several loose groups of galaxies beyond $\rho \sim 1.5$ Mpc of projected separation. More examples of baryonic reservoirs along galaxy filaments is given by Wakker et al. (2015). About 85% of the Lyα systems from their sample of 15 absorbers, which includes BLAs and multi-component systems, appear to be tracing intergalactic filament gas that are beyond 1.5 Mpc of the virial radii of the nearest galaxies that trace the filament.

The absorbers studied here are also consistent with an intragroup origin or gas associated with a much larger galaxy filament. The O VI and the associated BLA in the $z = 0.41614$ system can be produced by collisional process at the interface layers between the photoionized gas phase and a hot exterior medium. In the case of the $z = 0.41614$ system, the photoionized gas could be recycled material from earlier epochs of galaxy outflows or interactions within the group environment, as proposed for metal rich ($[\mathrm{X/H}] \gtrsim -0.3$) Lyman limit systems (Lehner et al., 2013). A conductive interface model (Boehringer and Hartquist, 1987) would also explain the kinematic differences between the profiles of O VI and low ions since the two gas phases are not co-spatial (Sembach et al., 2003; Fox et al., 2004, 2005, 2013). The O VI in the $z = 0.41950$ system is likely produced in a low density medium that is predominantly photoionized. However, even in this latter case, the BLA could be transition temperature plasma, with metallicity so low to have little O VI.

5.8 Summary

This chapter discuss the physical conditions in two intervening multiphase O VI absorbers at $z = 0.41614$ and $z = 0.41950$, separated from each other by $\Delta v =$ 710 km s^{-1}. Both absorbers are detected in the COS spectrum of the background quasar SBS 0957 + 599 and they show clear evidence for the presence of gas with $T \sim 7 \times 10^5$ K and $T \lesssim 2 \times 10^5$ K respectively. Our main conclusions are :

1. The $z = 0.41614$ absorber has C III, Si III and H I showing similar multi-component absorption profiles. In comparison, O VI has a kinematically simple component profile, indicating an origin distinct from the low and intermediate ionization metal lines.

2. The C II, C III, Si II, Si III, N II and N III in the $z = 0.41614$ system are consistent with cool photoionized clouds of $T \sim 4 \times 10^4$ K having densities of $n_{\rm H} \sim 0.4 \times 10^{-3}$ cm^{-3}, total hydrogen column densities of $N({\rm H}) \sim 3 \times 10^{19}$ cm^{-2} with absorption happening over path lengths of $\lesssim 20$ kpc. This gas phase has elemental abundances of [C/H] ~ -0.3 dex, [Si/H] ~ -0.2 dex, [N/H] $\lesssim -0.7$ dex and [S/H] $\lesssim -0.6$ dex, with uncertainties of ± 0.4 dex.

3. There is a BLA component to the H I absorption with log $N({\rm H\ I}) = 14.02 \pm 0.23$ dex and $b({\rm H\ I}) = 115^{+17}_{-19}$ km s^{-1}, revealing the presence of a warm medium. The BLA and O VI are consistent with origin from the same gas phase. The widths of the H I and O VI lines solve for $T = 7.1 \times 10^5$ K, a temperature too hot for any of the low or intermediate ionization species to survive. Under pure collisional ionization, this warm phase has [O/H] $= -0.3 \pm 0.2$ dex

and traces a substantial baryonic column of $N(\mathrm{H}) = 2.8 \times 10^{20}$ cm^{-2}. The amount of baryons present in this warm medium is a factor of 10 higher than the cooler photoionized gas where the H I column density is ~ 2.5 dex higher. Hybrid models that simultaneously allow for photoionzation and collisional ionization favor a lower abundance of $[\mathrm{O/H}] \lesssim -0.6$ dex set by constraints on the size of the absorber.

4. The $z = 0.41950$ absorber is detected only in H I and O VI. The Lyα profile shows the presence of a shallow, broad component and a stronger, narrow component offset from each other by ~ 70 km s^{-1}. The O VI does not show any evidence for sub-structure and is kinematically centered on the narrow H I component. The b(H I) and b(O VI) indicates $T = 4.6^{+0.3}_{-0.2} \times 10^4$ K where collisional ionization is not important. The O VI permits photoionization at low-densities of $n_{\mathrm{H}} \sim 10^{-5}$ cm^{-3}, $-0.7 \lesssim [\mathrm{O/H}] \lesssim -1.3$ dex, baryonic column densities of $N(\mathrm{H}) \sim 10^{19}$ cm^{-2} and line-of-sight thickness of $L \sim$ 130 kpc.

5. The BLA in the $z = 0.41950$ absorber has a $b(\mathrm{H\ I}) = 58 \pm 6$ km s^{-1} suggesting $T = (1.7 - 2.5) \times 10^5$ K for pure thermal broadening. The temperature supports collisonal ionization in gas with baryonic column densities of $N(\mathrm{H}) \lesssim 3 \times 10^{19}$ cm^{-2}. The oxygen abundance in this warm gas phase is constrained (from the non-detection of coincident O VI) to $[\mathrm{O/H}] < -0.8$ dex, if collisions are dominating the ionization in this medium.

6. From the SDSS database of extended sources with a 95% completeness at $L > 0.3L^*$, we find that there are four spectroscopically confirmed galaxies within 30 arcminute and $|\Delta v| = 500$ km s^{-1} velocity of the $z = 0.41614$ absorber. The nearest galaxy is at a projected separation of 1.2 Mpc. The narrow velocity dispersion of ~ 59 km s^{-1} between the four galaxies indicate that the absorber is tracing gas associated with a galaxy overdensity environment. There are three additional spectroscopically confirmed galaxies within 1000 km s^{-1} of the absorber. The nearest luminous source to the $z = 0.41950$ is a moderately star-forming disk galaxy whose systemic redshift places it at 235 km s^{-1} and 2.3 Mpc impact parameter. In either case, the absorption appears to be tracing multi-phase intragroup gas rather than

the virialized envelope of any galaxy.

7. Analysis of the two absorbers highlights the diverse ionization conditions as well as the physical environment in which O VI absorption arises. The metal species cannot be used as a blind tracer of $T \sim 10^5 - 10^7$ K gas. In multi-phase absorbers such as those presented here, the O VI data has to be interpreted in the light of additional information from thermally broad Lyα or more highly ionized species like Ne VIII or Mg X to discriminate the predominant ionization process.

CHAPTER 6

Detection of Ne V Absorbers at High Redshift IGM

6.1 Introduction

The study of the physical conditions of gas in IGM were mostly based on the far ultra-violet observations of C II, Si II, C IV, Si IV, O VI, Mg II and Ne VIII ions. In this chapter, we will discuss the detection of a new species Ne V in absorption.

Neon is the most abundant metal in the universe after carbon, oxygen and helium. Hence, the detection of their ions from different ionization states can give valuable insights to determine the physical conditions of IGM. For example, the highly ionized Ne VIII detections in IGM is to date the most successful method in finding warm hot baryons in the universe. Ne V is a moderate ion with moderate ionization potential (97 eV) which can arise in a gas which is photoionized as well as collisional ionized much like O VI ion.

The rest wavelength of Ne V is 357.67 Å and is not accessible at $z < 1$ for any FUV observations. Ne V transitions can be detected from gas at $z > 2.2$ using FUV spectra obtained with COS (Cosmic Origin Spectrograph) spectrum. The only Ne V absorption reported so far in IGM is at redshift $z = 1.1912$ towards LBQS $1435 - 0134$ where the absorber consists of highly ionized metal lines such as O VI, Ne VIII, Mg X along with Ne V, Ne VI transitions from a shock-heated warm-hot gas (Qu and Bregman, 2016). This makes the detection of Ne V an interesting case to study from a warm - hot baryonic perspective. In this chapter, we will discuss the five Ne V absorbers at redshift $z = 2.7356$, 2.4382, 2.3475, 2.4887 and 2.6910 detected in COS spectrum towards the quasar sightline HE $2347 - 4342$ ($z_{em} = 2.885$). We measure column densities of different species associated with these absorbers using high-resolution optical spectra obtained with VLT/UVES, HST/COS and KECK/HIRES. Using different ionisation modelling, we constrained the physical properties of each of these absorbers.

Table 6.1: Individual COS integrations for the quasar HE2347-4342

MAST ID	DATE	GRATING	λ_c (Å)	t (S)
LB6D02030	05 -11-2011	G130M	1291	8265
LB6D02040	05 -11-2011	G130M	1300	5962
LB6D03030	05 -11-2011	G130M	1291	8270
LB6D03040	05 -11-2011	G130M	1300	5962
LC8I01010	08 -07-2014	G130M	1222	14814
LC8I02010	28 -08-2014	G130M	1222	11767
LC8I03010	12 -07-2014	G130M	1222	14814

Table 6.1 Table show the details of individual exposures used to generate the final spectra. The column from left to right corresponds to the name of the exposure in MAST database, date of the observation, grating used for the observation, central wavelength of the grating and the exposure time respectively.

6.2 Observations

6.2.1 VLT-UVES and KECK-HIRES

The optical spectra of HE 2347 − 4342 ($z_{em} = 2.885$) from VLT UV Echelle Spectrograph is the primary data used in this analysis. The data is obtained as a part of the programme 'The Cosmic Evolution of the IGM' (Bergeron et al., 2004). The RAW data were reduced using UVES pipeline available as a dedicated context of MIDAS data reduction software (Ballester et al., 2000). The pipeline performs a precise inter-order background subtraction for science frame and master flat fields, apply optimal extraction to retrieve the object signal, rejecting cosmic ray impacts and performing sky subtraction at the same time. The correction in wavelength is performed using the standard conversion equations (Edlen, 1966; Stumpff, 1980). The observation used 2 × 2 binning mode yields a binned pixel size of 2 - 2.4 km s^{-1}. The spectra can achieve signal to noise of 30 -40 per pixel at 3300 Å and 60 - 70 per pixel at 5500 Å respectively. A resolution of 45,000 corresponds to a full width at half maximum (FWHM) of 6.6 km s^{-1} is possible in the entire wavelength range of the spectra. The final spectra cover a wavelength range of $3000 - 10000$ Å with occasional breaks. The break in the spectra within the wavelength $5755 - 5835$ Å is covered with the spectra of the same source from KECK/ HIRES observations.

The 10 m KECK telescope with high-resolution echelle spectrometer (HIRES) has resolution $R = 37,000$ while using a slit size of 1.14×7. The spectra of the source with 6.67 hr observation (Songaila, 1998) given a total signal to noise of 130 is used to cover the spectral gap in UVES observation. The data reduction techniques and extraction techniques are described in detail in Songaila 1998.

6.2.2 HST/COS

The *HST*/COS spectra of this source is obtained from the MAST public archive[1]. The observations of this sight line have done two times using HST/COS G130M grating to study He II re-ionization in detail. The individual exposures of these observations are tabulated in Table 6.1. Data reduction is done with STScI CalCOS (v3.0) pipeline. The exposures were coadded by using the routine developed by Danforth et al. 2010. The combined spectra have a wavelength coverage between $1135 - 1450$ Å. The spectra were oversampled with 6 pixels across one resolution element which we rebinned to an optimal level.

6.3 Detection of intervening Ne V absorbers

In a search of C IV and strong Lyα absorbers towards HE $2347 - 4342$ ($z_{em} = 2.885$) at redshift $z > 2.2$, we detected 11 intervening absorbers. Among these 11 absorbers, five of the systems show absorptions from Ne V 357 Å transition. No other transition of Ne V covered in the observed spectra, and hence, the identification of Ne V is only on the basis of the kinematic profile of their absorption. The observed equivalent width and column density of Ne V transitions are tabulated in Table 6.2.

---

[1] https://archive.stsci.edu/

Table 6.2: Intervening Ne V absorbers

Absorber(z)	Transition	W_r (m Å)	log N(Ne V) cm^{-2}	[-v, +v] (km s^{-1})	ΔV (km s^{-1})	ρ (Mpc)
2.7356	Ne V 357	25 ± 5	14.35 ± 0.05	$[-50, 100]$	3680	8.1
2.4382	Ne V 357	18 ± 4	14.00 ± 0.1	$[-30, 40]$	10000	4.4
2.3475	Ne V 357	5 ± 2	13.57 ± 0.05	$[-30, 40]$	- 4100	4.4
2.6910	Ne V 357	21 ± 3	14.15 ± 0.06	$[-100, 0]$	80	8.1
2.6910	Ne V 357	20 ± 4	14.13 ± 0.03	$[0, 100]$	80	8.1
2.4887	Ne V 357	11 ± 2	13.85 ± 0.05	$[-20, 20]$	12400	4.4
2.4824	Ne V 357	< 6	$<$	$[-20, 20]$	11800	4.4
2.3318	Ne V 357	< 3	< 13.17	$[-30, 30]$	1400	4.4
2.5725	Ne V 357	< 3	< 13.17	$[-30, 30]$	9698	8.1
2.6345	Ne V 357	< 5	< 13.46	$[-30, 30]$	4540	8.1

Table 6.2 Comments. - For all the intervening Ne V detections, their equivalent width, column density and the velocity range are tabulated in third, fourth and fifth columns. The separation of the absorber from the neighbouring quasars in the line of sight (velocity separation) and in sky (projected separation) are shown in next two columns [redshift of the foreground quasars are $z = 2.28$, $z = 2.32$ and 2.69 respectively].

In the following sections, we will discuss the line measurements and ionization modelling of each of the Ne V absorbers. The absorber at $z = 2.7356$ is the stronger one among all with several metal ions present. Hence, this system is modelled in great details and discussed separately in the following sections. The absorbers at $z = 2.6910$ and $z = 2.4887$ do not have enough constraints to develop a complete ionization models. For these systems, we only compare their properties with the conditions derived from other absorbers.

6.4 Line measurements of the absorbers

6.4.1 The absorber at $z = 2.7356$

The absorber is detected from the line transitions of Si IV, Si III, C III, C IV, Ne V and also from the Lyman series lines with $> 3\sigma$ significance. The region of O VI doublet transitions is covered in UVES. However, the strong absorptions from other redshifts prevent the possibility of their detection. Transitions of C IV lines fell in the spectral gap of UVES spectrum at $5755 - 5835$ Å however covered in the HIRES spectrum. We also find a tentative detection of Ne V 357 with $\lambda_{rest} = 357.95$ in the COS spectrum of this absorber. A continuum normalised spectrum of these lines is shown in Figure 6.1 in the absorber rest frame.

The line parameters were estimated using the VPFIT (ver 10.0)[2] fitting software. The absorption profile of all the lines shows the presence of multiple components. The metal doublet transitions of C IV and Si IV are features with least contamination clearly show five components in their absorber. The doublet lines of C IV and Si IV fitted simultaneously with five components. Similarly, all the neutral H I lines were fitted simultaneously.

The intermediate line of C III has a profile similar to H I where some of the components show saturation. These lines fitted independently from their kinematic evidence. The component at $v = 65$ km s^{-1} show least saturation which is also observed in other metal lines. Si III is another intermediate line in the

---

[2] http://www.ast.cam.ac.uk/~rfc/vpfit.html

Figure 6.1: Absorber at $z = 2.7356$

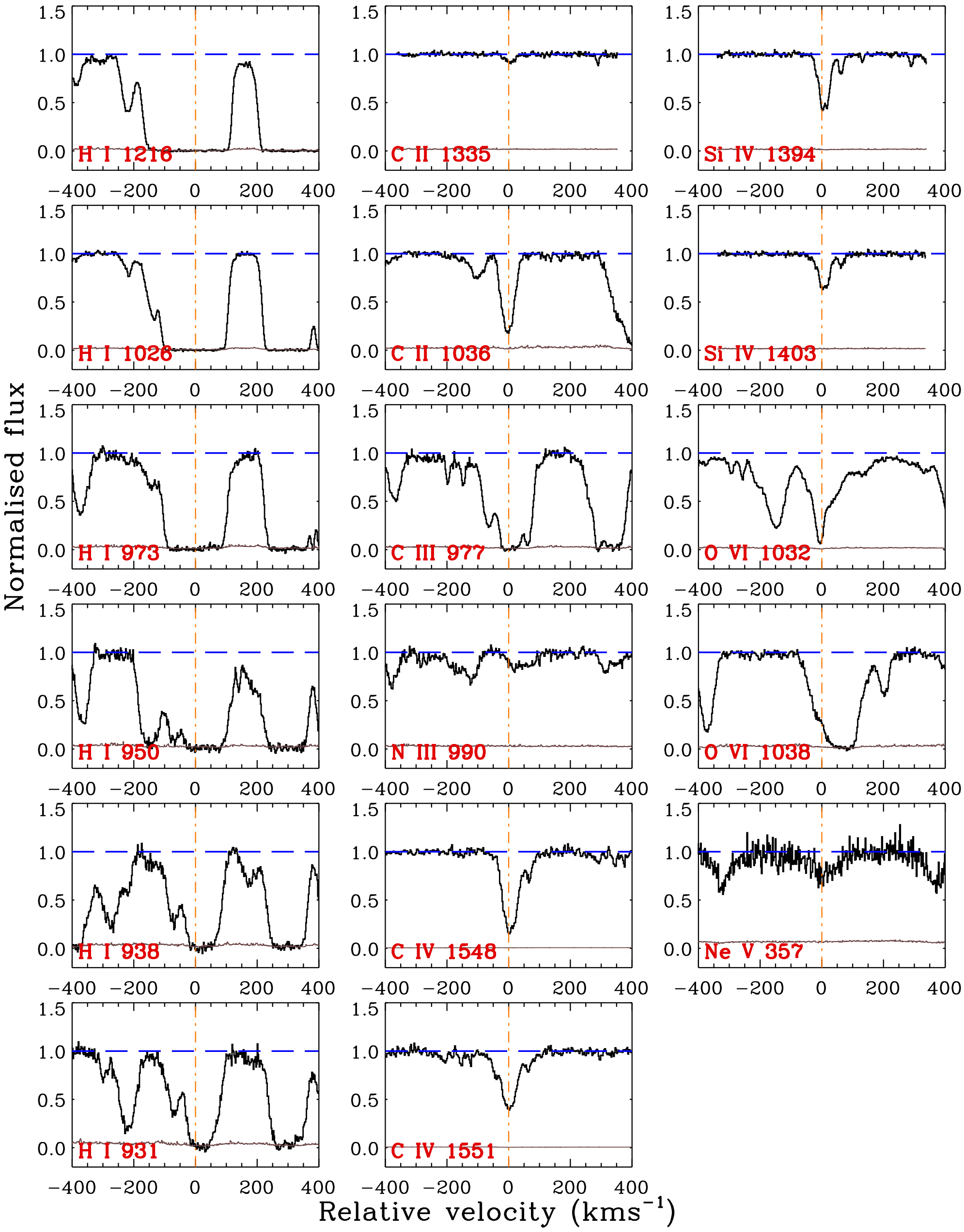

Figure 6.1 The $z = 2.7356$ absorber is shown in its rest-frame. The detected lines in the absorber consists of Si IV, Si III, C II, C III, C IV, Ne V. The profile fitting and the line measurements are shown in Figures 6.2, 6.3 and Table 6.3 respectively.

Figure 6.2: Profile fit of $z = 2.7356$

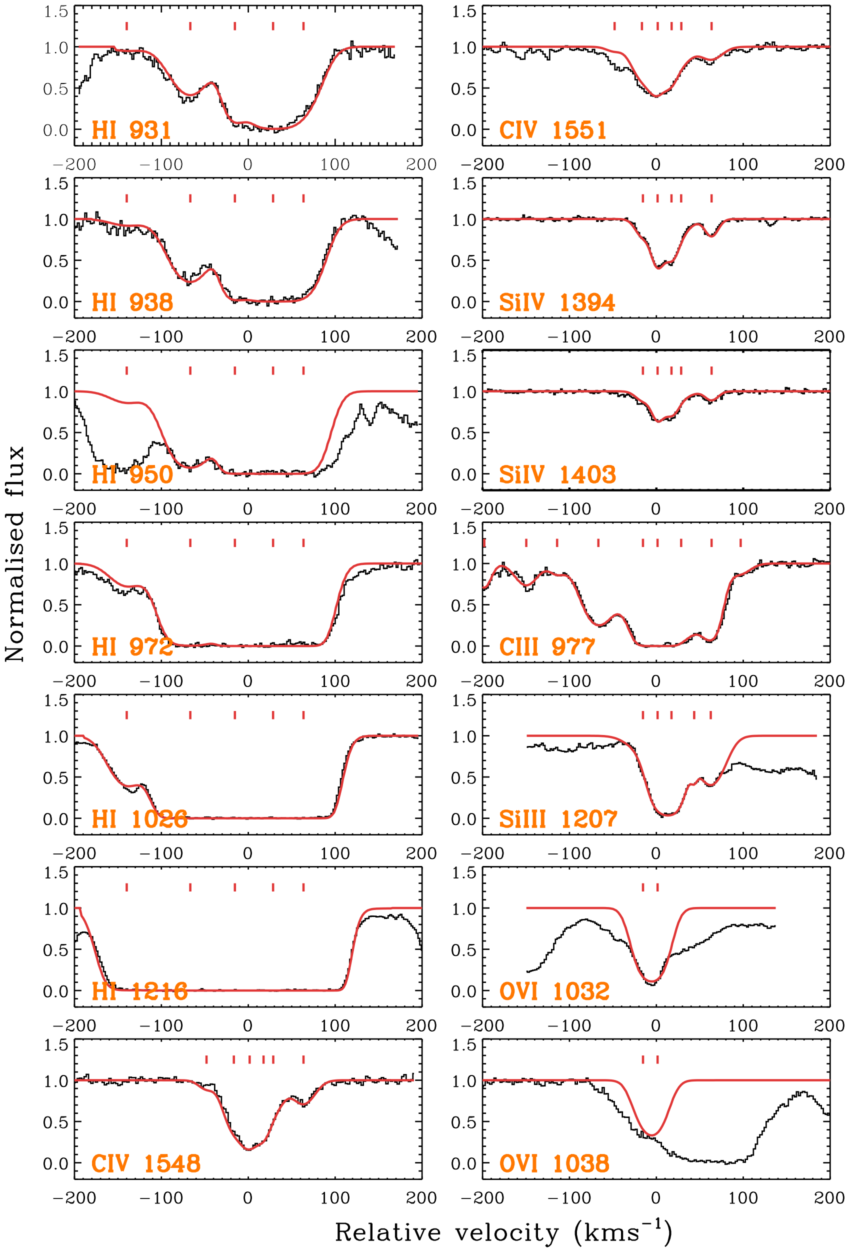

Figure 6.2 The Voigt profile fit results of the lines in the absorber at $z = 2.7356$ are shown. The red thick lines show the model absorption profile which is super imposed on the real spectra. The line measurements are tabulated in Table 6.3. The absorptions of C IV, Si IV are clean features with least contamination. The C III profile is similar to H I profile where few components are saturated. The lines of Si III and O VI lines are mostly contaminated.

Figure 6.3: Column density measurement for Ne V absorption

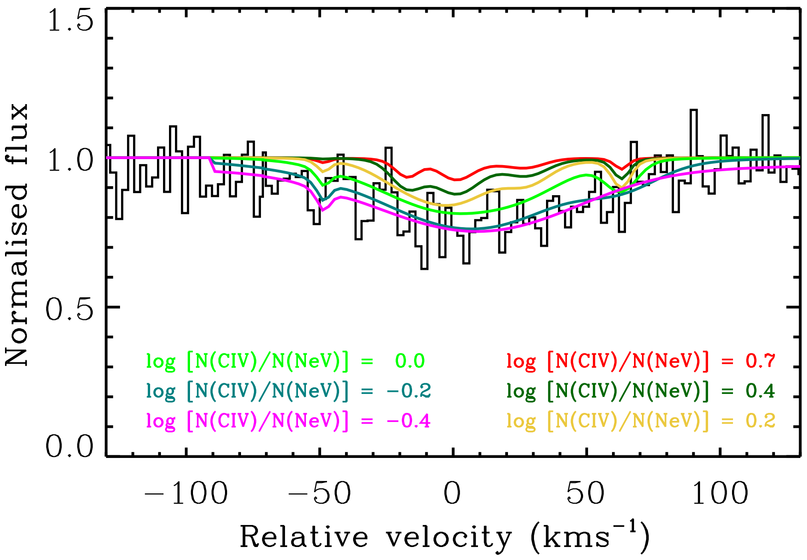

Figure 6.3 The normalised absorption profile of Ne V 357 is shown in the rest frame velocity of the absorber at $z = 2.7356$. The profile is superimposed with a synthesised model of Ne V for different column density ratio of C IV and Ne V. For log $N(\mathrm{Ne\ V})N(\mathrm{C\ IV}) = -0.4$, model fit the data with minimum χ^2.

absorber which shows strong contamination from other absorbers. Profile fit measurements of these lines are tabulated in Table 6.3.

For fitting Ne V, the model profile is convolved with the empirically determined line-spread functions of Kriss et al. (2011) which will account for the wavelength dependent line spread observed in COS spectrum. The profile of Ne V does not show any evidence for multiple components within the S/N of the spectra. Hence, Extracting the information from individual components using profile fitting routine does not provide a satisfactory result. For extracting the column density of individual components, we synthesized the profile of Ne V from C IV by scaling N(Ne V)/ N(C IV) ratio. The profile with least χ^2 is taken as the best fit profile for Ne V. For [N(Ne V)/ N(C IV)] $= -0.4$ dex, we produced the best fit model for Ne V line (See Figure 6.3). A single component fit result for this line is also shown in Table 6.3.

Table 6.3: Voigt Profile Measurements of $z = 2.7356$ absorber

Transition	v (km s^{-1})	b(km s^{-1})	log [N (cm^{-2})]
Si IV 1394	-15 ± 2	9 ± 1	12.34 ± 0.07
	-1 ± 1	6 ± 1	12.53 ± 0.10
	14 ± 1	15 ± 2	13.06 ± 0.03
	62 ± 1	10 ± 1	12.36 ± 0.02
C IV 1548 – 1551	-52 ± 4	12 ± 5	12.20 ± 0.14
	-15	15 ± 1	13.53 ± 0.02
	-1	11 ± 2	13.29 ± 0.06
	14	18 ± 1	13.75 ± 0.02
	62	20 ± 2	13.20 ± 0.03
Si III	-15	23 ± 5	12.19 ± 0.07
	1	15 ± 2	12.82 ± 0.04
	17	16 ± 1	13.20 ± 0.02
	44	3 ± 2	11.69 ± 0.15
	64	20 ± 2	12.80 ± 0.03
C III	-196 ± 1	11 ± 2	12.55 ± 0.04
	-150 ± 2	17 ± 2	12.70 ± 0.04
	-114 ± 3	12 ± 8	12.13 ± 0.47
	-67 ± 2	20 ± 4	13.31 ± 0.19
	-15	53 ± 27	13.56 ± 0.28
	1	20 ± 3	14.23 ± 0.15
	28 ± 3	21 ± 4	13.61 ± 0.08
	62 ± 6	14 ± 1	13.52 ± 0.05
	97 ± 4	18 ± 5	12.33 ± 0.15
O VI 1032 – 1038	-15	16 ± 2	< 14.18
	1	16 ± 2	< 14.25
Ne V 357	15 ± 3	53 ± 4	14.35 ± 0.03
H I 1216 – 931	-140	25 ± 2	14.29 ± 0.02
	-67	29 ± 1	15.58 ± 0.02
	-15	16 ± 1	15.71 ± 0.03
	28	26 ± 3	16.31 ± 0.06
	63	25 ± 1	15.64 ± 0.04

6.4.2 Other Ne v absorbers

Apart from $z = 2.7356$ absorber, there are four other instances of Ne v detection in the intervening absorbers. The profile fit results of these absorbers are tabulated in Table 6.4.

The absorber at $z = 2.4382$ detected from C iv, H i, O vi and Ne v transitions. The kinematic profile of C iv and O vi lines clearly shows the evidence for four distinct components in the absorber. The line parameters are estimated using VPFIT profile fitting routine. One of the transition of O vi in the absorber with rest wavelength $\lambda \sim 1032$ Å is contaminated. This line is modelled from the measurement of O vi 1038 is shown in Figure 6.4. It is difficult to extract the line parameters of individual components from the week Ne v detection. Thus, this line is fitted only with 2 components. The profile fits of the absorber is shown in Figure 6.4.

Similarly, the absorber at $z = 2.3475$ is detected from the transitions of C iv, O vi, Ne v and the Lyman series lines. The absorber has a simple profile which can be fitted with a single Gaussian component. A Voigt profile fitting for the tentative Ne v detection is difficult. Thus, the column density of this line is estimated using the Apparent Optical Depth (AOD) method.

The third absorber is also detected with similar ions at redshift $z = 2.4887$. The O vi lines in the absorber are contaminated, only useful to constraint the upper limit in column density. The doublet lines of C iv are also week which does not show any evidence for multiple components. Line parameters of the absorber are estimated using a simple Gaussian profile fitting.

In the forth absorber at $z = 2.6910$, only Lyman series and Ne v lines are detected. The kinematic profile of Ne v in the absorber is consistent with the neutral H i transitions. However, the $z = 2.6910$ absorber shows an offset of ~ 30 km s^{-1} between these two lines. Such off- centred metal lines and H i lines are already observed in an absorber at $z = 2.6498$ to the same sightline (Muzahid et al., 2011). Apart from Ne v, the absorber also shows the evidence for O vi lines which are mostly contaminated.

Table 6.4: Line Measurements of Ne V absorbers

z_{abs}	Transition	v (km s^{-1})	b(km s^{-1})	log [N (cm^{-2})]
2.4382	C IV 1548 − 1551	−53 ± 1	7 ± 2	11.94 ± 0.1
		−13	18 ± 6	12.56 ± 0.7
		−5 ± 1	7 ± 2	12.41 ± 0.57
		14 ± 6	11 ± 3	12.40 ± 0.45
	O VI 1032 − 1038	−53	10 ± 3	13.26 ± 0.08
		−35	11 ± 2	13.40 ± 0.1
		−5	17 ± 2	13.73 ± 0.06
		14	31 ± 3	14.04 ± 0.04
	Ne V 357	−5	27 ± 5	14.00 ± 0.1
		14	26 ± 9	13.44 ± 0.3
	H I 1026 − 1216	−53	16 ± 6	12.89 ± 0.4
		−13	62 ± 6	14.04 ± 0.1
		−5	32 ± 3	14.48 ± 0.05
		14	28 ± 1	14.48 ± 0.03
	AOD Measurements			
	Ne V 357	[−30, 40]	—	14.00 ± 0.1
2.3475	C IV 1548 − 1551	−2 ± 1	10 ± 1	13.50 ± 0.01
	O VI 1032 − 1038	2 ± 1	15 ± 2	13.69 ± 0.03
	Ne V 357	0	15	13.48
	H I 1026 − 1216	10 ± 1	35 ± 1	15.56 ± 0.06
	AOD Measurements			
	Ne V 357	[−30, 40]	—	13.57 ± 0.05
2.4887	C IV 1548 − 1551	−8 ± 1	7 ± 1	12.50 ± 0.02
	Ne V 357	−11 ± 4	39 ± 1	14.03 ± 0.04
	H I 972 − 1216	−12 ± 1	43 ± 1	14.88 ± 0.02
	AOD Measurements			
	Ne V 357	[-20,20]	—	13.85 ± 0.05
2.6910	H I 1026 − 1216	−9 ± 1	33 ± 4	14.81 ± 0.2
	H I 1026 − 1216	56 ± 2	24 ± 3	14.63 ± 0.2
	H I 1026 − 1216	113 ± 4	31 ± 2	13.77 ± 0.2
	H I 1026 − 1216	162 ± 5	33 ± 7	13.19 ± 0.2
	Ne V 357	−52 ± 5	32 ± 2	14.02 ± 0.09
	Ne V 357	27 ± 6	46 ± 2	14.23 ± 0.06
	AOD Measurements		—	
	C IV 1551	[−100, 0]	—	< 11.43
	C IV 1551	[0, 100]	—	< 11.39
	C IV 1548	[−100, 0]	—	< 11.14
	C IV 1548	[0, 100]	—	< 11.10
	Ne V 357	[−100, 0]	—	14.15 ± 0.06
	Ne V 357	[0, 100]	—	14.13 ± 0.03

Figure 6.4: Absorbers at $z = 2.3475$ and $z = 2.4382$

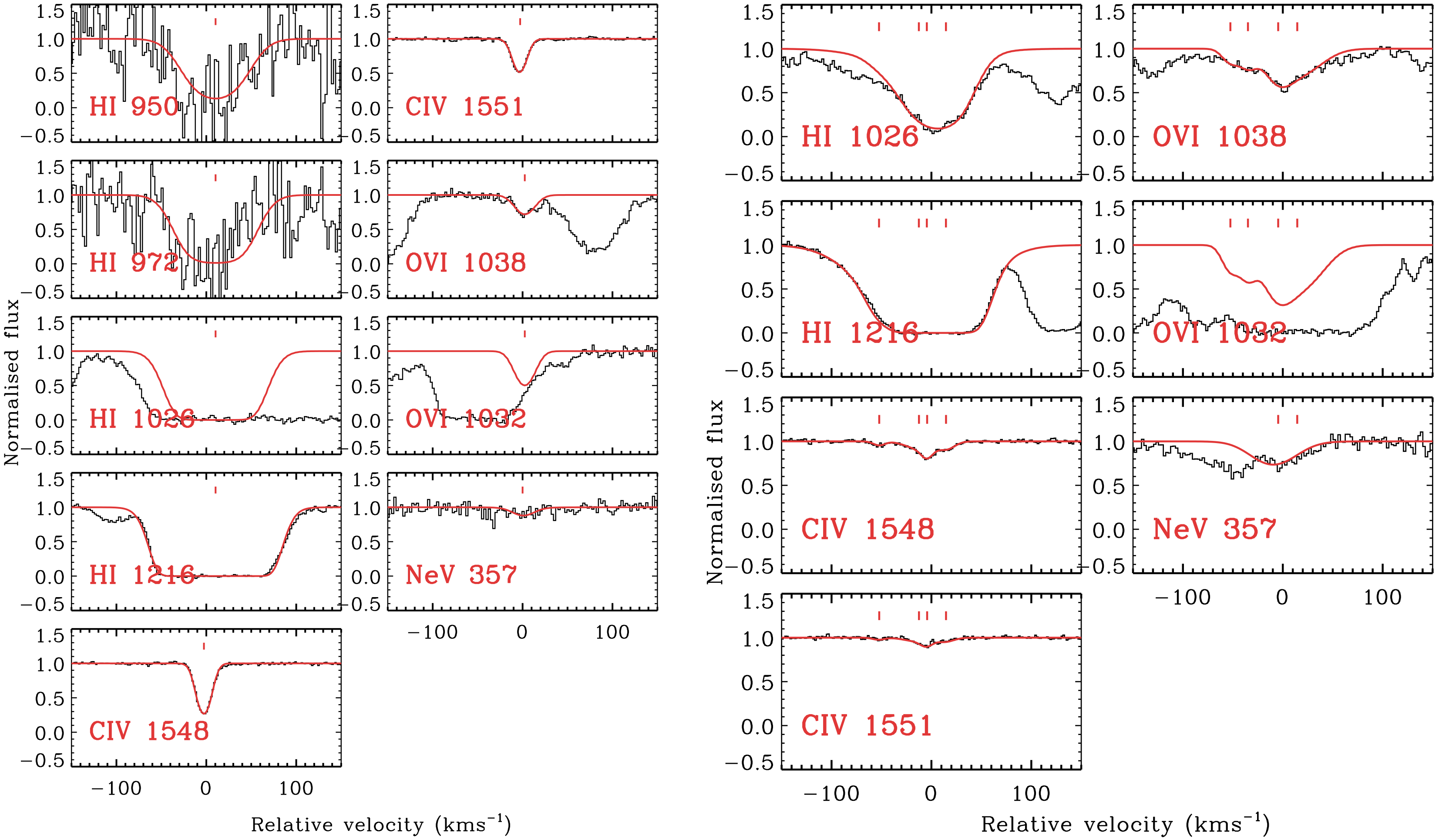

Figure 6.4 The Voigt profile fit results of the absorber at $z = 2.3475$ and $z = 2.4382$ is shown in the rest-frame of the absorber. The red thick line shows the model profile and the red tick marks indicate the centroid velocity of each component.

Figure 6.5: Absorbers at $z = 2.4887$ and $z = 2.6910$

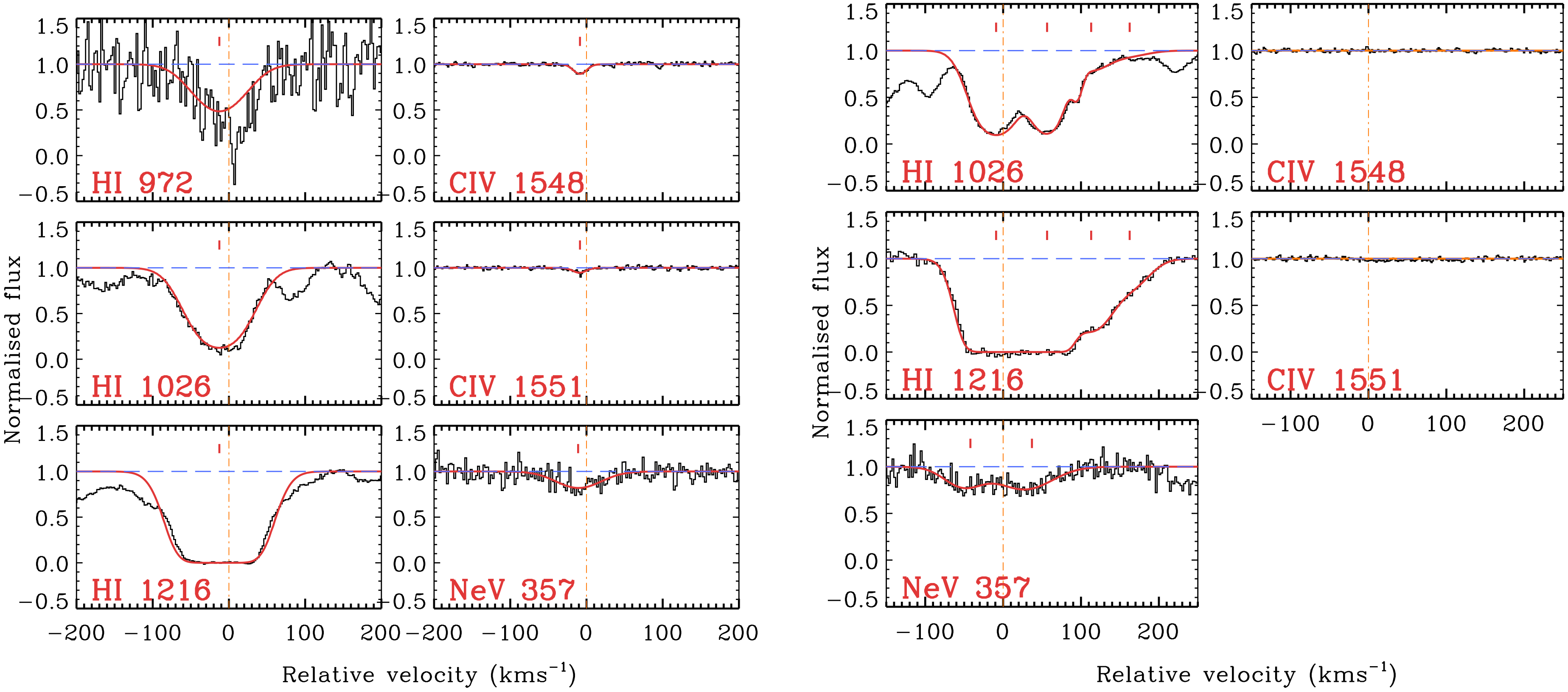

Figure 6.5 The systemplots of absorbers at $z = 2.4887$ and $z = 2.6910$ are shown. Transitions of Ne V and H I are detected in both instances. Only $z = 2.4887$ absorber detected with C IV transitions which is a clear non-detection in the $z = 2.6910$ absorber. Both the lines of O VI are contaminated in both systems.

6.5 Ionization Modelling of the absorbers

6.5.1 The $z = 2.7356$ Absorber

For understanding the ionization process in detail, we model the absorber with time-independent photoionization model. The lack of robust measurements in the individual components led us to assume a similar physical condition throughout absorber and model a component at $v = 65$ km s^{-1} which has the most reliable measurement available.

Photoionization model of this absorber was constructed using Cloudy (ver 13.03) for a gas with log N(H I) = 15.63 assumed to be plane parallel slabs of constant densities illuminated with the extragalactic radiation at $z = 2.73$. The absorber is assumed to have solar abundance ratios as described in Asplund et al. (2009). Modelling of the cloud was done with three different radiation fields-KS15, KS15 with spectral cutoff and HM12 respectively (Shown in Figure 6.6). The predicted column density ratios of N (C III)/N (C IV), N(Si III)/ N(Si IV) and N(Si IV)/N(C IV) are shown in Figure 6.7.

The ionisation model of the absorber that uses KS15 UVB can reproduce the observed ratio of N(C III)/ N(C IV) at density $n_H \sim 5 \times 10^{-3}$ cm^{-2}. From the upper limit of Si III column density, we calculated N(Si III)/ N(Si IV) which gives an upper limit in density $n_H \sim 5 \times 10^{-2}$ cm^{-2} from the model. The ratio of N(Si IV)/ N(C IV) adds another constraint to density which is consistent with the range of density that we already derived. Thus, we find a narrow range of density $10^{-3} - 10^{-2}$ cm^{-2} which can explain the observed ion ratios of carbon and silicon.

We find, for solar metal abundance, N(Si IV)/ N(Ne V) ratio is slightly off with the range of density that we derived. With a +0.5 dex increase in the abundance of neon, the model can produce Ne V as observed from the same gas phase from the same gas phase. A similar trend is observed from the ratio of N(C IV)/ N(Ne V) which require a +0.5 dex higher metal abundance ratio to be consistent with density we derived.

Change in the UV background does not improve the problem anyway, rather

Figure 6.6: UV background at $z = 2.73$

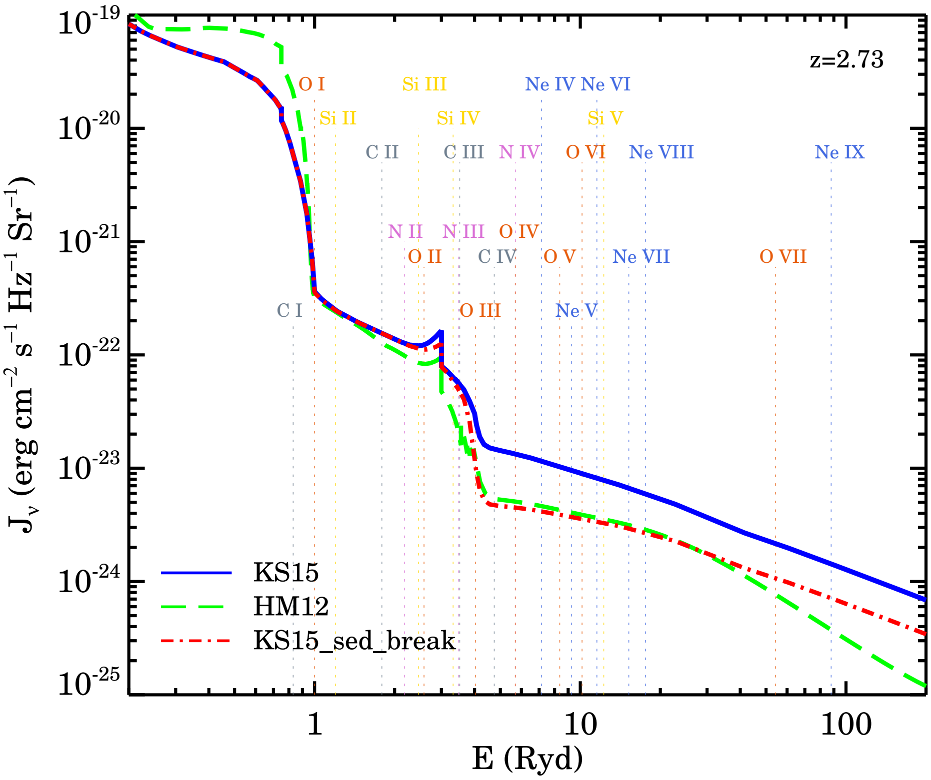

Figure 6.6 The figure shows a comparison of three UV background used to model the absorber at 2.7356. The model HM12 and KS15 UVB with SED break shows a break in the spectral energy distribution at $E \sim 3$ Ryd. Compared to these models, KS15 has a slightly hard UV radiations for $E \geq 3$ Ryd. On the subsequent models, we use KS15 UVB for photoionization modelling. The vertical dotted lines the plot show the ionization energy of different ions.

make it worse. For example, the predictions from HM12/ KS15 - without SED break produce C III, Si IV and C IV consistently from a density range of $n_H \sim 5 \times 10^{-3}$ cm^{-2}. To produce Ne V from this gas phase requires neon abundance increased more than an order of magnitude. Thus, we conclude, a single phase photoionized origin of Ne V along with the remaining ions is possible with a +0.5 dex rise in the abundance of neon when we use KS15 UV background (without break). The KS15 UV background with a break in the spectra or HM12 UVB requires a much higher abundance of Ne V which can not be the case.

Figure 6.7: Ionisation models of the absorber at $z = 2.7356$

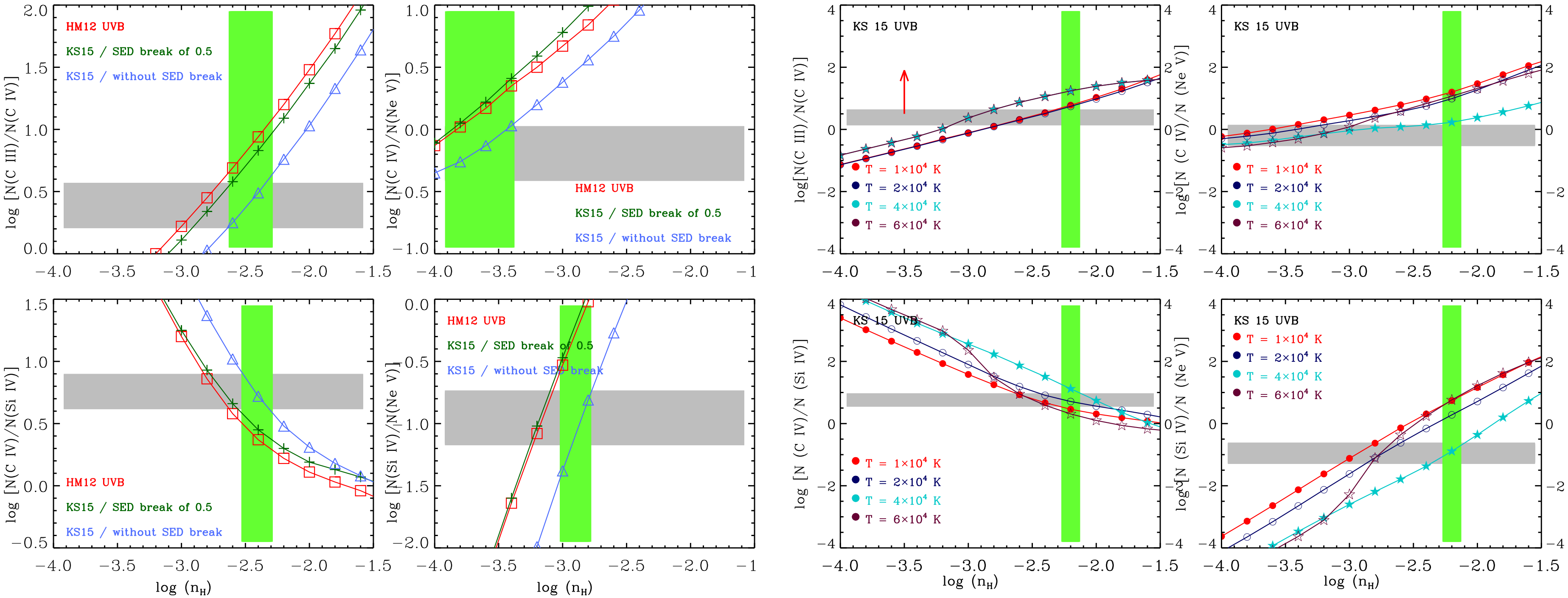

Figure 6.7 *Left Panel* : The change in column density ratio of C III, C IV, Si IV and Ne V with density for three different UV background HM12, KS 15 (with SED break) and KS15 (without SED brake) are shown in the figure. The grey marked region shows the observed column density ratio and the region in green show the density at which the observed ratio produced for a solar metal abundance. The model suggests that the observed ion ratios can not be produced via photoionization from a single gas phase. *Right Panel* : The change in column density ratio of these ions for a model with KS15 UVB at different temperatures is shown here. The grey marked region is the observed column density ratio and the green region shows the density at which the observation matches the model prediction. We find the model at temperature $T \sim 4 \times 10^4$ K predict all the ion ratios consistently.

Collisional ionization is one another way to produce Ne V. However, a pure collisional origin of the absorber is least expected in a normal astrophysical condition. Hence, we model the absorber at different temperature by including UV photons as in the photo-ionization model. The model result is shown in the Figure 6.7 for four different temperature.

We find the model is consistently producing all the ions in the absorber from a single phase with density of $n_H \sim 5 \times 10^{-3}$ cm^{-3}, temperature $T \sim 4 \times 10^4$ K and a metalicity of $z = -1.2$ respectively. The model is consistent for other UV background also. Both HM12 and KS15 UVB with SED cut off are consistent at a density $n_H \sim 3 \times 10^{-3}$ cm^{-3} and metallicity $z = -1.3$ dex at the same temperature.

The temperature at which we get the single-phase solution is ($T \sim 4 \times 10^4$) K is not widely different from the typical photoionization temperature. A pure photoionization of the absorber with UV background radiation alone could heat up the cloud to a temperature $T \sim 1.2 \times 10^4$ K naturally.

The contribution of collisions is important as we go to higher and higher temperature. The gradual rise in temperature increases the column density of all the three intermediate ions slowly (C IV, Si IV and also Ne V). The rise in column density via collisions is higher for Ne V at temperature $T < 5 \times 10^4$ K. This process increased the column density of Ne V compare to both C IV and Si IV. However, the collisional origin of Si IV and C IV drastically increased for temperature $T > 5 \times 10^4$ K. This can see as a sharp turn around in the ratio of N(Si IV)/ N (Ne V) and N(C IV)/ N(Ne V) in Figure 6.7. Further increase in temperature will reduce the production of Si IV via collisions whereas Ne V keeps rising till it peaks at 2×10^5 K. The collisional contribution to C IV peeks at 10^5 K. Note that a further turn around of N(Si IV)/ N (Ne V) and N (C IV)/ N (Ne V) ratio is expected at temperature $T > 10^5$ K. But at such high temperature, the ionisation fraction of C III, H I etc will reduce which invalidate a single phase origin of the absorber.

6.5.2 Other Ne V absorbers

The absorbers at $z = 2.3475$ and $z = 2.4382$

For the photoionization model of these absorbers, we used the recently modified KS15 UV background as the ionization source. The absorber is assumed to have a simple plane-parallel geometry and a solar metal abundance (Asplund et al., 2009). The column density ratios N(C IV)/N(O VI), N(C IV)/N(Ne V) and N(C IV)/N(O VI) predicted by the model for the absorbers at $z = 2.3475$ and $z = 2.4382$ are shown in Figure 6.8.

In the absorber at $z = 2.3475$, the model predicted column density ratios of N(C IV))/ N(O VI), N(C IV)/ N(Ne V) and N(O VI)/N(Ne V) are consistent for a gas with density $n_H \sim 10^{-3}$ cm^{-3}. This means that the absorber can have an intervening origin purely via photoionization of UV radiations. Model predicts a photoionization temperature of $T \sim 10^4$ K and a metallicity of -1.5 dex for the absorber.

A similar model of the absorber at $z = 2.4382$ is shown in the right panels of Figure 6.8. The model reproduced the column density ratio of N(C IV)/N(O VI) from a gas phase with density $n_H \sim 10^{-3}$ cm^{-3}. However, to produce the column density ratio of N(C IV)/N(Ne V) and N(O VI)/N(Ne V) from the same phase requires the abundance of carbon at least one order of magnitude less. This is not usually observed in normal astrophysical conditions. We looked further with hybrid ionization scenario which includes collisional ionisations as well. The model run in the temperature range of $8 \times 10^4 - 1.6 \times 10^5$ K. The column density ratio of N(C IV)/N(O VI), N(C IV)/N(Ne V) and N(C IV)/N(O VI) from the model is shown in Figure 6.9. We find the model can reproduce all the ratios at density $n_H \sim 10^{-3}$ cm^{-3}, temperature 1.6×10^5 K for a cloud with metallicity of -2.2 dex from solar. This revealed the presence of warm baryons with temperature $T \sim 10^5$ K at high redshift for the first time.

Figure 6.8: Photoionisation models of z = 2.3475 and z = 2.4382 absorbers

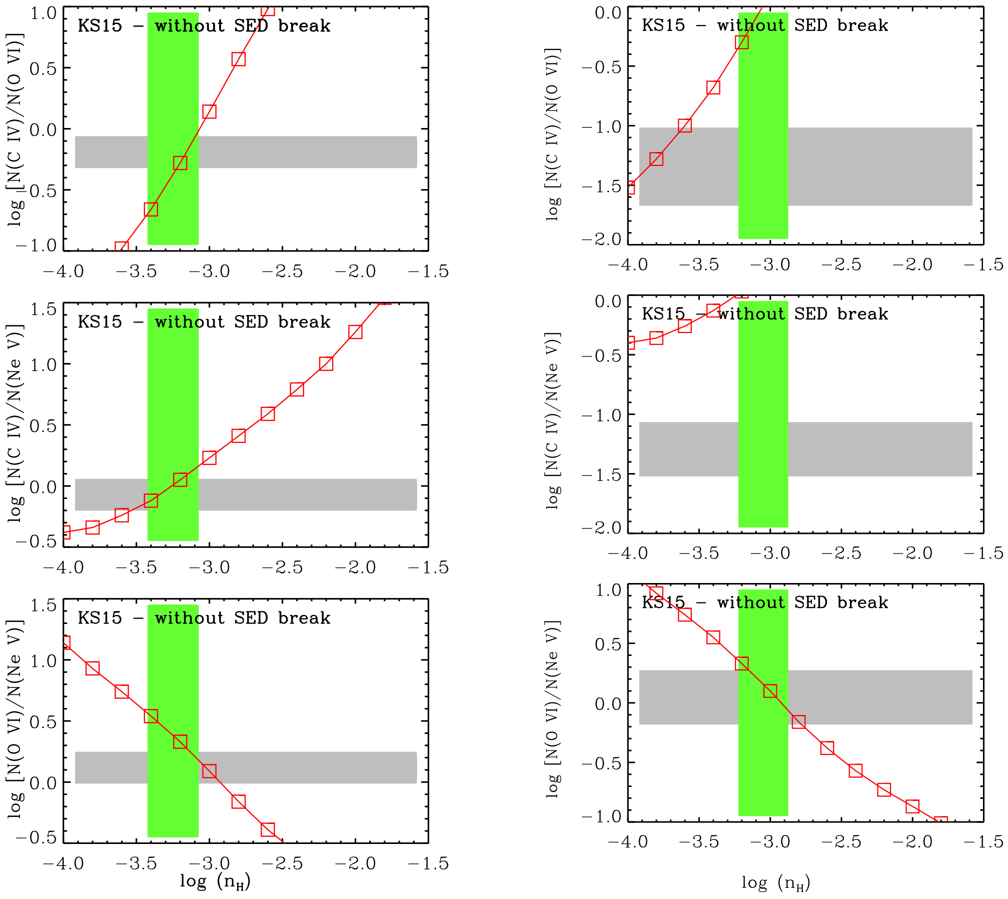

Figure 6.8 The model predicted column density ratio of C IV, Ne V and O VI ions with density for absorbers at $z = 2.3132$ and $z = 2.4382$ is shown in figure. The grey marked region is the observed column density ratio of the ions and the region marked in green is the density constrained from this model. The first absorber at $z = 2.3475$ is consistent with photoionization origin from a gas phase with density $n_H \sim 4 \times 10^{-4}$ cm^{-3}. However, the ratios observed in the $z = 2.4382$ absorber is not consistent with a pure photoionization model.

Figure 6.9: Hybrid model of the absorber at $z = 2.4382$

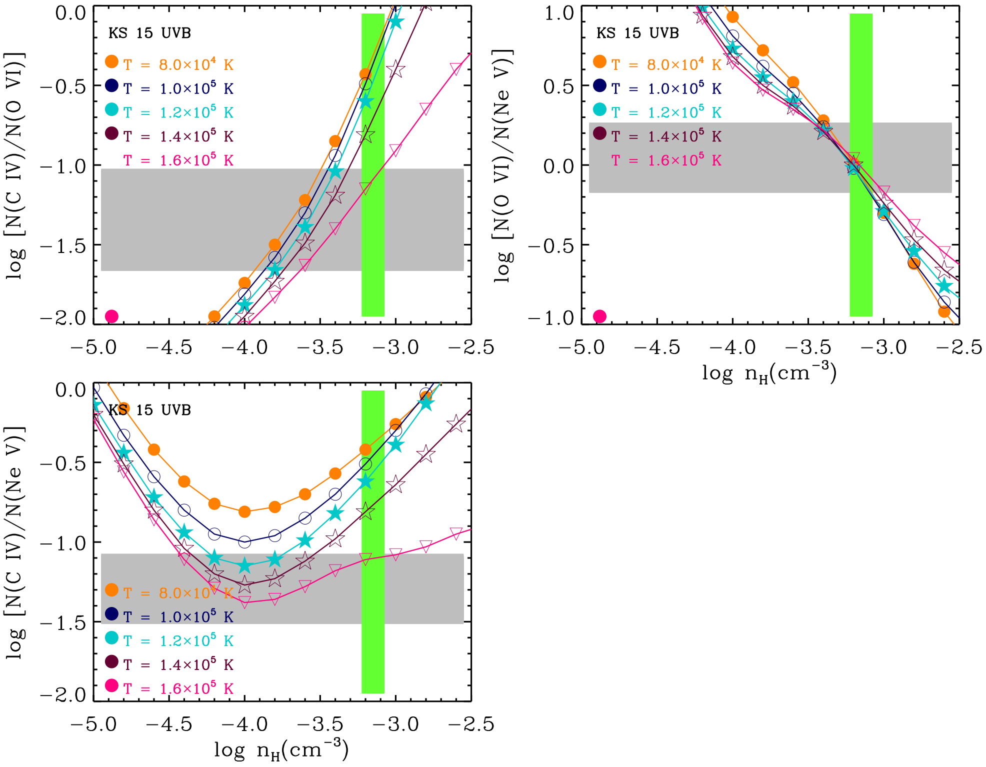

Figure 6.9 The change in the column density ratios of N(C IV), N(Ne V) and N(O VI) with density is shown four different temperature and KS15 UV background. The gray marked region show the observed column density ratio of each ions and the region in green is the density which simultaneously explain all the ratios. Model predict all the ratios at a temperature $T \sim 1.6 \times 10^5$ K.

The absorbers at 2.4887 and $z = 2.6910$

The absorbers at $z = 2.6910$ and $z = 2.4887$ are the two other instances with Ne V detections. The O VI transitions in these absorbers are contaminated which prevented us to have a complete ionization model for these absorbers. Both of these absorbers have properties similar to the absorber at $z = 2.4382$ where the detection of C IV is weak compared to Ne V and O VI lines. In the $z = 2.4887$ absorber, we found that a simple photoionization model cannot produce the observed $\dfrac{\log N(\text{C IV})}{\log N(\text{Ne V})} = -1.2$ dex ratio from gas with solar metallicity. Similarly, $\dfrac{\log N(\text{C IV})}{\log N(\text{Ne V})} = -1.3$ dex observed in the $z = 2.4887$ absorber is also not produced via photoionization alone (See the model of $z = 2.4382$ absorber in Figure 6.8 for details). However, a hybrid ionisation scenario can produce this ratio from a gas phase with temperature $T \sim 2 \times 10^5$ K, density $n_H \sim -3$ cm^{-3} and metallicity of $-2.5 dex$ respectively.

In the absorber at $z = 2.6910$, C IV is a non-detection. The upper limit in C IV corresponds to column density ratio of $\frac{\log \mathrm{N(C\ IV)}}{\log \mathrm{N(Ne\ V)}} < -2.8$ dex for the absorber. This ratio can be produced neither via photoionization nor via collisional ionization. The origin of this absorber is discussed in detail in the next Section.

6.6 On The Origin of the Absorbers

The Luminous Infra-red Galaxies (LIRGs) and Ultra Luminous Infrared Galaxies (ULIRGs) shows the atomic fine structure emissions from Ne V in mid-infrared region (Petric et al., 2011; Inami et al., 2013; Spinoglio et al., 2015; Armus et al., 2007, 2004). The ionization energy required to produce Ne V species is generally difficult from the photoionization of stellar radiations in the galaxies. The empirical relationship of Armus et al. 2007 showed that for $\frac{\log \mathrm{N(Ne\ V)}}{\log \mathrm{N(Ne\ II)}} \geq 0.75$ and $\frac{\log \mathrm{N(O\ IV)}}{\log \mathrm{N(Ne\ II)}} \geq 1.75$, more than 50 % of the nuclear emission is from the active galactic nuclei in the galaxy. This correlates the detection of Ne V in LIRGS to the presence of AGN at the centre of the galaxy. From the statistical analysis of 248 LIRGs, Petric et al. 2011 found 18% of LIRGs consists of an active nucleus at the centre of them.

Similarly, in the intergalactic medium, the energy density of UV photons with $\lambda < 1000$ Å is dominated by the radiations from quasars and AGN (Khaire and Srianand, 2015b,a; Haardt and Madau, 2012). The average distribution of the energy of these photons at different epoch is represented by UV background radiations and we used UV background of KS15 (without SED break) to model our absorbers. Using this UVB, the absorber at $z = 2.3475$ can be modelled via pure photoionization for solar abundance ratios. The ionization conditions of no other Ne V absorber can be reproduced via photoionization of a gas with solar abundance ratios. For the absorber at $z = 2.7356$, it requires either an enhancement of hard UV radiation or a mechanism which can raise the photoionization temperature from 1×10^4 K to 4×10^4 K to explain the observed ion ratio of the absorber. Similarly, to reproduce the observed ion ratios of $z = 2.4382$ and $z = 2.4887$ absorbers requires warm-hot gas phase with temperature $T \sim 2 \times 10^5$ K. Ne v is also detected in the $z = 2.6910$ absorber where both photoionization and collisional ionization processes failed to explain their observed line ratios.

A local enhancement of UV radiation is expected in the regions overpopulated with AGN and quasars (Fardal and Shull, 1993; Croft, 2004; McDonald et al., 2005). The study of Worseck et al. 2007 showed the presence of 14 quasars towards HE 2347-4342. Three foreground quasars are detected at redshift $z = 2.282$ (QSO J 23503-4328), $z = 2.302$ (QSO J 23500-4319) and $z = 2.69$ (QSO J 23495-4338) respectively. These quasars can cause a "transverse" proximity effect in the form of radiation-induced voids in the Lyα forest which is not observed (Worseck et al., 2007). However, Worseck et al. 2007 find a statistical excess of hard UV radiations from the variations in He II ratio. They looked further into the metal systems at $z = 2.275$, $z = 2.3132$ and $z = 2.7119$ to find the evidence for the proximity effects. But the strong contaminations in the absorber $z = 2.275$ and $z = 2.7119$ could not provide enough constraint to develop a complete ionization model. The third system at $z = 2.3132$ did not show any evidence for proximity effects. Muzahid et al. 2011 revisited the $\frac{\text{He II}}{\text{H I}}$ ratio towards this line of sight detected four absorbers at $z = 2.6346$, 2.6498, 2.6624 and 2.6910 in the region with low η measurements.

The origin of Ne v absorptions in some of our sample could be the evidence for the transverse proximate effect of the three foreground quasars. The separation of each absorber from the neighbouring quasars are shown in table 6.2. One of the absorber at $z = 2.6910$ is within ~ 100 km s^{-1} of the QSO J $23495 - 4338$ is most likely affected in this manner. We found $\frac{\text{C IV}}{\text{Ne V}} < -2.8$ in this absorber which can produce neither via photoionization nor via collisional ionization suggest the local influence of the foreground quasar. The components of H I and Ne v in this absorber show a kinematic offset between them could be the evidence for ionized gas associated with this quasar. Similarly, the velocity separation of the 2.7356 absorber and QSO J $23500 - 4319$ is only $\Delta v \sim 3400$ km s^{-1} with the projected separation of ~ 8 Mpc in the sky. The vicinity of the quasar in the neighbourhood of this absorber can provide the required of enhancement of hard UV radiation which can increase $\frac{\text{Ne V}}{\text{C IV}}$ ratio as observed. The absorbers at $z = 2.4382$ and

$z = 2.4887$ are > 6000 km s^{-1} from the neighbouring quasar with a projected separation of 4.4 Mpc. The large velocity separation of the absorber from the AGN is higher than the velocity of a typical in-falling cloud. If the cloud is not in-falling, this velocity separation translates into a distance of ~ 85 Mpc. In such a large separation no proximate effect is expected. However, note that the survey of Worseck et al. (2007) is not complete at this redshift to sample a full population of quasars with $M_B < -23$. This suggests the possibility of undetected quasars in the vicinity of the absorber.

The origin of absorbers in a warm-hot gas phase is the description is suitable for 2.4382 and 2.4887 absorbers. A hybrid ionization modeling at temperature $T \sim 2{\times}10^5$ K and density $n_H \sim 10^{-3}$ cm^{-3} easily recovered the observed properties of these absorbers. The metallicity derived for these absorbers are < -2 dex less than solar suggests that the absorbers reside in the region with low star-formation. A further understanding of the origin these absorbers requires a better understanding of their neighbourhood. Unfortunately, at present, no such details available at this redshift. We also note that modifications in the spectral lines due to the mechanical supply of energy in the form of winds or other turbulent processes could lead to the similar scenario.

From this study, we find that the origin of Ne V in the intervening systems are more complicated than their origin inside galaxies. In our sample of 5 intervening Ne V absorbers, one system tracing a gas purely photoionized by UVB radiations, two of the systems probing warm gas with $T \sim 10^5$ K and two other systems probing gas in the vicinity of quasars. For these absorbers, the ratio $\frac{\text{C IV}}{\text{Ne V}}$ is found to be more sensitive to the ionization mechanism. We note that the absorbers with $\frac{\text{C IV}}{\text{Ne V}} < -1$ are difficult to produce via photoionization of UV background alone.

6.7 SUMMARY & CONCLUSIONS

In this chapter, we have discussed the physical conditions in five intervening Ne V absorbers. Though all of these absorbers are ≥ 10000 km s^{-1} from the background quasar, the description of an "intervening system" is not valid for most of the absorbers. We find 3 of the 5 Ne V absorbers are within 5000 km s^{-1}

from their neighbouring quasars. To produce the metal ion ratios consistently via photoionization, four out of the five absorbers required an enhancement in UV radiation. However, the metal ion ratios of the absorber at $z = 2.3475$, which is ~ 4000 km s^{-1} from the nearby quasar is consistent with photoionization of UV background alone. Major conclusions from this work are summarized below.

1. From a sample of 11 intervening Ne V absorbers at redshift $z > 2.2$ towards HE 2347 − 4342, we detected five Ne V absorbers.

2. The absorber at $z = 2.7356$ consists of lines of Si III, C III, Si IV, C IV and Ne V. The origin of the absorber from a photoionization scenario cannot produce the metal ion as observed. A hybrid ionization scenario can explain the origin of the absorber at temperature $T \sim 5 \times 10^4$ K, density $n_H \sim 5 \times 10^{-3}$ cm^{-3} and metallicity of −1.3 dex. However, the velocity separation of the absorber $z = 2.69$ from the foreground quasar is only 3400 km s^{-1} which can cause proximity effects on the absorber.

3. The origin of Ne V and the non-detection of C IV in the absorber at $z = 2.6910$ can explain neither via photoionization of UV background radiation nor via collisional ionization. This system has a strong influence from the neighbouring quasar. The kinematic offset between the components of H I and Ne V in the absorber is likely an ionized gas flow connected with the associated quasar.

4. The absorber at $z = 2.4382$ is detected from the absorption of C IV, O VI and Ne V lines. The observed $\frac{\text{C IV}}{\text{Ne V}} = -1.2$ can be produced via hybrid ionization for a gas with temperature $T \sim 1.6 \times 10^5$ K. There is no quasars detected in the absorber neighbourhood. The nearest quasar is the one at $z = 2.32$ which is > 6000 km s^{-1} from the absorber cannot cause any proximity effects.

5. Similarly, the absorber at $z = 2.4887$ is also detected with C IV, O VI and Ne V ions with $\frac{\text{C IV}}{\text{Ne V}} = -1.3$. A hybrid model can produce this ratio for $T \sim 2 \times 10^5$ K. As in the previous case, no neighbouring quasar is detected within the vicinity of this region. The origin of the absorber can be from a medium

shock-heated to high temperature 10^5 K plasma or could be associated with any undetected quasar in the absorbers neighbourhood.

6. The absorber at $z = 2.3132$ also detected with C IV, O VI and Ne V absorption lines. The ratio of $\frac{\text{C IV}}{\text{Ne V}} = 0$ which can be easily produced from the photoionization of UV background. There is a neighbouring quasar with $\Delta v \sim 4000$ km s^{-1} which does not show any proximity effect on this absorber.

7. We also note that the ratio of $\frac{\text{C IV}}{\text{Ne V}}$ is sensitive to the ionization conditions of the absorber. We find that an absorber with $\frac{\text{C IV}}{\text{Ne V}} > -0.5$ can have photoionization origin from the typical UV background. On the other hand, if the ratio $\frac{\text{C IV}}{\text{Ne V}} < -1.0$, it is more likely produced via collisions or via quasar proximity effect.

CHAPTER 7

Conclusions & Future Directions

7.1 Summary of the Results

The observational studies of warm-hot baryons at low-redshift universe are mostly based on the detection of highly ionized metal lines of O VI and Ne VIII in the UV spectrum of background quasars. Among them, the origin of O VI was highly ambiguous whereas Ne VIII is treated as an explicit tracer of shock-heated warm hot baryons. The recent studies of Kollmeier et al. 2014 and Shull et al. 2015 independently measured the H I ionization rate at low redshift which is a factor of $2-5$ times higher than HM12. Kollmeier et al. 2014 referred this as photon underproduction crisis and suggests the contribution of additional radiation sources such as low luminosity hidden QSOs or decaying dark matter particles to solve this problem. However, using an updated star formation rate and QSO emissivity, KS15 updated the UV background which explains the observed H I ionization rate without the contribution from any additional sources. This new UV background has 3 times higher intensity at energies > 4 Ryd where the ionization potentials of O VI and Ne VIII resides. Such an increase in the intensity of UVB can also increase the production of higher ions at low redshift IGM. In a recent study, Hussain et al. (2017) showed that the updated UV background can also produce Ne VIII by invoking super-solar neon abundance. Though such high metalicities are unusual for gas outside of galaxies, the analysis nonetheless points to the fact that Ne VIII can no longer be regarded as an explicit tracer of warm-hot baryons. Understanding the ionization of these absorbers, their multiphase properties, and their total baryonic content requires careful analysis of individual absorption systems.

In this thesis, we have done a detailed analysis of four intervening absorbers consisting of highly ionized metal ions of O VI and Ne VIII. Among them, two of the absorbers are detected with Ne VIII and one with O VI and thermally broad-Lyα line which collectively revealed the presence of a warm hot gas phase in each case. At the same time, O VI absorption in the fourth absorber is produced from a photoionized gas phase. Thus, we conclude that the detection of O VI or Ne VIII with additional evidence for the presence of a BLA, still holds the capacity to reveal the presence of $T \geq 10^5$ K gas in complex multiphase absorbers.

We find one another species Ne V, which hold the properties similar to O VI and Ne VIII absorbers. In an analysis of five Ne V absorbers discussed in this thesis, we find two of them probing gas in the transverse proximity zone of foreground quasars, one is consistent with the intergalactic origin via photoionisation of UV background and the remaining two could be either associated with a warm baryonic gas phase or with some undetected quasars.

7.2 Highlights of the Research

1. Using O VI, Ne VIII doublet transition and also thermally Broad-Lyα, we find the evidence for the presence of warm hot baryons in the low-redshift universe. Our work shows the capability of Ne VIII, O VI and BLA in revealing the presence of $T \geq 10^5$ K gas in complex multiphase absorbers.

2. The studies of O VI absorbers are often ambiguous in determining whether the gas is photoionized or collisionally ionized. We detected two nearby O VI absorbers separated by ~ 700 km s^{-1} where one is tracing shock-heated gas whereas the other one is tracing photoionized cooler gas. This supports the ambiguous of O VI origin. With this, we demonstrate the importance of carrying out a detailed analysis on individual absorbers to understand the multiphase gas properties in a complete way than what large survey of such absorbers can afford.

3. Before this research work, there were 10 instances of Ne VIII detections in the intervening absorbers. We contribute two more detections to it, both of which are probing $T \geq 10^5$ K plasma in the galaxy overdensity regions.

4. The recently updated UV background questioned the origin of Ne VIII as an explicit tracer for warm - hot baryons. From a detailed analysis of the Ne VIII absorbers reported in this work, we find that metallicity plays a crucial role in determining the origin of the Ne VIII as either shock -heated or photoionized gas. One of the Ne VIII reported in this work can be explained by the photoionization model only with a super-solar abundance of neon, but the subsolar metallicity observed in the remaining ions do not favor such a scenario.

5. We studied the location where these absorbers originate. All the absorbers are likely coming from a galaxy overdensity regions. In one instance, we found the absorber tracing gas within the virial radii of a galaxy. In all the remaining cases, the absorber is tracing intra-group gas or warm galactic gas associated with galaxies whose luminosities are below the SDSS detection threshold.

6. For the first time, we report the detection of Ne V in absorption at high redshift intergalactic medium. The detection of this ion is useful to understand the local enhancement of UV radiation in intergalactic regions, to understand the origin of ionization of the gas and to discriminate various ionization processes in IGM. This is the only second instance of detection of Ne V absorption in the intergalactic medium.

7. There are five instances of Ne V detections in the high redshift intervening absorbers. The ionization modeling of these absorbers revealed the ambiguity of the origin Ne V in the intergalactic medium. We find $\frac{\text{C IV}}{\text{Ne V}}$ ratio is sensitive to the ionization scenario of the absorber. For $\frac{\text{C IV}}{\text{Ne V}} > -0.5$, the absorber is likely following a photoionization scenario whereas the ratio of $\frac{\text{C IV}}{\text{Ne V}} < -1.0$ is more likely dominated by other processes such as collisional ionisations, winds/turbulence or the proximity effects of associated quasars.

7.3 Future Directions

Absorption line spectroscopy has been highly successful in studying the physical and chemical properties of the gas in the circum-galactic and intergalactic regions. The study of absorption lines along the various quasar sightlines from the ground as well as from space has provided a statistical sampling of halo gas (Tumlinson et al., 2017). It has also improved our understanding of the warm-hot baryonic reservoirs at low redshift, their absorption line properties, chemical and ionization conditions, and their association with galaxies (Narayanan et al., 2012, 2011b, 2010a,b; Savage et al., 2005, 2011b,c).

The contribution to Ω_b from Ne VIII absorbers will add to the ongoing observational efforts to complete the baryon census in the low redshift universe. In one of the earlier detections of Ne VIII absorber, Narayanan et al. 2009 roughly estimated $\Omega_{\text{Ne VIII}} \sim 0.0026$ which corresponds to a total of $\sim 6\%$ of cosmic baryons. A similar estimate by Meiring et al. 2013 towards the quasar sightline PG 1148+549 (the only quasar sightline detected with 3 intervening Ne VIII absorbers) finds $\Omega_{\text{Ne VIII}} \leq 0.002$ corresponding to $\sim 4\%$ of cosmic baryons. All of these estimates indicates that the baryonic matter associated with Ne VIII absorber population tracing $T > 10^5$ K is comparable to the amount of baryons in galaxies ($\Omega_{\text{galaxies}} \sim 0.0035$, Fukugita and Peebles 2004). However, a precise estimate of their baryonic contribution requires a much larger sample of these absorbers. The future high S/N observations using HST/ COS at redshift $z > 0.4$ will be able to detect the weak doublet transitions of Ne VIII which can slowly increase the size of Ne VIII samples. Also, it is worth to note that we yet have to find an absorber with Ne VIII column density higher than O VI which is a direct evidence of a hot medium with temperature $\sim 10^6$ K. With a better sample of Ne VIII absorbers, one should be able to address these problems in future.

Apart from the absorption line studies using QSO spectroscopy, alternative ways to detect warm-hot baryons are being explored. Some of these methods are briefly discussed below.

- **Sunyaev-Zel'dovich effect**
  The enhancement of energy of CMB photons due to the inverse - Compton heating of high energy electrons is called Sunyaev-Zel'dovich effect. The effect is observationally detected as a shift in the blackbody power spectrum towards higher energy in galaxy clusters where they revealed the presence of hot plasma in the intercluster medium (Grego et al., 2001; Birkinshaw,

1999). The detection of WHIMs outside virialized structures (where the majority of the WHIM baryons resides) requires a limit of detection at least two orders of magnitude less than in galaxy clusters. Using the data from WMAP, Hansen et al. (2005) search for the evidence of these baryons, but could not find any detectable signal only managed to determine an upper limit in their signal strength. At present, there are several large surveys focusing on the detection of ICM which can significantly improve the information of gas in galaxy clusters (Swetz et al., 2011; Carlstrom et al., 2011; Planck Collaboration et al., 2016, 2017; Bengaly et al., 2017). The recent study of de Graaff et al. 2017 finds the evidence for WHIMs in the stacked filamentary structure which can account $\sim 30\%$ of the total baryons in the universe. This is a promising way to find a statistical evidence for the presence of WHIMs in IGM in future.

- **Dispersion Measurements**

  This method is based on the detection of frequency dependent variation of refractive index observed in ionized plasma. The change in refractive index can be calculated from the time delay in the pulse arrival at different frequencies. The observed time delay is proportional to the dispersion measurement which can be converted to the corresponding electron column density. To convert electron column density to the mass of WHIM, a prior knowledge of the metal abundance and ionization corrections are required. The major limitation of this method is that it requires a pulsating source in the background of the WHIM. The ideal source for such studies is the class of objects called pulsars. Unfortunately, there is no detection of pulsars at cosmological distances. The upcoming space telescope James Webb Space Telescope(JWST) expected to launch in 2018 may be able to detect pulsars at cosmological distances. Another class of objects suitable for dispersion measurement is the gamma-ray burst. Their radio emissions can be suitable for dispersion studies with the upcoming instrument such as Square Kilometer Array(SKA).

- **Radio Hyperfine Lines**

  The detection of the hyperfine transition from hydrogen-like atoms is another possible way to detect WHIMs. The transition of N VII at 53.2 GHz is accessible at $z > 0.1$ for ground-based felicities, but the line is weak for detection(Goddard and Ferland, 2003).

Recently, ISRO (Indian Space Research Organisation) launched the space-based telescope 'Astrosat' with UV imaging and spectral capabilities (UVIT) (Subramaniam, 2012). However, the spectral resolution and sensitivity of this telescope are not sufficient to detect the warm -hot baryons either from their absorption or from their emission. Detecting the shock-heated warm-hot gas in emission from IGM at low redshift would require higher sensitivity detectors in the far UV such as what is being planned for NASA's Large Ultraviolet/ Optical/ Near-Infrared Surveyor (LUVOIR). This space observatory, expected for launch in 2030, should be able to map temperature, density and the rate of flow of gas in CGM from their UV emission. This could answer various unanswered questions including the missing warm - hot baryons in the IGM, the role of CGM in the formation and evolution of galaxies, different feedback mechanism in galaxies in the form of inflows and outflows and the piece of information of the recycle mechanisms in galaxies.

REFERENCES

1. Allen, S. W., Rapetti, D. A., Schmidt, R. W., Ebeling, H., Morris, R. G., and Fabian, A. C. (2008). Improved constraints on dark energy from Chandra X-ray observations of the largest relaxed galaxy clusters. *MNRAS*, *383*, 879–896.

2. Allen, S. W., Schmidt, R. W., and Fabian, A. C. (2002). Cosmological constraints from the X-ray gas mass fraction in relaxed lensing clusters observed with Chandra. *MNRAS*, *334*, L11–L15.

3. Armus, L., Charmandaris, V., Bernard-Salas, J., Spoon, H. W. W., Marshall, J. A., Higdon, S. J. U., Desai, V., Teplitz, H. I., Hao, L., Devost, D., Brandl, B. R., Wu, Y., Sloan, G. C., Soifer, B. T., Houck, J. R., and Herter, T. L. (2007). Observations of Ultraluminous Infrared Galaxies with the Infrared Spectrograph on the Spitzer Space Telescope. II. The IRAS Bright Galaxy Sample. *ApJ*, *656*, 148–167.

4. Armus, L., Charmandaris, V., Spoon, H. W. W., Houck, J. R., Soifer, B. T., Brandl, B. R., Appleton, P. N., Teplitz, H. I., Higdon, S. J. U., Weedman, D. W., Devost, D., Morris, P. W., Uchida, K. I., van Cleve, J., Barry, D. J., Sloan, G. C., Grillmair, C. J., Burgdorf, M. J., Fajardo-Acosta, S. B., Ingalls, J. G., Higdon, J., Hao, L., Bernard-Salas, J., Herter, T., Troeltzsch, J., Unruh, B., and Winghart, M. (2004). Observations of Ultraluminous Infrared Galaxies with the Infrared Spectrograph (IRS) on the Spitzer Space Telescope: Early Results on Markarian 1014, Markarian 463, and UGC 5101. *ApJS*, *154*, 178–183.

5. Asplund, M., Grevesse, N., Sauval, A. J., and Scott, P. (2009). The Chemical Composition of the Sun. *ARA&A*, *47*, 481–522.

6. Bahcall, J. N., and Spitzer, L., Jr. (1969). Absorption Lines Produced by Galactic Halos. *ApJ*, *156*, L63.

7. Ballester, P., Modigliani, A., Boitquin, O., Cristiani, S., Hanuschik, R., Kaufer, A., and Wolf, S. (2000). The UVES Data Reduction Pipeline. *The Messenger*, *101*, 31–36.

8. Bechtold, J., Crotts, A. P. S., Duncan, R. C., and Fang, Y. (1994). Spectroscopy of the double quasars Q1343+266A, B: A new determination of the size of Lyman-alpha forest absorbers. *ApJ*, *437*, L83–L86.

9. Belli, S., Genzel, R., Förster Schreiber, N. M., Wisnioski, E., Wilman, D. J., Wuyts, S., Mendel, J. T., Beifiori, A., Bender, R., Brammer, G. B., Burkert, A., Chan, J., Davies, R. L., Davies, R., Fabricius, M., Fossati, M., Galametz, A., Lang, P., Lutz, D., Momcheva, I. G., Nelson, E. J., Saglia, R. P., Tacconi, L. J., Tadaki, K.-i., Übler, H., and van Dokkum, P. (2017). KMOS^{3D} Reveals Low-level Star Formation Activity in Massive Quiescent Galaxies at 0.7z2.7. *ApJ*, *841*, L6.

10. Bengaly, C. A. P., Bernui, A., Ferreira, I. S., and Alcaniz, J. S. (2017). Probing cosmological isotropy with Planck Sunyaev-Zeldovich galaxy clusters. *MNRAS*, *466*, 2799–2804.

11. Bennett, C. L., Larson, D., Weiland, J. L., and Hinshaw, G. (2014). The 1% Concordance Hubble Constant. *ApJ*, *794*, 135.

12. Bergeron, J., Petitjean, P., Aracil, B., Pichon, C., Scannapieco, E., Srianand, R., Boisse, P., Carswell, R. F., Chand, H., Cristiani, S., Ferrara, A., Haehnelt, M., Hughes, A., Kim, T.-S., Ledoux, C., Richter, P., and Viel, M. (2004). The large programme "Cosmic Evolution of the IGM". *The Messenger*, *118*, 40–44.

13. Birkinshaw, M. (1999). The Sunyaev-Zel'dovich effect: an update. In L. Maiani, F. Melchiorri, and N. Vittorio (Eds.), *3K cosmology* (pp. 298–309). volume 476 of *American Institute of Physics Conference Series*.

14. Birnboim, Y., and Dekel, A. (2003). Virial shocks in galactic haloes? *MNRAS*, *345*, 349–364.

15. Blanton, M. R., Hogg, D. W., Bahcall, N. A., Brinkmann, J., Britton, M., Connolly, A. J., Csabai, I., Fukugita, M., Loveday, J., Meiksin, A., Munn, J. A., Nichol, R. C., Okamura, S., Quinn, T., Schneider, D. P., Shimasaku, K., Strauss, M. A., Tegmark, M., Vogeley, M. S., and Weinberg, D. H. (2003). The Galaxy

Luminosity Function and Luminosity Density at Redshift z = 0.1. *ApJ*, *592*, 819–838.

16. Boehringer, H., Chon, G., and Fukugita, M. (2017). The extended ROSAT-ESO Flux-Limited X-ray Galaxy Cluster Survey (REFLEX II) VII The Mass Function of Galaxy Clusters. *ArXiv e-prints*, .

17. Boehringer, H., and Hartquist, T. W. (1987). Steady models of radiatively modified conductively driven evaporation from interstellar clouds. *MNRAS*, *228*, 915–931.

18. Bolton, J. S., and Becker, G. D. (2009). Resolving the high redshift Lyα forest in smoothed particle hydrodynamics simulations. *MNRAS*, *398*, L26–L30.

19. Bordoloi, R., Heckman, T. M., and Norman, C. A. (2016). The formation and physical origin of highly ionized cooling gas. *ArXiv e-prints*, .

20. Bordoloi, R., Tumlinson, J., Werk, J. K., Oppenheimer, B. D., Peeples, M. S., Prochaska, J. X., Tripp, T. M., Katz, N., Davé, R., Fox, A. J., Thom, C., Ford, A. B., Weinberg, D. H., Burchett, J. N., and Kollmeier, J. A. (2014). The COS-Dwarfs Survey: The Carbon Reservoir around Sub-L* Galaxies. *ApJ*, *796*, 136.

21. Bregman, J. N., and Lloyd-Davies, E. J. (2007). X-Ray Absorption from the Milky Way Halo and the Local Group. *ApJ*, *669*, 990–1002.

22. Briggs, F. H., and Wolfe, A. M. (1983). The incidence of 21 centimeter absorption in QSO redshift systems selected for MG II absorption - Evidence for a two-phase nature of the absorbing gas. *ApJ*, *268*, 76–89.

23. Bunn, E. F., and White, M. (1997). The 4 Year COBE Normalization and Large-Scale Structure. *ApJ*, *480*, 6–21.

24. Carlstrom, J. E., Ade, P. A. R., Aird, K. A., Benson, B. A., Bleem, L. E., Busetti, S., Chang, C. L., Chauvin, E., Cho, H.-M., Crawford, T. M., Crites, A. T., Dobbs, M. A., Halverson, N. W., Heimsath, S., Holzapfel, W. L., Hrubes, J. D., Joy, M., Keisler, R., Lanting, T. M., Lee, A. T., Leitch, E. M., Leong, J., Lu, W., Lueker, M., Luong-Van, D., McMahon, J. J., Mehl, J., Meyer, S. S., Mohr, J. J., Montroy, T. E., Padin, S., Plagge, T., Pryke, C., Ruhl, J. E., Schaffer, K. K.,

Schwan, D., Shirokoff, E., Spieler, H. G., Staniszewski, Z., Stark, A. A., Tucker, C., Vanderlinde, K., Vieira, J. D., and Williamson, R. (2011). The 10 Meter South Pole Telescope. *PASP*, *123*, 568.

25. Cen, R., Miralda-Escudé, J., Ostriker, J. P., and Rauch, M. (1994). Gravitational collapse of small-scale structure as the origin of the Lyman-alpha forest. *ApJ*, *437*, L9–L12.

26. Cen, R., and Ostriker, J. P. (1999). Where Are the Baryons? *ApJ*, *514*, 1–6.

27. Cen, R., and Ostriker, J. P. (2006). Where Are the Baryons? II. Feedback Effects. *ApJ*, *650*, 560–572.

28. Chapman, S. C., Blain, A. W., Smail, I., and Ivison, R. J. (2005). A Redshift Survey of the Submillimeter Galaxy Population. *ApJ*, *622*, 772–796.

29. Charlton, J., and Churchill, C. (2000). Quasistellar Objects: Intervening Absorption Lines. In P. Murdin (Ed.), *Encyclopedia of Astronomy and Astrophysics*.

30. Chen, H.-W., and Mulchaey, J. S. (2009). Probing The Intergalactic Medium-Galaxy Connection At z 0.5. I. A Galaxy Survey In Qso Fields And A Galaxy-Absorber Cross-Correlation Study. *ApJ*, *701*, 1219–1242.

31. Colless, M., Dalton, G., Maddox, S., Sutherland, W., Norberg, P., Cole, S., Bland-Hawthorn, J., Bridges, T., Cannon, R., Collins, C., Couch, W., Cross, N., Deeley, K., De Propris, R., Driver, S. P., Efstathiou, G., Ellis, R. S., Frenk, C. S., Glazebrook, K., Jackson, C., Lahav, O., Lewis, I., Lumsden, S., Madgwick, D., Peacock, J. A., Peterson, B. A., Price, I., Seaborne, M., and Taylor, K. (2001). The 2dF Galaxy Redshift Survey: spectra and redshifts. *MNRAS*, *328*, 1039–1063.

32. Cosmic Origins Spectrograph Instrument Handbook (), .

33. Croft, R. A. C. (2004). Ionizing Radiation Fluctuations and Large-Scale Structure in the Lyα Forest. *ApJ*, *610*, 642–662.

34. Croom, S. M., Richards, G. T., Shanks, T., Boyle, B. J., Strauss, M. A., Myers, A. D., Nichol, R. C., Pimbblet, K. A., Ross, N. P., Schneider, D. P., Sharp, R. G., and Wake, D. A. (2009). The 2dF-SDSS LRG and QSO survey: the QSO luminosity function at 0.4 z 2.6. *MNRAS*, *399*, 1755–1772.

35. Cyburt, R. H., Fields, B. D., Olive, K. A., and Yeh, T.-H. (2016). Big bang nucleosynthesis: Present status. *Reviews of Modern Physics*, *88*, 015004.

36. Danforth, C. W., Keeney, B. A., Tilton, E. M., Shull, J. M., Stocke, J. T., Stevans, M., Pieri, M. M., Savage, B. D., France, K., Syphers, D., Smith, B. D., Green, J. C., Froning, C., Penton, S. V., and Osterman, S. N. (2016). An HST/COS Survey of the Low-redshift Intergalactic Medium. I. Survey, Methodology, and Overall Results. *ApJ*, *817*, 111.

37. Danforth, C. W., and Shull, J. M. (2005). The Low-z Intergalactic Medium. I. O VI Baryon Census. *ApJ*, *624*, 555–560.

38. Danforth, C. W., and Shull, J. M. (2008). The Low-z Intergalactic Medium. III. H I and Metal Absorbers at z 0.4. *ApJ*, *679*, 194–219.

39. Danforth, C. W., Shull, J. M., Rosenberg, J. L., and Stocke, J. T. (2006). The Low-z Intergalactic Medium. II. Lyβ, O VI, and C III Forest. *ApJ*, *640*, 716–740.

40. Danforth, C. W., Stocke, J. T., and Shull, J. M. (2010). Broad H I Absorbers as Metallicity-independent Tracers of the Warm-Hot Intergalactic Medium. *ApJ*, *710*, 613–633.

41. Davé, R., Cen, R., Ostriker, J. P., Bryan, G. L., Hernquist, L., Katz, N., Weinberg, D. H., Norman, M. L., and O'Shea, B. (2001). Baryons in the Warm-Hot Intergalactic Medium. *ApJ*, *552*, 473–483.

42. Davé, R., Dubinski, J., and Hernquist, L. (1997). Parallel TreeSPH. *New A*, *2*, 277–297.

43. de Graaff, A., Cai, Y.-C., Heymans, C., and Peacock, J. A. (2017). Missing baryons in the cosmic web revealed by the Sunyaev-Zel'dovich effect. *ArXiv e-prints*, .

44. Decarli, R., Walter, F., Aravena, M., Carilli, C., Bouwens, R., da Cunha, E., Daddi, E., Elbaz, D., Riechers, D., Smail, I., Swinbank, M., Weiss, A., Bacon, R., Bauer, F., Bell, E. F., Bertoldi, F., Chapman, S., Colina, L., Cortes, P. C., Cox, P., Gónzalez-López, J., Inami, H., Ivison, R., Hodge, J., Karim, A., Magnelli, B., Ota, K., Popping, G., Rix, H.-W., Sargent, M., van der Wel, A., and van der Werf, P. (2016). The ALMA Spectroscopic Survey in the Hubble Ultra Deep Field: Molecular Gas Reservoirs in High-redshift Galaxies. *ApJ*, *833*, 70.

45. Dinshaw, N., Weymann, R. J., Impey, C. D., Foltz, C. B., Morris, S. L., and Ake, T. (1997). Additional Observations and Analysis of the Lyman-α Absorption Lines toward the QSO Pair Q0107-025A,B. *ApJ*, *491*, 45–68.

46. Dixon, W. (2010). STIS CCD Full-Field Sensitivity Monitor C18. HST Proposal.

47. Drake, J. J., and Testa, P. (2005). The 'solar model problem' solved by the abundance of neon in nearby stars. *Nature*, *436*, 525–528.

48. Dutta, R., Srianand, R., Rahmani, H., Petitjean, P., Noterdaeme, P., and Ledoux, C. (2014). A study of low-metallicity DLAs at high redshift and C II* as a probe of their physical conditions. *MNRAS*, *440*, 307–326.

49. Edlen, B. (1966). Report of the Committee on Standards of Wavelength. *Transactions of the International Astronomical Union, Series B*, *12*, 176.

50. Fang, T., Mckee, C. F., Canizares, C. R., and Wolfire, M. (2006). A Galactic Origin for the Local Ionized X-Ray Absorbers. *ApJ*, *644*, 174–179.

51. Fardal, M. A., and Shull, J. M. (1993). The Two-Point Correlation Function of Randomly Distributed Lyman-Alpha Clouds. *ApJ*, *415*, 524.

52. Ferland, G. J., Porter, R. L., van Hoof, P. A. M., Williams, R. J. R., Abel, N. P., Lykins, M. L., Shaw, G., Henney, W. J., and Stancil, P. C. (2013a). The 2013 Release of Cloudy. *Rev. Mexicana Astron. Astrofis.*, *49*, 137–163.

53. Ferland, G. J., Porter, R. L., van Hoof, P. A. M., Williams, R. J. R., Abel, N. P., Lykins, M. L., Shaw, G., Henney, W. J., and Stancil, P. C. (2013b). The 2013 Release of Cloudy. *Rev. Mexicana Astron. Astrofis.*, *49*, 137–163.

54. Field, G. B. (1959). An Attempt to Observe Neutral Hydrogen Between the Galaxies. *ApJ*, *129*, 525.

55. Fitzpatrick, E. L., and Spitzer, L., Jr. (1997). Composition of Interstellar Clouds in the Disk and Halo. IV. HD 215733. *ApJ*, *475*, 623–641.

56. Foltz, C. B., Weymann, R. J., Peterson, B. M., Sun, L., Malkan, M. A., and Chaffee, F. H., Jr. (1986). C IV absorption systems in QSO spectra - Is the character of systems with Z(abs) = about Z(em) different from those with Z(abs) much less than Z(em)? *ApJ*, *307*, 504–534.

57. Fox, A. J., Ledoux, C., Vreeswijk, P. M., Smette, A., and Jaunsen, A. O. (2008). High-ion absorption in seven GRB host galaxies at z = 2-4. Evidence for both circumburst plasma and outflowing interstellar gas. *A&A*, *491*, 189–207.

58. Fox, A. J., Lehner, N., Tumlinson, J., Howk, J. C., Tripp, T. M., Prochaska, J. X., O'Meara, J. M., Werk, J. K., Bordoloi, R., Katz, N., Oppenheimer, B. D., and Davé, R. (2013). The High-ion Content and Kinematics of Low-redshift Lyman Limit Systems. *ApJ*, *778*, 187.

59. Fox, A. J., Savage, B. D., Wakker, B. P., Richter, P., Sembach, K. R., and Tripp, T. M. (2004). Highly Ionized Gas Surrounding High-Velocity Cloud Complex C. *ApJ*, *602*, 738–759.

60. Fox, A. J., Wakker, B. P., Savage, B. D., Tripp, T. M., Sembach, K. R., and Bland-Hawthorn, J. (2005). Multiphase High-Velocity Clouds toward HE 0226-4110 and PG 0953+414. *ApJ*, *630*, 332–354.

61. Froning, C. S., and Green, J. C. (2009). The cosmic origins spectrograph: capabilities and prelaunch performance. *Ap&SS*, *320*, 181–185.

62. Fukugita, M., and Peebles, P. J. E. (2004). The Cosmic Energy Inventory. *ApJ*, *616*, 643–668.

63. Gaikwad, P., Khaire, V., Choudhury, T. R., and Srianand, R. (2016a). Intergalactic Lyman continuum photon budget in the past 5 billion years. *ArXiv e-prints*, .

64. Gaikwad, P., Srianand, R., Choudhury, T. R., and Khaire, V. (2016b). VoIgt profile Parameter Estimation Routine (VIPER): H I photoionization rate at z0.5. *ArXiv e-prints*, .

65. Ganguly, R., Sembach, K. R., Tripp, T. M., Savage, B. D., and Wakker, B. P. (2006). High-Resolution Absorption Spectroscopy of Multiphase, High-Metallicity Gas Associated with the Luminous Quasar HE 0226-4110. *ApJ*, *645*, 868–889.

66. Gawiser, E., Francke, H., Lai, K., Schawinski, K., Gronwall, C., Ciardullo, R., Quadri, R., Orsi, A., Barrientos, L. F., Blanc, G. A., Fazio, G., Feldmeier, J. J., Huang, J.-s., Infante, L., Lira, P., Padilla, N., Taylor, E. N., Treister, E., Urry,

C. M., van Dokkum, P. G., and Virani, S. N. (2007). Lyα-Emitting Galaxies at z = 3.1: L* Progenitors Experiencing Rapid Star Formation. *ApJ*, *671*, 278–284.

67. Ge, J., and Bechtold, J. (1997). Molecular Hydrogen Absorption in the z = 1.97 Damped Lyα Absorption System toward Quasi-Stellar Object Q0013-004. *ApJ*, *477*, L73–L77.

68. Gnat, O., and Sternberg, A. (2007). Time-dependent Ionization in Radiatively Cooling Gas. *ApJS*, *168*, 213–230.

69. Goddard, W. E., and Ferland, G. J. (2003). Hyperfine Structure Emission and Absorption Lines in Hot Gas. *PASP*, *115*, 647–650.

70. Green, J. C., Froning, C. S., Osterman, S., Ebbets, D., Heap, S. H., Leitherer, C., Linsky, J. L., Savage, B. D., Sembach, K., Shull, J. M., Siegmund, O. H. W., Snow, T. P., Spencer, J., Stern, S. A., Stocke, J., Welsh, B., Béland, S., Burgh, E. B., Danforth, C., France, K., Keeney, B., McPhate, J., Penton, S. V., Andrews, J., Brownsberger, K., Morse, J., and Wilkinson, E. (2012). The Cosmic Origins Spectrograph. *ApJ*, *744*, 60.

71. Grego, L., Carlstrom, J. E., Reese, E. D., Holder, G. P., Holzapfel, W. L., Joy, M. K., Mohr, J. J., and Patel, S. (2001). Galaxy Cluster Gas Mass Fractions from Sunyaev-Zeldovich Effect Measurements: Constraints on Ω_M. *ApJ*, *552*, 2–14.

72. Grevesse, N., Asplund, M., Sauval, A. J., and Scott, P. (2010). The chemical composition of the Sun. *Ap&SS*, *328*, 179–183.

73. Gunn, J. E., and Peterson, B. A. (1965). On the Density of Neutral Hydrogen in Intergalactic Space. *ApJ*, *142*, 1633–1641.

74. Haardt, F., and Madau, P. (1996). Radiative Transfer in a Clumpy Universe. II. The Ultraviolet Extragalactic Background. *ApJ*, *461*, 20.

75. Haardt, F., and Madau, P. (2012). Radiative Transfer in a Clumpy Universe. IV. New Synthesis Models of the Cosmic UV/X-Ray Background. *ApJ*, *746*, 125.

76. Hansen, F. K., Branchini, E., Mazzotta, P., Cabella, P., and Dolag, K. (2005). A full-sky prediction of the Sunyaev-Zeldovich effect from diffuse hot gas in the local universe and the upper limit from the WMAP data. *MNRAS*, *361*, 753–762.

77. Hernquist, L., Katz, N., Weinberg, D. H., and Miralda-Escudé, J. (1996). The Lyman-Alpha Forest in the Cold Dark Matter Model. *ApJ*, *457*, L51.

78. Hewett, P. C., and Wild, V. (2010). Improved redshifts for SDSS quasar spectra. *MNRAS*, *405*, 2302–2316.

79. Howk, J. C., Savage, B. D., Sembach, K. R., and Hoopes, C. G. (2002). Far-Ultraviolet Spectroscopic Explorer Observations of Degree-Scale Variations in Galactic Halo OVI. *ApJ*, *572*, 264–275.

80. Huchra, J. P., Macri, L. M., Masters, K. L., Jarrett, T. H., Berlind, P., Calkins, M., Crook, A. C., Cutri, R., Erdoğdu, P., Falco, E., George, T., Hutcheson, C. M., Lahav, O., Mader, J., Mink, J. D., Martimbeau, N., Schneider, S., Skrutskie, M., Tokarz, S., and Westover, M. (2012). The 2MASS Redshift SurveyDescription and Data Release. *ApJS*, *199*, 26.

81. Hussain, T., Khaire, V., Srianand, R., Muzahid, S., and Pathak, A. (2017). Implications of an updated ultraviolet background for the ionization mechanisms of intervening Ne VIII absorbers. *MNRAS*, *466*, 3133–3142.

82. Hussain, T., Muzahid, S., Narayanan, A., Srianand, R., Wakker, B. P., Charlton, J. C., and Pathak, A. (2015). HST/COS detection of a Ne VIII absorber towards PG 1407+265: an unambiguous tracer of collisionally ionized hot gas? *MNRAS*, *446*, 2444–2455.

83. Ikeuchi, S. (1986). The baryon clump within an extended dark matter region. *Ap&SS*, *118*, 509–514.

84. Ilbert, O., Tresse, L., Zucca, E., Bardelli, S., Arnouts, S., Zamorani, G., Pozzetti, L., Bottini, D., Garilli, B., Le Brun, V., Le Fèvre, O., Maccagni, D., Picat, J.-P., Scaramella, R., Scodeggio, M., Vettolani, G., Zanichelli, A., Adami, C., Arnaboldi, M., Bolzonella, M., Cappi, A., Charlot, S., Contini, T., Foucaud, S., Franzetti, P., Gavignaud, I., Guzzo, L., Iovino, A., McCracken, H. J., Marano, B., Marinoni, C., Mathez, G., Mazure, A., Meneux, B., Merighi, R., Paltani, S., Pello, R., Pollo, A., Radovich, M., Bondi, M., Bongiorno, A., Busarello, G., Ciliegi, P., Lamareille, F., Mellier, Y., Merluzzi, P., Ripepi, V., and Rizzo, D. (2005). The VIMOS-VLT deep survey. Evolution of the galaxy luminosity function up to z = 2 in first epoch data. *A&A*, *439*, 863–876.

85. Inami, H., Armus, L., Charmandaris, V., Groves, B., Kewley, L., Petric, A., Stierwalt, S., Díaz-Santos, T., Surace, J., Rich, J., Haan, S., Howell, J., Evans, A. S., Mazzarella, J., Marshall, J., Appleton, P., Lord, S., Spoon, H., Frayer, D., Matsuhara, H., and Veilleux, S. (2013). Mid-infrared Atomic Fine-structure Emission-line Spectra of Luminous Infrared Galaxies: Spitzer/IRS Spectra of the GOALS Sample. *ApJ*, *777*, 156.

86. Johnson, S. D., Chen, H.-W., and Mulchaey, J. S. (2015). On the possible environmental effect in distributing heavy elements beyond individual gaseous haloes. *MNRAS*, *449*, 3263–3273.

87. Kaastra, J. S., Werner, N., Herder, J. W. A. d., Paerels, F. B. S., de Plaa, J., Rasmussen, A. P., and de Vries, C. P. (2006). The O VII X-Ray Forest toward Markarian 421: Consistency between XMM-Newton and Chandra. *ApJ*, *652*, 189–197.

88. Kanekar, N., and Chengalur, J. N. (2003). A deep search for 21-cm absorption in high redshift damped Lyman-alpha systems. *A&A*, *399*, 857–868.

89. Kauffmann, G., Heckman, T. M., White, S. D. M., Charlot, S., Tremonti, C., Peng, E. W., Seibert, M., Brinkmann, J., Nichol, R. C., SubbaRao, M., and York, D. (2003). The dependence of star formation history and internal structure on stellar mass for 10^5 low-redshift galaxies. *MNRAS*, *341*, 54–69.

90. Kawasaki, M., Kohri, K., Moroi, T., and Yotsuyanagi, A. (2008). Big-bang nucleosynthesis and gravitinos. *Phys. Rev. D*, *78*, 065011.

91. Kennicutt, R. C., Jr., Tamblyn, P., and Congdon, C. E. (1994). Past and future star formation in disk galaxies. *ApJ*, *435*, 22–36.

92. Keres, D., Yun, M. S., and Young, J. S. (2003). CO Luminosity Functions for Far-Infrared- and B-Band-selected Galaxies and the First Estimate for Ω_{HI}+H_2. *ApJ*, *582*, 659–667.

93. Khaire, V., and Srianand, R. (2013). He II optical depth and ultraviolet escape fraction of galaxies. *MNRAS*, *431*, L53–L57.

94. Khaire, V., and Srianand, R. (2015a). Photon underproduction crisis: Are QSOs sufficient to resolve it? *MNRAS*, *451*, L30–L34.

95. Khaire, V., and Srianand, R. (2015b). Star Formation History, Dust Attenuation, and Extragalactic Background Light. *ApJ*, *805*, 33.

96. Kollmeier, J. A., Weinberg, D. H., Oppenheimer, B. D., Haardt, F., Katz, N., Davé, R., Fardal, M., Madau, P., Danforth, C., Ford, A. B., Peeples, M. S., and McEwen, J. (2014). The Photon Underproduction Crisis. *ApJ*, *789*, L32.

97. Kriek, M., van Dokkum, P. G., Franx, M., Quadri, R., Gawiser, E., Herrera, D., Illingworth, G. D., Labbé, I., Lira, P., Marchesini, D., Rix, H.-W., Rudnick, G., Taylor, E. N., Toft, S., Urry, C. M., and Wuyts, S. (2006). Spectroscopic Identification of Massive Galaxies at z ˜ 2.3 with Strongly Suppressed Star Formation. *ApJ*, *649*, L71–L74.

98. Kriss, G. A., Arav, N., Kaastra, J. S., Ebrero, J., Pinto, C., Borguet, B., Edmonds, D., Costantini, E., Steenbrugge, K. C., Detmers, R. G., Behar, E., Bianchi, S., Blustin, A. J., Branduardi-Raymont, G., Cappi, M., Mehdipour, M., Petrucci, P., and Ponti, G. (2011). Multiwavelength campaign on Mrk 509. VI. HST/COS observations of the far-ultraviolet spectrum. *A&A*, *534*, A41.

99. Le Floc'h, E., Duc, P.-A., Mirabel, I. F., Sanders, D. B., Bosch, G., Diaz, R. J., Donzelli, C. J., Rodrigues, I., Courvoisier, T. J.-L., Greiner, J., Mereghetti, S., Melnick, J., Maza, J., and Minniti, D. (2003). Are the hosts of gamma-ray bursts sub-luminous and blue galaxies? *A&A*, *400*, 499–510.

100. Lehner, N., Howk, J. C., Tripp, T. M., Tumlinson, J., Prochaska, J. X., O'Meara, J. M., Thom, C., Werk, J. K., Fox, A. J., and Ribaudo, J. (2013). The Bimodal Metallicity Distribution of the Cool Circumgalactic Medium at z ˜ 1. *ApJ*, *770*, 138.

101. Lehner, N., Prochaska, J. X., Kobulnicky, H. A., Cooksey, K. L., Howk, J. C., Williger, G. M., and Cales, S. L. (2009). The Connection Between a Lyman Limit System, a Very Strong O VI Absorber, and Galaxies at z ˜ 0.203. *ApJ*, *694*, 734–750.

102. Lu, L., and Savage, B. D. (1993). Clear evidence for the presence of O VI absorption in QSO metal systems. *ApJ*, *403*, 127–134.

103. Mathes, N. L., Churchill, C. W., Kacprzak, G. G., Nielsen, N. M., Trujillo-Gomez, S., Charlton, J., and Muzahid, S. (2014). Halo Mass Dependence of H I and O VI Absorption: Evidence for Differential Kinematics. *ApJ*, *792*, 128.

104. McDonald, P., Seljak, U., Cen, R., Bode, P., and Ostriker, J. P. (2005). Physical effects on the Lyα forest flux power spectrum: damping wings, ionizing radiation fluctuations and galactic winds. *MNRAS*, *360*, 1471–1482.

105. Meiring, J. D., Tripp, T. M., Werk, J. K., Howk, J. C., Jenkins, E. B., Prochaska, J. X., Lehner, N., and Sembach, K. R. (2013). QSO Absorption Systems Detected in Ne VIII: High-metallicity Clouds with a Large Effective Cross Section. *ApJ*, *767*, 49.

106. Meyer, M. J., Zwaan, M. A., Webster, R. L., Staveley-Smith, L., Ryan-Weber, E., Drinkwater, M. J., Barnes, D. G., Howlett, M., Kilborn, V. A., Stevens, J., Waugh, M., Pierce, M. J., Bhathal, R., de Blok, W. J. G., Disney, M. J., Ekers, R. D., Freeman, K. C., Garcia, D. A., Gibson, B. K., Harnett, J., Henning, P. A., Jerjen, H., Kesteven, M. J., Knezek, P. M., Koribalski, B. S., Mader, S., Marquarding, M., Minchin, R. F., O'Brien, J., Oosterloo, T., Price, R. M., Putman, M. E., Ryder, S. D., Sadler, E. M., Stewart, I. M., Stootman, F., and Wright, A. E. (2004). The HIPASS catalogue - I. Data presentation. *MNRAS*, *350*, 1195–1209.

107. Miralda-Escudé, J., Cen, R., Ostriker, J. P., and Rauch, M. (1996). The Ly alpha Forest from Gravitational Collapse in the Cold Dark Matter + Lambda Model. *ApJ*, *471*, 582.

108. Morton, D. C. (2003). Atomic Data for Resonance Absorption Lines. III. Wavelengths Longward of the Lyman Limit for the Elements Hydrogen to Gallium. *ApJS*, *149*, 205–238.

109. Mulchaey, J. S., and Chen, H.-W. (2009). The Galactic Environment of the Ne VIII Absorber Toward HE0226 - 4110. *ApJ*, *698*, L46–L50.

110. Mulchaey, J. S., Mushotzky, R. F., Burstein, D., and Davis, D. S. (1996). High-Ionization Quasar Absorption Lines: A Test of the Existence of Hot Gas in Spiral-rich Groups. *ApJ*, *456*, L5.

111. Muzahid, S. (2014). Probing the Large and Massive Circumgalactic Medium of a Galaxy at z ˜ 0.2 using a Pair of Quasars. *ApJ*, *784*, 5.

112. Muzahid, S., Kacprzak, G. G., Churchill, C. W., Charlton, J. C., Nielsen, N. M., Mathes, N. L., and Trujillo-Gomez, S. (2015). An Extreme Metallicity, Large-scale Outflow from a Star-forming Galaxy at z ˜ 0.4. *ApJ*, *811*, 132.

113. Muzahid, S., Srianand, R., Arav, N., Savage, B. D., and Narayanan, A. (2013). HST/COS observations of a new population of associated QSO absorbers. *MNRAS*, *431*, 2885–2906.

114. Muzahid, S., Srianand, R., Bergeron, J., and Petitjean, P. (2012). A high-resolution study of intergalactic O VI absorbers at z
2.3. *MNRAS*, *421*, 446–467.

115. Muzahid, S., Srianand, R., Charlton, J., and Eracleous, M. (2016). On the covering fraction variability in an EUV mini-BAL outflow from PG 1206+459. *MNRAS*, *457*, 2665–2674.

116. Muzahid, S., Srianand, R., and Petitjean, P. (2011). Revisiting the He II to H I ratio in the intergalactic medium. *MNRAS*, *410*, 2193–2202.

117. Narayanan, A., Savage, B. D., and Wakker, B. P. (2010a). Highly Ionized Plasma in the Halo of a Luminous Spiral Galaxy Near z = 0.225. *ApJ*, *712*, 1443–1460.

118. Narayanan, A., Savage, B. D., and Wakker, B. P. (2012). Cosmic Origins Spectrograph Observations of Warm Intervening Gas at z ˜ 0.325 toward 3C 263. *ApJ*, *752*, 65.

119. Narayanan, A., Savage, B. D., Wakker, B. P., Danforth, C. W., Yao, Y., Keeney, B. A., Shull, J. M., Sembach, K. R., Froning, C. S., and Green, J. C. (2011a). Cosmic Origins Spectrograph Detection of Ne VIII Tracing Warm-Hot Gas Toward PKS 0405-123. *ApJ*, *730*, 15.

120. Narayanan, A., Savage, B. D., Wakker, B. P., Danforth, C. W., Yao, Y., Keeney, B. A., Shull, J. M., Sembach, K. R., Froning, C. S., and Green, J. C. (2011b). Cosmic Origins Spectrograph Detection of Ne VIII Tracing Warm-Hot Gas Toward PKS 0405-123. *ApJ*, *730*, 15.

121. Narayanan, A., Wakker, B. P., and Savage, B. D. (2009). Detection of Ne VIII in an Intervening Multiphase Absorption System Toward 3C 263. *ApJ*, *703*, 74–80.

122. Narayanan, A., Wakker, B. P., Savage, B. D., Keeney, B. A., Shull, J. M., Stocke, J. T., and Sembach, K. R. (2010b). Cosmic Origins Spectrograph and FUSE Observations of T ~ 10^5 K Gas in a Nearby Galaxy Filament. *ApJ*, *721*, 960–974.

123. Nicastro, F., Mathur, S., Elvis, M., Drake, J., Fiore, F., Fang, T., Fruscione, A., Krongold, Y., Marshall, H., and Williams, R. (2005). Chandra Detection of the First X-Ray Forest along the Line of Sight To Markarian 421. *ApJ*, *629*, 700–718.

124. Nicastro, F., Zezas, A., Drake, J., Elvis, M., Fiore, F., Fruscione, A., Marengo, M., Mathur, S., and Bianchi, S. (2002). Chandra Discovery of a Tree in the X-Ray Forest toward PKS 2155-304: The Local Filament? *ApJ*, *573*, 157–167.

125. Noterdaeme, P., Laursen, P., Petitjean, P., Vergani, S. D., Maureira, M. J., Ledoux, C., Fynbo, J. P. U., López, S., and Srianand, R. (2012). Discovery of a compact gas-rich damped Lyman-α galaxy at z = 2.2: evidence of a starburst-driven outflow. *A&A*, *540*, A63.

126. O'Meara, J. M., Burles, S., Prochaska, J. X., Prochter, G. E., Bernstein, R. A., and Burgess, K. M. (2006). The Deuterium-to-Hydrogen Abundance Ratio toward the QSO SDSS J155810.16-003120.0. *ApJ*, *649*, L61–L65.

127. Oppenheimer, B. D., and Davé, R. (2009). The nature and origin of low-redshift OVI absorbers. *MNRAS*, *395*, 1875–1904.

128. Oppenheimer, B. D., Davé, R., Katz, N., Kollmeier, J. A., and Weinberg, D. H. (2012). The intergalactic medium over the last 10 billion years - II. Metal-line absorption and physical conditions. *MNRAS*, *420*, 829–859.

129. Osterman, S., Green, J., Froning, C., Béland, S., Burgh, E., France, K., Penton, S., Delker, T., Ebbets, D., Sahnow, D., Bacinski, J., Kimble, R., Andrews, J., Wilkinson, E., McPhate, J., Siegmund, O., Ake, T., Aloisi, A., Biagetti, C., Diaz, R., Dixon, W., Friedman, S., Ghavamian, P., Goudfrooij, P., Hartig, G., Keyes, C., Lennon, D., Massa, D., Niemi, S., Oliveira, C., Osten, R., Proffitt, C., Smith, T., and Soderblom, D. (2011). The Cosmic Origins Spectrograph: on-orbit instrument performance. *Ap&SS*, *335*, 257–265.

130. Ostriker, J. P., Lubin, L. M., and Hernquist, L. (1995). Using X-rays to determine which compact groups are illusory. *ApJ*, *444*, L61–L64.

131. Pachat, S., Narayanan, A., Muzahid, S., Khaire, V., Srianand, R., Wakker, B. P., and Savage, B. D. (2016). A pair of O VI and broad Ly α absorbers probing warm gas in a galaxy group environment at z
0.4. *MNRAS*, *458*, 733–746.

132. Palanque-Delabrouille, N., Magneville, C., Yèche, C., Eftekharzadeh, S., Myers, A. D., Petitjean, P., Pâris, I., Aubourg, E., McGreer, I., Fan, X., Dey, A., Schlegel, D., Bailey, S., Bizayev, D., Bolton, A., Dawson, K., Ebelke, G., Ge, J., Malanushenko, E., Malanushenko, V., Oravetz, D., Pan, K., Ross, N. P., Schneider, D. P., Sheldon, E., Simmons, A., Tinker, J., White, M., and Willmer, C. (2013). Luminosity function from dedicated SDSS-III and MMT data of quasars in 0.7 z 4.0 selected with a new approach. *A&A*, *551*, A29.

133. Paschos, P., Jena, T., Tytler, D., Kirkman, D., and Norman, M. L. (2009). The Lyα forest at redshifts 0.1-1.6: good agreement between a large hydrodynamic simulation and HST spectra. *MNRAS*, *399*, 1934–1953.

134. Penton, S. V., Stocke, J. T., and Shull, J. M. (2002). The Local Lyα Forest. III. Relationship between Lyα Absorbers and Galaxies, Voids, and Superclusters. *ApJ*, *565*, 720–742.

135. Petitjean, P., and Srianand, R. (1999). The z_{abs} ˜ z_{em} absorption line systems toward QSO J 2233-606 in the Hubble Deep Field South: NE viii lambda lambda 770,780 absorption and partial coverage absorption line systems toward QSO J 2233-606. *A&A*, *345*, 73–80.

136. Petitjean, P., Srianand, R., and Ledoux, C. (2000). Molecular hydrogen and the nature of damped Lyman-alpha systems. *A&A*, *364*, L26–L30.

137. Petric, A. O., Armus, L., Howell, J., Chan, B., Mazzarella, J. M., Evans, A. S., Surace, J. A., Sanders, D., Appleton, P., Charmandaris, V., Díaz-Santos, T., Frayer, D., Haan, S., Inami, H., Iwasawa, K., Kim, D., Madore, B., Marshall, J., Spoon, H., Stierwalt, S., Sturm, E., U, V., Vavilkin, T., and Veilleux, S. (2011). Mid-Infrared Spectral Diagnostics of Luminous Infrared Galaxies. *ApJ*, *730*, 28.

138. Planck Collaboration, Ade, P. A. R., Aghanim, N., Armitage-Caplan, C., Arnaud, M., Ashdown, M., Atrio-Barandela, F., Aumont, J., Aussel, H., Baccigalupi, C., and et al. (2015). Planck 2013 results. XXXII. The updated Planck catalogue of Sunyaev-Zeldovich sources. *A&A*, *581*, A14.

139. Planck Collaboration, Ade, P. A. R., Aghanim, N., Arnaud, M., Ashdown, M., Aumont, J., Baccigalupi, C., Banday, A. J., Barreiro, R. B., Bartolo, N., and et al. (2016). Planck intermediate results. XL. The Sunyaev-Zeldovich signal from the Virgo cluster. *A&A*, *596*, A101.

140. Planck Collaboration, Aghanim, N., Akrami, Y., Ashdown, M., Aumont, J., Baccigalupi, C., Ballardini, M., Banday, A. J., Barreiro, R. B., Bartolo, N., Basak, S., Battye, R., Benabed, K., Bernard, J.-P., Bersanelli, M., Bielewicz, P., Bond, J. R., Borrill, J., Bouchet, F. R., Burigana, C., Calabrese, E., Carron, J., Chiang, H. C., Comis, B., Contreras, D., Crill, B. P., Curto, A., Cuttaia, F., de Bernardis, P., de Rosa, A., de Zotti, G., Delabrouille, J., Di Valentino, E., Dickinson, C., Diego, J. M., Doré, O., Ducout, A., Dupac, X., Elsner, F., Enßlin, T. A., Eriksen, H. K., Falgarone, E., Fantaye, Y., Finelli, F., Forastieri, F., Frailis, M., Fraisse, A. A., Franceschi, E., Frolov, A., Galeotta, S., Galli, S., Ganga, K., Gerbino, M., Górski, K. M., Gruppuso, A., Gudmundsson, J. E., Handley, W., Hansen, F. K., Herranz, D., Hivon, E., Huang, Z., Jaffe, A. H., Keihänen, E., Keskitalo, R., Kiiveri, K., Kim, J., Kisner, T. S., Krachmalnicoff, N., Kunz, M., Kurki-Suonio, H., Lamarre, J.-M., Lasenby, A., Lattanzi, M., Lawrence, C. R., Le Jeune, M., Levrier, F., Liguori, M., Lilje, P. B., Lindholm, V., López-Caniego, M., Lubin, P. M., Ma, Y.-Z., Macías-Pérez, J. F., Maggio, G., Maino, D., Mandolesi, N., Mangilli, A., Martin, P. G., Martínez-González, E., Matarrese, S., Mauri, N., McEwen, J. D., Melchiorri, A., Mennella, A., Migliaccio, M., Miville-Deschênes, M.-A., Molinari, D., Moneti, A., Montier, L. et al. (2017). Planck intermediate results. LIII. Detection of velocity dispersion from the kinetic Sunyaev-Zeldovich effect. *ArXiv e-prints*, .

141. Prochaska, J. X., Hennawi, J. F., and Herbert-Fort, S. (2008). The SDSS-DR5 Survey for Proximate Damped Lyα Systems. *ApJ*, *675*, 1002–1013.

142. Prochaska, J. X., and Tumlinson, J. (2009). Baryons: What,When and Where? *Astrophysics and Space Science Proceedings*, *10*, 419.

143. Prochaska, J. X., Weiner, B., Chen, H.-W., Mulchaey, J., and Cooksey, K. (2011). Probing the Intergalactic Medium/Galaxy Connection. V. On the Origin of Lyα and O VI Absorption at z 0.2. *ApJ*, *740*, 91.

144. Qu, Z., and Bregman, J. N. (2016). A Hot Gaseous Galaxy Halo Candidate with Mg X Absorption. *ApJ*, *832*, 189.

145. Rao, S. M., Nestor, D. B., Turnshek, D. A., Lane, W. M., Monier, E. M., and Bergeron, J. (2003). Low-Redshift Damped Lyα Galaxies toward the Quasars B2 0827+243, PKS 0952+179, PKS 1127-145, and PKS 1629+120. *ApJ*, *595*, 94–108.

146. Rao, S. M., and Turnshek, D. A. (2000). Discovery of DampedLyα Systems at Redshifts Less than 1.65 and Results on Their Incidence and Cosmological Mass Density. *ApJS*, *130*, 1–35.

147. Rasmussen, A., Kahn, S. M., and Paerels, F. (2003). X-ray IGM in the Local Group. In J. L. Rosenberg, and M. E. Putman (Eds.), *The IGM/Galaxy Connection. The Distribution of Baryons at z=0* (p. 109). volume 281 of *Astrophysics and Space Science Library*.

148. Rasmussen, A., Kahn, S. M., Paerels, F., den Herder, J., Kaastra, J., and de Vries, C. (2006). On the Putative Detection ofz0 X-ray Absorption Featuresin the Spectrum of Mrk 421. In *AAS/High Energy Astrophysics Division #9* (p. 354). volume 38 of *Bulletin of the American Astronomical Society*.

149. Rauch, M. (1998). The Lyman Alpha Forest in the Spectra of QSOs. *ARA&A*, *36*, 267–316.

150. Rauch, M., Miralda-Escudé, J., Sargent, W. L. W., Barlow, T. A., Weinberg, D. H., Hernquist, L., Katz, N., Cen, R., and Ostriker, J. P. (1997). The Opacity of the Lyα Forest and Implications for Ω_b and the Ionizing Background. *ApJ*, *489*, 7–20.

151. Reiprich, T. H., and Böhringer, H. (2002). The Mass Function of an X-Ray Flux-limited Sample of Galaxy Clusters. *ApJ*, *567*, 716–740.

152. Riess, A. G., Filippenko, A. V., Challis, P., Clocchiatti, A., Diercks, A., Garnavich, P. M., Gilliland, R. L., Hogan, C. J., Jha, S., Kirshner, R. P., Leibundgut,

B., Phillips, M. M., Reiss, D., Schmidt, B. P., Schommer, R. A., Smith, R. C., Spyromilio, J., Stubbs, C., Suntzeff, N. B., and Tonry, J. (1998). Observational Evidence from Supernovae for an Accelerating Universe and a Cosmological Constant. *AJ*, *116*, 1009–1038.

153. Rines, K., Diaferio, A., and Natarajan, P. (2008). WMAP5 and the Cluster Mass Function. *ApJ*, *679*, L1.

154. Rosenberg, J. L., and Schneider, S. E. (2002). The Arecibo Dual-Beam Survey: The H I Mass Function of Galaxies. *ApJ*, *567*, 247–257.

155. Ryu, D., Ostriker, J. P., Kang, H., and Cen, R. (1993). A cosmological hydrodynamic code based on the total variation diminishing scheme. *ApJ*, *414*, 1–19.

156. Sargent, W. L. W., Boksenberg, A., and Steidel, C. C. (1988). C IV absorption in a new sample of 55 QSOs - Evolution and clustering of the heavy-element absorption redshifts. *ApJS*, *68*, 539–641.

157. Sargent, W. L. W., Young, P. J., Boksenberg, A., and Tytler, D. (1980). The distribution of Lyman-alpha absorption lines in the spectra of six QSOs - Evidence for an intergalactic origin. *ApJS*, *42*, 41–81.

158. Savage, B. D., Kim, T.-S., Wakker, B. P., Keeney, B., Shull, J. M., Stocke, J. T., and Green, J. C. (2014). The Properties of Low Redshift Intergalactic O VI Absorbers Determined from High S/N Observations of 14 QSOs with the Cosmic Origins Spectrograph. *ApJS*, *212*, 8.

159. Savage, B. D., and Lehner, N. (2006). Properties of O VI Absorption in the Local Interstellar Medium. *ApJS*, *162*, 134–160.

160. Savage, B. D., Lehner, N., and Narayanan, A. (2011a). COS Observations of Metal Line and Broad Lyman-α Absorption in the Multi-phase O VI and Ne VIII System at z = 0.20701 toward HE 0226-4110. *ApJ*, *743*, 180.

161. Savage, B. D., Lehner, N., and Narayanan, A. (2011b). COS Observations of Metal Line and Broad Lyman-α Absorption in the Multi-phase O VI and Ne VIII System at z = 0.20701 toward HE 0226-4110. *ApJ*, *743*, 180.

162. Savage, B. D., Lehner, N., Wakker, B. P., Sembach, K. R., and Tripp, T. M. (2005). Detection of Ne VIII in the Low-Redshift Warm-Hot Intergalactic Medium. *ApJ*, *626*, 776–794.

163. Savage, B. D., Narayanan, A., Lehner, N., and Wakker, B. P. (2011c). A Multiphase Absorber Containing O VI and Broad H I Directly Tracing 10^6 K Plasma at Low Redshift Toward HE 0153-4520. *ApJ*, *731*, 14.

164. Savage, B. D., and Sembach, K. R. (1991). The analysis of apparent optical depth profiles for interstellar absorption lines. *ApJ*, *379*, 245–259.

165. Savage, B. D., Sembach, K. R., Tripp, T. M., and Richter, P. (2002). Far Ultraviolet Spectroscopic Explorer and Space Telescope Imaging Spectrograph Observations of Intervening O VI Absorption Line Systems in the Spectrum of PG 0953+415. *ApJ*, *564*, 631–649.

166. Savage, B. D., Tripp, T. M., and Lu, L. (1998). The intervening and associated O VI absorption-line systems in the ultraviolet spectrum of H1821+643. *AJ*, *115*, 436.

167. Schaye, J. (2001). Model-independent Insights into the Nature of the Lyα Forest and the Distribution of Matter in the Universe. *ApJ*, *559*, 507–515.

168. Schmidt, M. (1963). 3C 273 : A Star-Like Object with Large Red-Shift. *Nature*, *197*, 1040.

169. Scott, J., Bechtold, J., Dobrzycki, A., and Kulkarni, V. P. (2000). A Uniform Analysis of the Lyα Forest at z=0-5. II. Measuring the Mean Intensity of the Extragalactic Ionizing Background Using the Proximity Effect. *ApJS*, *130*, 67–89.

170. Sembach, K. R., and Savage, B. D. (1992). Observations of highly ionized gas in the Galactic halo. *ApJS*, *83*, 147–201.

171. Sembach, K. R., Savage, B. D., Shull, J. M., Jenkins, E. B., Murphy, E. M., York, D. G., Ake, T., Blair, W. P., Davidsen, A. F., Friedman, S. D., Gibson, B. K., Kruk, J. W., Moos, H. W., Oegerle, W. R., Sahnow, D., and Sonneborn, G. (2000). Far Ultraviolet Spectroscopic Explorer Observations of O VI in High-Velocity Clouds. *ApJ*, *538*, L31–L34.

172. Sembach, K. R., Wakker, B. P., Savage, B. D., Richter, P., Meade, M., Shull, J. M., Jenkins, E. B., Sonneborn, G., and Moos, H. W. (2003). Highly Ionized High-Velocity Gas in the Vicinity of the Galaxy. *ApJS*, *146*, 165–208.

173. Shen, Y., and Ménard, B. (2012). On the Link between Associated Mg II Absorbers and Star Formation in Quasar Hosts. *ApJ*, *748*, 131.

174. Shull, J. M., Moloney, J., Danforth, C. W., and Tilton, E. M. (2015). The Metagalactic Ionizing Background: A Crisis in UV Photon Production or Incorrect Galaxy Escape Fractions? *ApJ*, *811*, 3.

175. Shull, J. M., Roberts, D., Giroux, M. L., Penton, S. V., and Fardal, M. A. (1999). The Metagalactic Ionizing Radiation Field at Low Redshift. *AJ*, *118*, 1450–1460.

176. Skrutskie, M. F., Cutri, R. M., Stiening, R., Weinberg, M. D., Schneider, S., Carpenter, J. M., Beichman, C., Capps, R., Chester, T., Elias, J., Huchra, J., Liebert, J., Lonsdale, C., Monet, D. G., Price, S., Seitzer, P., Jarrett, T., Kirkpatrick, J. D., Gizis, J. E., Howard, E., Evans, T., Fowler, J., Fullmer, L., Hurt, R., Light, R., Kopan, E. L., Marsh, K. A., McCallon, H. L., Tam, R., Van Dyk, S., and Wheelock, S. (2006). The Two Micron All Sky Survey (2MASS). *AJ*, *131*, 1163–1183.

177. Smette, A., Surdej, J., Shaver, P. A., Foltz, C. B., Chaffee, F. H., Weymann, R. J., Williams, R. E., and Magain, P. (1992). A spectroscopic study of UM 673 A and B - On the size of Lyman-alpha clouds. *ApJ*, *389*, 39–62.

178. Smith, B. D., Hallman, E. J., Shull, J. M., and O'Shea, B. W. (2011). The Nature of the Warm/Hot Intergalactic Medium. I. Numerical Methods, Convergence, and O VI Absorption. *ApJ*, *731*, 6.

179. Songaila, A. (1998). The Redshift Evolution of the Metagalactic Ionizing Flux Inferred from Metal Line Ratios in the Lyman Forest. *AJ*, *115*, 2184–2205.

180. Spinoglio, L., Pereira-Santaella, M., Dasyra, K. M., Calzoletti, L., Malkan, M. A., Tommasin, S., and Busquet, G. (2015). Far-infrared Line Spectra of Seyfert Galaxies from the Herschel-PACS Spectrometer. *ApJ*, *799*, 21.

181. Srianand, R., Petitjean, P., Ledoux, C., Ferland, G., and Shaw, G. (2005). The VLT-UVES survey for molecular hydrogen in high-redshift damped Lyman α systems: physical conditions in the neutral gas. *MNRAS*, *362*, 549–568.

182. stevans, M. L., Shull, J. M., Danforth, C. W., and Tilton, E. M. (2014). HST-COS Observations of AGNs. II. Extended Survey of Ultraviolet Composite Spectra from 159 Active Galactic Nuclei. *ApJ*, *794*, 75.

183. Stocke, J. T., Keeney, B. A., Danforth, C. W., Syphers, D., Yamamoto, H., Shull, J. M., Green, J. C., Froning, C., Savage, B. D., Wakker, B., Kim, T.-S., Ryan-Weber, E. V., and Kacprzak, G. G. (2014). Absorption-line Detections of 10^5-10^6 K Gas in Spiral-rich Groups of Galaxies. *ApJ*, *791*, 128.

184. Strauss, M. A., Weinberg, D. H., Lupton, R. H., Narayanan, V. K., Annis, J., Bernardi, M., Blanton, M., Burles, S., Connolly, A. J., Dalcanton, J., Doi, M., Eisenstein, D., Frieman, J. A., Fukugita, M., Gunn, J. E., Ivezić, Ž., Kent, S., Kim, R. S. J., Knapp, G. R., Kron, R. G., Munn, J. A., Newberg, H. J., Nichol, R. C., Okamura, S., Quinn, T. R., Richmond, M. W., Schlegel, D. J., Shimasaku, K., SubbaRao, M., Szalay, A. S., Vanden Berk, D., Vogeley, M. S., Yanny, B., Yasuda, N., York, D. G., and Zehavi, I. (2002). Spectroscopic Target Selection in the Sloan Digital Sky Survey: The Main Galaxy Sample. *AJ*, *124*, 1810–1824.

185. Stumpff, P. (1980). Two Self-Consistent FORTRAN Subroutines for the Computation of the Earth's Motion. *A&AS*, *41*, 1.

186. Subramaniam, A. (2012). Upcoming Indian facility: UVIT on ASTROSAT. In *Astronomical Society of India Conference Series* (p. 165). volume 4 of *Astronomical Society of India Conference Series*.

187. Sutherland, R. S., and Dopita, M. A. (1993). Cooling functions for low-density astrophysical plasmas. *ApJS*, *88*, 253–327.

188. Swetz, D. S., Ade, P. A. R., Amiri, M., Appel, J. W., Battistelli, E. S., Burger, B., Chervenak, J., Devlin, M. J., Dicker, S. R., Doriese, W. B., Dünner, R., Essinger-Hileman, T., Fisher, R. P., Fowler, J. W., Halpern, M., Hasselfield, M., Hilton, G. C., Hincks, A. D., Irwin, K. D., Jarosik, N., Kaul, M., Klein, J., Lau, J. M., Limon, M., Marriage, T. A., Marsden, D., Martocci, K., Mauskopf, P., Moseley,

H., Netterfield, C. B., Niemack, M. D., Nolta, M. R., Page, L. A., Parker, L., Staggs, S. T., Stryzak, O., Switzer, E. R., Thornton, R., Tucker, C., Wollack, E., and Zhao, Y. (2011). Overview of the Atacama Cosmology Telescope: Receiver, Instrumentation, and Telescope Systems. *ApJS*, *194*, 41.

189. Teng, S. H., Veilleux, S., and Baker, A. J. (2013). Green Bank Telescope Detection of Polarization-dependent H I Absorption and H I Outflows in Local ULIRGs and Quasars. *ApJ*, *765*, 95.

190. Tepper-García, T., Richter, P., and Schaye, J. (2013). Absorption signatures of warm-hot gas at low redshift: Ne VIII. *MNRAS*, *436*, 2063–2081.

191. Tepper-García, T., Richter, P., Schaye, J., Booth, C. M., Dalla Vecchia, C., Theuns, T., and Wiersma, R. P. C. (2011). Absorption signatures of warm-hot gas at low redshift: O VI. *MNRAS*, *413*, 190–212.

192. Thom, C., and Chen, H.-W. (2008a). A Space Telescope Imaging Spectrograph Survey for O VI Absorption Systems at 0.12 z lesssim 0.5. II. Physical Conditions of the Ionized Gas. *ApJS*, *179*, 37–70.

193. Thom, C., and Chen, H.-W. (2008b). A Space Telescope Imaging Spectrograph Survey for O VI Absorption Systems at 0.12 z lesssim 0.5. II. Physical Conditions of the Ionized Gas. *ApJS*, *179*, 37–70.

194. Thom, C., and Chen, H.-W. (2008c). A STIS Survey for O VI Absorption Systems at 0.12 z lesssim 0.5. I. The Statistical Properties of Ionized Gas. *ApJ*, *683*, 22–32.

195. Tinker, J. L., and Conroy, C. (2009). The Void Phenomenon Explained. *ApJ*, *691*, 633–639.

196. Tripp, T. M., Giroux, M. L., Stocke, J. T., Tumlinson, J., and Oegerle, W. R. (2001). The Ionization and Metallicity of the Intervening O VI Absorber at z=0.1212 in the Spectrum of H1821+643. *ApJ*, *563*, 724–735.

197. Tripp, T. M., Meiring, J. D., Prochaska, J. X., Willmer, C. N. A., Howk, J. C., Werk, J. K., Jenkins, E. B., Bowen, D. V., Lehner, N., Sembach, K. R., Thom, C., and Tumlinson, J. (2011). The Hidden Mass and Large Spatial Extent of a Post-Starburst Galaxy Outflow. *Science*, *334*, 952.

198. Tripp, T. M., Savage, B. D., and Jenkins, E. B. (2000). Intervening O VI Quasar Absorption Systems at Low Redshift: A Significant Baryon Reservoir. *ApJ*, *534*, L1–L5.

199. Tripp, T. M., Sembach, K. R., Bowen, D. V., Savage, B. D., Jenkins, E. B., Lehner, N., and Richter, P. (2008). A High-Resolution Survey of Low-Redshift QSO Absorption Lines: Statistics and Physical Conditions of O VI Absorbers. *ApJS*, *177*, 39–102.

200. Tumlinson, J., Peeples, M. S., and Werk, J. K. (2017). The Circumgalactic Medium. *ARA&A*, *55*, 389–432.

201. Tumlinson, J., Werk, J. K., Thom, C., Meiring, J. D., Prochaska, J. X., Tripp, T. M., O'Meara, J. M., Okrochkov, M., and Sembach, K. R. (2011a). Multiphase Gas in Galaxy Halos: The O VI Lyman-limit System toward J1009+0713. *ApJ*, *733*, 111.

202. Tumlinson, J., Werk, J. K., Thom, C., Meiring, J. D., Prochaska, J. X., Tripp, T. M., O'Meara, J. M., Okrochkov, M., and Sembach, K. R. (2011b). Multiphase Gas in Galaxy Halos: The O VI Lyman-limit System toward J1009+0713. *ApJ*, *733*, 111.

203. Turnshek, D. A., Rao, S., Nestor, D., Lane, W., Monier, E., Bergeron, J., and Smette, A. (2001). The z=0.0912 and z=0.2212 Damped Lyα Galaxies along the Sight Line toward the Quasar OI 363. *ApJ*, *553*, 288–298.

204. Verner, D. A., Verner, E. M., and Ferland, G. J. (1996). Atomic Data for Permitted Resonance Lines of Atoms and Ions from H to Si, and S, Ar, Ca, and Fe. *Atomic Data and Nuclear Data Tables*, *64*, 1.

205. Vogelsberger, M., Genel, S., Springel, V., Torrey, P., Sijacki, D., Xu, D., Snyder, G., Nelson, D., and Hernquist, L. (2014). Introducing the Illustris Project: simulating the coevolution of dark and visible matter in the Universe. *MNRAS*, *444*, 1518–1547.

206. Wakker, B. P., Hernandez, A. K., French, D. M., Kim, T.-S., Oppenheimer, B. D., and Savage, B. D. (2015). Nearby Galaxy Filaments and the Ly-alpha Forest:

Confronting Simulations and the UV Background with Observations. *ApJ*, *814*, 40.

207. Wakker, B. P., and Savage, B. D. (2009). The Relationship Between Intergalactic H I/O VI and Nearby (z 0.017) Galaxies. *ApJS*, *182*, 378–467.

208. Wang, Q. D., Yao, Y., Tripp, T. M., Fang, T.-T., Cui, W., Nicastro, F., Mathur, S., Williams, R. J., Song, L., and Croft, R. (2005). Warm-Hot Gas in and around the Milky Way: Detection and Implications of O VII Absorption toward LMC X-3. *ApJ*, *635*, 386–395.

209. Werk, J. K., Prochaska, J. X., Cantalupo, S., Fox, A. J., Oppenheimer, B., Tumlinson, J., Tripp, T. M., Lehner, N., and McQuinn, M. (2016). The COS-Halos Survey: Origins of the Highly Ionized Circumgalactic Medium of Star-Forming Galaxies. *ApJ*, *833*, 54.

210. Werk, J. K., Prochaska, J. X., Thom, C., Tumlinson, J., Tripp, T. M., O'Meara, J. M., and Peeples, M. S. (2013). The COS-Halos Survey: An Empirical Description of Metal-line Absorption in the Low-redshift Circumgalactic Medium. *ApJS*, *204*, 17.

211. Westra, E., Geller, M. J., Kurtz, M. J., Fabricant, D. G., and Dell'Antonio, I. (2010). Empirical Optical k-Corrections for Redshifts. *PASP*, *122*, 1258–1284.

212. Weymann, R. J., Vogel, S. N., Veilleux, S., and Epps, H. W. (2001). A New Observational Upper Limit to the Low-Redshift Ionizing Background Radiation. *ApJ*, *561*, 559–572.

213. Williams, R. J., Mathur, S., and Nicastro, F. (2006). Chandra Detection of Local Warm-Hot Gas toward Markarian 279. *ApJ*, *645*, 179–185.

214. Williams, R. J., Mathur, S., Nicastro, F., Elvis, M., Drake, J. J., Fang, T., Fiore, F., Krongold, Y., Wang, Q. D., and Yao, Y. (2005). Probing the Local Group Medium toward Markarian 421 with Chandra and the Far Ultraviolet Spectroscopic Explorer. *ApJ*, *631*, 856–867.

215. Wolfe, A. M., Gawiser, E., and Prochaska, J. X. (2005). Damped Ly α Systems. *ARA&A*, *43*, 861–918.

216. Wolfe, A. M., Turnshek, D. A., Smith, H. E., and Cohen, R. D. (1986). Damped Lyman-alpha absorption by disk galaxies with large redshifts. I - The Lick survey. *ApJS*, *61*, 249–304.

217. Worseck, G., Fechner, C., Wisotzki, L., and Dall'Aglio, A. (2007). The transverse proximity effect in spectral hardness on the line of sight towards HE 2347-4342. *A&A*, *473*, 805–818.

218. Wright, E. L. (2006). A Cosmology Calculator for the World Wide Web. *PASP*, *118*, 1711–1715.

219. York, D. G., Adelman, J., Anderson, J. E., Jr., Anderson, S. F., Annis, J., Bahcall, N. A., Bakken, J. A., Barkhouser, R., Bastian, S., Berman, E., Boroski, W. N., Bracker, S., Briegel, C., Briggs, J. W., Brinkmann, J., Brunner, R., Burles, S., Carey, L., Carr, M. A., Castander, F. J., Chen, B., Colestock, P. L., Connolly, A. J., Crocker, J. H., Csabai, I., Czarapata, P. C., Davis, J. E., Doi, M., Dombeck, T., Eisenstein, D., Ellman, N., Elms, B. R., Evans, M. L., Fan, X., Federwitz, G. R., Fiscelli, L., Friedman, S., Frieman, J. A., Fukugita, M., Gillespie, B., Gunn, J. E., Gurbani, V. K., de Haas, E., Haldeman, M., Harris, F. H., Hayes, J., Heckman, T. M., Hennessy, G. S., Hindsley, R. B., Holm, S., Holmgren, D. J., Huang, C.-h., Hull, C., Husby, D., Ichikawa, S.-I., Ichikawa, T., Ivezić, Ž., Kent, S., Kim, R. S. J., Kinney, E., Klaene, M., Kleinman, A. N., Kleinman, S., Knapp, G. R., Korienek, J., Kron, R. G., Kunszt, P. Z., Lamb, D. Q., Lee, B., Leger, R. F., Limmongkol, S., Lindenmeyer, C., Long, D. C., Loomis, C., Loveday, J., Lucinio, R., Lupton, R. H., MacKinnon, B., Mannery, E. J., Mantsch, P. M., Margon, B., McGehee, P., McKay, T. A., Meiksin, A., Merelli, A., Monet, D. G., Munn, J. A., Narayanan, V. K., Nash, T., Neilsen, E., Neswold, R., Newberg, H. J., Nichol, R. C., Nicinski, T., Nonino, M., Okada, N., Okamura, S., Ostriker, J. P., Owen, R. et al. (2000). The Sloan Digital Sky Survey: Technical Summary. *AJ*, *120*, 1579–1587.

220. Young, J. S., and Scoville, N. Z. (1991). Molecular gas in galaxies. *ARA&A*, *29*, 581–625.

221. Zwaan, M. A., Briggs, F. H., Sprayberry, D., and Sorar, E. (1997). The H I Mass Function of Galaxies from a Deep Survey in the 21 Centimeter Line. *ApJ*, *490*, 173–186.

222. Zwaan, M. A., Meyer, M. J., Staveley-Smith, L., and Webster, R. L. (2005). The HIPASS catalogue: Ω_{HI} and environmental effects on the HI mass function of galaxies. *MNRAS*, *359*, L30–L34.

223. Zwaan, M. A., and Prochaska, J. X. (2006). Where Is the Molecular Hydrogen in Damped Lyα Absorbers? *ApJ*, *643*, 675–679.

LIST OF PAPERS BASED ON THESIS

1. Detection of two intervening Ne VIII absorbers probing warm gas at z $\sim$ 0.6
   Pachat, S., Narayanan, A., Khaire, V., et al. 2017, MNRAS, 471, 792

2. A pair of O VI and broad Lyα absorbers probing warm gas in a galaxy group environment at z $\sim$ 0.4
   Pachat, S., Narayanan, A., Muzahid, S., et al. 2016, MNRAS, 458, 733